CROSS SECTIONS FOR NEUTRON-DEUTERON ELASTIC SCATTERING IN THE ENERGY RANGE 135–250 MeV

by

Erol Ertan

M.S., Physics, Boğaziçi University, 2007

Submitted to the Institute for Graduate Studies in
Science and Engineering in partial fulfillment of
the requirements for the degree of
Doctor of Philosophy

Graduate Program in Physics
Boğaziçi University
2013

ACKNOWLEDGEMENTS

My biggest thanks go to my thesis supervisor Taylan Akdoğan for his active involvement, patience and constant support in every way. Next, I would like to thank Chair Yani Skarlatos and Dean Gülen Aktaş for providing the financial support for one of my scientific trips. June Matthews helped me elaborate my work and she was kind enough to be a part of my thesis jury.

I am truely grateful to my family and all my friends for their support.

This work was supported in part by the U.S. Department of Energy and the National Science Foundation, the Scientific and Technological Research Council of Turkey (107T538), and Bogazici University Research Fund (BAP6057).

ABSTRACT

CROSS SECTIONS FOR NEUTRON-DEUTERON ELASTIC SCATTERING IN THE ENERGY RANGE 135–250 MeV

New results for neutron-deuteron elastic scattering cross sections at energies from 135 to 250 MeV and center-of-mass angles from 80° to 130° have been measured at the WNR facility of the Los Alamos Neutron Science Center at the Los Alamos National Laboratory [1,2]. The measurements were made with a pulsed neutron beam which allowed the use of time-of-flight techniques and with a cryogenic liquid deuterium and liquid hydrogen target. The neutron-proton elastic cross-section data were used for normalization purposes. An array of pure CsI crystal along with a set of thin scintillator detectors used for charged particle identification on one side of the beam, and a set of long horizontal plastic scintillator bars were used as a neutron detector wall on the other side of the beam. Our measurements are compared to both previous measurements and theoretical predictions at relevant energies and favors the predictions including three-nucleon forces.

ÖZET

135-250 MeV ENERJİ ARALIĞINDA NÖTRON-DÖTERON ESNEK SAÇILMA TESİR KESİTLERİ

Bu calışmada, 135-250 MeV enerji ve 80°-130° kütle merkezi açı aralığındaki nötron-döteron esnek saçılma tesir kesiti ölçümleri Los Alamos Ulusal Laboratuvar'ındaki WNR Tesis'inde yapılmıştır [1, 2]. Ölçümler, uçuş zamanı tekniklerine olanak veren atımlı nötron ışını ve sıvı döteryum ve sıvı hidrojen dolu kriyojenik hedefle yapılmıştır. Nötron-proton esnek saçılma tesir kesiti verileri normalizasyon amacıyla kullanılmıştır. Saf CsI dedektörler ince sintilatörlerle birlikte bir tarafta parçacık tanımlamada kullanılırken, diğer tarafta uzun yatay plastik sintilatör çubukları nötronlari algılamakla görevlidir. Ölçümlerimiz ilgili enerjilerde yapılmış diğer deney verileri ve kuramsal tahminlerle karşılaştırılmıştır ve üçlü nükleon kuvvetini içeren kuramsal tahminleri desteklediği görülmüştür.

TABLE OF CONTENTS

LIST OF FIGURES

LIST OF TABLES

LIST OF ACRONYMS/ABBREVIATIONS

3NF	Three-Nucleon Force
C.M.	Center of Mass
eV	Electron-Volts
MeV	Mega Electron-Volts
LANSCE	Los Alamos Neutron Science Center
NN	Nucleon-Nucleon
WNR	Weapons Neutron Research
QCD	Quantum Chromodynamics
OBE	One-Boson Exchange
LH_2	Liquid Hydrogen
LD_2	Liquid Deuteron
PMT	Photo Multiplier Tube
CsI	Cesium Iodide
ADC	Analog-to-Digital Converter
TDC	Time-to-Digital Converter
CFD	Constant Fraction Discriminator
FIFO	Fan In Fan Out
FERA	Fast Encoding and Read-out ADC
TOF	Time-Of-Flight
mb	mili-barns
KVI	Kern- Pysisch Versneller Institute
MC	Monte Carlo

1. INTRODUCTION

This work presents the results of the analysis of a neutron-deuteron scattering experiment conducted at the LANSCE/WNR facility within the Los Alamos National Laboratory. The primary reaction under investigation is ^{2}H(n, dn) for which the scattered neutrons are detected by a wall of plastic scintillators and the recoil deuterons are captured by CsI scintillators at five different angles giving us an angular range of about 80° to 130° in the center-of-mass frame. The incident neutron beam has a continuous energy spectrum from as low as a few MeV up to about 800 MeV. We present absolute cross-section results in the energy from 135 MeV to 250 MeV. The main purpose of the study is to compare the experimental results with theoretical predictions in the cross-section minima with or without the inclusion of a three-nucleon force (3NF).

1.1. Theory

According to Yukawa's proposal, the nucleon-nucleon (NN) interactions are mediated by mesons, but now it is known that the interactions among the constituents of nucleons, the quarks, are responsible for nuclear force through so called color exchange. Quantum chromodynamics (QCD) is the underlying physics explaining this interaction, however, performing such calculation in QCD is extremely difficult due to the degrees of freedom involved in such calculations and the fact that QCD is nonperturbative in the energy regime of interest. Therefore, Yukawa's idea of meson exchange is still the best tool to explain NN interactions. There are different approaches, but the most commonly employed method is to build models, usually called "bag models" [22], since the interaction is modeled to be confined within a radius. These models aim to realize the characteristics of the nuclear force for different ranges, namely a repulsive core, an attractive region and a long range part typically characterized by one boson exchange as depicted in Figure 1.1 [7]. In modern models, all possible bosons are included and multi-boson exchange is also included.

The models for the interaction potential between two nucleons, like the ones in

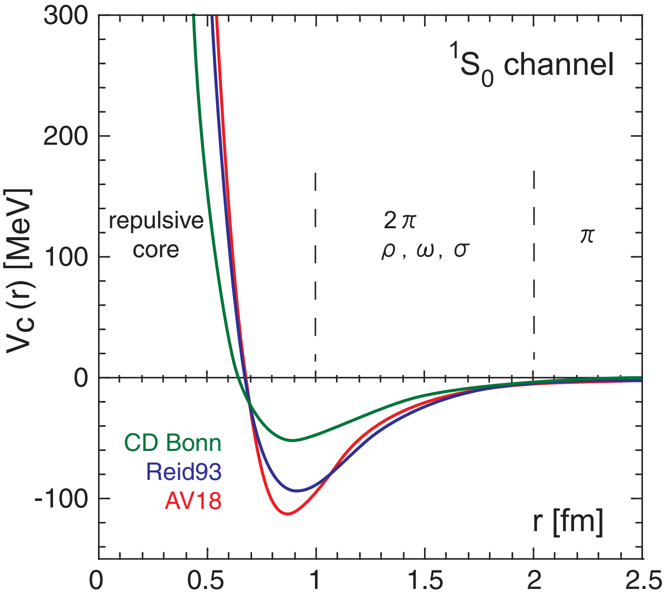

Figure 1.1. The nucleon-nucleon potential outained by modern models CD-Bonn [3], Reid93 [4] AV18 [5].

Figure 1.1, are consistent with the experiments to a great extent, however, the results cannot be reproduced for the interactions including three nucleons with these potential models especially around the region where the Nd scattering cross section is minimum. Since the late 1930's, it is known that many-body potentials cannot be represented using a sequence of two-body potentials [23] as there are some irreducible properties unique to the number of particles. Furthermore, the binding energies of the 3N bound systems (^{3}H and ^{3}He) is indescribable by only nucleon-nucleon models [24–26]. This leads to two main conclusions. Either the models that are believed to be correct are missing some aspects of the two-nucleon interaction or the three-nucleon interaction has a significant effect for, at least, some energy range. The latter is believed to be the case. For either case, experimental results are essential to put the model driven theory to test which eventually leads to an understanding of the nature of the interaction.

The Fujita-Miyazawa force [27], which incorporates two pion exchange with an intermediate delta excitation as in Figure 1.2, laid a foundation for more advanced models like the Tucson-Melbourne model [28, 29] and the Urbana-Argonne force [30, 31]. These models are the generalized forms of the previously mentioned nucleon-nucleon potentials where there is an additional term representing the 3NF besides the 2NF's between the nucleons in the Schrodinger's equation. Moreover, these models also consider more subtle aspects of 3NF like chiral symmetry breaking, charge dependence, etc. and serve as a comparison basis for the experimental findings.

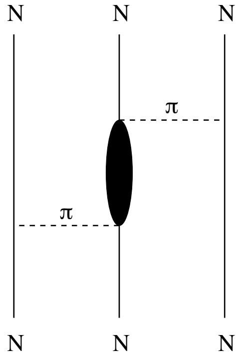

Figure 1.2. Feynman diagram representing 2-π exchange model for 3NF.

1.1.1. Faddeev Formalism

The potentials based on the aforementioned models are then incorporated in what is known as Faddeev Formalism [32] where the hamiltonian of the three-body interaction can be written as

$$H = H_0 + \sum_{i<j} V_{ij} + \sum_{i=1}^{3} V_4^{(i)} \tag{1.1}$$

where H_0 is the free hamiltonian or kinetic energy, V_{ij}'s are the two-body forces and $V_4^{(i)}$ is the decomposed 3NF force. The only condition on the decomposition of the 3NF is that the parts $V_4^{(i)}$ should be symmetric under the exchange of nucleons jk. The two-nucleon potentials can be denoted as the index of the non-interacting nucleon, namely, $V_k \equiv V_{ij}$.

The aim of the procedure is to calculate the transition amplitude from the initial state $|\phi\rangle = |\phi_d, q_0\rangle$, where ϕ_d is the deuteron wave function and q_0 represents the incoming nucleon to the final state $|\phi'\rangle$. Here, we will focus on elastic scattering in which the magnitude of the momentum of the incident and the scattered nucleon are the same. Writing Schrödinger equation for the hamiltonian in Equation 1.1 yields

$$\left(H_0 + \sum_{i=1}^{3} (V_i + V_4^{(i)})) \right) |\psi^+\rangle = E\, |\psi^+\rangle \tag{1.2}$$

leading to

$$|\psi^+\rangle = G_0 \sum_{i=1}^{3} (V_i + V_4^{(1)})\, |\psi^+\rangle \tag{1.3}$$

where

$$G_0 = \frac{1}{E - H_0 + i\epsilon}.$$

Equation 1.3 is the Lippmann-Schwinger equation for the total scattering state. Faddeev defined [32] the decomposition of the total wave function as

$$|\psi^+\rangle = \sum_{i=1}^{3} |\psi_i^+\rangle\,. \tag{1.4}$$

When (1.4) is inserted in (1.3), we obtain

$$|\psi_i^+\rangle = G_0(V_i + V_4^{(i)})\, |\psi^+\rangle = G_0(V_i + V_4^{(i)})\, |\psi_i^+\rangle + G_0(V_i + V_4^{(i)}) \sum_{i \neq j} |\psi_j^+\rangle\,. \tag{1.5}$$

Further manipulation leads to

$$\begin{aligned} (1 - G_0 V_i)\, |\psi_i^+\rangle &= G_0 V_4^{(i)}\, |\psi_i^+\rangle + G_0 V_i \sum_{i \neq j} |\psi_j^+\rangle + G_0 V_4^{(i)} \sum_{i \neq j} |\psi_j^+\rangle \\ &= G_0 V_i \sum_{i \neq j} |\psi_j^+\rangle + G_0 V_4^{(i)} \sum_{j} |\psi_j^+\rangle \end{aligned} \tag{1.6}$$

which, in turn, results in

$$|\psi_i^+\rangle = (1 - G_0V_i)^{-1}G_0V_i \sum_{i\neq j} |\psi_j^+\rangle + (1 - G_0V_i)^{-1}G_0V_4^{(i)} \sum_j |\psi_j^+\rangle\,. \tag{1.7}$$

These equations can be simplified by use of two-body Lippmann-Schwinger transition operators [33]

$$t_i = V_i + V_iG_0t_i. \tag{1.8}$$

Then, the equalities

$$\begin{aligned}(1 - G_0V_i)^{-1} &= 1 + G_0V_i + G_0V_iG_0V_i + \ldots. \\ &= 1 + G_0(V_i + V_iG_0V_i + V_iG_0V_iG_0V_i + \ldots.) \\ &= 1 + G_0t_i \end{aligned}\tag{1.9}$$

and

$$\begin{aligned}(1 - G_0V_i)^{-1}G_0V_i &= G_0V_i + G_0t_iG_0V_i = G_0V_i + G_0V_iG_0V_i + G_0V_iG_0V_iG_0V_i \\ &= G_0(V_i + V_iG_0V_i + V_iG_0V_iG_0V_i + \ldots.) \\ &= G_0t_i \end{aligned}\tag{1.10}$$

are substituted into Equation 1.7 to write the coupled homogeneous Faddeev equations in the following form:

$$|\psi_i^+\rangle = G_0\left(t_i \sum_{i\neq j} |\psi_j^+\rangle + (1 + t_iG_0)V_4^{(i)} \sum_j |\psi_j^+\rangle\right). \tag{1.11}$$

The nucleons are treated as identical particles aside from the third component of isospin, therefore, the functional form of the wave functions should be the same and one can obtain all the wavefunctions by merely permuting the particles without disrupting the original symmetry of the system. This is achieved through permutation operators as in

$$|\psi_2^+\rangle = P_{12}P_{23}\,|\psi_1^+\rangle\,, \quad |\psi_3^+\rangle = P_{13}P_{23}\,|\psi_1^+\rangle \tag{1.12}$$

leading to

$$|\psi_1^+\rangle = G_0 t_1 P\,|\psi_1^+\rangle + G_0(1+t_1G_0)V_4^{(1)}(1+P)\,|\psi_1^+\rangle \tag{1.13}$$

where $P = P_{12}P_{23} + P_{13}P_{23}$.

We have to impose the boundary condition arising from the initial channel state $|\phi_1\rangle = |\phi_d, q_0\rangle$ which has the hamiltonian $H_1 = H_0 + V_1$ assuming the particle 1 initiated the scattering. Dropping the subscripts, the full equation for the Faddeev component of the scattering state becomes

$$|\psi^+\rangle = |\phi\rangle + G_0 tP\,|\psi^+\rangle + G_0(1+tG_0)V_4^{(1)}(1+P)\,|\psi^+\rangle\,. \tag{1.14}$$

The presence of $|\phi\rangle$ does not disrupt the equations governing $|\psi^+\rangle$ which can be clearly seen by inspecting Equation 1.7 and by the fact that $(1 - G_0V_i)^{-1}\,|\phi_i\rangle = 0$.

The total transition operator T is defined as

$$|\psi^+\rangle = |\phi\rangle + G_0T\,|\phi\rangle\,, \tag{1.15}$$

thus, using Equation 1.14 we obtain

$$T\,|\phi\rangle = tP\,|\psi^+\rangle + (1+tG_0)V_4^{(1)}(1+P)\,|\psi^+\rangle\,. \tag{1.16}$$

Inserting Equation 1.15 into 1.16 and dropping $|\phi\rangle$, we get

$$T = tP + (1+tG_0)V_4^1(1+P) + tPG_0T + (1+tG_0)V_4^1(1+P)G_0T. \tag{1.17}$$

The condition related to the elastic interaction has not been introduced yet, therefore, this total transition operator includes break-up precesses, too. The condition for elastic scattering is that the channel propagator

$$G_i = \frac{1}{E - H_0 - V_i + i\epsilon}$$

is explicit and the elastic transition operator is defined as

$$|\psi^+\rangle = |\phi\rangle + GU\,|\phi\rangle\,. \tag{1.18}$$

T and U can be related using the free propagator and the two-body transition operator. Using

$$\begin{aligned} G_0 t_i &= G_0 V_i + G_0 V_i G_0 V_i + ... = (G_0 + G_0 V_i G_0 + ...)V_i \\ &= G_i V_i \end{aligned} \tag{1.19}$$

and

$$\begin{aligned} G_0(1 + t_i G_0) &= G_0 + G_0 t_i G_0 = G_0 + G_0(V_i + V_i G_0 V_i + ...)G_0 \\ &= G_0 + G_0 V_i G_0 + ... = G, \end{aligned} \tag{1.20}$$

Equation 1.14 can be rewritten as

$$|\psi^+\rangle = |\phi\rangle + GVP\,|\psi^+\rangle + GV_4^{(1)}(1+P)\,|\psi^+\rangle\,. \tag{1.21}$$

Comparing this with the definition of the elastic transition operator, we deduce

$$U\,|\phi\rangle = VP\,|\psi^+\rangle + V_4^{(1)}(1+P)\,|\psi^+\rangle\,. \tag{1.22}$$

Recalling that $\langle\phi| V = \langle\phi| G_0^{-1}$ for elastic channel, Equation 1.22 becomes

$$U|\phi\rangle = G_0^{-1}P|\psi^+\rangle + V_4^{(1)}(1+P)|\psi^+\rangle\,. \tag{1.23}$$

Lastly, Equation 1.15 can be plugged in to obtain

$$U = PG_0^{-1} + V_4^1(1+P) + V_4^1(1+P)G_0T + PT. \tag{1.24}$$

Further inspecting Equation 1.24, the first term corresponds to the nucleon exchange term, the second term is the pure 3NF term and the rest is mixed.

Equation 1.17 can be solved in an iterative manner. The chosen basis for this calculation is given in Equation 1.25 and the quantum numbers are illustrated in Figure 1.3.

$$\begin{aligned} |pq\alpha\rangle &\equiv |p(ls)j\,q(\lambda\frac{1}{2})IJM(t\frac{1}{2})TM_T\rangle \\ &= |p(ls)j\rangle\,|q(\lambda\frac{1}{2})I\rangle\,|JM\rangle\,|(t\frac{1}{2})TM_T\rangle\,. \end{aligned} \tag{1.25}$$

The momenta in the basis are the Jacobi momenta [34] which are expressed as follows:

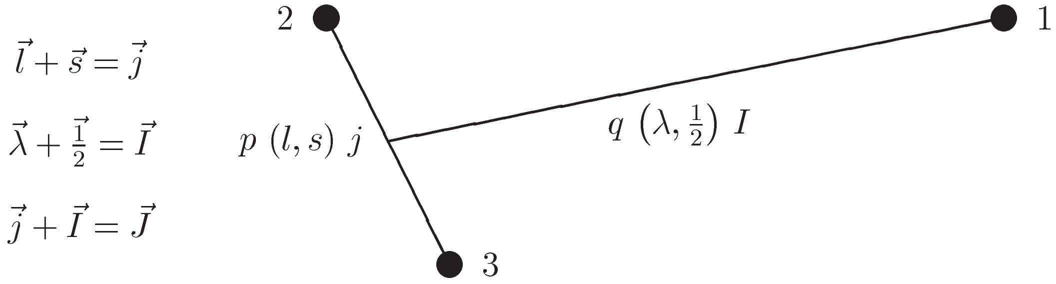

Figure 1.3. The Jacobi momenta and the quantum numbers [6].

$$\begin{aligned} \mathbf{p_i} &\equiv \frac{1}{2}(\mathbf{k_j}-\mathbf{k_k}) \\ \mathbf{q_i} &\equiv \frac{2}{3}\left(\mathbf{k_i}-\frac{1}{2}(\mathbf{k_j}+\mathbf{k_k})\right) \end{aligned} \tag{1.26}$$

meaning p_i are the relative momenta in the jk subsystem and q_i are the momenta of the i^{th} particle with respect to the center of mass of the jk subsystem. $|(l,s)j\rangle$ stands for the angular momentum, spin and total angular momentum state of the subsystem whereas $|(\lambda,\frac{1}{2})I\rangle$ represent that for the incident particle. $|JM\rangle$ is the total angular momentum state of the system and $|(t\frac{1}{2})TM_T\rangle$ symbolizes the isospin quantum numbers of the whole system. In the end, the basis state and the initial state act on the T operator, $\langle pq\alpha| T |\phi\rangle$, to extract the amplitudes.

Although the limits of the integrals one comes across in this calculation extend to infinity, truncation is possible due to the short-ranged nature of the nucleon-nucleon force [6]. Nevertheless, the truncated system is also far from directly solvable, therefore iterative methods are utilized. Our basic Equation 1.17 can be written as

$$T = T_0 + KT \tag{1.27}$$

where

$$T_0 = tP + (1 + tG_0)V_4^1(1 + P) \tag{1.28}$$

and

$$K = tPG_0 + (1 + tG_0)V_4^1(1 + P)G_0. \tag{1.29}$$

This equation can be iterated in the following manner

$$T = T_0 + KT_0 + K^2T_0 + ... \tag{1.30}$$

This series converges for some specific quantum numbers and can be summed using special methods [6,34].

1.1.2. Modern 2N and 3N Potentials

Now that we are in a position to calculate the transition amplitudes, we need to insert the NN and 3N potentials. The most famous of the NN potentials, also known as the realistic potentials, are Nijmegen [4, 35], CD Bonn [3] and Argonne [5] potentials. The Nijmegen group concentrated on one-boson exchange (OBE) including scalar, vector and pseudo-scalar mesons and used Regge Pole theory to calculate the amplitudes. The Bonn group utilized field theoretic perturbation theory for OBE amplitudes and the potential is charge dependent needing only six parameters which are the coupling constants of the nucleon-meson-nucleon/isobar vertices and the cut-off parameters. The Argonne potential is composed of a one-pion exchange part which is responsible for the long range behaviour and a phenomenological part taking care of short and intermediate range behaviour with the incorporation of central, orbital, tensor and spin-orbit terms.

As for the 3N potentials, Fujita and Miyazawa [27] laid the foundation for later studies by introducing 2π exchange with an intermediate Δ isobar as in Figure 1.4. The potential resulting from this interaction is given by Equation 1.31

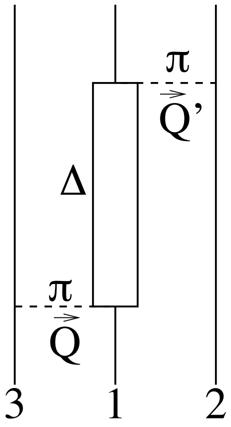

Figure 1.4. Feynman diagram Fujita-Miyazawa 2-π exchange model for 3NF [6].

$$\begin{aligned} V_4^1 &\sim \frac{\boldsymbol{\sigma_2} \cdot \mathbf{Q}}{\mathbf{Q}^2 + m_\pi^2} \frac{\boldsymbol{\sigma_3} \cdot \mathbf{Q}'}{\mathbf{Q}'^2 + m_\pi^2} \frac{1}{m_\Delta^2 - Q_\Delta} \\ &\times \left\{ \frac{16}{9} \boldsymbol{\tau_2} \cdot \boldsymbol{\tau_3} \mathbf{Q} \cdot \mathbf{Q}' + \frac{4}{9} \boldsymbol{\tau_3} \otimes \boldsymbol{\tau_2} \cdot \boldsymbol{\tau_1} \boldsymbol{\sigma_1} \cdot \mathbf{Q} \otimes \mathbf{Q}' \right\} \end{aligned} \tag{1.31}$$

where Q_Δ and m_Δ are the isobar's momentum and mass, respectively, $\sigma_{\mathbf{i}}$ and $\tau_{\mathbf{i}}$ are spin and isospin of the nucleon i. The pion momenta $\mathbf{Q}$ and $\mathbf{Q}'$ are defined as

$$\begin{aligned}
\mathbf{Q} &= \mathbf{p} - \mathbf{p}' - \frac{1}{2}(\mathbf{q} - \mathbf{q}') \\
\mathbf{Q}' &= \mathbf{p} - \mathbf{p}' + \frac{1}{2}(\mathbf{q} - \mathbf{q}')
\end{aligned} \tag{1.32}$$

where $(\mathbf{p}, \mathbf{q})$ and $(\mathbf{p}', \mathbf{q}')$ are the Jacobi momenta of the incoming and outgoing nucleons, respectively.

The Tucson-Melbourne (TM) potential is formed taking this idea further by generalizing the intermediate excited state to any state achievable by a π-N interaction [28]. Then the modified potential becomes

$$\begin{aligned}
V_4^1 &= \frac{1}{(2\pi)^6} \frac{g_{\pi NN}^2}{4m_N^2} \frac{\sigma_{\mathbf{2}} \cdot \mathbf{Q}}{\mathbf{Q}^2 + m_\pi^2} \frac{\sigma_{\mathbf{3}} \cdot \mathbf{Q}'}{\mathbf{Q}'^2 + m_\pi^2} H(\mathbf{Q}^2) H(\mathbf{Q}^2) \\
&\times \left\{ \tau_{\mathbf{2}} \cdot \tau_{\mathbf{3}} [a + b\mathbf{Q} \cdot \mathbf{Q}' + c(\mathbf{Q}^2 + \mathbf{Q}'^2)] + id\tau_{\mathbf{3}} \otimes \tau_{\mathbf{2}} \cdot \tau_{\mathbf{1}} \sigma_{\mathbf{1}} \cdot \mathbf{Q} \otimes \mathbf{Q}' \right\}
\end{aligned} \tag{1.33}$$

where the constants a, b, c, d are the constants given in terms of m_π and $g_{\pi NN}^2$ is the $\pi - N$ coupling constant. The form factor $H(\mathbf{Q}^2)$ is parametrized as

$$H(\mathbf{Q}^2) = \left(\frac{\Lambda^2 - m_\pi^2}{\Lambda^2 + \mathbf{Q}^2} \right)^2 \tag{1.34}$$

with Λ being the strength factor fixed by ^{3}H binding energy. Other meson exchanges like π-ρ and ρ-ρ are also considered while their effects are minor at long ranges [29, 36–38].

The TM potential should be modified due to the violation of chiral symmetry [39, 40]. The a and c parameter terms can be altered to satisfy chiral symmetry with the c term gaining two characteristic parts, one for short range and one for long range. These modifications also lead to changes in the the values of these parameters. One of the forms after these modifications is now known as TM′ [40].

Another well-known 3NF potential is Urbana IX 3NF [31] where the traditional Fujita-Miyazawa approach is combined with a spin and isospin independent short range part, namely

$$V_4^1 = V_4^{1^{2\pi}} + V_4^{1^R}, \tag{1.35}$$

$$V_4^{1^{2\pi}} = A_{2\pi}\left(\{X_{12}, X_{13}\}\{\boldsymbol{\tau_1}\cdot\boldsymbol{\tau_2}, \boldsymbol{\tau_1}\cdot\boldsymbol{\tau_3}\} + \frac{1}{4}[X_{12}, X_{13}][\boldsymbol{\tau_1}\cdot\boldsymbol{\tau_2}, \boldsymbol{\tau_1}\cdot\boldsymbol{\tau_3}]\right), \tag{1.36}$$

$$X_{ij} = \frac{e^{-m_\pi r_{ij}}}{m_\pi r_{ij}}(1-e^{-cr_{ij}^2})\sigma_\mathbf{i}\cdot\sigma_\mathbf{j} + \left(1 + \frac{3}{m_\pi r_{ij}} + \frac{3}{(m_\pi r_{ij})^2}\right)\frac{e^{-m_\pi r_{ij}}}{m_\pi r_{ij}}(1-e^{-cr_{ij}^2})S_{ij}. \tag{1.37}$$

S_{ij} is the standard tensor force and the $(1-e^{-cr_{ij}^2})$ part is the short range cut-off. The other part of the potential is expressed as

$$\begin{aligned} V_4^{1^R} &= U_0\left(\left(1 + \frac{3}{m_\pi r_{12}} + \frac{3}{(m_\pi r_{12})^2}\right)\frac{e^{-m_\pi r_{12}}}{m_\pi r_{12}}(1-e^{-cr_{12}^2})\right)^2 \\ &\times \ (\text{same} \quad \text{term}(12) \rightarrow (13)). \end{aligned} \tag{1.38}$$

The free parameters $A_{2\pi}$ and U_0 are again fixed using the experimental ^{3}H binding energy.

All in all, the transition amplitudes can be calculated choosing one of these potential models. See [6] and [41] for further details, calculation methods and some results.

1.1.3. Lattice QCD

Aside from the phenomenological approach, it is perhaps possible to compute the nuclear potential from the first principles via Lattice QCD methods. The basic idea is to calculate the propagation of wave functions or fields, namely the path integrals, on a discrete space-time lattice. The probability amplitude for the transition from initial to final state can be given by a weighted sum [42]

$$\langle x_f(t_f)|x_i(t_i)\rangle \sim \sum_{paths(x,\dot{x})} \exp\left(iS(x(t),\dot{x}(t))\right) \tag{1.39}$$

where S is the action defined as

$$S \equiv \int_{t_i}^{t_f} dtL[x(t),\dot{x}(t)].$$

A similar equation can be written for fields which are functions of both space and time:

$$\langle \phi(x,t_f)|\phi(x,t_i)\rangle \sim \sum_{paths(\phi,\partial_\mu\phi)} \exp\left(iS(\phi_P,\partial_\mu\phi_P\right). \tag{1.40}$$

Discretization of the space-time coordinates leads to

$$\langle \phi(x,t_f)|\phi(x,t_i)\rangle \sim \lim_{N_x\to\infty,N_t\to\infty} \int \prod_m^{N_x}\prod_n^{N_t} d\phi(x_m,t_n)\exp\left(iS(\phi(x_m,t_n),\partial_\mu\phi(x_m,t_n)\right). \tag{1.41}$$

For QCD, equally spaced hyper-cubic discretization is utilized such that

$$x_\mu \to (te_0 + ie_1 + je_2 + ke_3)a$$

where a is the lattice spacing. With this, quark and gluon fields are inserted and the calculations are carried out. Even with the finite space-time lattice spacing, the calculations are not doable, however, most of the observables depend on a small number of points which opens up the possibility to use Monte Carlo methods using Metropolis Algorithm [43], etc.

Using these basic principles, it is possible to calculate the NN potential. Ishii and co-workers published such a study [7] where they present the NN potential for two channels calculated using lattice QCD. Their results can be seen in Figure 1.5.

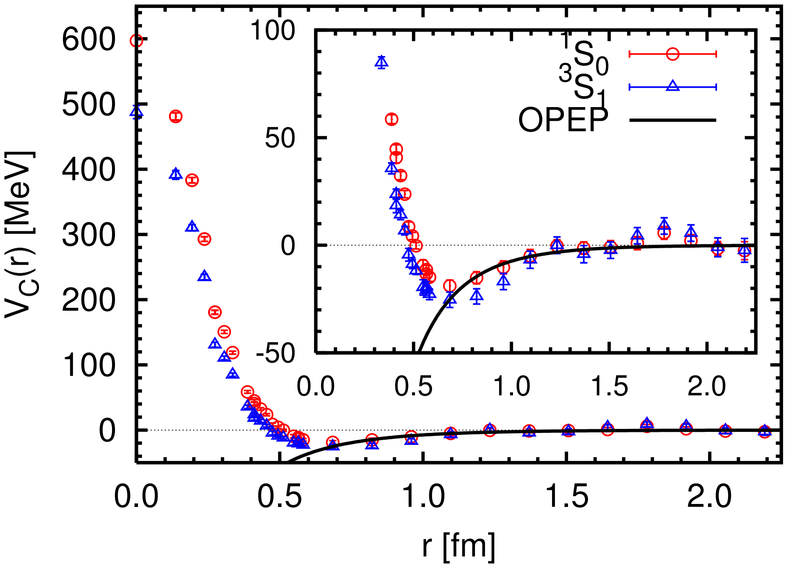

Figure 1.5. The nucleon-nucleon potential presented by [7] for the channels $^1S_0$ and $^3S_1$. Solid line is the one boson exchange potential.

1.2. Previous Experiments

Several experiments have been performed previously to investigate three-nucleon interaction mostly using proton beam, i.e. $d(p, dp)$. A summary of what has been measured before our study will be given in this section.

J. N. Palmieri and his colleagues presented the results of the experiments using mono-energetic neutron beam of 152 MeV at the Harvard University Cyclotron [12] in 1972. Similar to our study, they both used liquid hydrogen and liquid deuterium targets inside a vertical cylinder with a diameter of 5cm and a length of 7.7cm covered by kapton polyimide film of 0.005cm in thickness. The charged particle detectors were NaI crystals and the angular resolution was about 2° which changes with respect to the angle. They measured the differential cross section for the deuteron recoil angle range of 10° to 80° in the center-of-mass frame. The cross-section results have on average 8% total error. They found that the neutron-deuteron cross-section results are in agreement with those of deuteron-proton elastic collision, the small disagreement at the backward angles is discussed to be the result of "Coulomb effects".

R. E. Adelberger and C. N. Brown published the results of an experiment conducted at the Rochester 130-inch cyclotron investigating the *p*-*d* elastic cross section [15] using a polarized proton beam of 198 ± 6 MeV energy. The signature of the elastic events was the high energy deuterons in the forward direction whose energy were determined by time of flight and energy deposited in the plastic scintillators. The cross-section results covered from 80 to 180° and included an average error of about 5%. These results were used to test their one-nucleon-exchange model and the need for more data was expressed.

The reaction $^1H(d, dp)$ was investigated by G. Igo *et al.* and the elastic cross section was measured for the recoil proton lab angle range of 0-30° using a deuteron beam with the energies 433, 362 and 291 MeV [14]. They attempted to test the nucleon-exchange models that predicts a rapid decrease of differential cross section at recoil proton angle 180 in the center-of-mass frame with increasing energy and to find a way of calculating the deuteron D-state probability. The energy of the beam was obtained with the help of a set of copper degraders and both the energy and the orientation of the beam were continuously monitored throughout the experiment. The beam had a width of 5.6 cm and 7.6 cm, and a height of 7.6 cm and 12 cm at the target, the former numbers correspond to the core and the latter to the tail. High energy recoil protons were detected with Ne-102 plastic scintillators and matched with the coinciding deuterons while the quasi elastic protons were filtered out by a degrader. The results had total error of 5-10% depending on the angle. The results showed clear indication that the D-state dominates in the region of interest and the calculation of D-state probability would be addressed next.

The RIKEN Accelerator Facility hosted another experiment where a deuteron beam with vector and tensor polarization of 135 MeV/N is used. H. Sakai *et al.* [18] analyzed the data and obtained differential cross section and analyzing powers for the reaction ^{1}H(d, pd) for an angle range of 10° to 180°. The momentum of the deuteron or the scattered proton from a CH_2 target of thickness 46.7 mg/cm^2 was analyzed by the magnetic spectrometer SMART. The results came with statistical uncertainty of less than 1.3% and systematic uncertainty of less than 2%. The inclusion of 3NF in the theoretical models shows great agreement with the cross-section results, however there are still some discrepancies when it comes to the tensor analyzing power.

Another experiment took place at KVI (Kern-Pysisch Versneller Institute) whose results were presented by K. Ermisch *et al.* [44] in 2003 and in 2005 [10]. Polarized proton beams from the AGOR cyclotron were used at the energies 108, 120, 135, 150, 170 and 190 MeV. The targets were mixed solid CD_2-CH_2. The target thickness was calibrated by comparing the results of proton-proton elastic scattering with several calculations. The differential cross section for a wide range of angles has been obtained along with the analyzing power to monitor the polarization of the beam. The results had 2% and 7% statistical and systematic uncertainty, respectively. The conclusion was that even though the inclusion of 3N effects improve the agreement of calculations with the findings, for some specific angle ranges the disagreement is considerable.

At KVI , using Big Instrument for Nuclear-polarization Analysis (BINA), Ramazani-Moghaddam-Arani and his team investigated the reactions ^{2}H(p, dp) with a proton-beam energy of 135 MeV [11]. The target was liquid deuterium with 3.85mm thickness and they presented differential cross section for scattering angles between 120° to 160° in the center-of-mass frame. The systematic uncertainties were found using a deuteron beam of the same energy, which leads to the inverse reaction ^{1}H(d, dp), and by the fact that the cross section at this energy is known. BINA has almost full geometrical acceptance, consisting of a forward part which includes Multi-Wire Proportional Chamber, vertical thin (2 mm) scintillators and horizontal thick (12 cm) scintillators and a backward part which is made of phoswich scintillators covering 40° to 165°. The beam is polarized protons whose typical current is 15 pA. The meaningful events were extracted via coincidence of deuterons in the forward part with a proton in the backward part. The results for the elastic cross section with 6% systematics clearly exceed the predictions and the other KVI measurements.

Hatanaka *et al.* measured the *pd* elastic cross section along with other spin observables at 250 MeV at Research Center for Nuclear Physics (RCNP), Osaka in 2002 [16]. They used a proton beam of alternating polarization with a period of 20 seconds. The target was isotopically enriched deuterated polyethylene foils (CD_2) with an areal density of 44 mg/cm^2 and the carbon scattering background was measured using a pure carbon target. The constant scattering rate was monitored using a large acceptance spectrometer spectrometer (LAS). The effective target thickness was found employing a *pp* analysis and comparing the cross sections with SAID [45] as well as with a Monte Carlo simulation. The systematic errors in the experiment are due to the normalization and inhomogeneity of the target, 3% and 2.5%, respectively. The obtained cross sections are in agreement with the predictions in the forward angle region and around the minima but discrepancies are observed in the backward angle region which authors suggest are due to relativistic effects as the disagreement increases with increasing energy.

RCNP hosted another experiment carried out by Maeda *et al.* [17]. The *nd* elastic cross section and analyzing powers were measured at 248 ± 2 MeV where the neutron beam was produced by the ^{7}Li($\vec{p}$, $\vec{n}$)^{7}Be reaction, the polarized proton beam supplied by the high intensity polarized ion source (HIPIS). The targets used were deuterated polyethylene foils (CD_2) with an areal density of 100-220 mg/cm^2 and polyethylene films (CH_2) with an areal density of 90-190 mg/cm^2. The scattering cross sections were measured with a nearly full angular coverage where the statistical and systematic errors were 5-9% and 15%, respectively. These measurements agree well with [16] and the discrepancy in the backward angle region is thought to be due to the lack of explicit inclusion of heavier meson exchange and relativistic effects.

Let us summarize the topics that will be discussed in this thesis. In Chapter 2, the beam production, target detectors and their electronics will be explained in the light of [2]. The timing calibration which is very crucial since all the energies are derived from this information, the beam flux, the energy loss estimation, target thickness normalization as it is unknown due to some physical effects, neutron efficiency measurement, neutron-deutron elastic cross-section results and polarization correction will be presented in Chapter 3. The results will be presented in Section 3.9. We will discuss our findings in Chapter 4. In the appendices, we will discuss in detail the analysis steps, target geometry deformation, the kinematical calculations and a brief explanation of

Monte Carlo simulation.

2. THE EXPERIMENT

The experiment was conducted at the Los Alamos Neutron Science Center (LANSCE) of the Los Alamos National Laboratory. The production of the white neutron beam is achieved by bombarding a tungsten spallation target with an unpolarized proton (H^-) beam which is accelerated to 800 MeV by LANSCE linear accelerator. The flux of the neutron beam was monitored by a ^{238}U foil fission chamber. The primary target in the experiment was liquid deuterium (LD_2) while liquid hydrogen (LH_2) was also used for normalization purposes. The charged particles were detected by an array of cesium-iodide telescopes, spanning from 24 to 54° in the laboratory frame, in coincidence with the neutrons which were detected by a wall of plastic scintillators. The data acquisition was performed using standard NIM and CAMAC modules. This chapter will continue with the detailed information of the components of the experiment which will be followed by data acquisition and trigger electronics.

Figure 2.1 shows the fission chamber, target, charged particle detectors, ΔE and veto detectors along with some dimensions and the PMTs attached to them in a not-to-the-scale manner. Each of the main components will be introduced in the following sections.

Table 2.1 lists average laboratory and c.m. angles for both deuteron and neutron. The smallest laboratory deuteron angle corresponds to largest neutron angle which is referred as “backward neutron angle” and vice versa.

Table 2.1. The average angles in lab and center-of-mass frames.

θ_d (Lab)	**θ_n (Lab)**	**θ_n (c.m.)**
24	100	131
30	86	119
36	75	107
42	65	95
48	56	83

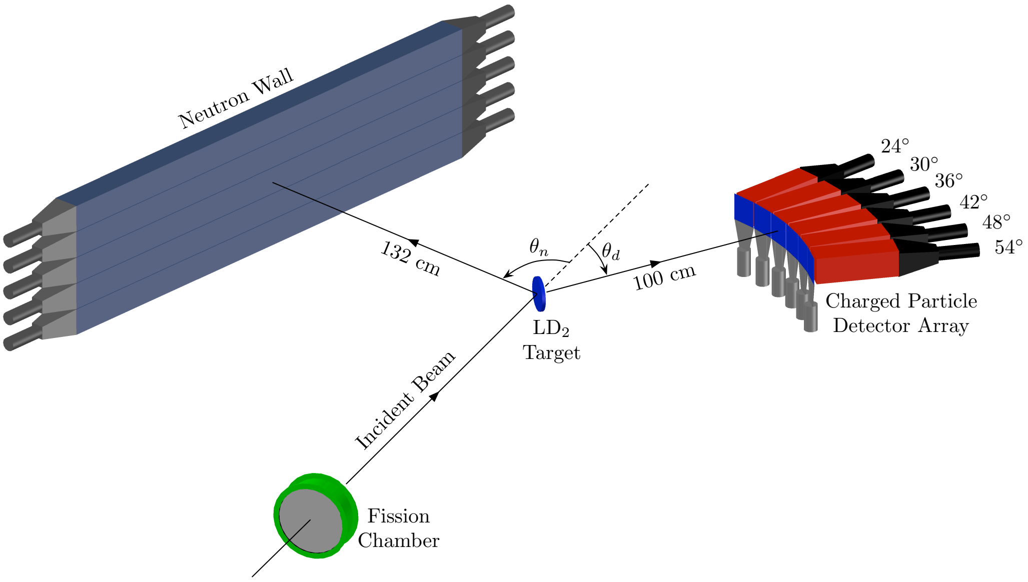

Figure 2.1. The schematic of the experimental setup.

2.1. Beam Production

The source of the neutron beam is the pulsed proton beam accelerated to 800 MeV by the LANSCE linear accelerator. The pulse structure of the proton beam can be seen in Figure 2.2 where there are micro-pulses and macro-pulses. The micro-pulses have a width of 0.2 ns and a separation of 1.8 μs which ensures that no event belonging to different micro-pulses can overlap in time. A micro-pulse lasts 625 μs followed by a gap of about 7.5 ms which together form the macro-pulse. This gap is reserved for the read-out electronics as the reading process is much slower than writing the data. About 100 macro-pulses per second were fed to the spallation target in this experiment.

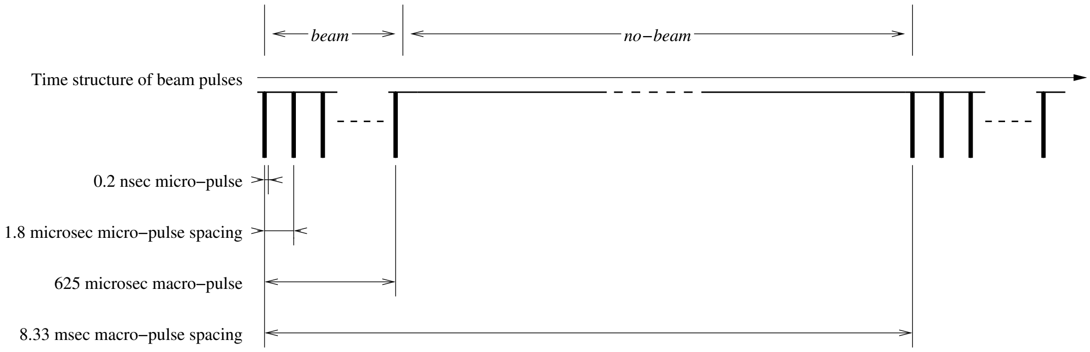

Figure 2.2. The pulse structure of the proton beam. This allows the usage of time-of-flight techniques.

The beam is directed to a cylindrical, water-cooled tungsten spallation target with a diameter of 3 cm and a length of 7.5 cm in a vacuum chamber at the Weapons Neutron Research Facility (WNR). One of the high flux arms of the spallation neutrons, namely 15R meaning 15° to the right of the target, was used for this experiment. The neutron beam has a continuous energy profile from a few MeV up to 800 MeV. The flux of the low energy neutrons was so high that beam hardeners were used to reduce the low energy flux and very low energy neutrons (∼30 MeV) were discarded using triggers based on time of flight. The schematic of the WNR facility and the flight path can be seen in Figure 2.3.

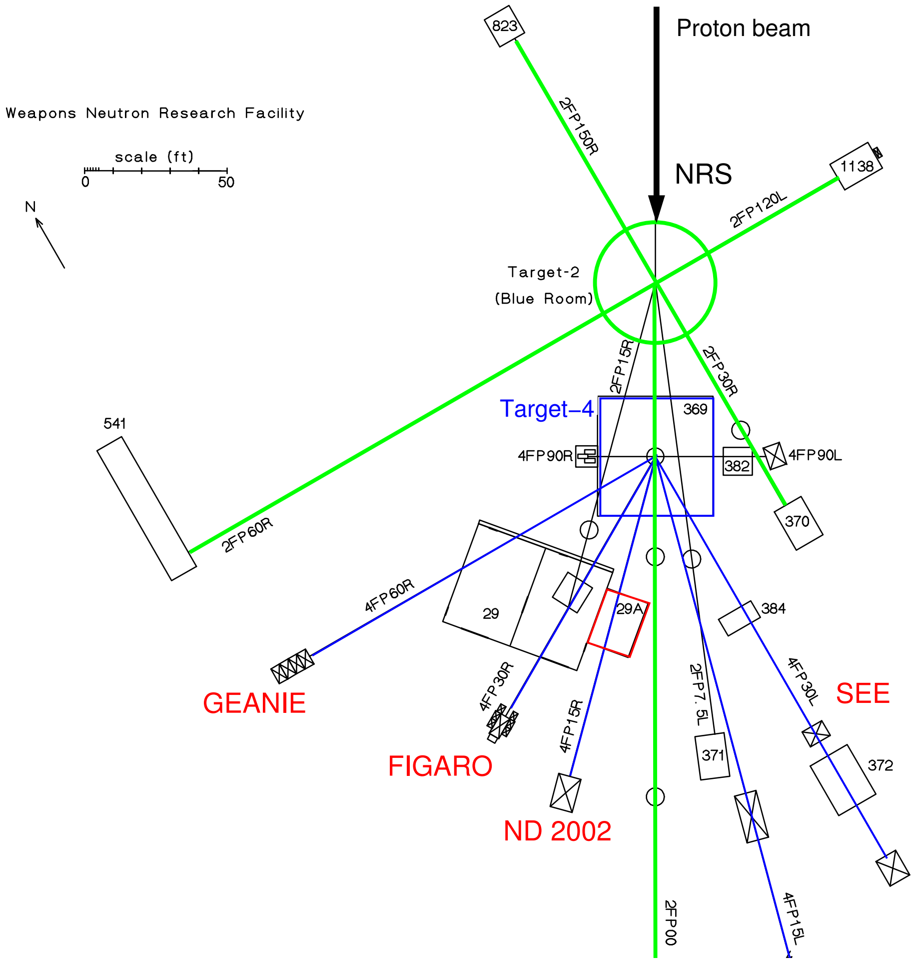

Figure 2.3. The schematic of WNR. The neutron target is labeled as *Target-4* and the blue outgoing lines are the neutron flight paths. Our experiment's flight path can be identified by the *ND 2002* tag.

The definition of the beam was achieved by horizontal and vertical sets of Cu shutters with a typical aperture of 3.8 cm × 3.8 cm. The charged particles in the beam were eliminated with a set of sweep magnets and then the beam was enclosed by an evacuated pipe which had a steel collimator of 2.7 m long with an aperture of 1.3 cm in diameter achieving further definition. In order to shield the environment from the beam, the collimator was surrounded by magnetite. The structure of the collimator is depicted in Figure 2.4.

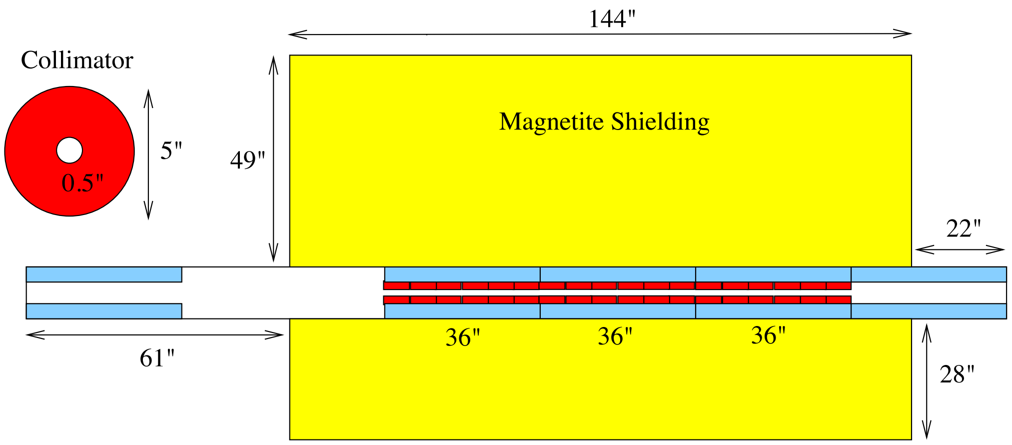

Figure 2.4. The structure and dimensions of the collimator and the evacuated pipe. The blue strips represent the iron sleeves inside the pipe.

After collimation, the beam travels towards the fission chamber which is about 16 m from the spallation target. Storage-phosphor image plates were exposed to the beam in order to obtain the beam profile and position information. A typical image obtained with such an exposure can be seen in Figure 2.5. The details of the process can be found in [46].

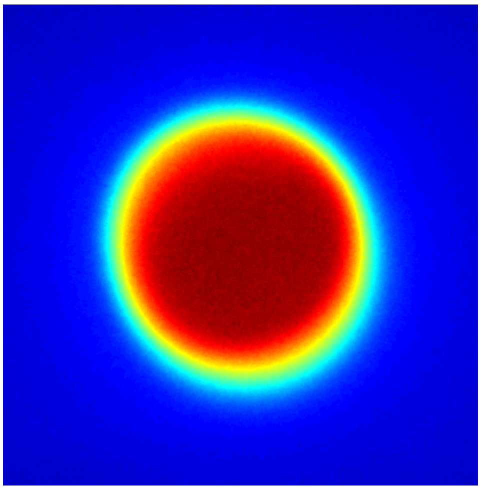

Figure 2.5. The image representing the neutron beam profile extracted from storage-phosphor image plates.

2.2. Fission Chamber

As stated earlier, the flux monitoring was done by a fission ionization detector shown in Figure 2.6. ^{238}U was deposited onto 0.013 mm stainless steel foils as the active plates. The foils are thin enough that the existence of the fission chamber in the flight path does not introduce a background. In addition, the circuitry is fast enough so that the detector can be used as an online monitoring device. The flux is measured by measuring the neutron induced fission fragment yields and extracting the number of incident neutrons using the known uranium fission cross section.[1] The details of this detector can be found in [47].

---

[1] Actually, in the energy range of this work, the uranium cross section is not known precisely which in turn introduces some systematic. However, we can eliminate this uncertainty as will be explained in Section 3.4.

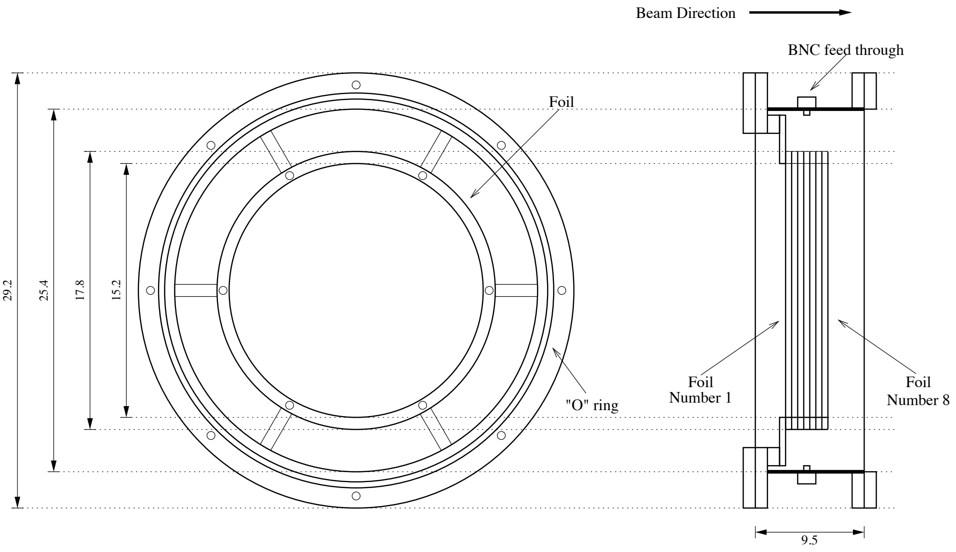

(a) The fission chamber schematics, both front and sideway view. The dimensions are in cm.

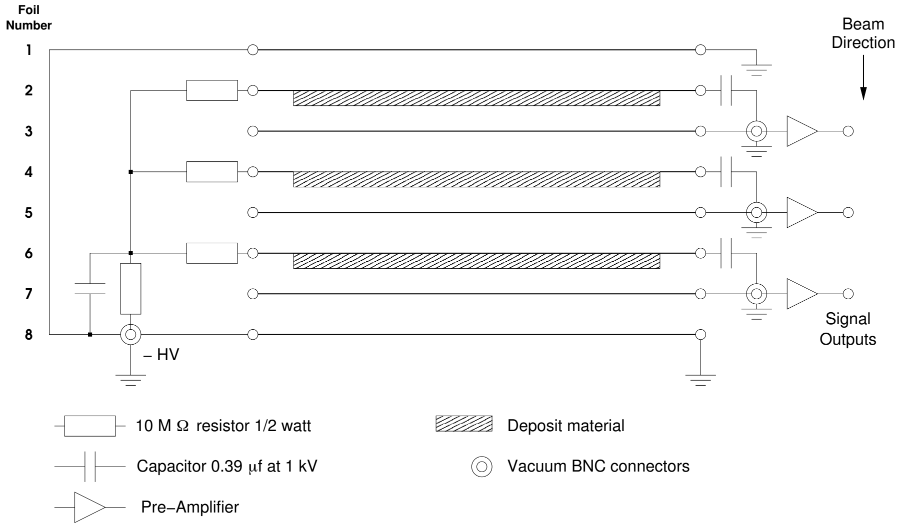

(b) The electrical circuit diagram of the ionization chamber.

Figure 2.6. The fission chamber: a) Schematics b) Electrical circuit diagram.

2.3. Target

After passing through the fission chamber, the beam reaches the target. As mentioned before, the target can be LD_2 or LH_2 contained in a cryogenic target flask which is a cylindrical disk with 12.7 cm diameter and 1.3 cm thickness as seen in Figure 2.7. The entrance and exit windows are made of Aramica of thickness 51 μm. The flask was placed such that its principal axis made an angle of about 50° with respect to the beam direction in order to minimize charged particle energy loss by reducing the path of a recoil particle traveling in the target material.

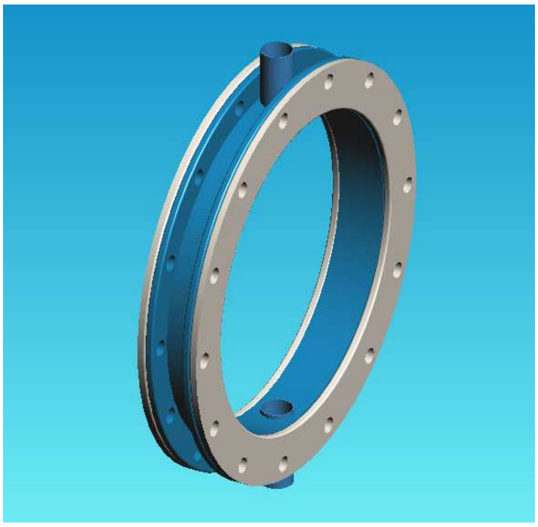

Figure 2.7. The cryogenic target flask whose specifications are given in the text.

The flask is placed inside a vertical cylindrical vacuum chamber with a 127 μm kapton exit window which had an opening angle of 70° and 110° on the charged particle and neutron side, respectively. The refrigeration system can be seen in Figure 2.8 which contains a CTI Model 1020 whose nominal cooling capacity is 10 W at 20 K. The target was kept at 14 psia pressure via a resistive heater.

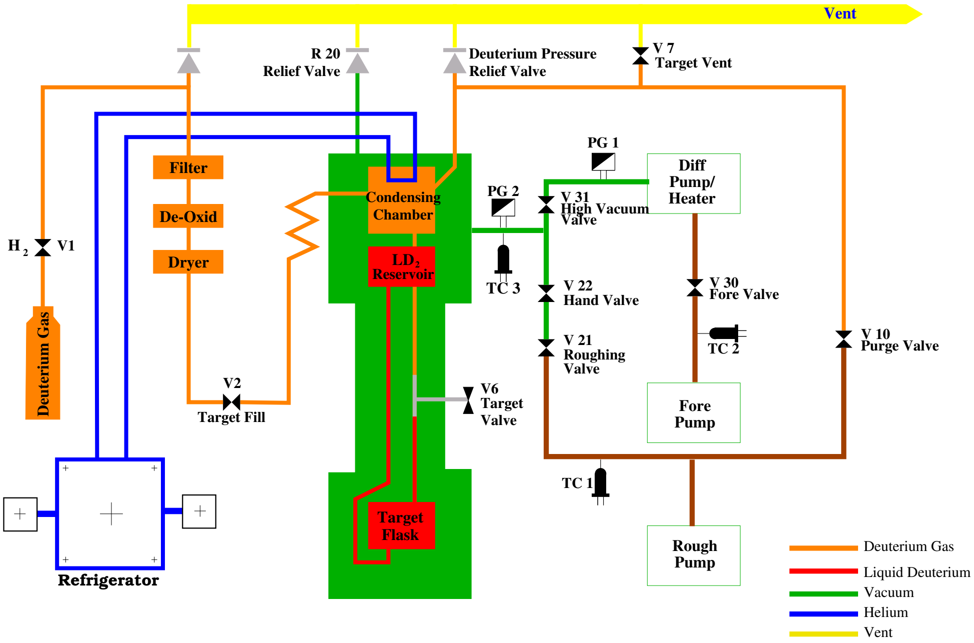

Figure 2.8. Diagram of refrigeration system. ^{4}He gas is used by the refrigerator to condense the deuterium gas and the liquid is then filled in the flask.

2.4. Charged Particle Detectors

The charged particle detectors define the number of cross-section measurements for a given energy and there are six of them located at the angles $\theta_{\mathrm{lab}} = 24^\circ$, 30°, 36°, 42°, 48° and 54° with respect to the incident beam, 1 m away from the target. The detectors are made of cesium iodide (CsI) crystals with the dimensions 9.2 cm × 9.2 cm front face and 30 cm depth. The depth of the detector is sufficient to stop all the incoming particles for our energy range of interest, therefore, pulse height information can be related to the particles energy. However, we did not used that information in our analysis for energy determination. Nevertheless, this ability gave us a valuable information for particle identification. The threshold of these detectors are so low that all the particles reaching the detector are assumed to be accepted leading to an effective 100% efficiency. Exactly covering the face of the CsI detctors, there are six thin scintillators, so called ΔE detectors, which have 2.5 mm of depth. These thin detectors serve two main purposes: precise time measurement and particle identification when combined with the information from the CsI detectors.

2.5. Neutron Detectors

The neutrons are detected in coincidence with the charged particle detectors by a wall of BC408 plastic scintillators consisting of five separate bars whose dimensions are 10 (height) × 10 (depth) × 200 (length) cm^3. Therefore, the face of the wall is 50 × 200 cm^2 which is theoretically enough to accept all the neutrons corresponding to both neutron-proton and neutron-deuteron elastic scattering interactions with an angular coverage of 34 to 108° in the laboratory frame. The normal of the face of the wall makes an angle of 71° with respect to the beam direction and this normal lies in the same plane with the centers of the CsI detectors. The distance of the wall from the target is 132 cm. The neutron bars have a nominal efficiency of about 10%, however, the actual efficiency depends strongly on the energy and the hit position of the neutron so a part of the analysis is the measurement of the neutron detection efficiency. Two photomultiplier tubes (PMT) were used at both ends of the bars whose timing information is essential for event identification and background subtraction. The face of the wall is covered with a set of thin plastic scintillators, like the CsI detectors, which are used to veto the charged particle events firing the neutron bars.

2.6. Data Acquisition System Electronics

The data we see in our histograms correspond to the ones eligible to represent real events through a set of triggers. The generation of these triggers are performed by electronic modules and each set of detectors have their own data acquisition procedure although they resemble each other in certain ways.

2.6.1. Charged Particle Electronics

The data collected with the PMTs in both CsI and ΔE are eventually written into ADCs and TDCs going through operations summarized in Figure 2.9. On the CsI path, the signal is split and pulse height information reaches ADC with some delay and through a linear gate in which the time information of the pulse is fed. This gate determines the width of the window of integration of the signal. The other copy of the signal goes through a constant fraction discriminator (CFD) to extract the timing information and the output of the CFD reaches TDC with some delay. The ΔE path is identical to the CsI path except the signal splitting is performed via a linear fan-in fan-out unit opposed to a splitter. The CFD outputs of CsI and ΔE paths are fed to a coincidence logic unit to generate deuteron logic (D logic) which is used by the trigger electronics.

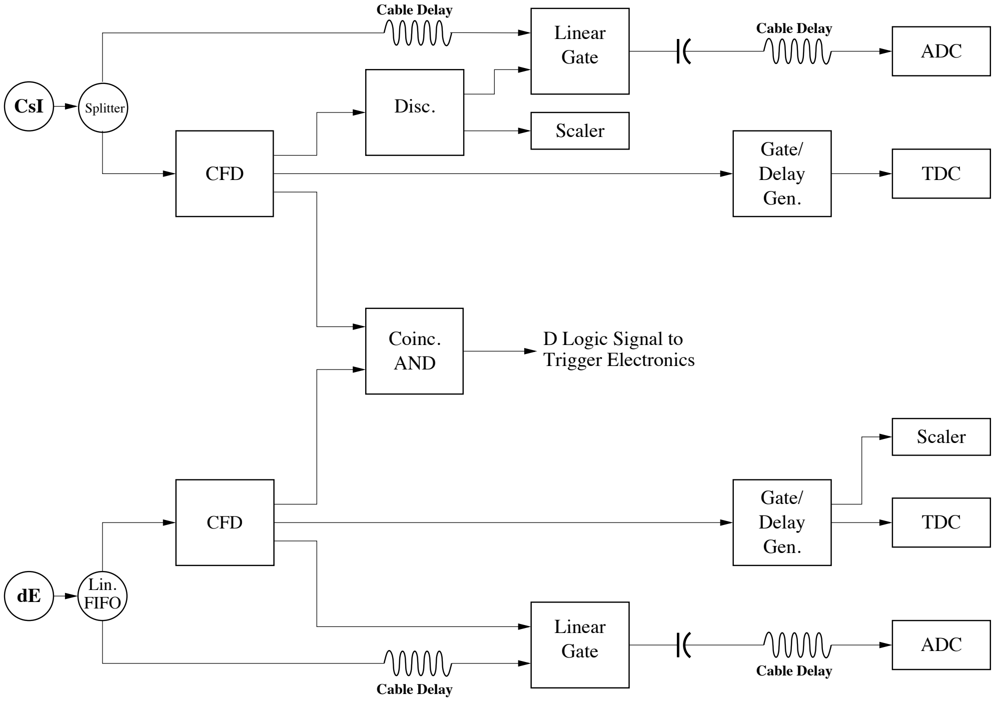

Figure 2.9. The charged particle electronics.

2.6.2. Neutron Wall Electronics

As can be seen in Figure 2.10, the electronics for a single bar is very similar to that for the charged particle detectors, but this time, the PMTs supplying the signals are the ones at the bar ends represented with *L* standing for left and with *R* standing for right. Like before, the PMT signal is split into two; one of them goes to the ADC with some delay and through a linear gate and the other goes through CFD to reach the TDC. The time coincidence of *L* and *R* generates a neutron logic (N logic) signal) indicating a detected neutron. However, there are some distinctions such that the electronics here has to deal with the uneven light attenuation, so the CFD thresholds are kept very low. In addition, the coincidence window has to be wide since the bars are long enough to suffer light propagation delays.

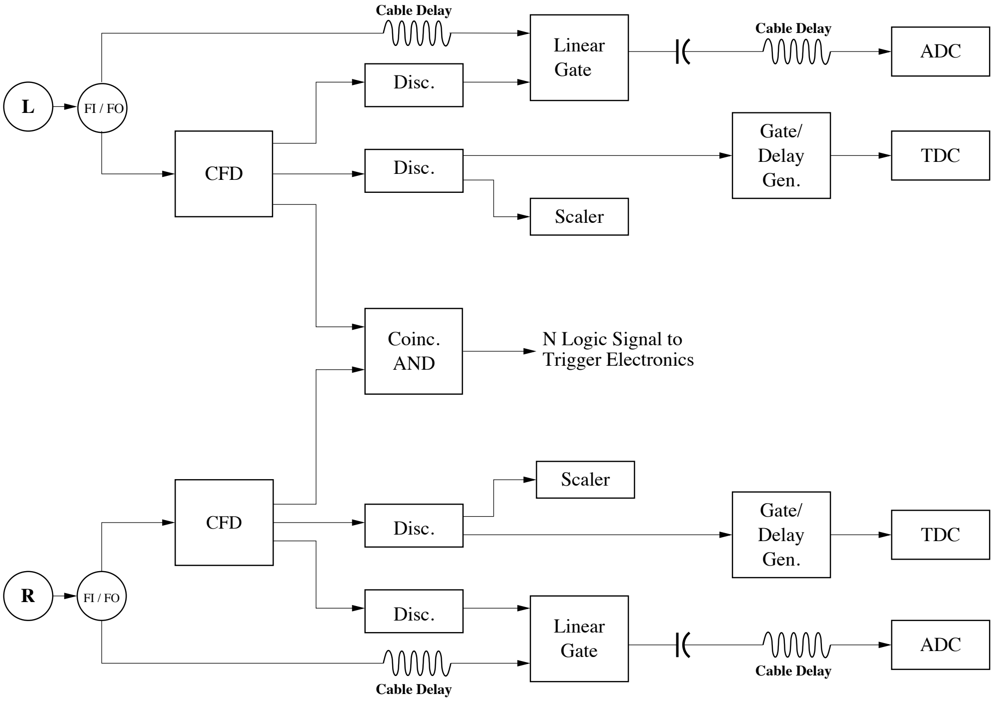

Figure 2.10. The neutron wall electronics.

The veto detectors in front of the wall have a similar block diagram as in Figure 2.11 with one important exception that this electronic does not generate a veto trigger signal meaning the invalidation of charged particles are performed at the software level. This fact also reduces the accuracy requirements.

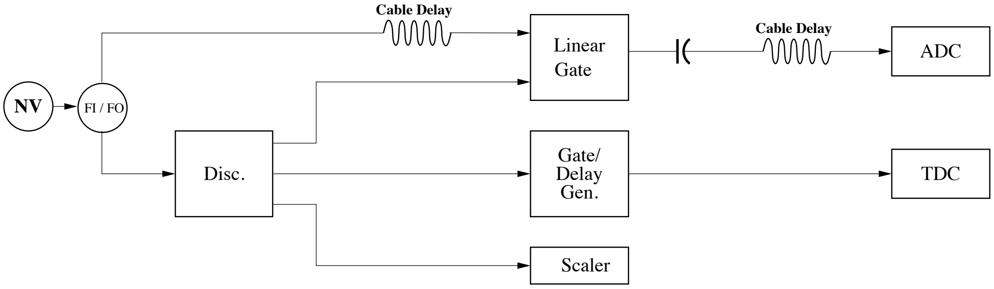

Figure 2.11. The neutron veto electronics.

2.6.3. Time Reference Signal (t_0) Electronics

The t_0 signal is produced at the spallation target which marks the generation of the neutron beam, therefore, its primary role is to act as the reference time for each event. In physical terms, this is the stopping signal of the TDCs which are started by the signals arriving at the particular detectors. Figure 2.12 illustrates the block diagram of the t_0 electronics where the signal is split in three branches and the uppermost branch is the stopping signal we have just mentioned. One other important duty of this signal is to prevent the trigger generation when there is no beam, that is, in between the beam bursts. The second branch in the figure makes sure that no trigger is produced after 1.8 μs corresponding to that particular burst. The lowermost branch shows how the read-out signal is given. Since reading the buffers is a lengthy process compared to the writing, the idea is to generate a signal right after a macro-pulse and start the read-out if there is significant event for that macro-pulse, i.e. one or more trigger. The feedback sector picks the first t_0 signal in the macro-pulse and its coincidence with the master trigger indicates whether or not there should be a read-out signal.

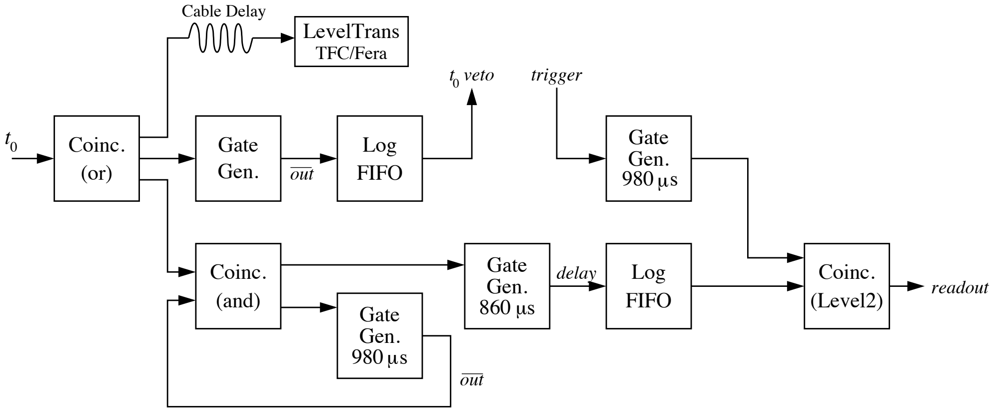

Figure 2.12. The t_0 electronics.

2.6.4. Trigger Electronics

The triggers are the indicators and identifiers of the significant events recorded during the experiment. Of course, not all identifications are true, however, it is a useful and necessary classification that makes the data analysis possible. Up to now, we have presented how N or D logic signals are generated via one of the bars or one of the charged particle detectors. Figure 2.13 explains how the master trigger, D-single, N-single and ND-coincidence triggers are generated. D logic signals from each charged particle detector are seen as D24, meaning "deuteron at 24° CsI detector", and so on, and N logic signals from each bar are labeled as Nbar0, etc. (If any of the D logic and N logic signals coincide with coincidence bit, which is the identifier of the events of primary interest, is produced.) Moreover, D-single and/or N-single events are also interesting, for instance, the np elastic cross-section data are so clean that it can be measured without the neutron information, therefore, the triggers for each are additionally created. The event rates are very high with these singles triggers so a prescaler is used to accept only a fraction of these events such as 1/9 or 1/200 as in the Figure 2.13.

Other types of triggers appear in the figure in addition to the main ones. The laser trigger[2] separates the events from others when the laser is on. The laser obviously carries a monoenergetic beam which is used to determine the gain of the CsI detectors. The cosmic rays are also capable of firing neutron bars and when they do, simultaneous firing occurs in multiple bars. The low energy deposit and the mentioned simultaneity helps us identify the cosmic events. The cosmic trigger is generated between the beam bursts and only when 3 or more bars are fired simultaneously.

All the triggers, are combined (logically ORed) giving rise to the master trigger. Additional information about the component electronics mentioned so far can be found in [2].

2.6.5. Fission Chamber Electronics

The block diagram of fission chamber electronics in Figure 2.14 looks similar to those we have already discussed; however, two copies of the pre-amplified uranium foil signals are used to provide trigger and timing information. Each copy passes through constant fraction discriminator (CFD) and an additional discriminator and their coincidence in addition to the t_0 signal gives out necessary signals which are in turn sent to the trigger logic, to the ADC as a gate signal for the third copy of the pre-amplifier output and to the TDC as both gate signal and raw signal. The TDC is

---

[2] A pulsed nitrogen laser was used to monitor the gain and timing stability of the detectors. The laser pulses were transmitted to the detectors using fiber optic cables.

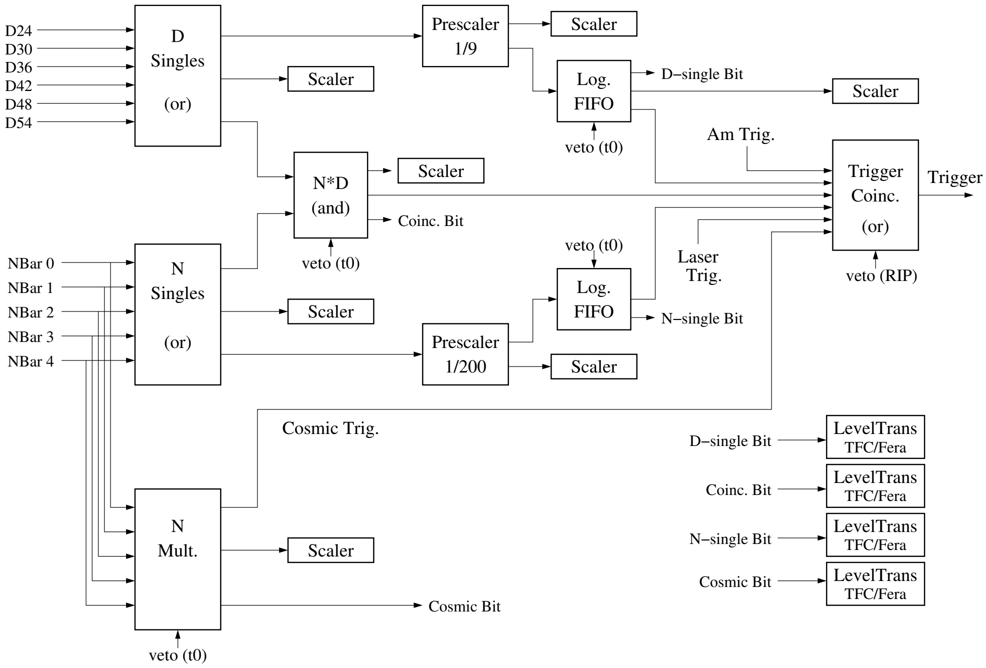

Figure 2.13. The trigger electronics.

again stopped by delayed version of t_0 signal. The benefit of employing two copies of the signal to determine the timing information is to apply a lower level cut off without affecting the timing information. Details of the fission chamber and its electronics can be found in [47].

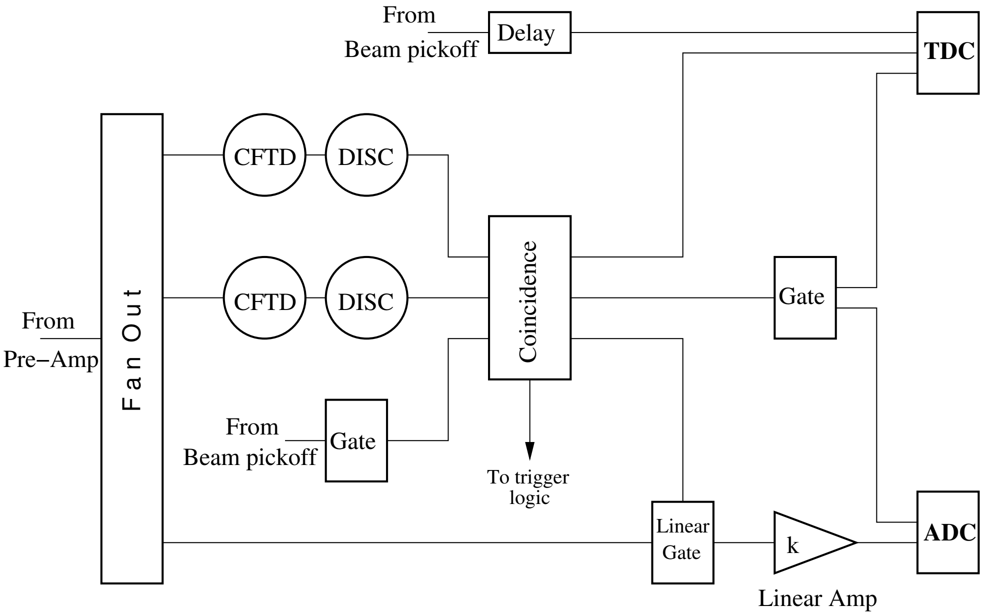

Figure 2.14. The fission chamber electronics.

3. ANALYSIS

3.1. Time of Flight Calibration

Since the TOF information is essential to our calculations and analysis, we must calibrate the coefficients that convert the TDC values to the actual time. The relation is assumed to be linear and given as

$$TOF = c_0 \times TDC + c_1 - t_0. \tag{3.1}$$

where t_0 is the reference time signal generated at the spallation target, c_0 is the conversion factor and c_1 is the offset due to cabling and electronic delays. c_0 is the property of channel, usually very stable, and measured several times during the data taking phase of the experiment. c_1 is calibrated using physics data as will be explained. Since the experiment was carried out over a long time, c_1 coefficient may vary for different run intervals due to several factors like cable change, temperature, etc. We pick the coefficients for the run interval we would like to analyze as a starting point. Let us look at a TDC histograms for a ΔE/CsI detector in Figure 3.1 where one can identify the sharp gamma peak. The mean of this peak should sit at a certain value ($\sim$ 60 ns in our case) since gamma rays travel with (almost) the speed of light, and we know the length of the path they travel.

We first applied the transformation in (3.2)

$$\Delta TOF = TOF - \frac{L_0 + D_{\mathrm{CsI}}}{c} \tag{3.2}$$

where L_0 is the distance from the spallation target to our LH_2 or LD_2 target and D_{CsI} is the distance from LH_2 or LD_2 target to the CsI detector. This transformation ideally yields a gaussian distribution around 0. We applied a gaussian fit around the peak and with the value of the mean of the gaussian, we adjusted the offset coefficient c_1 such that the peak is moved to 0. The result of the calibration can be seen in the right half

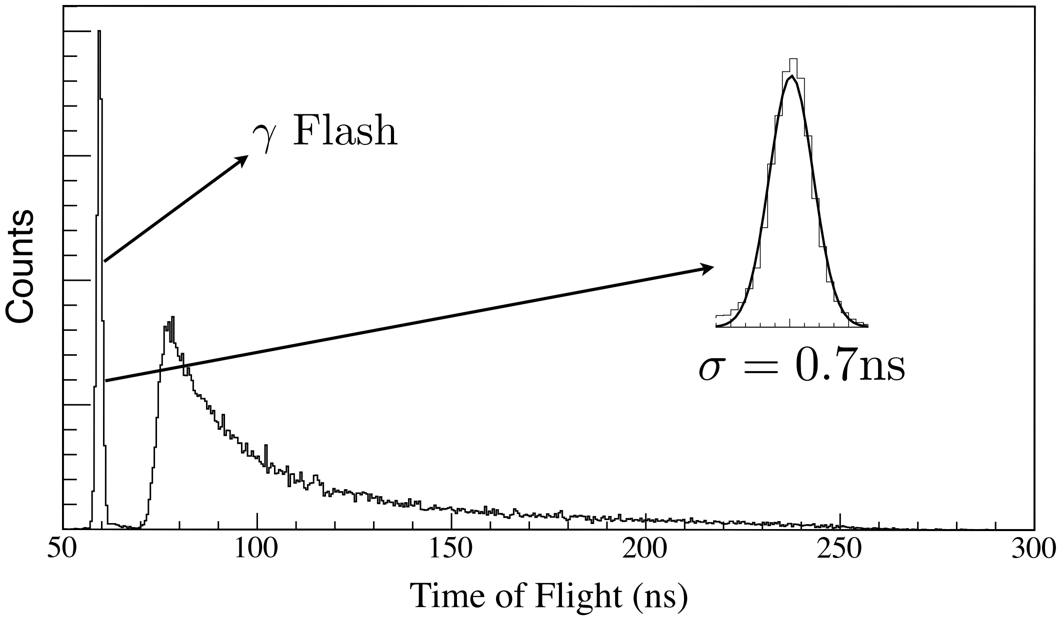

Figure 3.1. Typical time-of-flight spectrum for a Δ E detector, measured with respect to the arrival time of the proton burst at the spallation target (t_0). The "gamma flash" is observed at ∼60 ns. Charged particles are seen between 70 and 250 ns.

of Figure 3.1.

This procedure is applied to all six charged particle telescopes for different run periods. Actually, the timing resolution of the ΔE detectors are better as stated in chapter 2, hence energy calculations are based on the timing data of these detectors. These calculations assume elastic scattering, however, energy loss corrections are made with the help of Monte Carlo simulations. Other than adjusting these offsets, this procedure determines the timing resolution of our experiment which is found to be ±0.67 ns (electronics) ±0.20 ns (beam pulse width).

3.2. Fission Chamber

In Section 2.2, how the fission chamber can measure the beam flux using the yields of fission fragments as shown in Figure 3.2 was discussed. These fragments are clearly separated from the α particle and the pulse height information directly translates into the flux. Figure 3.3 illustrates the result of this conversion. We need to know the number of incident neutrons for a particular energy to obtain the cross section. With the histogram in the figure at hand, it is an as easy task as multiplying the counts corresponding to the energy of choice with the energy window (10 MeV in our case).

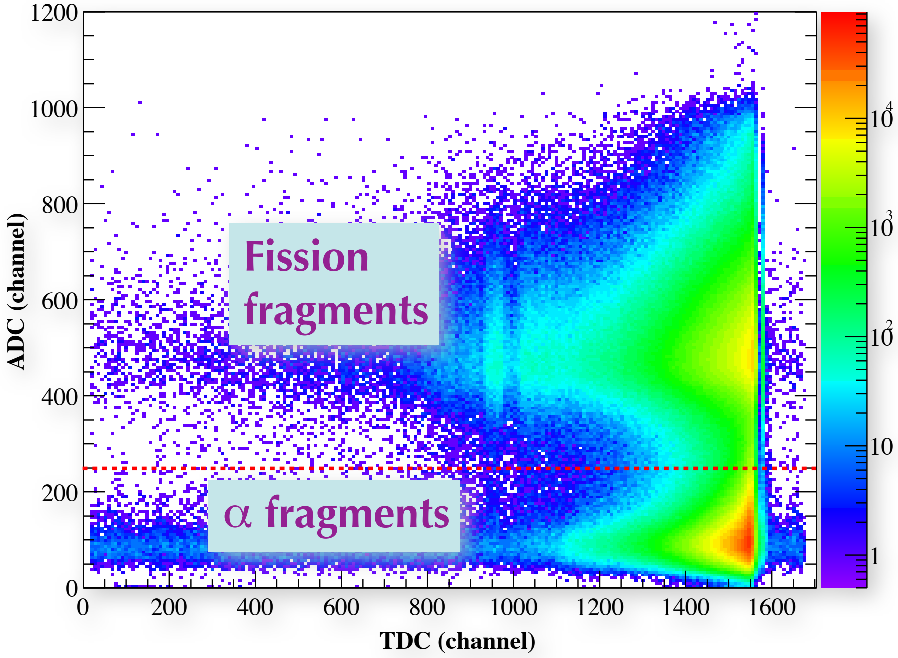

Figure 3.2. ADC vs TDC histogram of fission chamber illustrating heavier fission fragments.

A crude calculation shows that about $3{\times}10^5$ neutrons/s is generated over the full energy range. As mentioned earlier, the high low-energy flux was reduced using beam hardeners and one can notice the the absence of very low-energy neutrons which are cut off using triggers.

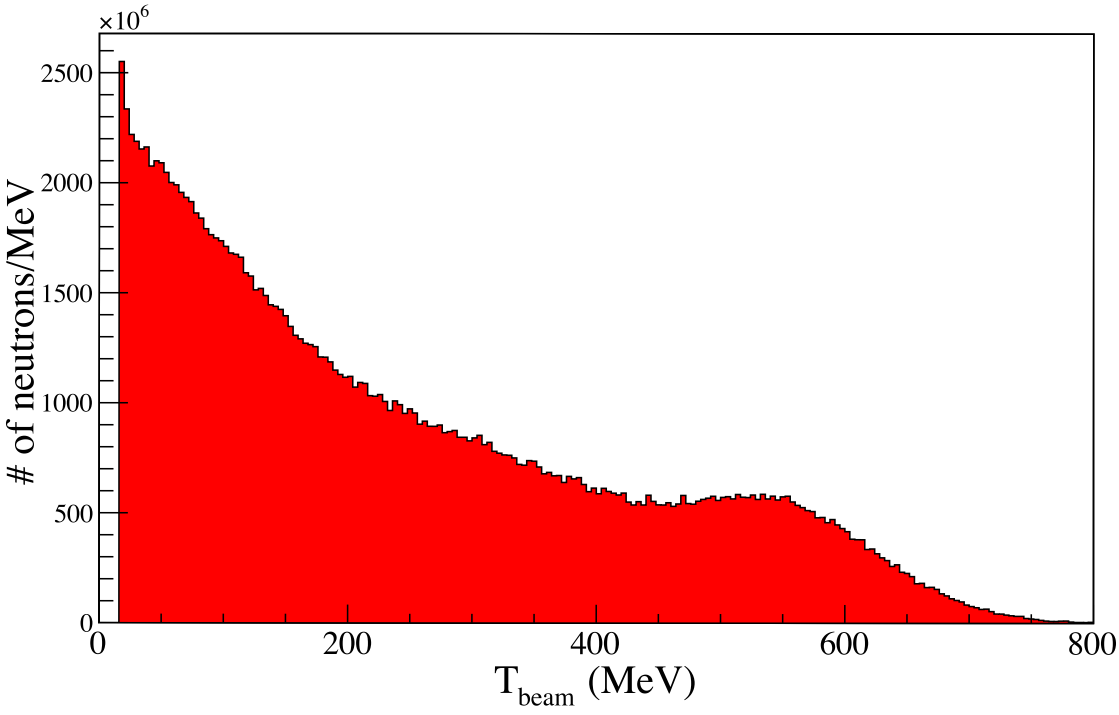

Figure 3.3. Neutron Flux vs. Beam Energy for the run range 126 − 208.

3.3. Energy Loss

This section aims to explain the methods used to account for the energy loss of the recoil charged particle while it passes through some layers of matter as it reaches the active area of the CsI detector. The interaction of the neutron is negligible since it is a neutral particle. The two body interaction that we are concerned with is simulated by a Monte Carlo program. The simulation basically reads the properties of the incident beam such as the energy range or energy window and the geometrical layout of the experimental setup from a file, then produces events and as a result calculates the energies, energy losses, time-of-flight, etc. The beam profile generated by the simulation is shown in Figure 3.4, and may be compared with the profile in Figure 2.5.

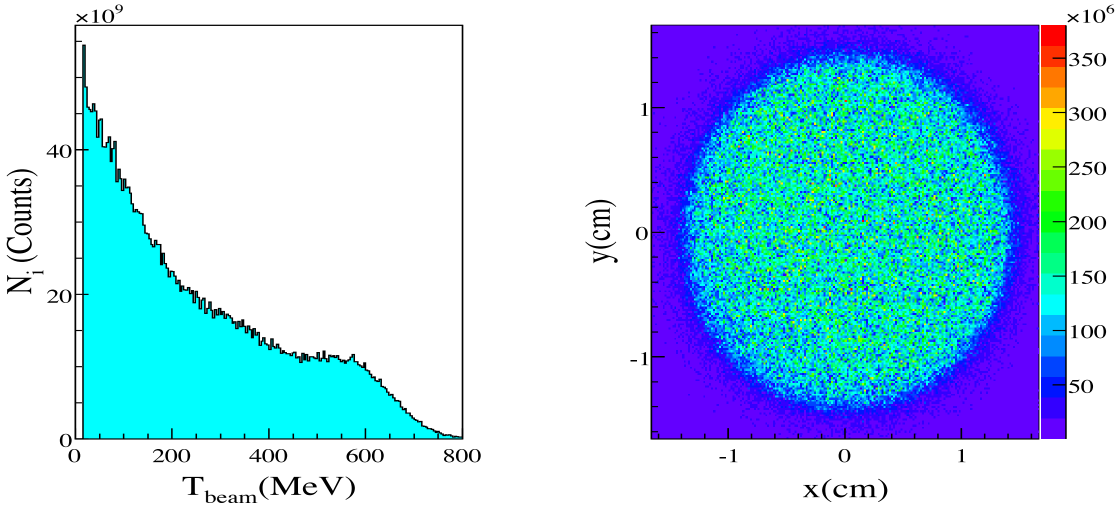

Figure 3.4. The profile of the neutron beam.

As we have just mentioned, our primary concern is the energy loss, however the program was used for other purposes as well. For example, we checked the geometric acceptance of the neutron wall by calculating the hit position of each neutron on the wall. The results are shown in Figure 3.5 and Figure 3.6 for *nd* elastic scattering and *np* elastic scattering, respectively. From the figures, since the position and the size of the wall is chosen to be sufficient for the neutron deuteron elastic scattering, no acceptance problem was spotted with the LD_2 target, however, some of the neutrons for the detector with the smallest angle (16°) miss the wall for the LH_2 target. This does not concern us as in this case, we used the proton single events as will be explained later.

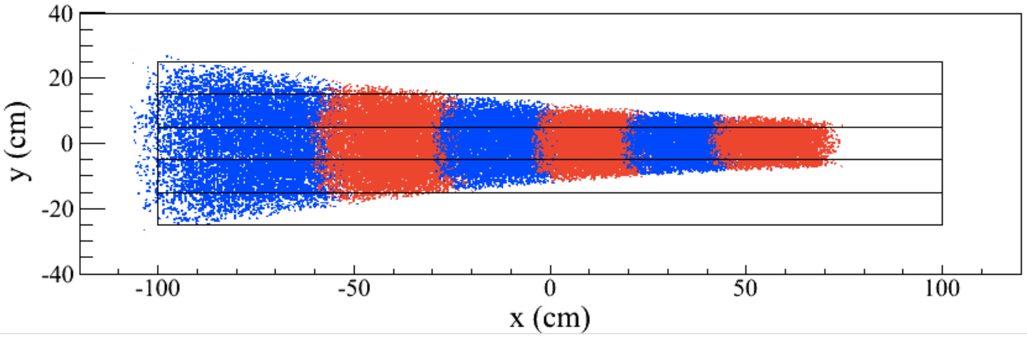

Figure 3.5. The profile of neutrons hitting the neutron wall after *nd* elastic scattering at 200 ± 5 MeV. Alternating colors symbolize the hits corresponding to CsI detectors at different angles.

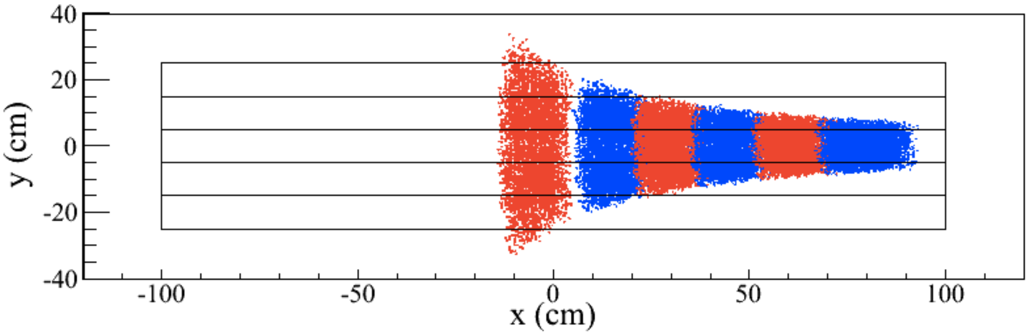

Figure 3.6. The profile of neutrons hitting the neutron wall after *np* elastic scattering 200 ± 5 MeV.

The energy loss calculation is based on *range* data files listed as a function of kinetic energy. The files are supplied by the PSTAR [48]. According to the thickness of the material that the charged particle passes through, the passage is approximated as occurring in a number (50) of steps each assumed to be linear. Then, the energy and the time of passage is found within each step using the data files and kinematic calculations. As a result, the final energy and the time it takes to penetrate the layer is recorded and the procedure is repeated for all the layers. In the end, we form a table which contains the total time-of-flight of the charged particle with the corresponding beam energy. This table is used in the actual analysis instead of the kinematic calculations which do not take the energy loss into account.

Note that PSTAR provides range tables only for protons. We need a similar table for deuterons as well. The energy loss for heavy particles is mostly due to the

Coulomb (electromagnetic) interaction and mean rate of loss is well characterized by the Bethe-Bloch formula.

$$-\frac{dE}{dx} = Kz^2\frac{Z}{A\beta^2}\left[\frac{1}{2}ln\frac{2m_ec^2\beta^2\gamma^2T_{max}}{I^2} - \beta^2 - \frac{\delta(\beta\gamma)}{2}\right] \tag{3.3}$$

where z is the charge of the incident particle in terms of electron charge, Z and A are the atomic number and mass of the absorber, respectively, I is the mean excitation energy of the absorber, T_{max} is the maximum kinetic energy delivered to a free electron in a single collision and δ is the density effect correction for high energies which accounts for the characteristics of the field of the incident particle and the polarization of the absorber. For our purposes, we ignore the density effect when calculating the stopping power. To see if our assumption is valid, we applied the formula without the density effect to the protons and compared the result with the values in the PSTAR files. The results are shown in Figure 3.7 in which we can conclude that assumption is valid since there is no important difference in the energy range we are considering. The equation can be manipulated and integrated to get the total distance a particle travels in a material given the initial energy. Therefore, we can have a set of data which shows the total range versus the initial energy which serve as basis to calculate the total time-of-flight as mentioned before.

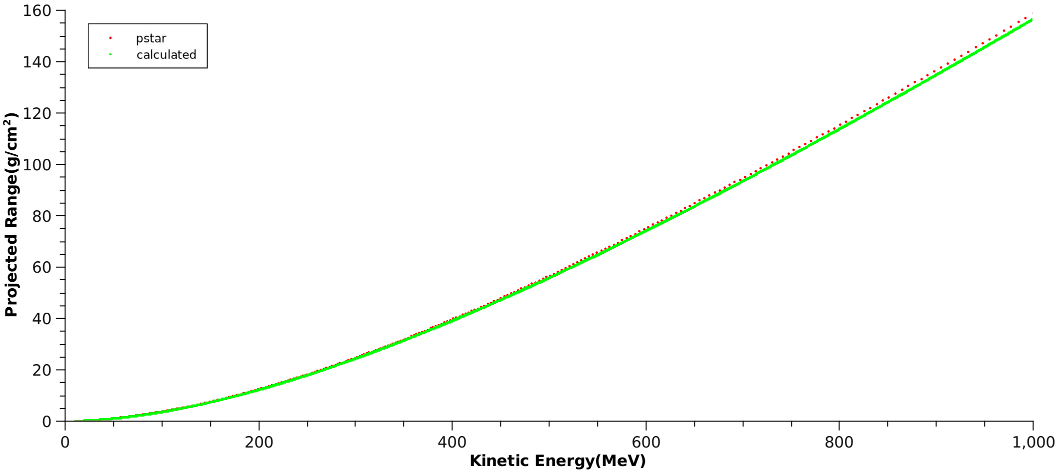

Figure 3.7. The comparison of Bethe-Bloch formula and PSTAR database.

The basic idea is the same whether the target is LH_2 or LD_2, however there are two important distinctions. The first one is that we introduce the target thickness correction in the neutron deuteron cross section simulation and in turn, we account for the deformation of the target. The second one is the lack of the ready-to-use data files from which the energy loss is extracted, therefore, we had to use the Bethe-Bloch formula and formed the files ourselves.

The effective path that the charged particle travels increases because of the bulging of the target flask as will be discussed in the following section. The position of the vertex point, the point where the interaction occurs inside the target, spreads a little as well. With the introduction of the target thickness correction, the target looks like two spherical caps connected with a cylindrical lateral part. The radius of the spheres are calculated using the distance from one window to another in the center, where the distance is largest . The incident neutron enters from the upstream sphere cap and somewhere inside the target the interaction occurs. The interaction vertex is assumed to be uniformly distributed between the entrance point and the point where the incident neutron would exit if it passes through without interaction. The details of the geometry and the calculation of the vertex can be found in Appendix B. The profile of the neutron beam as seen in Figure 3.4 is uniformly created in the simulation in accordance with an input file in which we can characterize the properties of the beam such as energy range, energy window and duration. The resulting vertex profile can be seen in Figure 3.8. Then, tables using Bethe-Bloch formula are used to determine the energy loss during the particle's trajectory as it reaches the detector.

The energy losses found for all the detectors are depicted in Figure 3.9. The red lines are $y = x$ lines and all the points in the histogram are below these lines as they should be since a particle that reaches the detectors cannot lose more than its kinetic energy. Figure 3.10 relates the true time of flight for a given kinetic energy with the inclusion of energy loss. These are the histograms that we use to construct our TOF versus kinetic energy tables which we use instead of kinematic calculations without the losses in our main analysis. For each time bin in the histograms, we find the profile of the y-axis, make a gaussian fit and hence obtain the corresponding energy with its uncertainty.

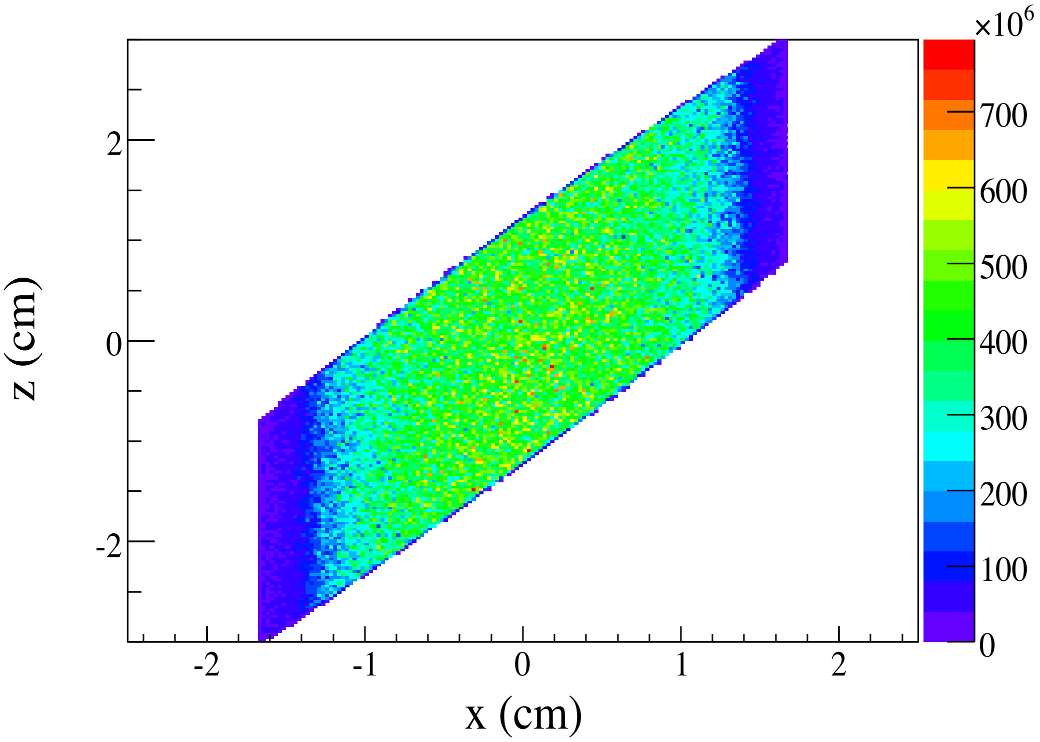

Figure 3.8. The histogram of interaction vertices.

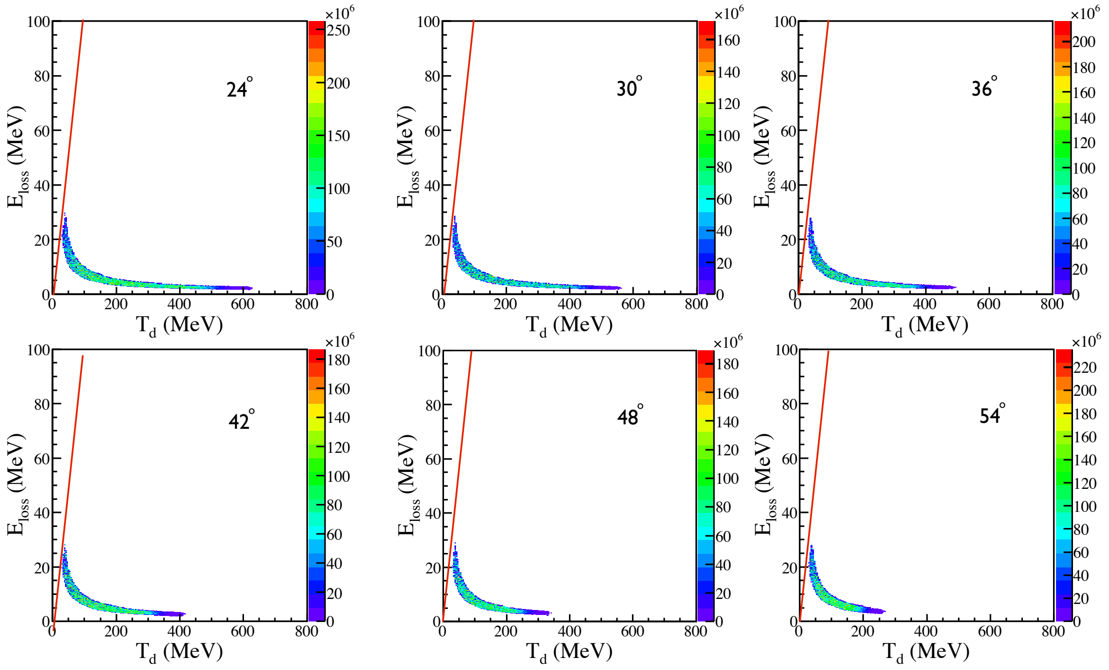

Figure 3.9. The energy loss histograms for CSI detectors.

More information on the Monte Carlo simulation is given in Appendix D.

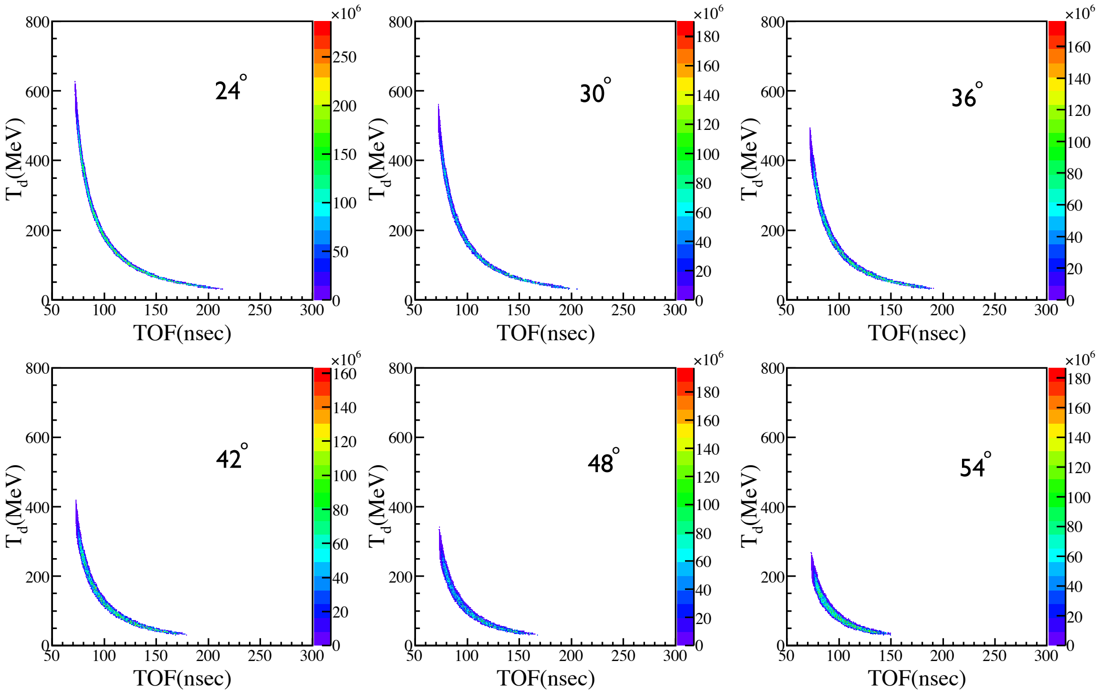

Figure 3.10. The kinetic energy vs. time-of-flight histograms for CSI detectors with energy loss.

3.4. Target Thickness Normalization

In this section, we present the analysis of the np elastic cross section and compare our results with the SAID [45] data. To understand the problem of thickness normalization, we first look at the expression in Equation 3.4 being used to calculate the cross section.

$$\left(\frac{\mathrm{d}\sigma}{\mathrm{d}\Omega_p}\right)_{lab} = \frac{N_p}{N_i \epsilon_p} \frac{k}{\Delta\Omega_p \rho_t l}. \tag{3.4}$$

In the expression, N_p and N_i are the number of detected protons and incident neutrons, respectively, ϵ_p denote the efficiency of detecting proton, k is the electronic pre-scaler factor, $\Delta\Omega_p$ is the solid angle of the proton detectors, ρ_t represents the areal density of the target and l is the live time of the electronics.

Among all the parameters in the expression, the areal density ρ_t is the most uncertain one since the target thickness is difficult to determine. The target container is placed in vacuum, on the other hand, the target material, LH_2 or LD_2, has some pressure. As a result of this pressure, the container bulges which means the path length of the beam increases and, moreover, the amount of increase depends on the radial position. The deformed shape of the container is illustrated in Appendix B. In addition, the liquid in the target was observed to bubble continuously during operation which also changes the effective target thickness. That is why we need to normalize our results with respect to the SAID np eleastic cross section results to find the target thickness correction and use this for the nd analysis. With this motivation, let us now go over all the details and how to obtain them.

The number of incident neutrons N_i is obtained from the fission chamber flux histograms in Section 3.2, seen in Figure 3.3. As mentioned before, the histogram is with respect to the neutron kinetic energy and it can be used to get the number of incoming neutrons for an energy interval. Suppose, we choose 10 MeV energy interval, want to calculate the cross section for 140 ± 5 MeV and use the flux per MeV histogram. First, we need to determine the bin number for the desired energy in the flux histogram from a histogram listing file. Since histogram is smooth enough for the given energy, we just multiply the bin value by 10 MeV, which is the energy window of the analysis, to get N_i (If the histogram were not smooth, we would have to apply a linear or quadratic fit around the desired bin and then get the value for the specific energy or we could decrease the bin size and take the sum of the contents of an appropriate number of bins which is determined by the bin size and the energy interval.).

The number of protons N_p is found by counting the number of events that satisfy some conditions specified by a set of "cuts". The first of these conditions is the event type, namely *coincidence* or *proton-single*. Coincidence events are those for which both a proton and a neutron is detected. The decision is made by the electronic triggering mechanism considering the timing of proton detection by the CsI detectors and neutron detection by the neutron wall as explained in Section 2.6. Of course, there could occur some accidental events and management of those kind of events along with background is left for neutron-deuteron elastic scattering analysis since we only deal with singles events for this portion of the analysis. The proton-singles events, as the name suggests, represent the events in which only protons are detected without requiring detection of a neutron. The reason why we used single events is that we did not want to require the knowledge of the neutron detection efficiency at this stage. Secondly, we take only the events whose beam energy is in the desired interval, $[135, 145]$ MeV for instance. Obviously, the CsI detectors at different angles are handled separately and the events are validated by checking if valid data are present in the ADC and TDC of the specific detector. The rest is simply the counting of the events that constitute the number N_p in Equation 3.4.

An example of the protons detected at a specific angle using the singles trigger can be seen in Figure 3.11. The region where the elastic protons accumulate is shown with an arrow and a red graphical cut. Note that this graphical cut is not a criteria for event acceptance as all the events detected are counted as valid events. What produce the background are the protons arising from elastic (higher energy) and inelastic (lower energy) scattering from, e.g., carbon, nitrogen and oxygen nuclei in the target and scattering chamber windows. A horizontal band is also apparent in the figure and it is due to the protons experiencing strong interaction inside CsI detectors. The background subtraction was done using empty target runs with appropriate normalization.

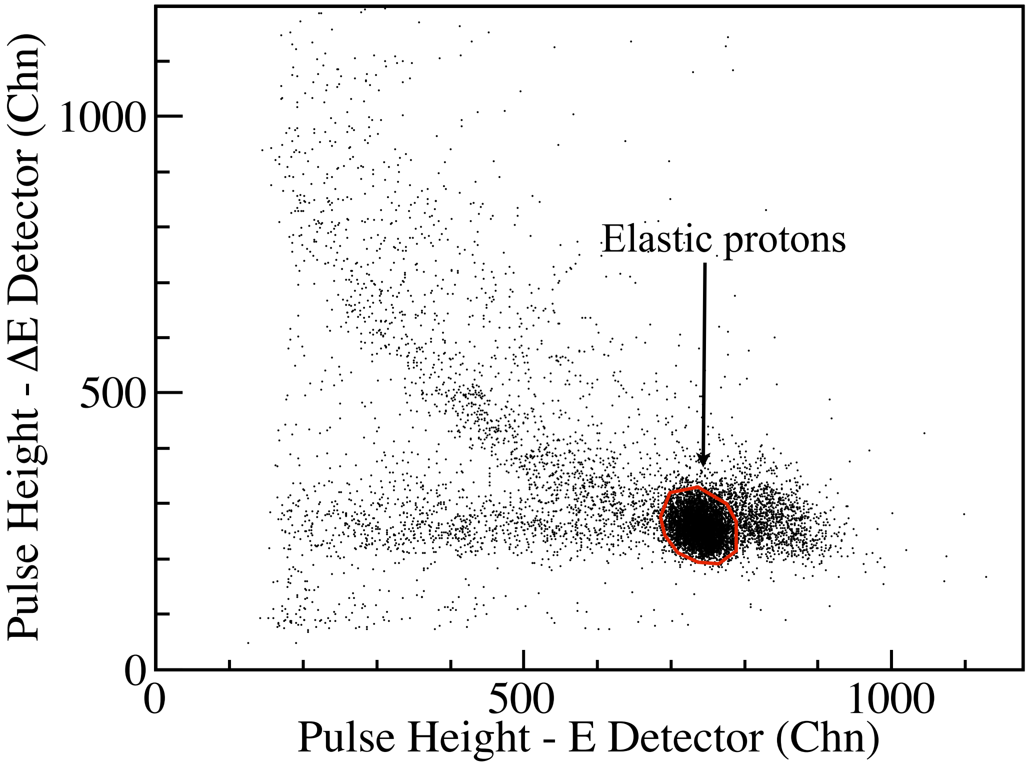

Figure 3.11. Protons for the beam energy 170 ± 5 MeV.

As for the efficiencies, we only need to consider proton detection efficiency since we are analyzing proton-singles events. First of all, we assume that when an energetic proton hits the CsI detector it is certainly detected, namely the efficiency of the detectors is unity. We performed the analysis utilizing the TOF information alone which provides us with an important advantage; we do not have to use a proton identification cut on CsI and ΔE detectors which could introduce detection inefficiency. Presumably, none of the events is lost during the analysis process. As a result, the total efficiency is regarded as unity for the proton-singles events.

The dimensions and the orientation of the CsI detectors are given in Chapter 2 from which the solid angle of the detectors is found to be 8.446×10^{-3}sr. The pre-scaling is employed by the electronic system for the specific types of events. The reason is to make sure that the electronic system handles all the events without being overwhelmed. Since the coincidence events are providing us the data of primary interest, we do not want to pre-scale the coincidence events thus the factor is 1, however, the pre-scaler factor for the single events is 9. The live time l is obtained similarly as the ratio of the recorded events to the triggered events. The value was measured to be 0.86 for the run range we used. Both the pre-scaler factor and the live time were measured using the scalar modules.

The areal density of the of the LH_2 target can be found using the following formula

$$\rho_t = \frac{\rho_{H_2} \times N_A}{A_{H_2}} \times \Delta x$$

where ρ_{H_2} is the volume density, N_A is Avogadro's number, A_{H_2} is the molar mass and Δx is the effective thickness of the target. The normal of the target makes an angle of 50° with the beam direction, therefore $\Delta x = 1.94$cm and the areal density is found to be 8.33×10^{-2}atoms/barn for the undeformed target. However, this value is not the effective thickness, it is used with a correction coefficient for which the reasons are stated at the beginning of this section.

All that is left now is to perform the analysis and calculate the elastic cross section. However, there are two crucial points that need to be discussed. The recoil particle (proton or deuteron) loses energy before hitting the CsI detector while passing through different layers of matter which in turn affects the time it takes to reach the detector (TOF). Hence, this energy loss should be taken into account. In Section 3.3, we gave the details of the Monte Carlo simulation to account for the energy loss and to correct the TOF with respect to this energy loss forming a table to be used in the analysis. The other essential point is the background subtraction. Not all the events detected by the CsI detectors are elastic neutron-proton events and so far we did not mention anything done to separate these events. Fortunately we have empty target runs, thus the difference between the cross-section results of full target runs and the empty target runs will give us the true cross section up to a normalization of the empty target data with the beam flux.

It is conventional (also universal) to present the findings in the center-of-mass frame so we need a transformation to obtain the results in the desired frame. The following equations govern this transformation. The derivation of these equations along with other kinematic relations are given in Appendix C.

$$\beta_{\mathbf{cm}} = \frac{\mathbf{P_{n_0}} + \mathbf{P_t}}{E_{n_0} + E_t}, \tag{3.5}$$

$$\tan(\theta_r^*/2) = \gamma_{cm}\tan\theta_r \tag{3.6}$$

which lead to the jacobian

$$\frac{\mathrm{d}\Omega_{lab}}{\mathrm{d}\Omega^*} = \frac{(1+\gamma_{cm}^2\tan^2\theta_r)^2\cos^3\theta_r}{4\gamma_{cm}^2} \tag{3.7}$$

where superscript "*" indicates the center-of-mass frame and subscripts n_0, t and r denote the incident neutron, target and recoil, respectively. Then, we are able to express our results with the following transformation

$$\frac{\mathrm{d}\sigma}{\mathrm{d}\Omega^*} = \frac{\mathrm{d}\sigma}{\mathrm{d}\Omega_{lab}} \times \frac{\mathrm{d}\Omega_{lab}}{\mathrm{d}\Omega*}. \tag{3.8}$$

The results of the *np* elastic cross section analysis is given **without** the target thickness correction in Figure 3.12. The results are consistently higher by a constant factor as expected. The error bars are hardly noticeable since only statistical errors are shown. The systematic errors will be introduced later.

In order to find the correction factor, we calculated the χ^2 value including all data points with respect to the corresponding SAID *np* elastic cross-section value, performed a linear search over the possible correction factor values. The coefficient which makes the χ^2 sum minimum serves as the target thickness correction factor. Figure 3.13 shows the result of the analysis. The value we obtain from the fit is in fact the inverse of the correction factor so the value we are looking for is $corr\_fact = 1.25 \pm 0.06$ where the error was found by the double-χ^2 method. The corrected results for the *np* elastic

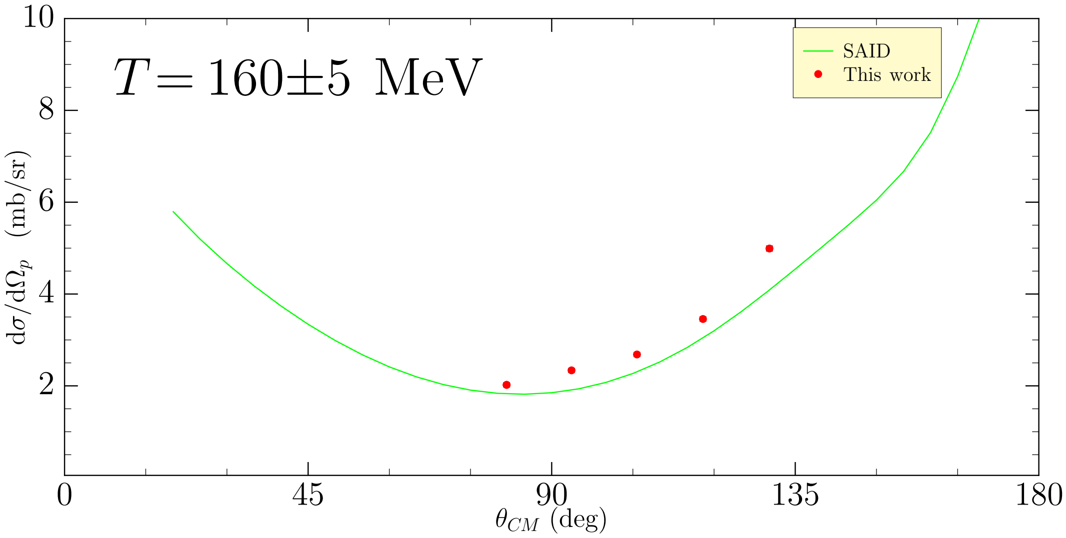

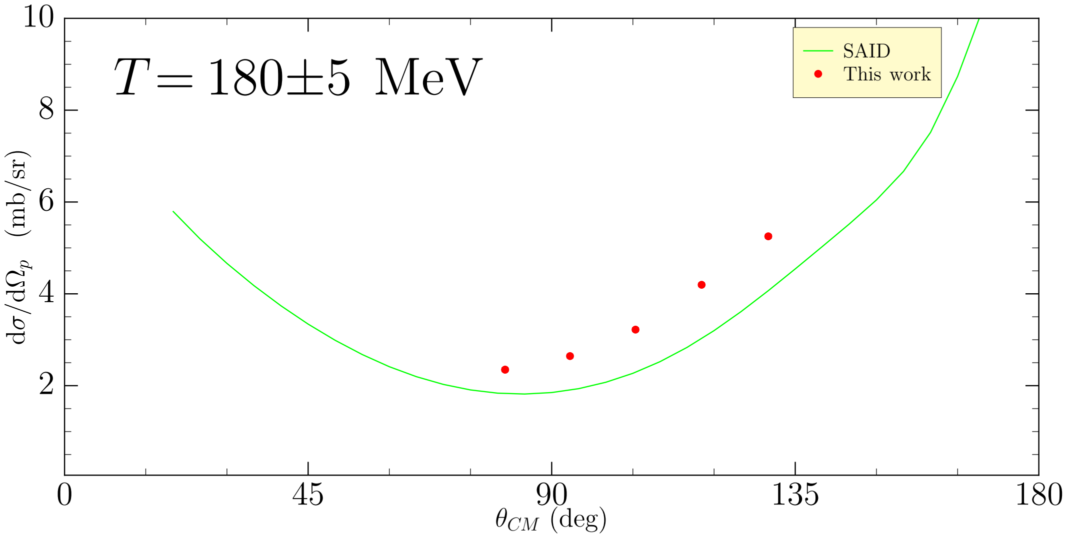

scattering cross section is given in Figure 3.14.

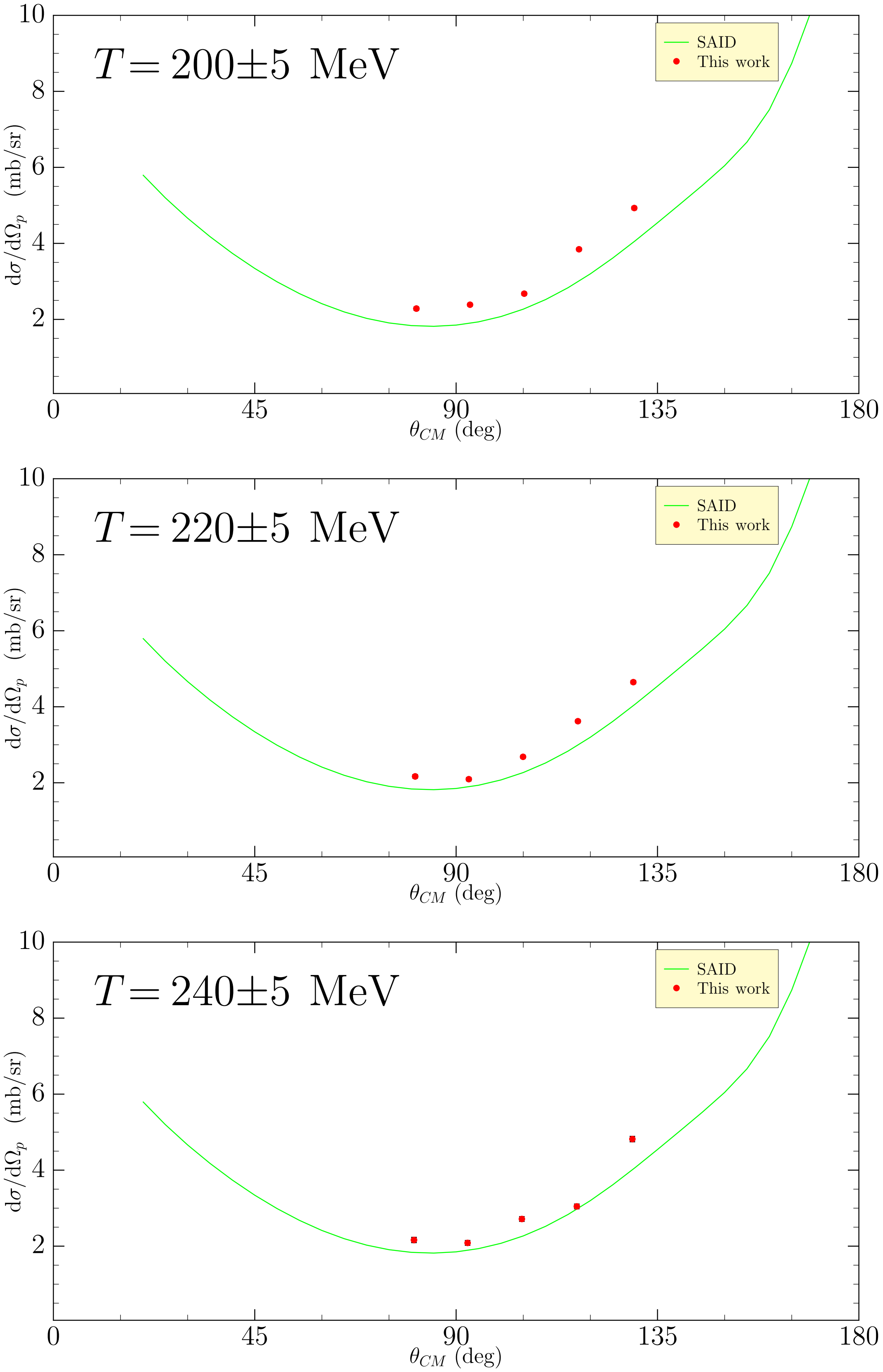

Figure 3.12. *np* elastic cross-section results.

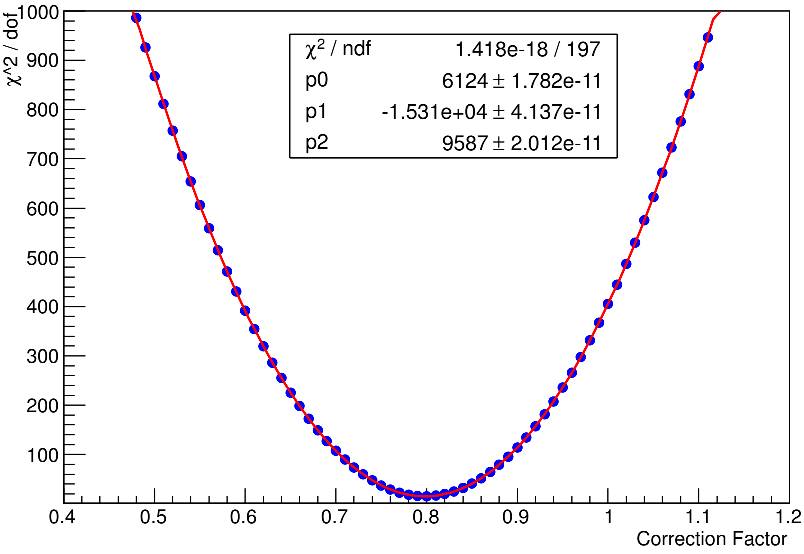

Figure 3.13. Target thickness correction - minimization of χ^2/dof.

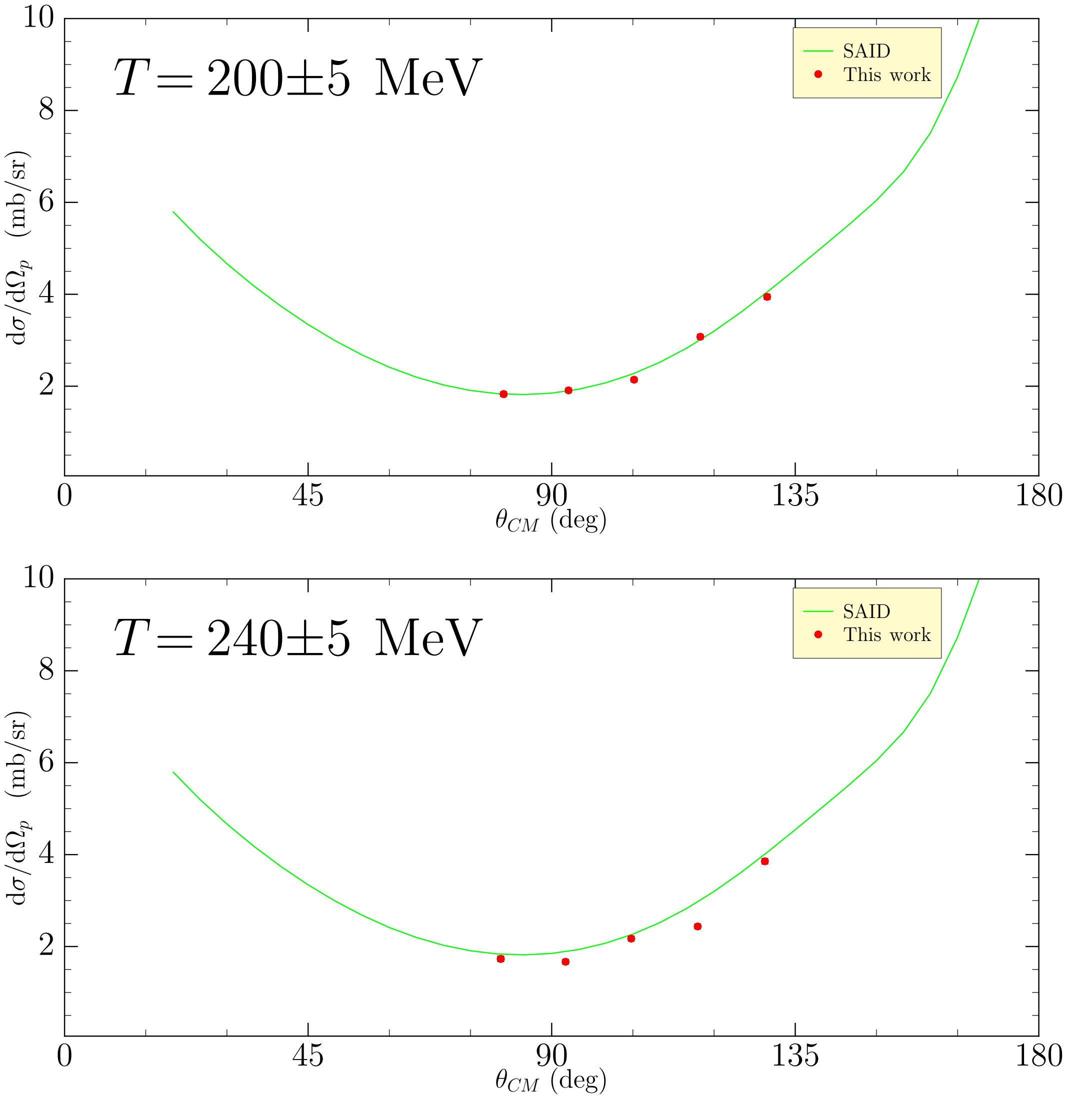

Figure 3.14. Typical corrected np elastic cross-section results.

3.5. Determination of Neutron Efficiency

3.5.1. Geometric Acceptance

Before going into the determination of the efficiency, we should first check the neutron bar hit profile using a Monte Carlo (MC) simulation. The reason is that we would like to make sure that monoenergetic neutrons scattered from the protons detected by different CsI detectors cover somewhat distinct areas on the wall for a specific incident beam energy. This check tests the correctness of our kinematic calculations and confirms that geometric acceptance is close to 100 % for the range of interest.

The position, orientation and dimensions of the wall are known and we used the incoming beam energy slice of 200 ± 1 MeV which gave us the profile similar to that shown in Figure 3.6.

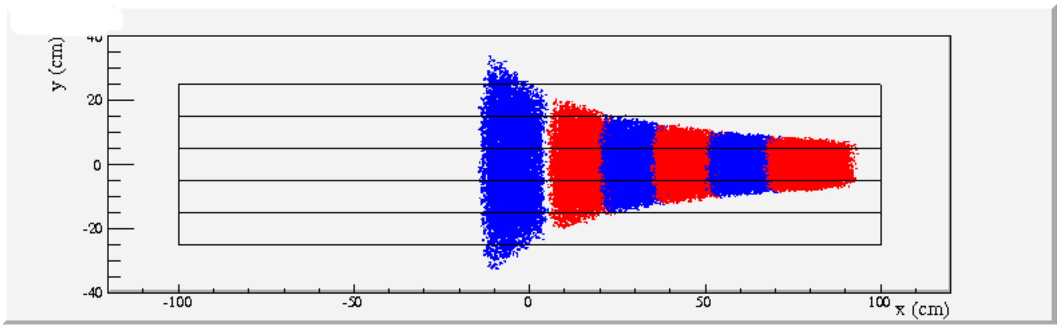

Figure 3.15. Neutron wall hit profile.

The hits scattered from protons detected by six different CsI detectors are clearly seen. In addition, the neutron bars are also indicated. We decided not to use data from 16° CsI detector since some of the scattered neutrons for that detector (the left-most blue hits) get away as easily seen in the figure so the geometric acceptance for that angle is not unity. Another important point is that the hits corresponding to proton hits at different angles mostly do not overlap which is also consistent with the expectations as we used a narrow incident neutron energy range.

3.5.2. Neutron Detection Efficiency

The difference between the time information obtained from the PMT's at the right and left of a specific bar gives us the position of the neutron hit on the bar. Therefore, if we make a histogram of this time differences for a specific CsI angle, we easily recognize the region on the histogram where the neutron hits form a peak. Then, all we have to do is, for a specific incoming energy and CsI angle, to count the proton single events and the neutron hits in the region of interest. The ratio will gives us the neutron detection efficiency.

Naturally, we want to find the neutron efficiency with respect to the energy of the neutron hitting the bar, so we need to map the energy of the neutron hitting the bar to the energy of the beam. This is done using elastic kinematics, given the energy of the neutron hitting the bar and the angle of the CsI detector, the energy of the neutrons in the beam can be (numerically) found. We expected to find the efficiency in the range of about 25-150 MeV since the maximum energy of a neutron in an *nd* elastic scattering is calculated to be $\sim$ 146 MeV for 250 MeV incident neutron. The steps of the analysis can be summarized as below:

- The kinetic energy of a proton in the proton-single event is calculated using the TOF information. It is worth noting that this calculation now includes the energy losses.
- The incoming neutron energy is calculated via the proton kinetic energy and the CsI angle. We pick the events with the energy values that correspond to the energy at which the efficiency is calculated. For example, for the efficiency at 25 MeV, the energy of the neutron beam is calculated to be 142 MeV for 24° CsI detector. Then we accept the events with the incoming neutron energy 142 ± 5 MeV.
- Among the accepted events, we make an E-ΔE histogram and determine the proton region in this histogram. Around the proton region, we apply a graphical cut, which is our second filter. We count the protons inside the region. An example cut is shown in Figure 3.16.

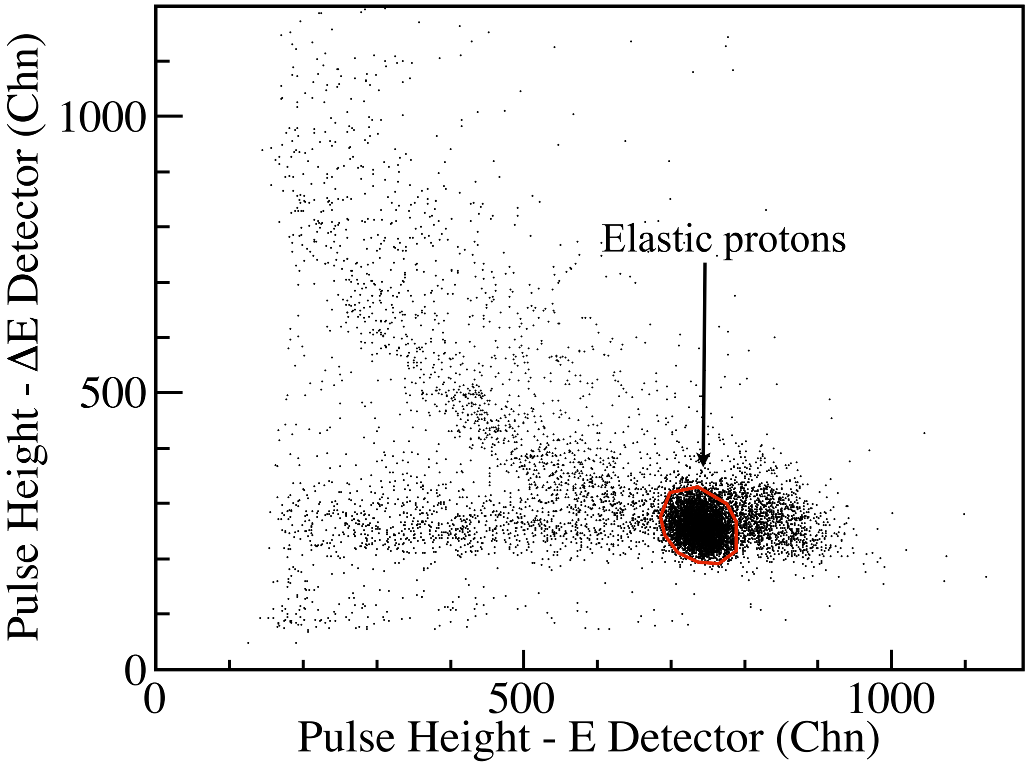

Figure 3.16. Proton identification (ID) cut for the beam energy 170 ± 5 MeV.

- For the CsI angle and the proton events inside the cut, we fill histograms for the neutron bar time differences, for a specific beam energy. Then we count the neutrons inside the pile-up regions of the bars. The neutron counting part of the analysis is in fact subtle since there are two issues to be considered: Double (or triple) counting and subtraction of the background. In some cases, a single neutron hitting the bar can fire more than one bars. If both of these records are in the regions of interest, a single event may be counted multiple times. In order to prevent this, we count the event once even if it leaves a trace more than once. To deal with the background subtraction, we pick regions far from the pile-up regions and same size with the pile-up regions on the histograms and count the neutrons inside these regions (again avoiding double counting) and we subtract this number from the neutron count inside the regions of interest. It is important to note that we assume the background is independent of the position on the bar which allowed us to use different regions. We confirmed this observing a flat background in Figure 3.17. In addition, due to cross-talk, a neutron outside but close to the region of interest can manifest itself inside the region of interest of a neighbour bar, hence we may have included some extra neutrons which must not be counted. However this has a very little effect when compared to other uncertainties. Below is an example histogram for the middle bar. The region of interest is clearly noticed, it is between 3 ns and 10 ns, and the background region is chosen between -10 ns and -3 ns for this case.

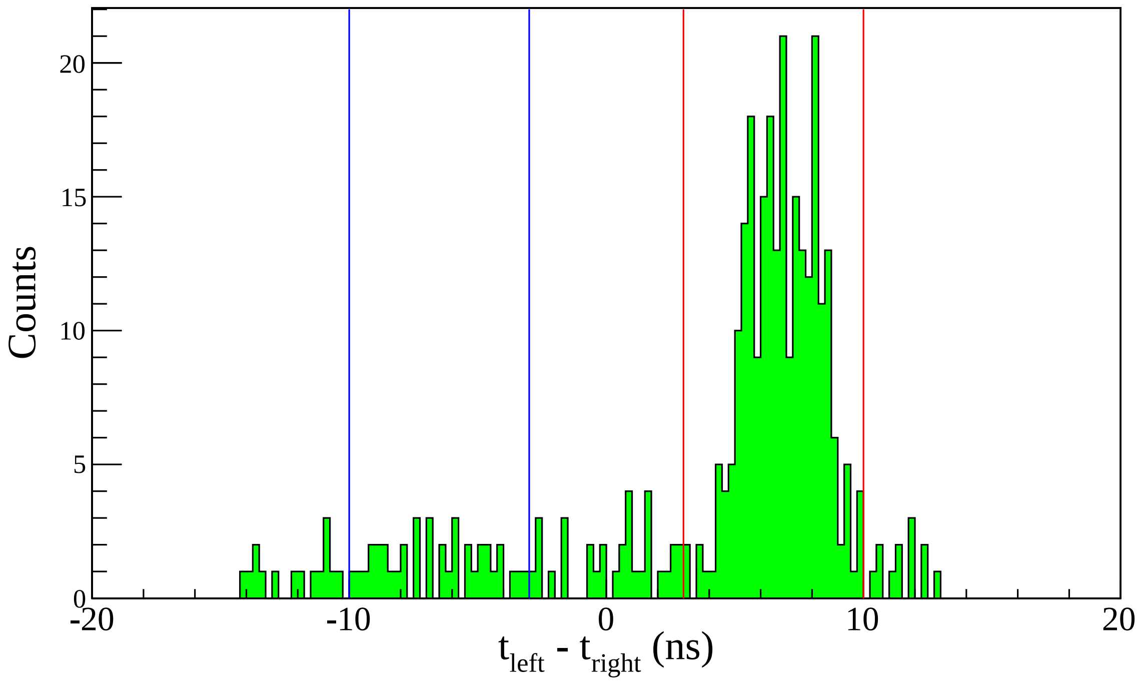

Figure 3.17. Time difference histogram of the middle bar the beam energy 170 ± 5 MeV. Region of interest and background region is illustrated with red and blue boundaries, respectively.

- The efficiency is then found as

$$\epsilon_N(T_n) = \frac{N_n - N_{n-bg}}{N_p}$$

Below is the table showing the results. The columns **Np**, **Nn** and **bg** are the proton count inside the proton ID cut, the total neutron count in the regions of interest (of five bars) and the total count in the background regions, respectively. The column *np_bit* is a control column telling how many of these counted neutrons are also recorded as a coincidence event, the **np_bit** and **N_n** counts are close which confirms the reliability of the electronic trigger system. The **eff** column is the result obtained without the background and the column **eff_bg** is the result with the background taken into account and of course the error column belongs to the **eff_bg** values.

We also noted a deviation from the “smooth” behavior as a function of T_n at $T_n = 62.5$ MeV, thus decided to include another point at $T_n = 69$ MeV, and concluded that it was a statistical fluctuation.

Table 3.1. The detailed neutron efficiency results.

Tn (MeV)	**CsI (deg)**	**Tno (MeV)**	**Np**	**Nn**	**np_bit**	**bg**	**t_diff (ns)**	**eff**	**eff_bg**	**eff_er**
25	24	142	11048	3194	3182	364	2.10	0.289	0.256	0.005
	30	96	20680	5448	5432	645	5.15	0.263	0.232	0.004
	36	70	31391	8158	8136	1002	7.81	0.260	0.228	0.003
37,5	24	208	4627	1051	1045	116	2.54	0.227	0.202	0.007
	30	142	10554	2389	2371	367	5.37	0.226	0.191	0.005
	36	105	14805	3169	3163	433	8.06	0.214	0.184	0.004
50	24	270	3544	697	689	96	2.72	0.197	0.170	0.008
	30	186	6744	1249	1249	138	5.63	0.185	0.165	0.006
	36	138	9135	1615	1614	193	8.20	0.177	0.156	0.005
62.5	24	331	1502	271	271	18	3.18	0.180	0.168	0.011
	30	230	3915	679	678	100	5.91	0.173	0.148	0.007
	36	171	5597	923	923	93	8.51	0.165	0.148	0.006
69	24	361	1116	187	187	32	3.45	0.167	0.139	0.013
	30	252	3114	464	464	49	6.12	0.149	0.133	0.007
	36	188	4621	756	756	74	8.71	0.164	0.148	0.006
75	24	388	821	119	117	28	3.80	0.145	0.111	0.015
	30	271	3291	455	455	52	6.19	0.138	0.122	0.007
	36	203	4070	585	584	71	8.82	0.144	0.126	0.006
	42	160	4269	537	537	50	11.23	0.126	0.114	0.006
87.5	30	312	1842	244	244	35	6.47	0.132	0.113	0.009
	36	235	3043	381	380	43	8.96	0.125	0.111	0.007
	42	186	2736	314	314	29	11.33	0.114	0.104	0.007
100	30	352	1298	168	167	14	6.83	0.129	0.119	0.010
	36	266	2610	373	373	25	9.33	0.143	0.133	0.008
112.5	30	392	875	116	116	10	6.98	0.132	0.121	0.013
	36	296	1890	238	238	22	9.39	0.126	0.114	0.009
125	30	430	750	76	76	9	7.51	0.101	0.089	0.012
	36	327	1552	179	179	24	9.79	0.115	0.100	0.009
137.5	30	468	356	45	45	1	7.74	0.126	0.124	0.019
	36	356	1178	139	139	18	9.95	0.118	0.103	0.011
150	30	505	412	56	56	8	7.56	0.136	0.116	0.019
	36	386	931	123	122	11	10.21	0.132	0.120	0.012

The final results then are listed as

Table 3.2. The final neutron efficiency results.

Tn(MeV)	**n_eff**	**n_eff_err**
25	0.234	0.002
37.5	0.189	0.003
50	0.162	0.003
62.5	0.151	0.005
69	0.141	0.005
75	0.120	0.005
87.5	0.109	0.004
100	0.128	0.006
112.5	0.116	0.008
125	0.096	0.008
137.5	0.108	0.011
150	0.119	0.011

We also know that the efficiency depends on the position of the hit on the bar. The hit position of neutrons with the same energy changes between *np* and *nd* events, therefore, the cross-section results may be affected by this dependence. Moreover, it is expected that the ends of the neutron bars are less sensitive compared to the middle. We will continue as if there is no dependence and in the next subsection, we will outline our treatment of the position dependence.

The efficiency and its error for a specific neutron energy is found by standard procedures considering each efficiency value to be independent, thus we averaged them using the proper weights. Then the results are fit by an empirical function of the following form

$$\epsilon(T_n) = A + Be^{-T_n/C}.$$

We will use this function for the rest of the analysis. Figure 3.18 shows the values and the fit parameters along with the data and the model.

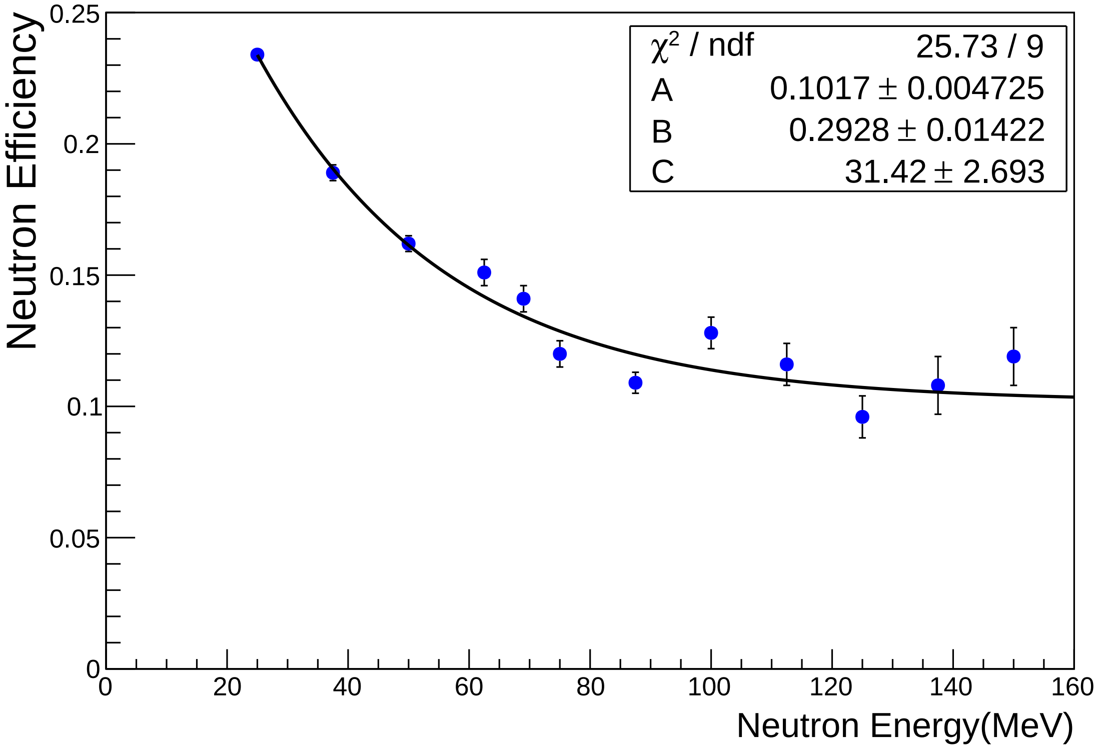

Figure 3.18. The neutron efficiency fit using a simple model.

The parameters of the fit function also have errors which means the fit function has some uncertainty or in other words, there is a possible band of functions for these data. Assuming A, B and C are weakly correlated, the uncertainty of the function can be found as

$$\sigma_f^2 \approx \left(\frac{\partial f}{\partial A}\right)^2 \sigma_A^2 + \left(\frac{\partial f}{\partial B}\right)^2 \sigma_B^2 + \left(\frac{\partial f}{\partial C}\right)^2 \sigma_C^2 + \Theta(\text{terms with covariances}),$$

which is also a function of energy. The upper and lower boundaries of the band shown in Figure 3.19 indicate 1-σ errors using this.

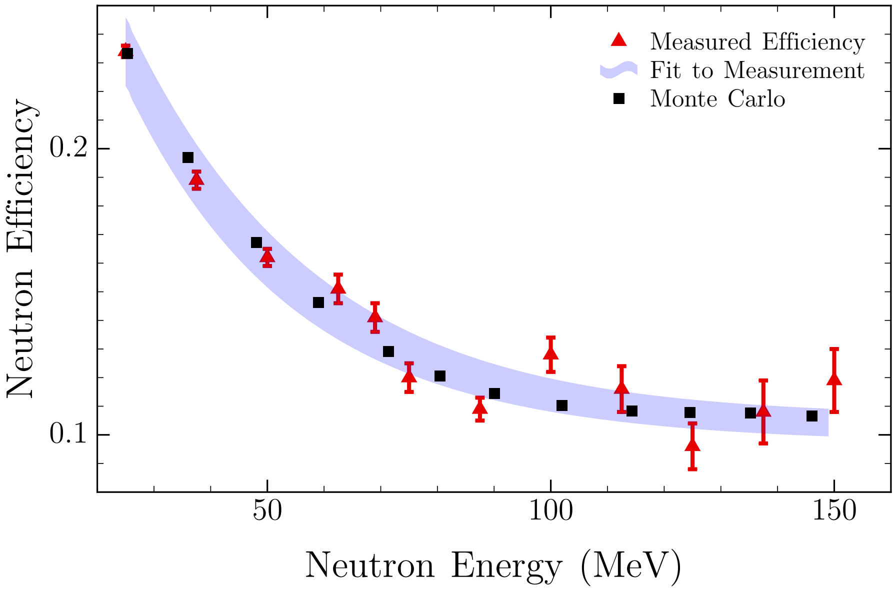

Figure 3.19. Neutron detection efficiency in the scintillator bars as a function of neutron kinetic energy. The circles represent the data obtained in the present measurement, the diamonds a Monte Carlo simulation [8]. The band is a fit to the data as described in the text.

3.5.3. The Position Dependence of Neutron Efficiency

Observing Table 3.1, we see that the neutrons with the same energy yield slightly different results depending on the angle of the CsI detectors, thus the neutron position on the bar. Our strategy here is similar: We will find the efficiencies for the same energy associated with different CsI angles and since different angle means different position on the bar, the variations will give us the dependence. Figure 3.20 demonstrates the results of this analysis.

The position dependence of the efficiency is assumed to be smooth, simple and symmetrical with respect to the bar center, therefore, we used the polynomial model in Equation 3.9

$$\epsilon_n(x) = Ax^2 + B \tag{3.9}$$

where x is the distance from the center of the bar. The fit does not look good for 70 MeV, however, the statistics is poorer for that energy evident from the larger error bars and χ^2/dof is acceptable. The average hit positions of neutrons are about 75 cm and 40 cm for 24° and 30°, respectively according to Figure 3.5 which leads to Table 3.3. The other angles are excluded since the correction is insignificant compared to the associated error and we do not use coincidence events for 54°, thus neutron efficiency. The errors presented are due to the modeling, however, we could only use 4 points for each plot due to the limitations of the experiment and we ignored the spread of the neutrons on the bars. To account for these, we introduced an additional 10% systematic error.

Table 3.3. The position correction factors.

Lab Angle(deg)	**Correction Factor**	**Correction Factor Error**
24	1.62	0.15
30	1.12	0.04

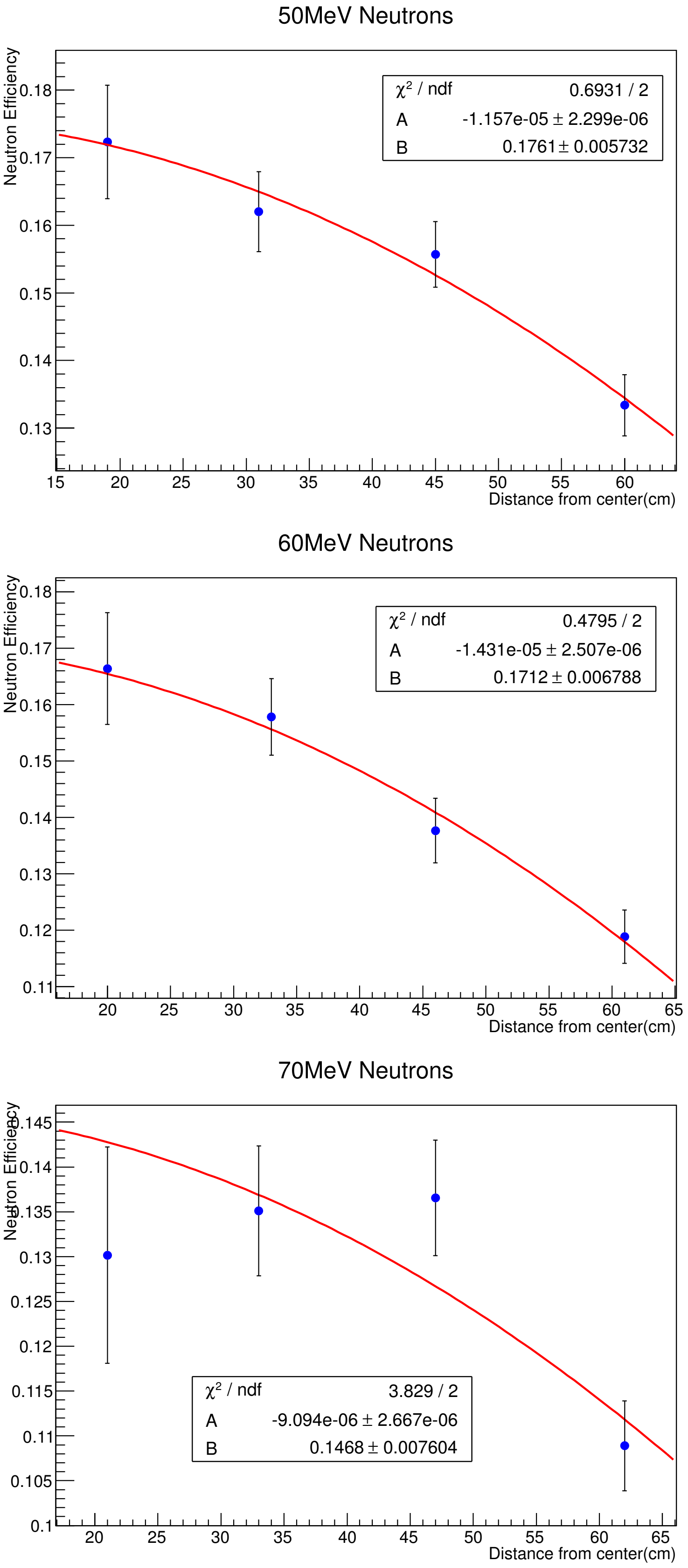

Figure 3.20. The position dependence of neutron efficiency.

3.6. Elastic Neutron-Deuteron Cross-Section Analysis

The basic methodology for finding the *nd* cross section is very similar to that of the *np* analysis, which is outlined in Section 3.4. The cross-section formula 3.10 gives us the elastic cross section in the lab frame which will be transformed in exactly the same manner to the center-of-mass frame as discussed in Section 3.4 and Appendix C.

$$\left(\frac{\mathrm{d}\sigma}{\mathrm{d}\Omega_n}\right)_{lab} = \frac{N_n}{N_i \epsilon_n \epsilon_p} \frac{k}{\Delta\Omega_d \rho_t l}. \tag{3.10}$$

The symbol N_i represents the number of incident neutrons in the energy cut we applied. $\Delta\Omega_d$ is the solid angle of one CsI detector and ϵ_p is its efficiency. Since the detectors, detector geometry and the setup are the same as in the *np* case, the values are also the same, namely $\Delta\Omega_d = 8.446 \times 10^{-3}$ sr and $\epsilon_p = 1$ as discussed in Section 3.4. The live time l for the deuteron runs is 85%. For this case, however, we use coincidence events, hence the pre-scaler $k = 1$ and the appropriate neutron efficiency ϵ_n with respect to the energy is used. The measurement of ϵ_n has been thoroughly discussed in Section 3.5. Another quantity that differs from the *np* case is the target thickness since the target is LD_2, and the areal density comes out as $0.1002\mathrm{g/cm}^2$ using density of the LD_2, $0.1690\mathrm{g/cm}^3$, and the target geometry. Of course, the number that appears in the formula is the effective target thickness, namely this number times the correction factor 1.25 ± 0.06.[3] The number N_n is the number of particles that are the products of elastic collision. The rest of this section is dedicated to the obtaining of N_n.

The task was simple for the *np* case as the elastic events were clear in E-ΔE

---

[3] With regard to the validity of applying the same renormalization factor to the *nd* data: the fission chamber calibration and the window-bulging will certainly be the same for both hydrogen and deuterium. Following the experiment, the target cell was observed (at room temperature and atmospheric pressure) to have a permanent deformation; its physical thickness had increased by a factor of 1.45. The reduction of the effective target thickness due to bubbling apparently leads to the factor 1.25. In principle the reduction could be different for LH_2 and LD_2, since the boiling point temperature for LD_2 is lower. However, the systematic error in the cross section associated with the assumption of a constant renormalization factor was estimated to be an additional 3% at worst, and has been included in the analysis.

histograms, we did not need to use graphical cuts and the neutron efficiency did not play a role. For the *nd* case, however, we observe two loci, one belonging to the elastic deuterons, the other belonging to the quasi-elastic protons originating from the target as well as the windows. A typical plot, Figure 3.22a, is shown after an incident beam energy cut. As one may observe, the separation is not so clear and there is some quasi-elastic proton contamination in the deuteron region. The situation gets worse for backward angles and higher energies. Therefore, we had to invent some methods to clearly distinguish the deuterons and these methods include the use of neutron bars. The sum of left and right PMT responses from the neutron bars should kinematically give a constant value for a specific deuteron angle, therefore we applied a cut on this value to remove a considerable number of protons and background as in Figure 3.21 which transforms the histogram from (a) to (b) in Figure 3.22.

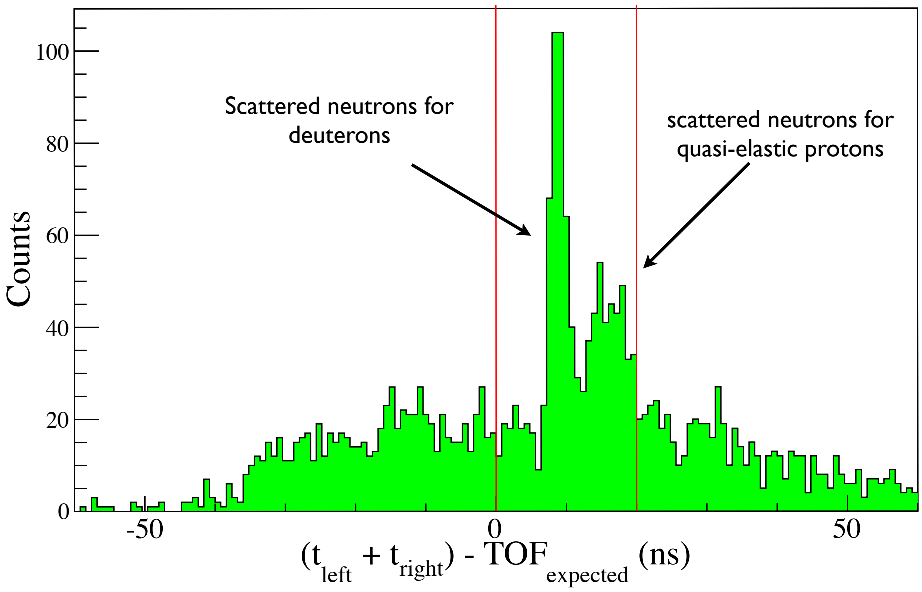

Figure 3.21. The total of time readings of one of the bars for deuteron recoil angle θ_d = 36° and incident neutron energy T_{beam}= 210 MeV.

For each recoil deuteron angle, the angle of elastically scattered neutron is determined by kinematics. The time difference of left and right PMT signals from the neutron bars is directly related to the hit position of the neutrons and thus the scattering angle. Figure 3.23 shows that the neutrons from elastic collisions appear between red lines and the rest of the data is from neutrons in coincidence with quasi-elastic protons and accidental events. Hence, we can obtain the number N_n by counting the

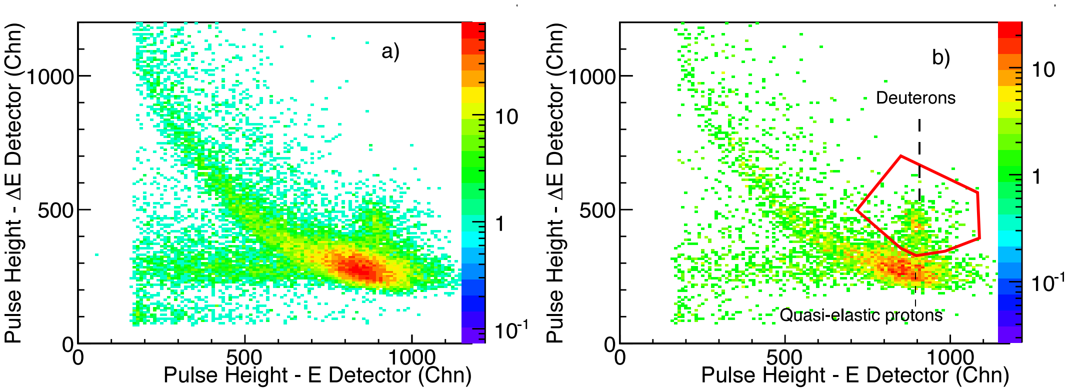

Figure 3.22. $\Delta E - E$ histograms of nd events for deuteron recoil angle $\theta_d = 36°$ and incident neutron energy T_{beam}= 210 MeV a) before, b) after the cuts on the neutron timing as described in the text.

events in the region of interest and calculate the differential elastic cross section with appropriate background subtraction. Unfortunately, it is not a simple task to obtain such histograms nor to identify background for all cases. Therefore, we had to devise two methods for different cases.

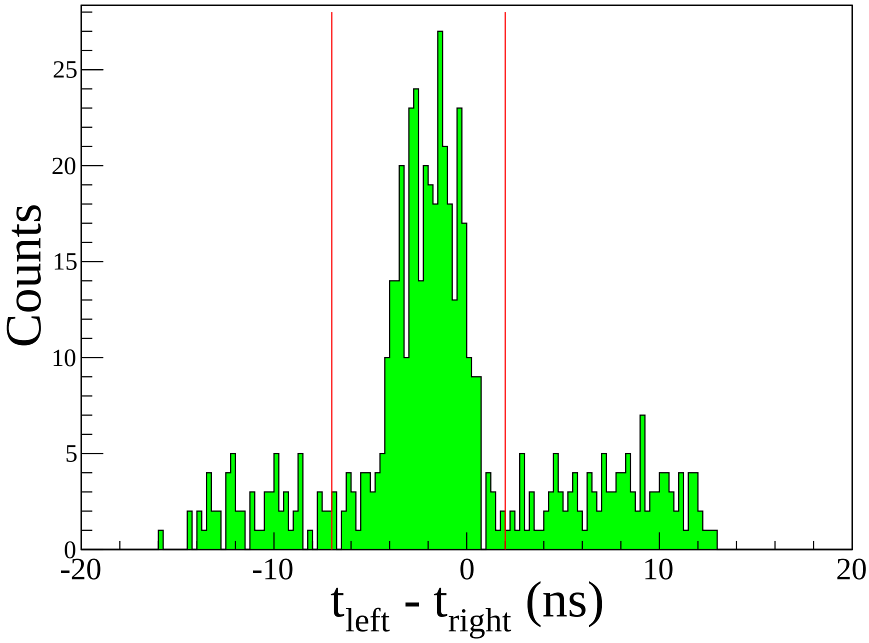

Figure 3.23. The t_{diff} histogram of middle bar at 170 ± 5 MeV for 36° (lab) deuteron angle.

3.6.1. Main Method of Coincidence Analysis

Apart from the neutron backward angle, corresponding to deuterons at 24° in the laboratory frame, all the coincidence results are found using what we call as the *Main Method*. The method here refers to the succession of filters employed to obtain a clear picture where we can extract the number of neutrons of interest for a desired energy. The first filter we apply is the energy cut on the incident beam. We use incident energy bins of 10 MeV (±5 MeV) and Appendix D.3 justifies this choice.

After this cut, our E-ΔE histograms look like Figure 3.24. In this specific case, $T_{beam} = 200 \pm 5$ MeV. We can see the deuterons to the right of the prominent proton locus, and the separation improves as the angle increases. The proton contamination is severe especially for backward angles. To reduce the contamination, we use the neutron bar information. We have two type of histograms for this purpose, $t_{\mathrm{l}} - t_{\mathrm{r}} = t_{\mathrm{diff}}$ and $(t_{\mathrm{l}} + t_{\mathrm{r}}) - t_{\mathrm{expected}} = \Delta\mathrm{TOF}$, mainly the difference and sum of the time information coming from the PMT's at the bar ends. (t_{expected} is evaluated according to the geometry, thus we expect a peak "around" zero for deuteron coincidence events.)

The second cut applied is on the ΔTOF whose histogram is seen in Figure 3.25. The higher peak corresponds to the deuterons and the lower and wider one is due to protons. This cut is a generous one as the limits on ΔTOF are adjusted to include all the deuterons and even some of the protons in order not to lose efficiency. After this cut, we fill another set of E-ΔE histograms as in Figure 3.26 which are significantly cleaner than the original, in which we can apply a graphical cut around the deuterons. Rather than calculating the efficiency of this cut, we make it large enough so that almost no deuteron can escape it even at the cost of some background which makes sure we do not lose efficiency again, and we investigated the associated systematic errors as will be explained later.

The last phase of the analysis is to fill t_{diff} histograms of the events inside the graphical cut and count the neutrons due to *nd* elastic scattering, which will be referred as neutrons-of-interest from now on. These histograms look like Figure 3.29 and peaks of neutrons-of-interest are clear (Those to the left end of the histogram). These peaks are not well-shaped so instead of modelling and fitting, we need to count the events inside those peak ranges. For every CsI and every bar, we identify the neutrons-of-interest region, i.e. between -15 and -9 ns for bar 1, and count the events with that characteristic. Similarly, assuming flat background, we identified a background region with the same width for the same bar, i.e. between 0 and 6 ns, and count the background events. In principle, one event can fire more than one bar or accidental events can produce erronous information. Therefore, for 200 MeV, we looked at the multiplicity situation, that is, we count how many times the detectors fired one at a time, two at a time, etc. The ratio of multiple firing to single firing was about 7.5% which is not large but must be handled properly. This method gives very good results for the intermediate angle CsI detectors like the one in Figure 3.30; however, the forward neutron angle result is lower than expected, and the situation for backward angle is even worse as mentioned earlier and shown in Figure 3.29.

For the forward neutron angle, 54°, we claim that there is a geometrical and electronics acceptance issue even though the simulations showed that this should not be the case. In Figure 3.27, we can clearly see that the rightmost part of the neutrons-of-interest peak ends abruptly. The discrepancy between the simulation and the data may be explained by either a small error in detector position or $ne_{\text{left}} - ne_{\text{right}}$ coincidence window in the trigger. Therefore, we cannot make a correction to that point since we cannot determine the acceptance ratio for sure. Solution we attempted was to use singles data, however, those data were discarded eventually. The details of this issue will be given later.

One can find the figures outlining the main method in Appendix A.

3.6.2. Alternative Method of Coincidence Analysis

The main method gives very good results for the intermediate angle CsI detectors, however, the situation for the backward neutron angle is not so favorable. The reason why the main method does not work is that the background is not flat, the nearby quasi-elastic proton peak produces higher background levels. The sketch in Figure 3.28 summarizes the situation as there is no bump due to quasi-elastic protons in the second figure, at least in the background region to the left of the peak due to deuterons. Figures 3.29 and 3.30 shows the actual data.

Therefore, we need to model the background and obtain an estimate. Unlike the neutrons-of-interest peak, the background looks like a wider gaussian on top of a flat background. However, the amount of data in the t_{diff} histograms after the graphical cut is not sufficient for a good fit, thus we employed the t_{diff} histograms of the events outside the graphical cut as they contain more data and show a definite smeared peaks due to quasi-elastic protons. We apply a four-parameter fit, the parameters being mean, amplitude and standard deviation of a gaussian plus a constant. We are only interested in the location and the width of the neutrons due to protons which are precisely determined by this first fit. We apply the same fit to the t_{diff} histograms for the events inside the graphical cut forcing the mean and the σ found by the previous fit. These two parameters are expected to be the same for neutrons due to protons for both inside and outside the graphical cut. As a result, the value of the constant fit parameter will give us the level of the background. This approach assumes that the multiple firing is insignificant when compared to the single firing which is the actual case since the 7.5% multiple firing cannot significantly change the fit parameters. We estimate the systematic error due to this will be small. The only thing remains is to estimate the error resulting from this analysis. The most effective element is the graphical cut as it actively shapes the histograms. Therefore, we repeated the analysis for a tight and a very broad cut which includes some of the quasi-elastic protons. The results of a normal cut and a broad cut are within error bars which is as expected since even if the background is high, our method must determine the background correctly. The results for the tighter cut came out low, again as expected as we obviously lose some deuterons (Note that we used the normal cut for the final results.). The deviation gives us an estimation on the systematic error of this approach. The results deviated 15% for 200 MeV and 10% for 135 MeV, we included these deviations as systematic errors which are, we believe, a little overestimated. One can find all the figures and fit parameters in Appendix E. Figure 3.31 focuses on the results of the alternative method for the forward angle at 200 ± 5 MeV. The vertical lines are two different predictions for this energy and one can clearly see that this analysis is superior to the singles analysis which is why we use it instead of singles.

3.6.3. The Singles Analysis

As stated previously, there is a geometrical acceptance issue regarding the neutron wall as clearly seen in Figure 3.27 which rules out a coincidence analysis. We may turn our attention to singles, however, there is no direct way of subtracting background. Therefore, we decided to calculate the cross sections without any background subtraction and then perform a scaling.

The singles analysis is the same as that for the *np* case except for the background part. We are also confident about the cross-section results of the intermediate angles so they serve as our reference points. The graphical cuts used are the same as the ones used in the coincidence analysis. The scaling factor is the ratio of the coincidence results to the singles results for the intermediate angles, found by calculating the weighted mean of the scaling factors for each point.

Like the alternative method, the analysis depends heavily on the graphical cuts, therefore, the method is used once again with wider cuts and in turn another scale factor is obtained. Quantitatively, the scaling factor with normal cuts is found to be 0.464 whereas the factor with wider cuts turned out to be 0.754. The presented singles results are the combination of the two results with cuts with different sizes. In addition, the difference of the two scaling factors helps us estimate the systematic error for this analysis. We simply assign percent difference of the factors as the systematic error, which is 25%. The number may look large, but it is reasonable for such a crude analysis.

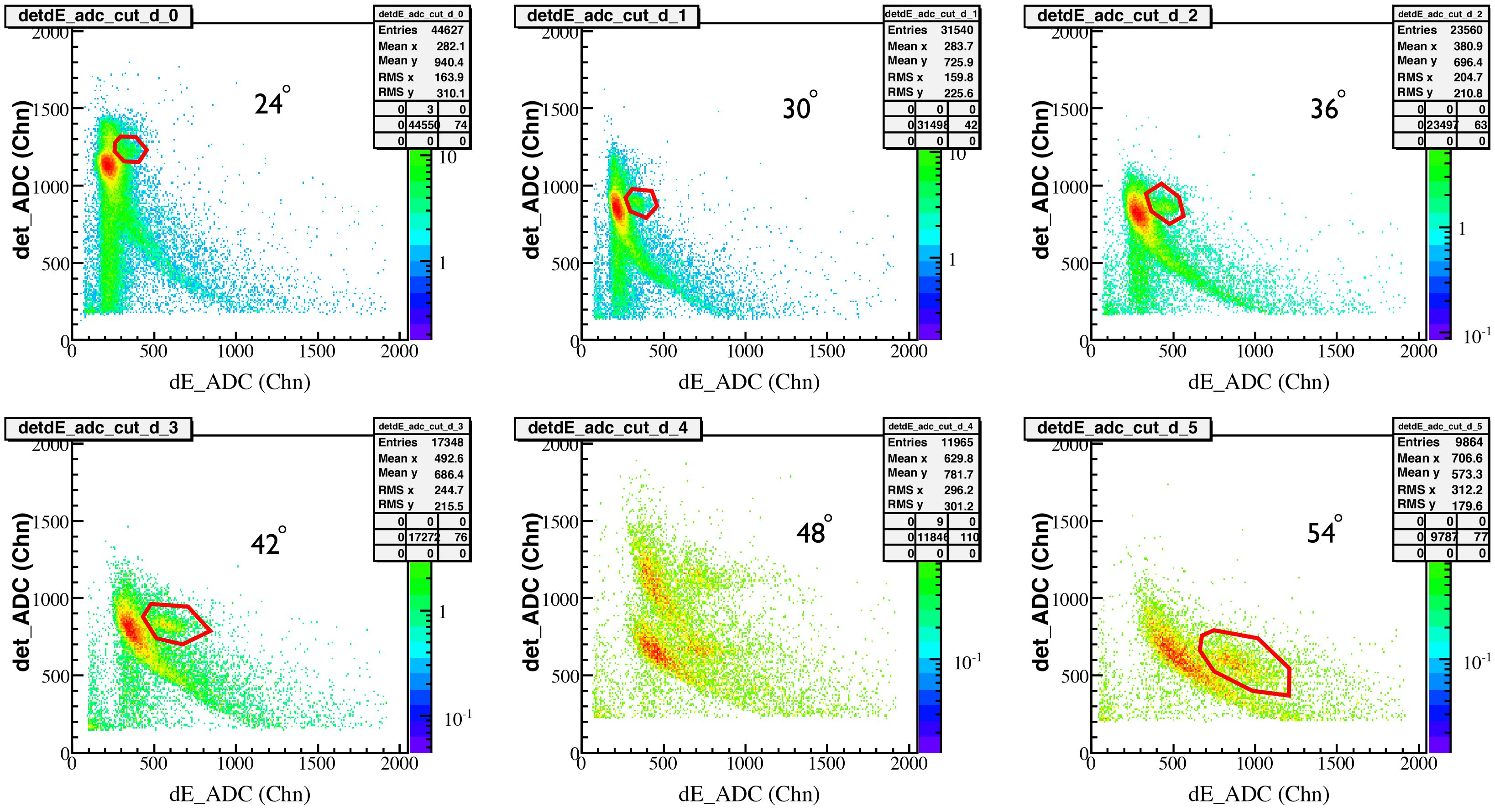

Figure 3.24. E-ΔE histograms for 200 ± 5 MeV. (Note that 48° detector shows a gain shift. We analyze the data for this specific detector with two separate run ranges.)

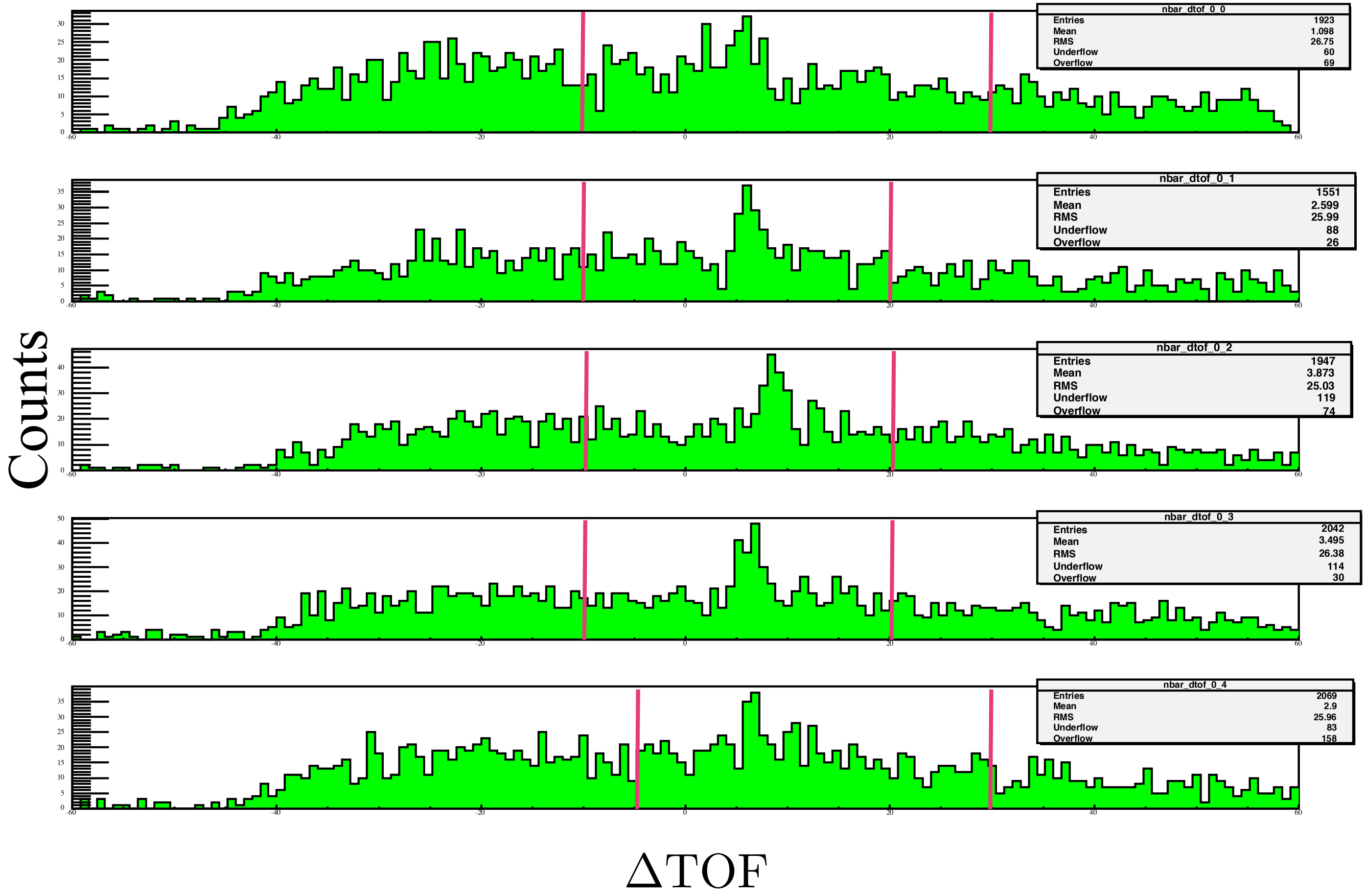

Figure 3.25. ΔTOF histogram of forward angle for 200 ± 5 MeV, the red bar shows region of interest.

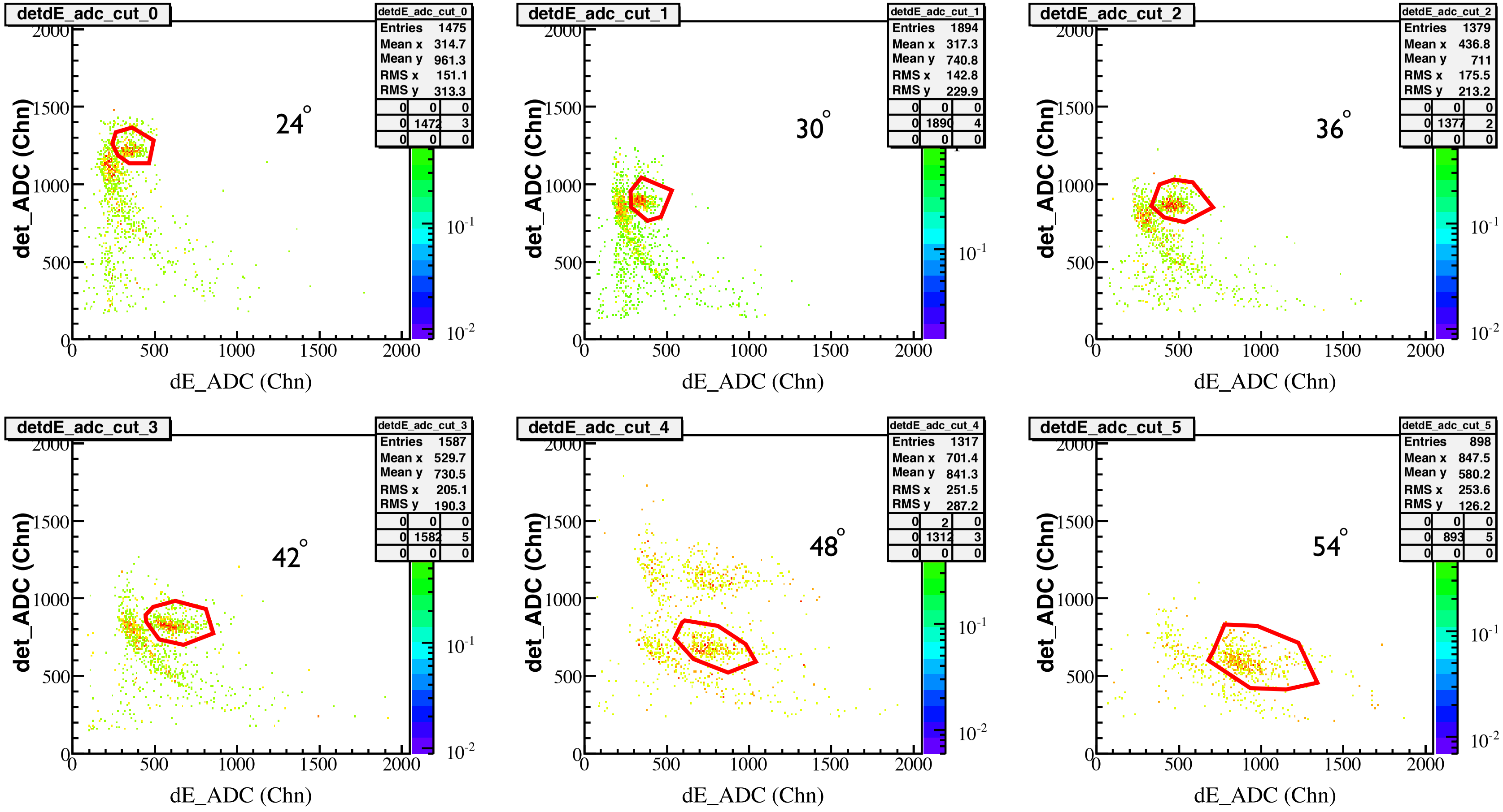

Figure 3.26. E-ΔE histograms for 200 ± 5 MeV after ΔTOF cut.

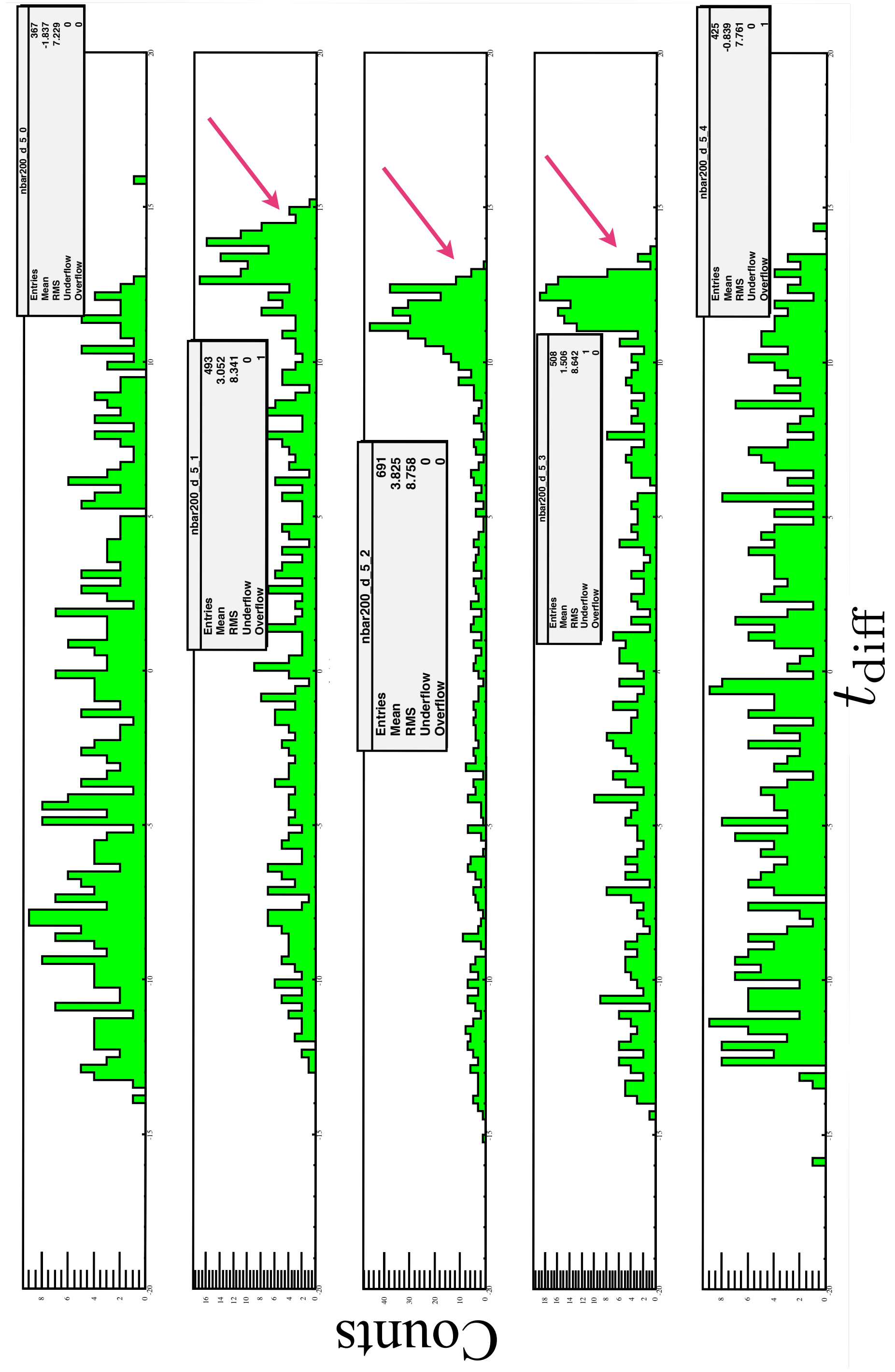

Figure 3.27. t_{diff} histograms of forward neutron angle for 200 ± 5 MeV, arrows show the missing part.

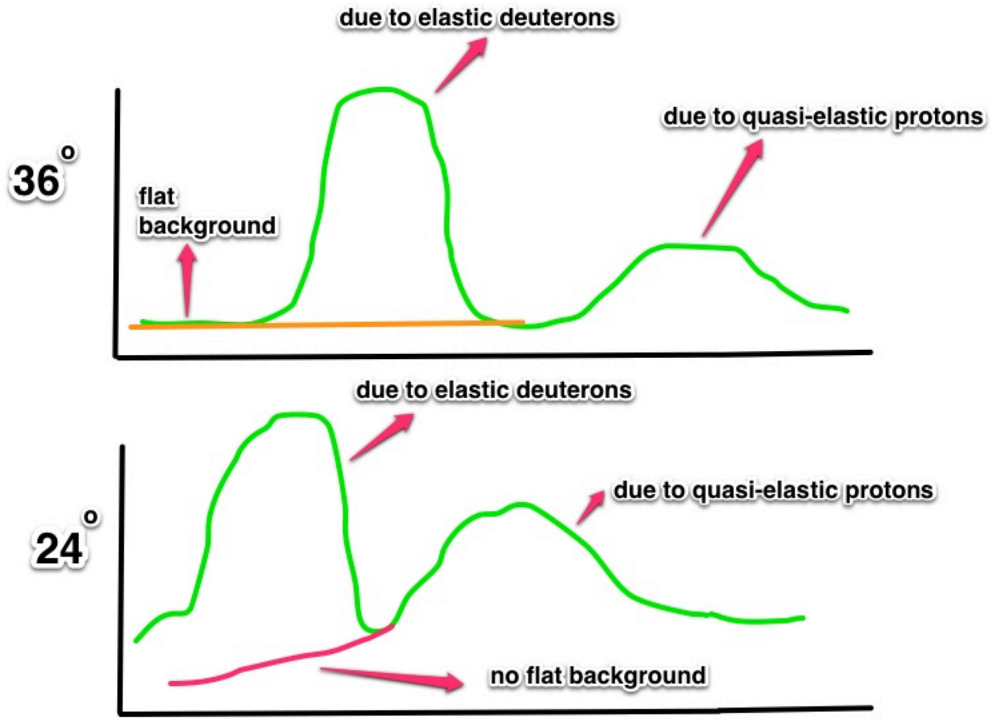

Figure 3.28. The sketch of neutron bars belonging to different CsI detectors. For 36° the background can be detected from the flat region to the left-most edge of the histogram.

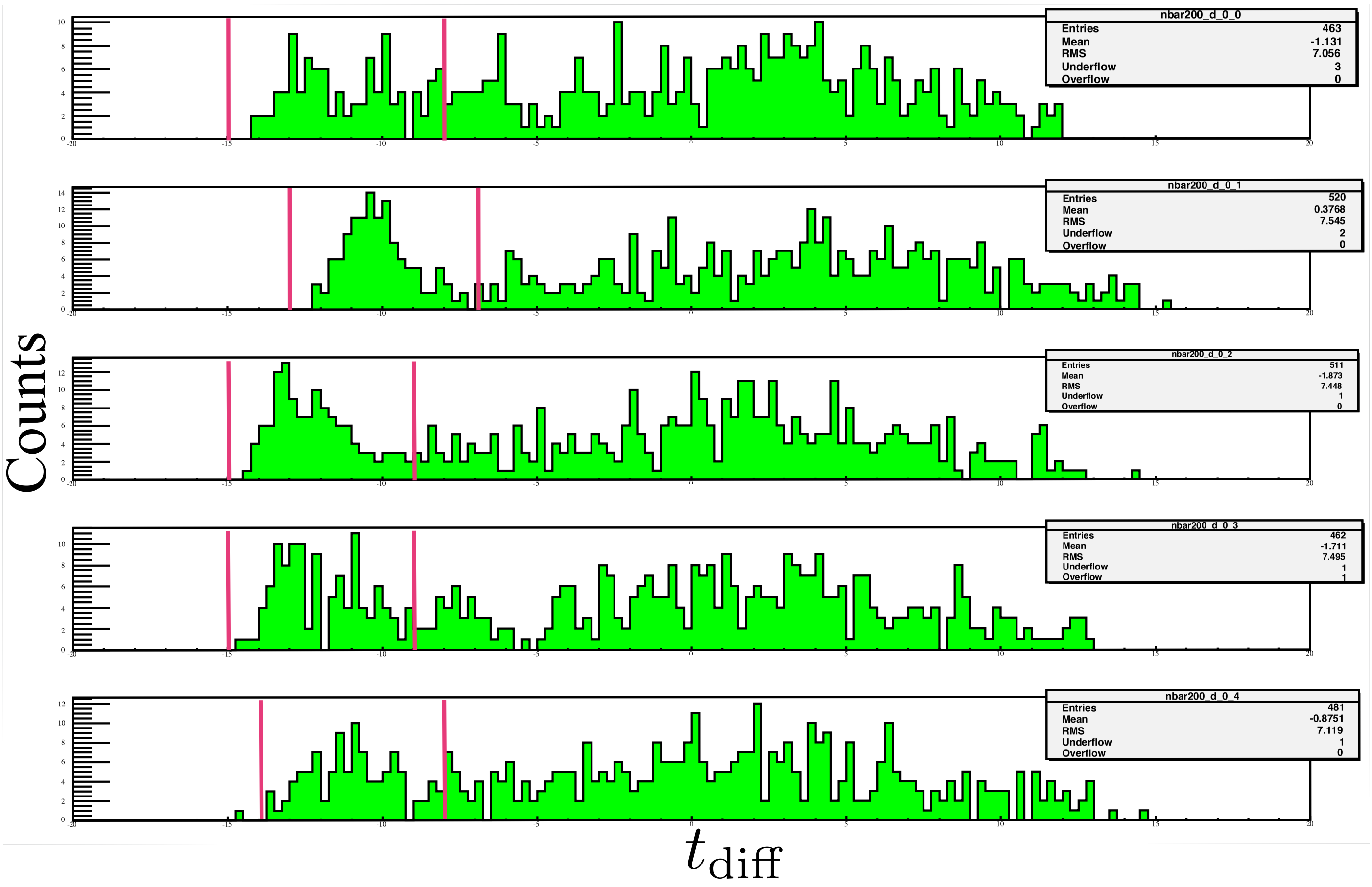

Figure 3.29. t_{diff} histograms of forward angle for 200 ± 5 MeV, the regions of nd elastic scattering is between red bars.

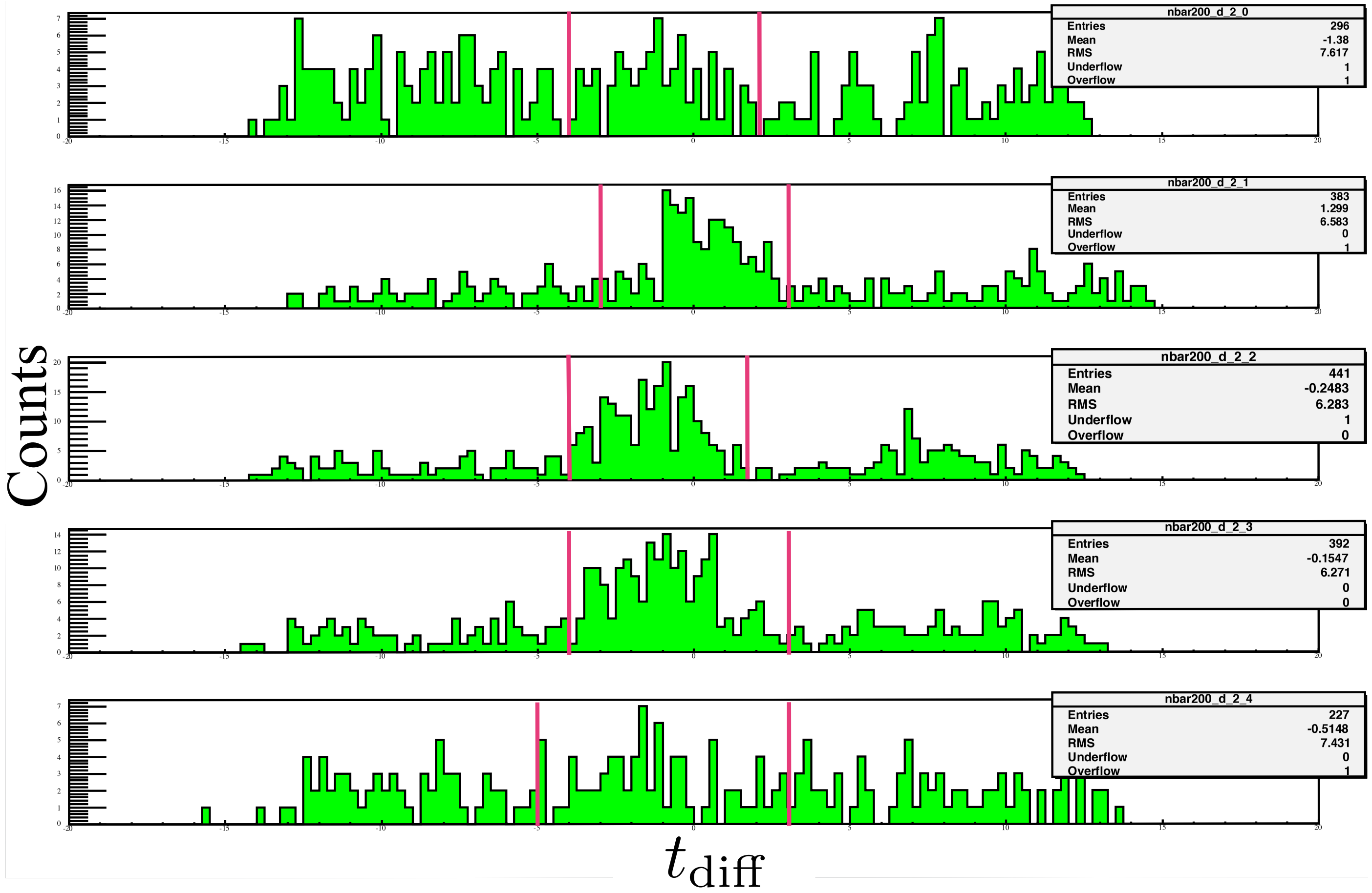

Figure 3.30. t_{diff} histograms of 36° for 200 ± 5 MeV, the regions of nd elastic scattering is between red bars.

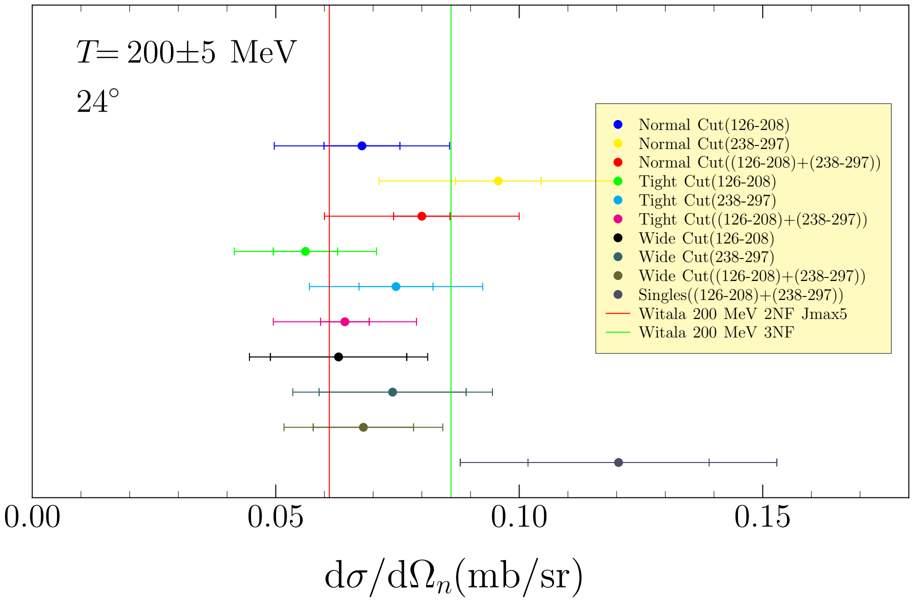

Figure 3.31. Elastic cross-section results for differents ranges of data and singles result at 200 ± 5 MeV.

3.7. Polarization Correction

Since the neutron beam is produced at a non-zero angle with respect to the proton beam direction, we expect neutron beam to exhibit some polarization. A separate experiment was carried out with the same neutron beam to measure its polarization whose details can be found in [9]. In short, Equation 3.11, which gives the number of particles scattered into the angle θ from a beam of polarization P, is used to extract the beam polarization.

$$N(\theta,\phi) = N_0(\theta)(1 + A(\theta)P_z \cos\phi) \tag{3.11}$$

In this equation, ϕ indicates the angle between the scattering plane and the polarization and $A(\theta)$ is the analyzing power of the carbon scattered. In the experiment, a rotatable detector assembly was used such that it can be rotated 180° which allowed making two separate measurements where angle $\phi = 0°, 180°$, respectively. Assuming the analyzing power is known and utilizing the symmetry of the setup, we can get

$$P_z = \frac{r-1}{A(r+1)} \tag{3.12}$$

where r is a function of the yields of the detectors placed for the two different values of ϕ.

The result of the polarization measurement is presented in Figure 3.32. We applied a $C_0 - C_1 e^{-(t-t_0)/\tau}$ type of model and obtained the curve and the error band in the figure. Even though the curve does not perfectly reproduce the fluctuating data at higher energy, it is acceptable in the energy range of interest, namely 130 MeV to 250 MeV.

There are many studies from which we can obtain the analyzing power values. The analyzing power for 140 and 160 MeV is taken from H. Witala[4] whereas the values for 150, 170 and 190 MeV are from [10] and that for 250 MeV comes from [17]. The

---

[4] Private communication.

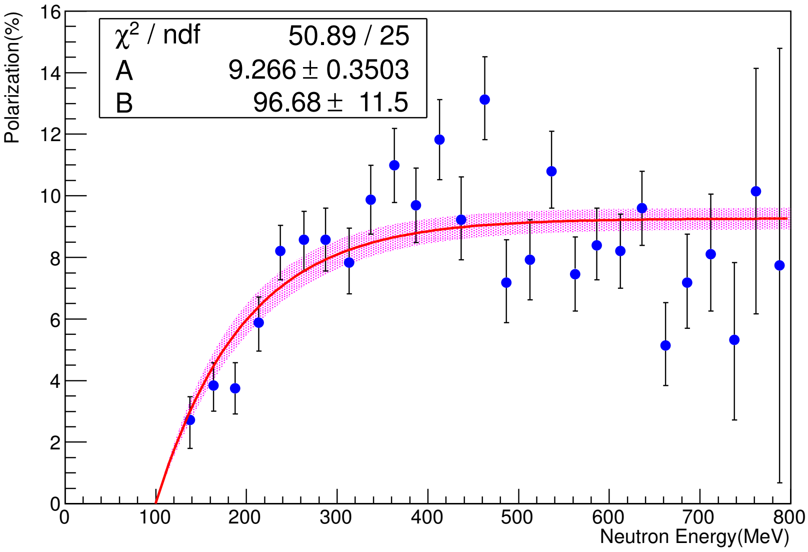

Figure 3.32. The polarization vs neutron energy [9].

values for the rest of the energies and angles are obtained by interpolating these existing data such as [10, 15].

Our final results include the (small) polarization corrections. The polarization error is about 10% in our energy range.

3.8. Systematic Errors

In this section, we will introduce the sources of systematic error and explain the methods used to obtain their magnitudes. There are several sources of systematic errors from properties of the experimental setup to the uncertainties arising from our analysis methods. In addition, the errors for each angle may differ from others since the analysis method, the type of events used (coincidence or singles) varies from point to point and some points received extra corrections.

3.8.1. Unknown Uranium Cross Section

The flux of the neutrons in the beam is determined using a fission chamber. The details of the chamber can be found in Section 3.2. The basic idea is to bombard ^{238}U with the neutrons and measure the ionization generated by the fission products. In order to determine the correct number of neutrons, we need to know the cross section for the neutron-induced fission, however, the cross-section data do not exist for the energy range we are interested in. This forces us to interpolate the existing data to obtain the needed values. Figure 3.33 shows the actual ^{238}U data, linear and spline interpolation curves with respect to the neutron kinetic energy. The y-axis is arbitrary.

As clearly seen, there is no data between 120 MeV and 380 MeV which unfortunately covers our energy interval of 135 MeV to 240 MeV. There is a considerable difference between the two interpolations which gives an idea of what the associated error could be. The largest difference was found to be 4.5% with respect to the average of that specific point and since this is a crude approximation, we double this difference and assigned the error for unknown uranium cross section as 9%.

3.8.2. Target Thickness Correction

The details of determination of target thickness correction are given in Section 3.4 and in Figure 3.13. The error for the correction factor is obtained by determining the

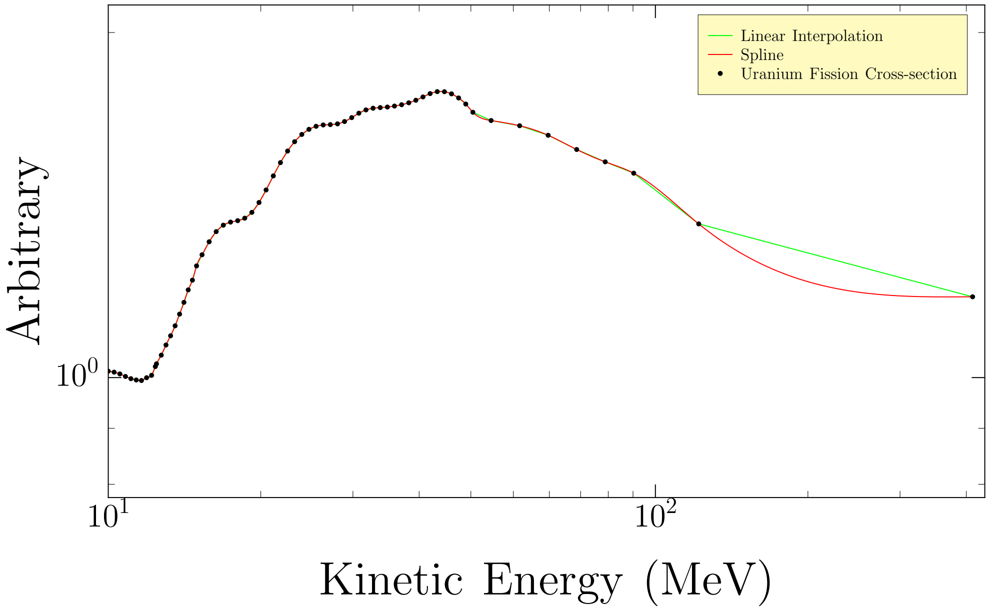

Figure 3.33. The ^{238}U cross section versus neutron kinetic energy.

width of the curve at twice the minimum value which resulted in 5%. As mentioned earlier, we assume that the target thickness normalization is the same for LD_2 and LH_2, however, this may not be the case as the targets' boiling points are different which may cause different amounts of bubbling. For this reason, we assign 10% error on account for this uncertainty which is a worst case assumption obtained by comparing bubbling and no bubbling cases.

3.8.3. Deviations in the Detector Placement

These deviations may lead to decrease in the geometrical acceptance and/or a change in the solid angle. In Appendix D, the error for the geometrical acceptance is mentioned to be 2% and the way it is calculated is given there. Apart from that, the differential solid angle changes with respect to the target-to-detector distance. This introduces another error of 1% calculated by propagating the distance error.

3.8.4. Neutron Efficiency Error

The particulars of the determination of neutron efficiency are given in Section 3.5. To summarize, we obtain the efficiency using experimental data and apply a decaying exponential fit plus a constant to the findings. The errors of the parameters of this fit determines the error for the analysis and the band in Figure 3.19 demonstrates the situation. Since the energy of each neutron differs with respect to the beam energy and the CsI angle, this error for each point is different, nevertheless, it is about 5%. Note that the error for neutron efficiency is only considered in the coincidence analysis.

3.8.5. The Error due to Singles Scaling

The cross section for the forward neutron angle can only be found using singles data as mentioned before in Section 3.6.3. One recalls that the analysis is repeated twice with graphical cuts of different sizes to minimize the cut dependence and to have an idea of the associated error. Since the analysis is performed using wide and tight cuts, it is quite safe to assume that error can be extracted from the percent difference of the two correction factors which came out to be 25%.

3.8.6. The Error due to Alternative Method

As you may recall, the backward neutron angle cross section cannot be obtained in the same way as the other angles due to the nonuniform background as discussed in Section 3.6.2. Similar to the singles case, the graphical cuts are quite influential hence for some energies (200 MeV and 250 MeV); we repeated our analysis with varying cut sizes. The results changed about 10-15% with respect to the designated value so we concluded that this is the contribution of the cut dependence error of the alternative method.

3.8.7. The Position Dependence Error

The neutron detection efficiency varies with respect to the hit position of the neutron on the neutron wall as explained in Section 3.5. The detailed treatment for the correction is also outlined in that section which in turn introduces some error to our cross-section result. Since the statistics is not particularly good for this analysis, we assigned an additional 10% on top of the error in the correction factors, which resulted in a 14% error for the 24° and a 11% error for the 30° charged particle detectors.

3.8.8. Polarization Correction Error

This is a very small correction as stated in Section 3.7, the polarization itself has an error for each energy about 10% which is added accordingly to our total systematic error.

Figure 3.34 summarizes all of the mentioned sources of errors, affected angles and their amounts. Taking all the errors into account, our singles results have a total systematic error of 30%, the results for intermediate deuteron angles, namely 36°, 42° and 48° in the lab frame, have about 16% total systematic error, whereas the error in the result for 30° is 19% due to the additional position dependence correction and the error in the result for 24° is 24% on account of the alternative method.

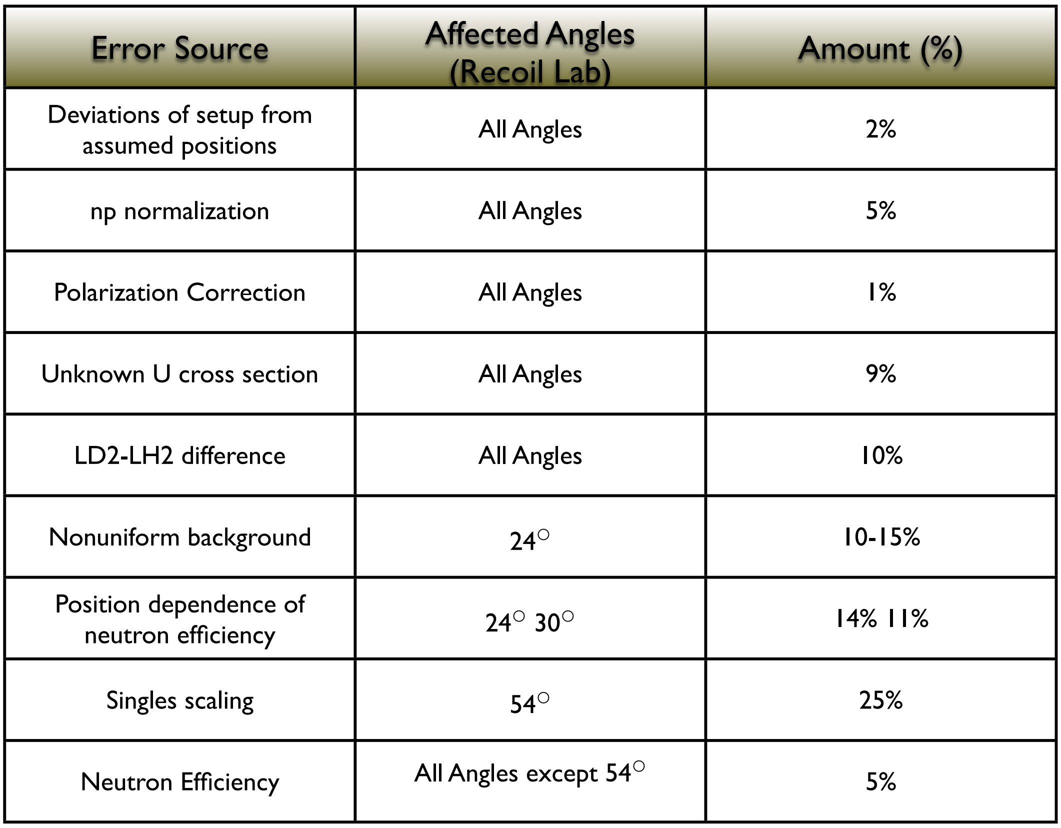

Error Source	Affected Angles (Recoil Lab)	Amount (%)
Deviations of setup from assumed positions	All Angles	2%
np normalization	All Angles	5%
Polarization Correction	All Angles	1%
Unknown U cross section	All Angles	9%
LD2-LH2 difference	All Angles	10%
Nonuniform background	24°	10-15%
Position dependence of neutron efficiency	24° 30°	14% 11%
Singles scaling	54°	25%
Neutron Efficiency	All Angles except 54°	5%

Figure 3.34. A summary of all the systematic errors.

3.9. Results and Discussion

The measurements were made in the energy range of 135 to 250 MeV which is the most suitable range to make use of all the charged particle detectors with acceptable resolution. With higher beam energies, the resolution is lost especially for the backward neutron angle, i.e. 24° deuteron data. At the other end of the spectrum, the charged particles cannot reach the detectors due to the energy loss for forward neutron angle data. We present here *nd* elastic scattering cross-section measurements at 12 different beam energies separated by 10 MeV bins in Figures 3.35, 3.36 and 3.37. Tables 3.4 and 3.5 give our measurements in tabulated form.

In the figures, the relevant past measurements as well as theoretical predictions are included along with our data, if any. Our work is in good agreement with [18] at 135 MeV. The cross sections measured at KVI seems always to be greater than our data, as in the comparison with [11] at 135 MeV and with [10] at 135, 150, 170 and 190 MeV. The agreement with [14] is good at 150 and 180 MeV, but the level of agreement worsens somewhat at 210 MeV. At 250 MeV, the data of [16] and [17], agreeing well among themselves, differ somewhat around the cross-section minima from our measurements.

As for the theoretical predictions, our measurements favour the predictions that include 3NF effect although at some energies (150, 170 and 190 MeV) there is no clear preference. Nevertheless, our data are in very good agreement with the predictions with 3NF around the critical region, i.e. the cross-section minima.

We need make a final remark regarding the forward neutron angle result obtained using singles analysis. The singles analysis is quite crude and is not exactly correct methodologically. It can be improved using a larger set of cuts with varying sizes or determining the signal-to-noise ratio for other angles and extrapolating it for the forward angle as a measure of background. However, this data point is hardly useful as it is the farthest from sensitive region, therefore, even though this data point is shown in the plots, we decided not to include it in the publication.

Table 3.4. The *nd* cross-section results.

$\mathbf{T}_{\text{beam}}$ **(MeV)**	$\theta_{\mathbf{d}}^{\text{Lab.}}$ (deg)	$\theta_{\mathbf{n}}^{\text{c.m.}}$ **(deg)**	$\text{d}\sigma/\text{d}\mathbf{\Omega}_{\mathbf{n}}^{\text{c.m.}}$ **(μb/sr)**	±	ϵ_{stat}	±	ϵ_{sys}
135 ± 5	24	131	206	±	6	±	45
	30	119	230	±	6	±	44
	36	107	218	±	5	±	34
	42	95	255	±	7	±	40
	48	83	337	±	14	±	53
150 ± 5	24	131	187	±	6	±	45
	30	119	156	±	5	±	29
	36	107	164	±	5	±	27
	42	95	213	±	6	±	34
	48	83	270	±	9	±	42
160 ± 5	24	131	143	±	5	±	33
	30	119	161	±	5	±	31
	36	107	142	±	5	±	22
	42	95	209	±	7	±	33
	48	83	301	±	9	±	48
170 ± 5	24	131	134	±	6	±	32
	30	119	113	±	5	±	21
	36	107	117	±	5	±	18
	42	95	164	±	6	±	26
	48	83	187	±	8	±	30
180 ± 5	24	131	149	±	7	±	34
	30	119	120	±	6	±	22
	36	107	102	±	5	±	16
	42	95	155	±	6	±	25
	48	83	229	±	9	±	36
190 ± 5	24	131	109	±	6	±	26
	30	119	85	±	5	±	16
	36	107	87	±	4	±	14
	42	95	128	±	6	±	20
	48	83	170	±	12	±	26

Table 3.5. The *nd* cross-section results (continued).

$\mathbf{T}_{\text{beam}}$ **(MeV)**	$\theta_{\mathbf{d}}^{\text{Lab.}}$ (deg)	$\theta_{\mathbf{n}}^{\text{c.m.}}$ **(deg)**	$\text{d}\sigma/\text{d}\mathbf{\Omega}_{\mathbf{n}}^{\text{c.m.}}$ **(μb/sr)**	±	ϵ_{stat}	±	ϵ_{sys}
200 ± 5	24	131	82	±	6	±	23
	30	119	72	±	5	±	14
	36	107	83	±	5	±	13
	42	95	117	±	6	±	18
	48	83	149	±	11	±	23
210 ± 5	24	131	69	±	6	±	18
	30	119	69	±	5	±	13
	36	107	65	±	4	±	10
	42	95	96	±	6	±	15
	48	83	110	±	11	±	17
220 ± 5	24	131	60	±	6	±	16
	30	119	78	±	5	±	15
	36	107	86	±	4	±	13
	42	95	116	±	6	±	18
	48	83	211	±	9	±	33
230 ± 5	24	131	64	±	6	±	16
	30	119	51	±	6	±	10
	36	107	69	±	6	±	11
	42	95	77	±	7	±	12
	48	83	93	±	11	±	14
240 ± 5	24	131	40	±	6	±	12
	30	119	42	±	5	±	8
	36	107	52	±	4	±	8
	42	94	90	±	5	±	14
	48	82	127	±	8	±	20
250 ± 5	24	131	55	±	6	±	12
	30	119	44	±	5	±	8
	36	106	53	±	4	±	8
	42	94	71	±	5	±	11
	48	82	104	±	10	±	16

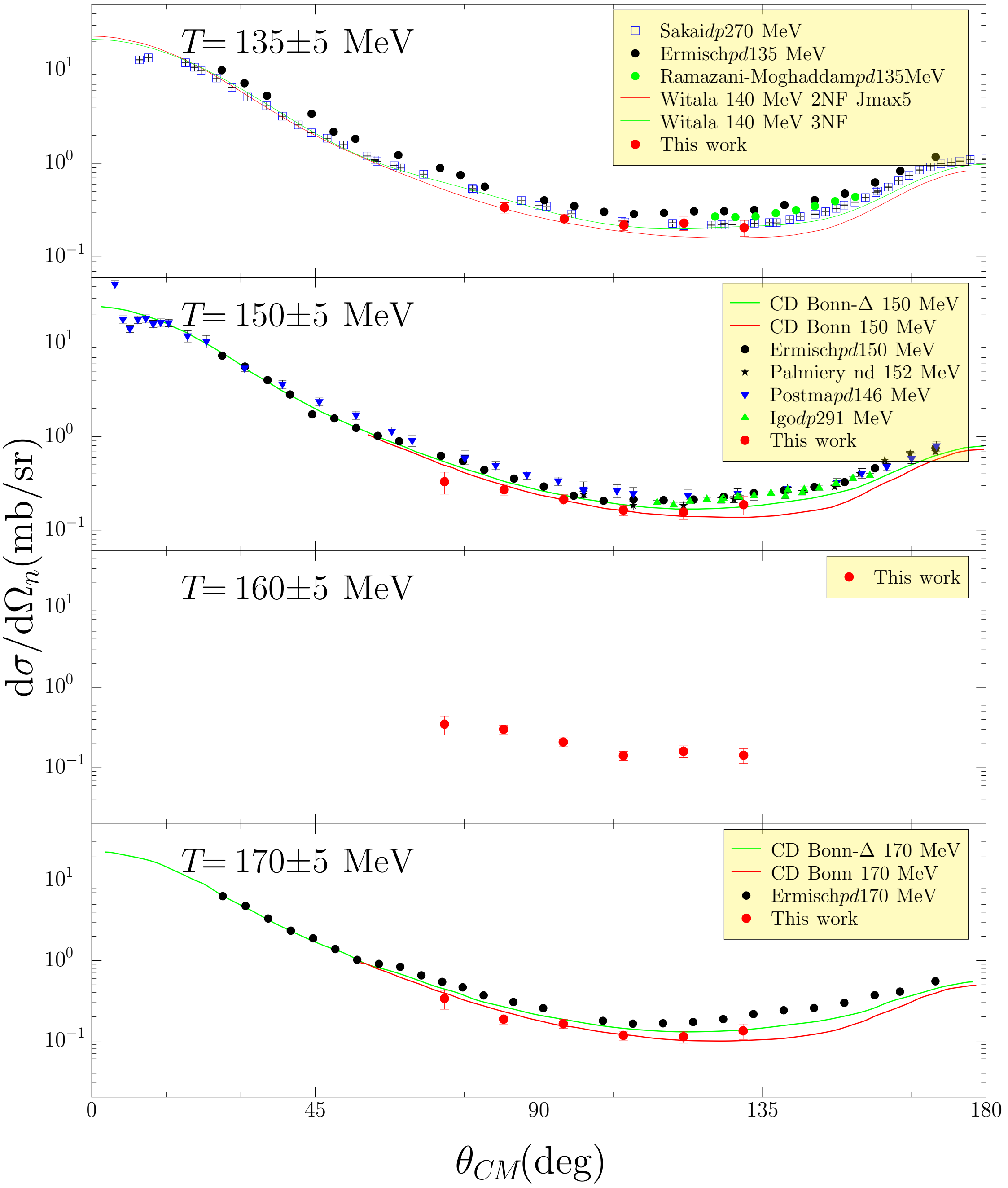

Figure 3.35. The cross-section results. The experimental data and the theoretical work prior to this study is taken from [10–18] and [3, 19–21], respectively.

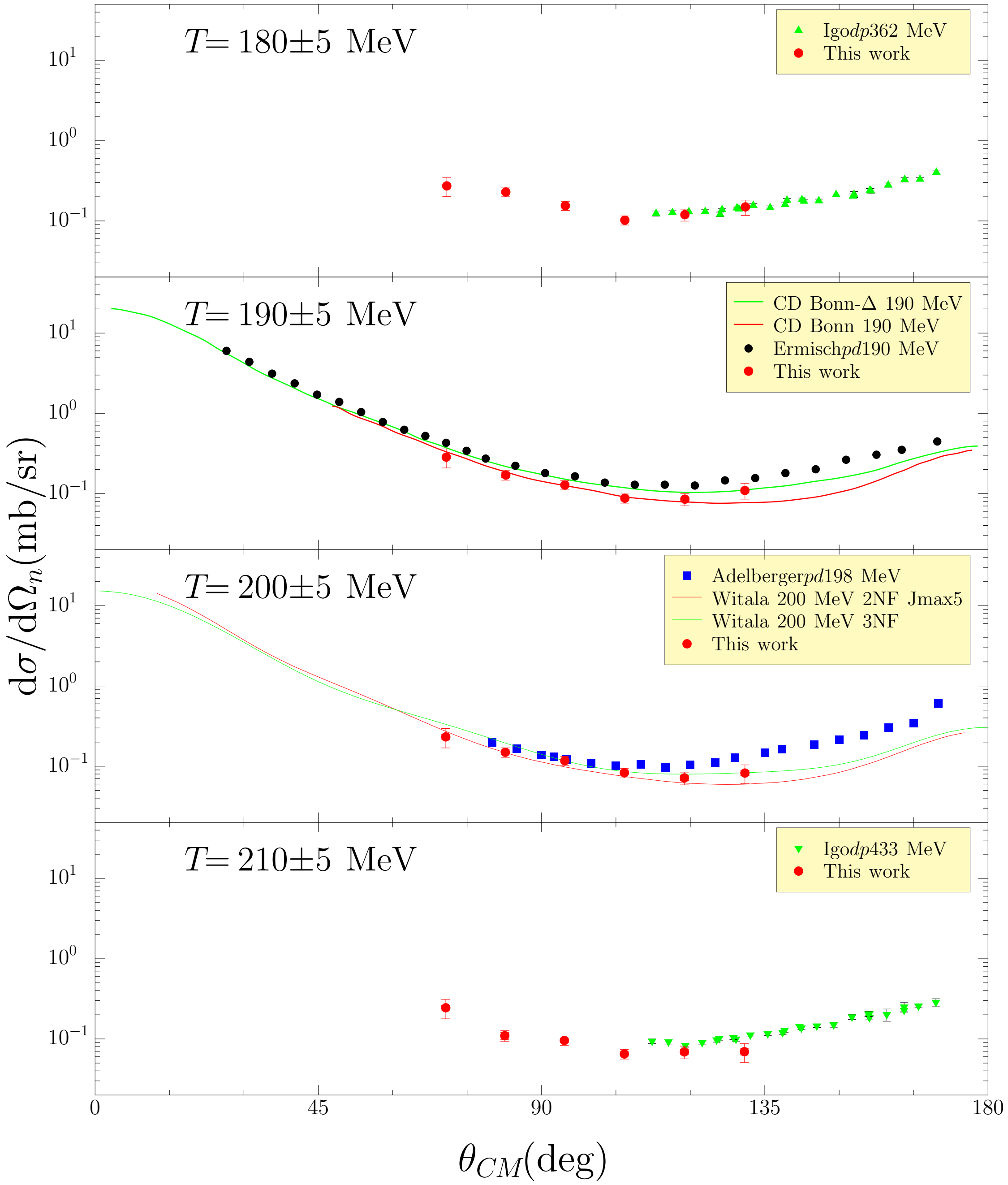

Figure 3.36. The cross-section results (continued).

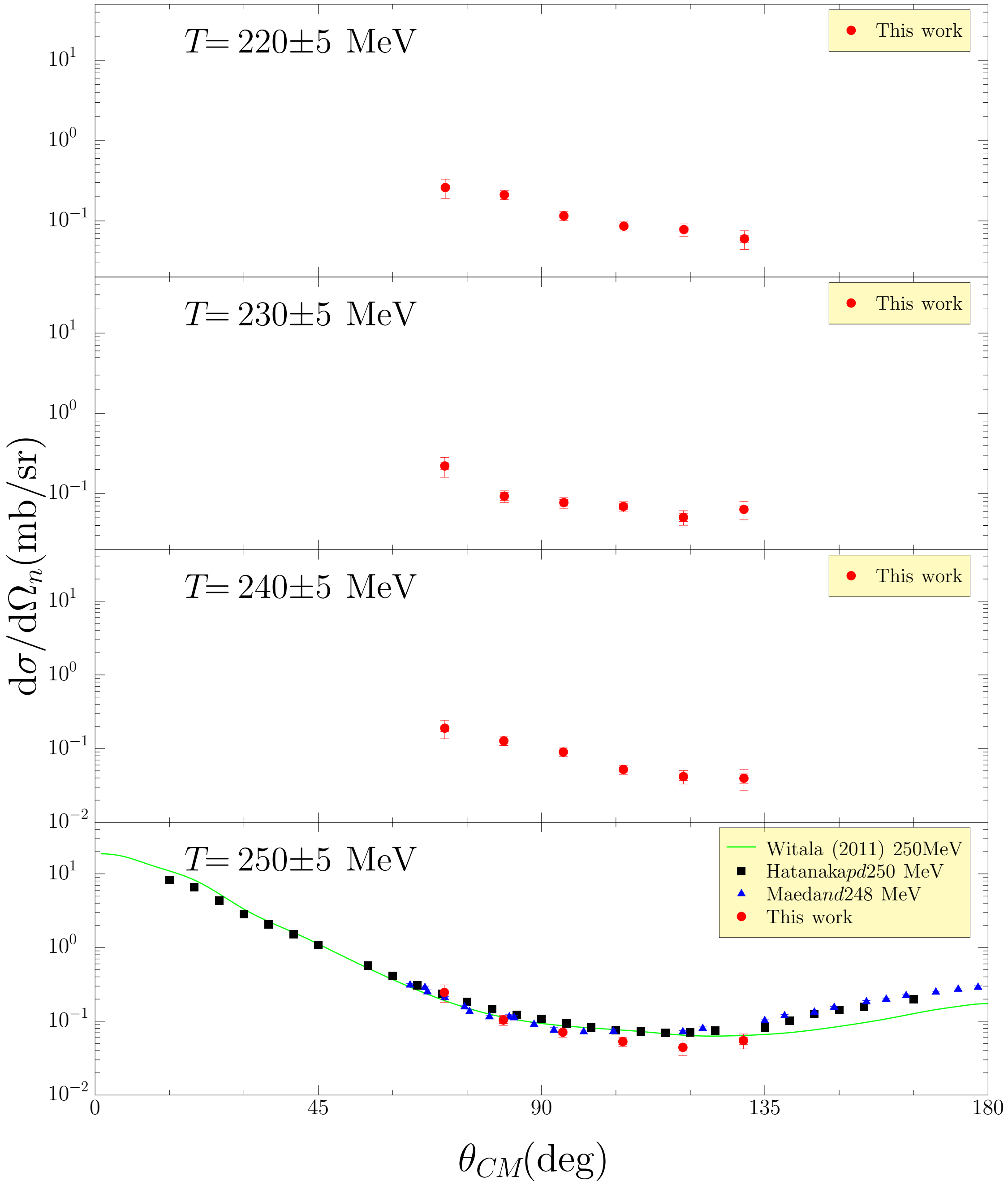

Figure 3.37. The cross-section results (continued).

4. CONCLUSION

In this work, we measured the neutron-deuteron elastic scattering cross section in the energy range 135 - 250 MeV to shed some light on the three-nucleon interaction. The measurement is an absolute cross-section measurement, that is, no external parameter is included. The normalization was performed using the same experimental setup with a hydrogen target and the neutron detection efficiency was measured using the experimental data, making the predictions by a Monte Carlo simulation redundant. Moreover, this study is distinguished from many others in that the probe used is a neutral one with a continuous energy spectrum whereas many of the previous works utilize charged particle probes and/or fixed energy beams. Consistent with the main motivation, the experiment focused on the region where the effects of three-nucleon forces (3NF) are pronounced.

As discussed in the previous section, the agreement with both previous experimental work and theoretical predictions of our data is generally satisfactory. More interestingly, our measurements favour the predictions with 3NF effect almost without exception in the angular region of the cross-section minima, the region most sensitive to 3NF effects.

Another important aspect of this work arises from the fact that the beam used has a continuous energy spectrum which makes the investigation of 3NF effects as a function of energy possible. More specifically, this work is an excellent test ground if one carries out a theoretical study incorporating 3NF as a function of neutron energy at fixed angles.

APPENDIX A: The Analysis Route for All Energies

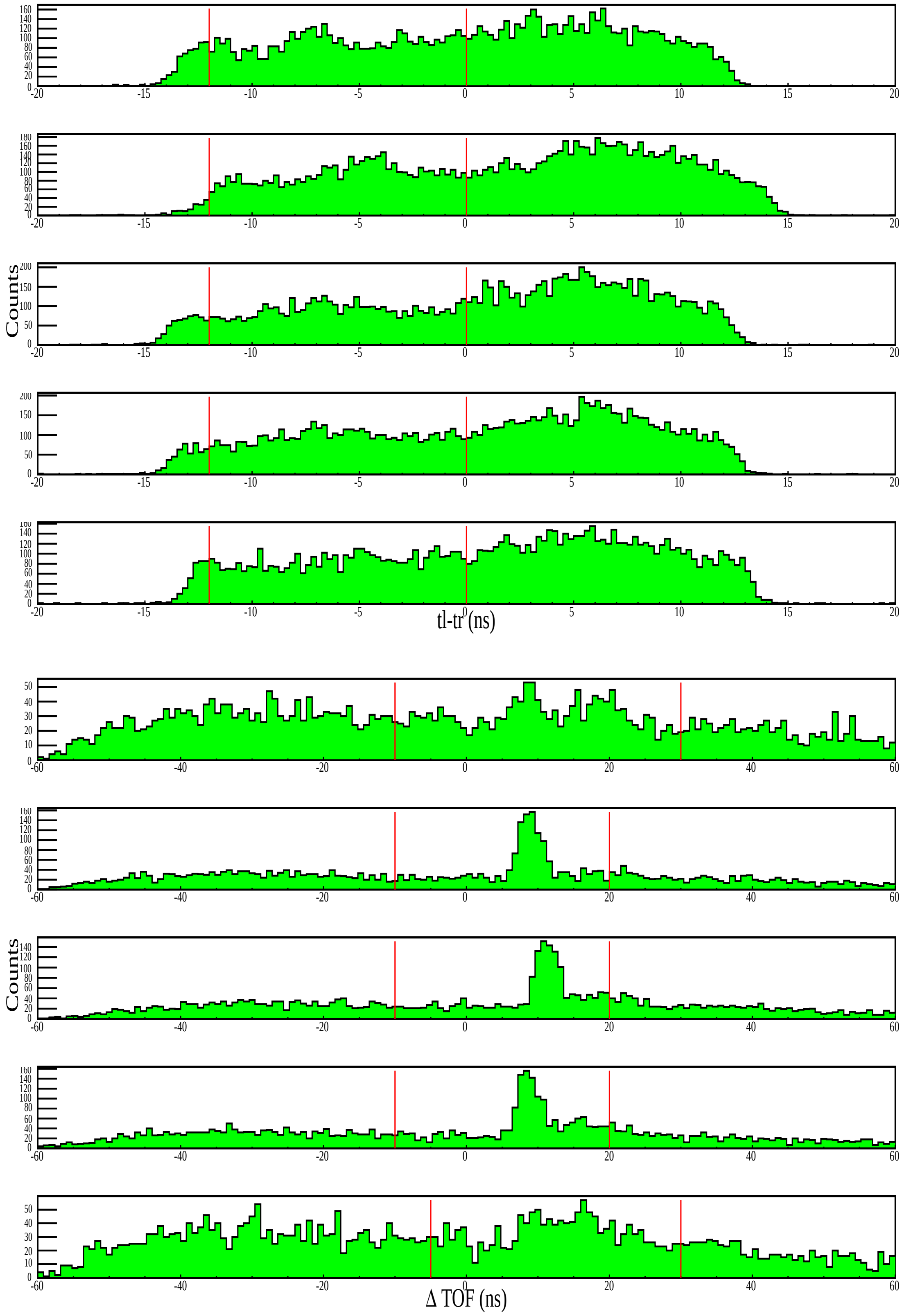

Figure A.1. Figures for 30° at 135 MeV.

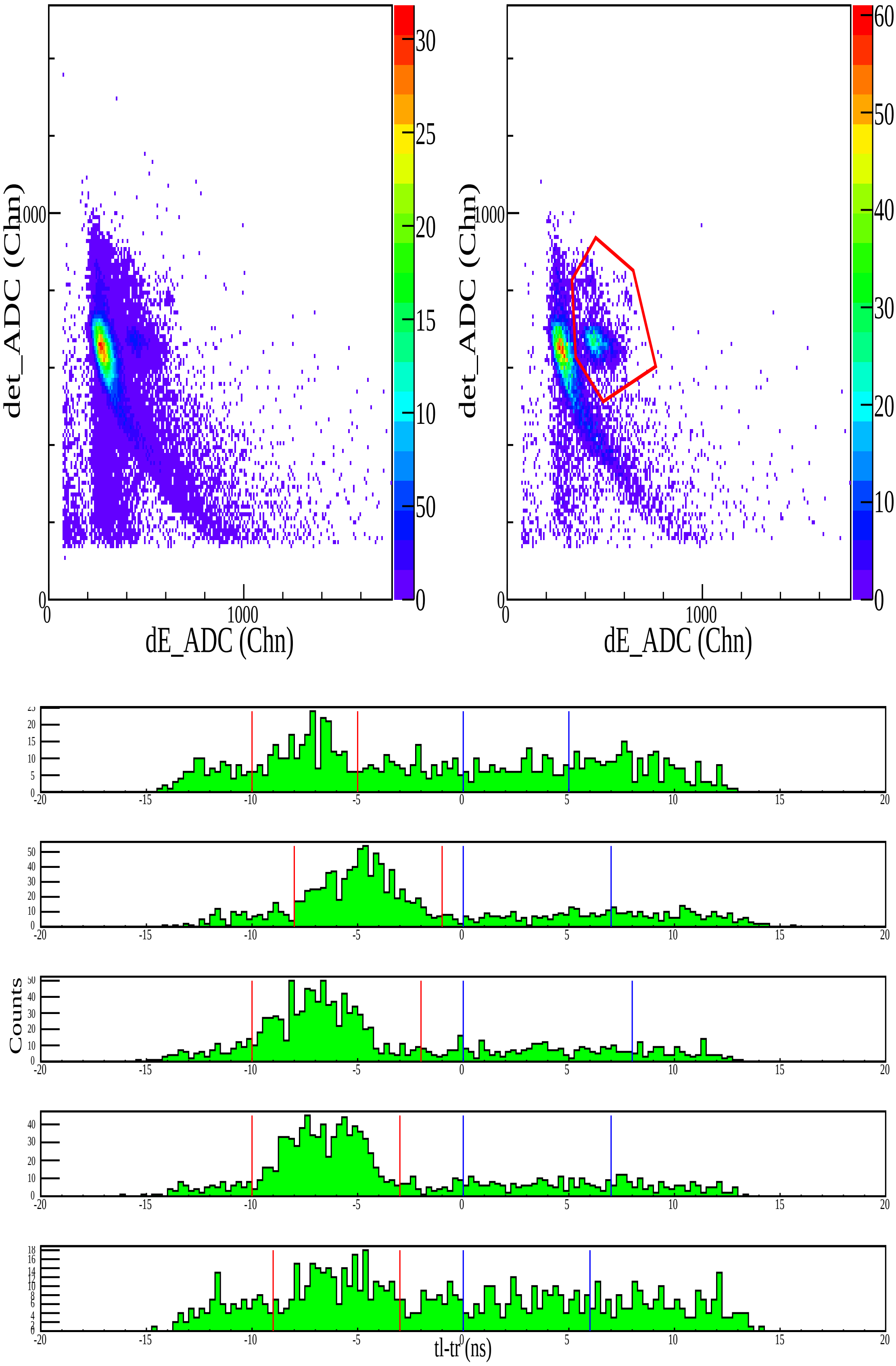

Figure A.2. Figures for 30° at 135 MeV (continued).

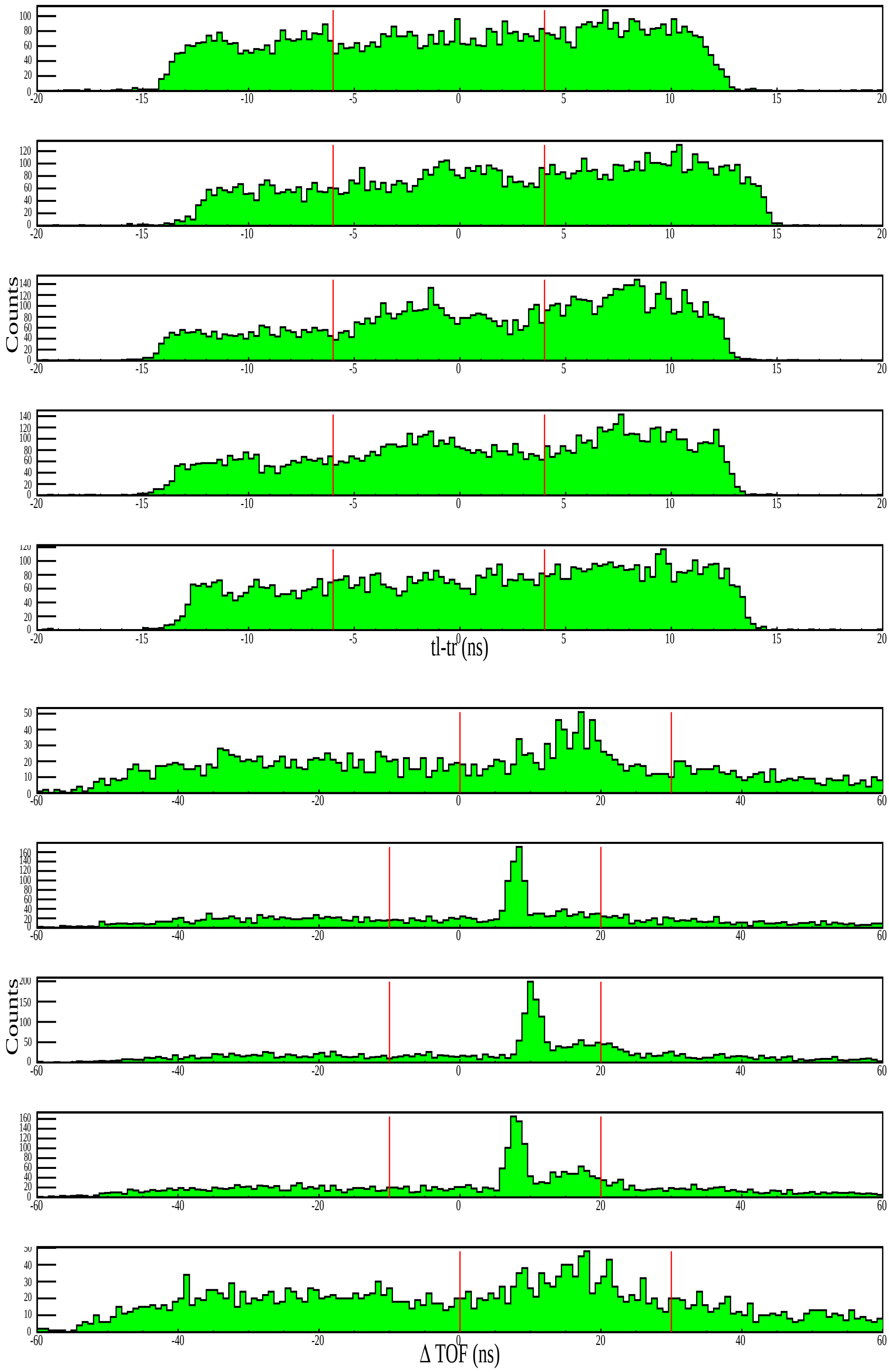

Figure A.3. Figures for 36° at 135 MeV.

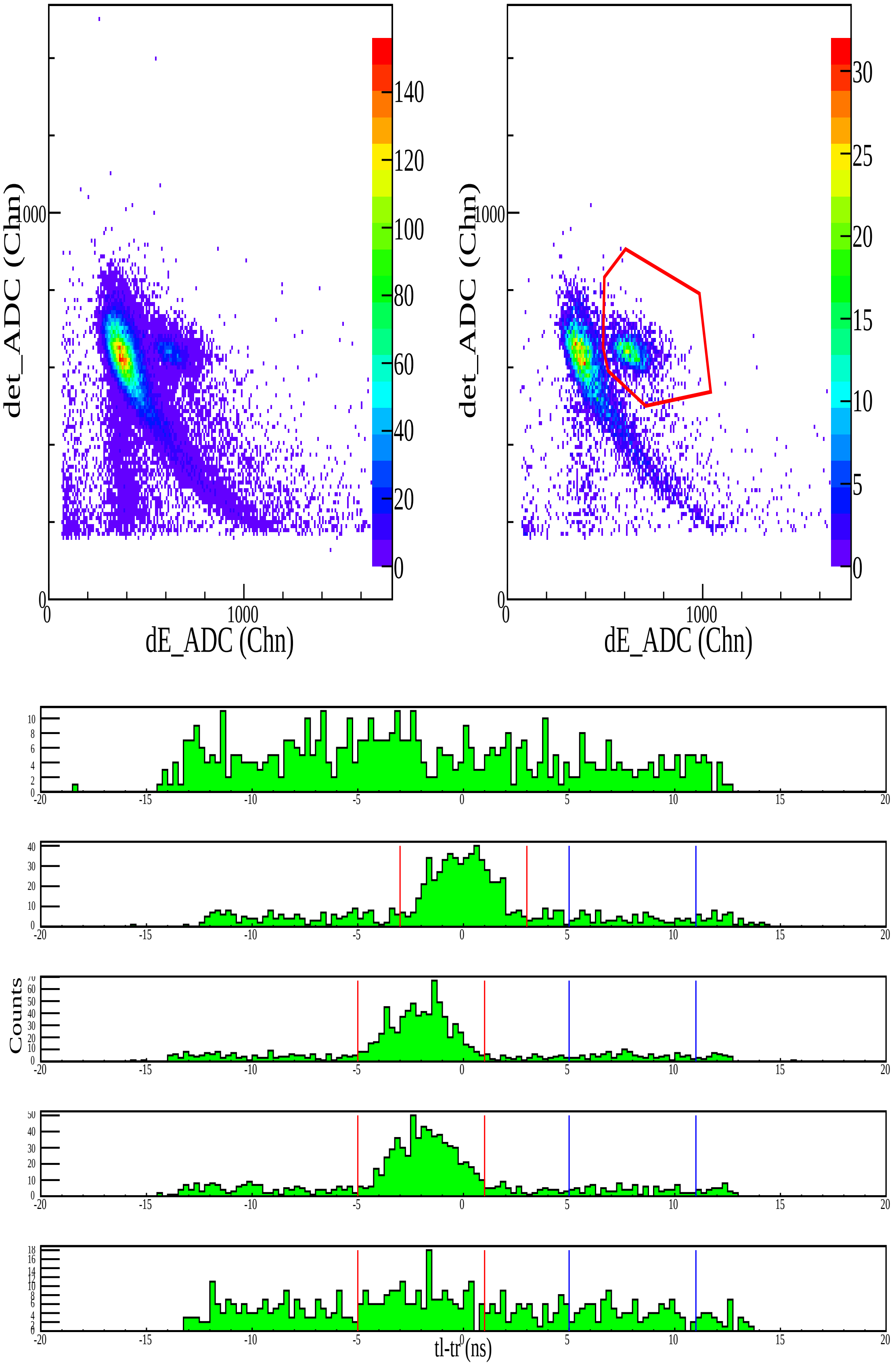

Figure A.4. Figures for 36° at 135 MeV (continued).

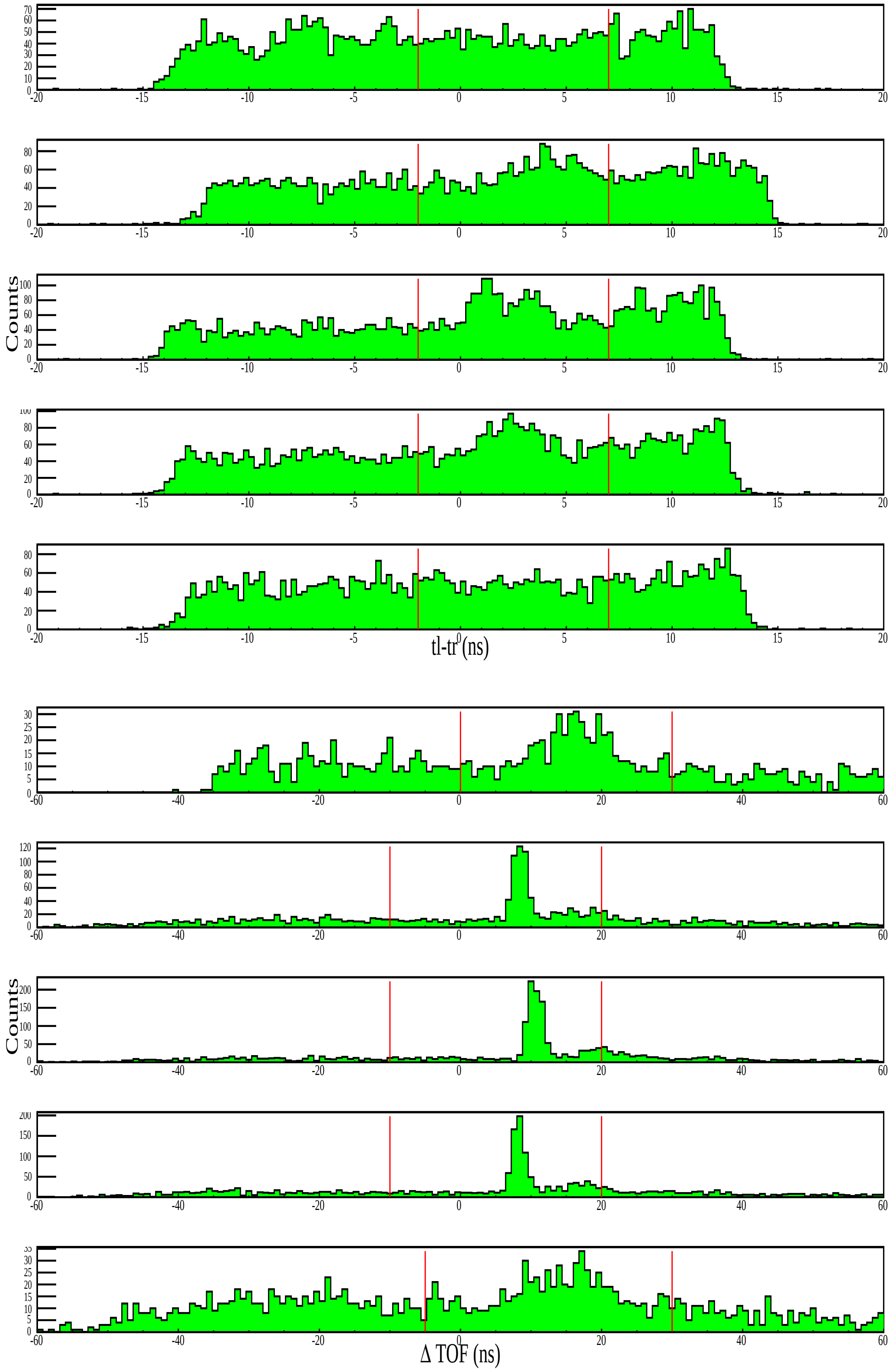

Figure A.5. Figures for 42° at 135 MeV.

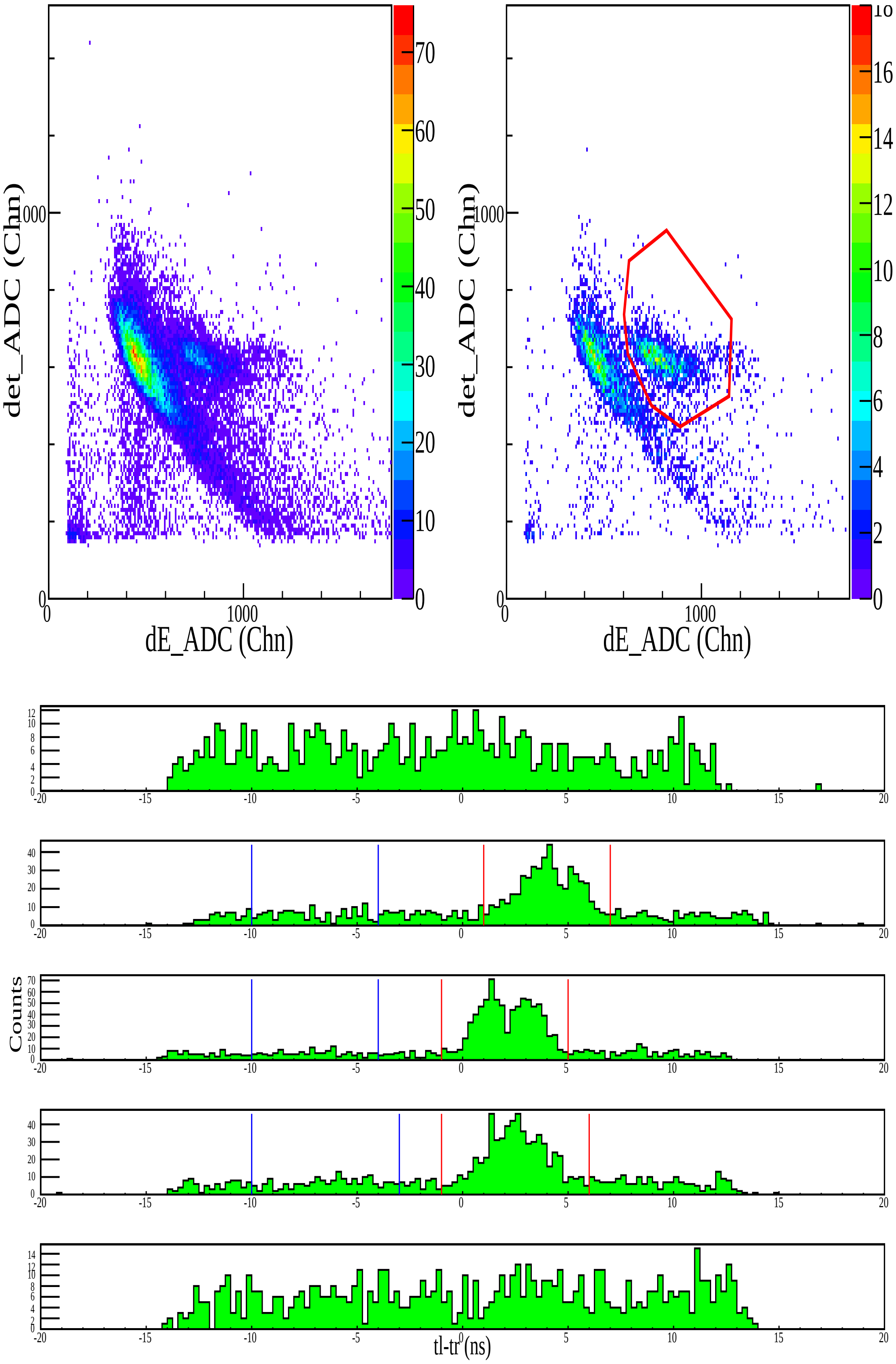

Figure A.6. Figures for 42° at 135 MeV (continued).

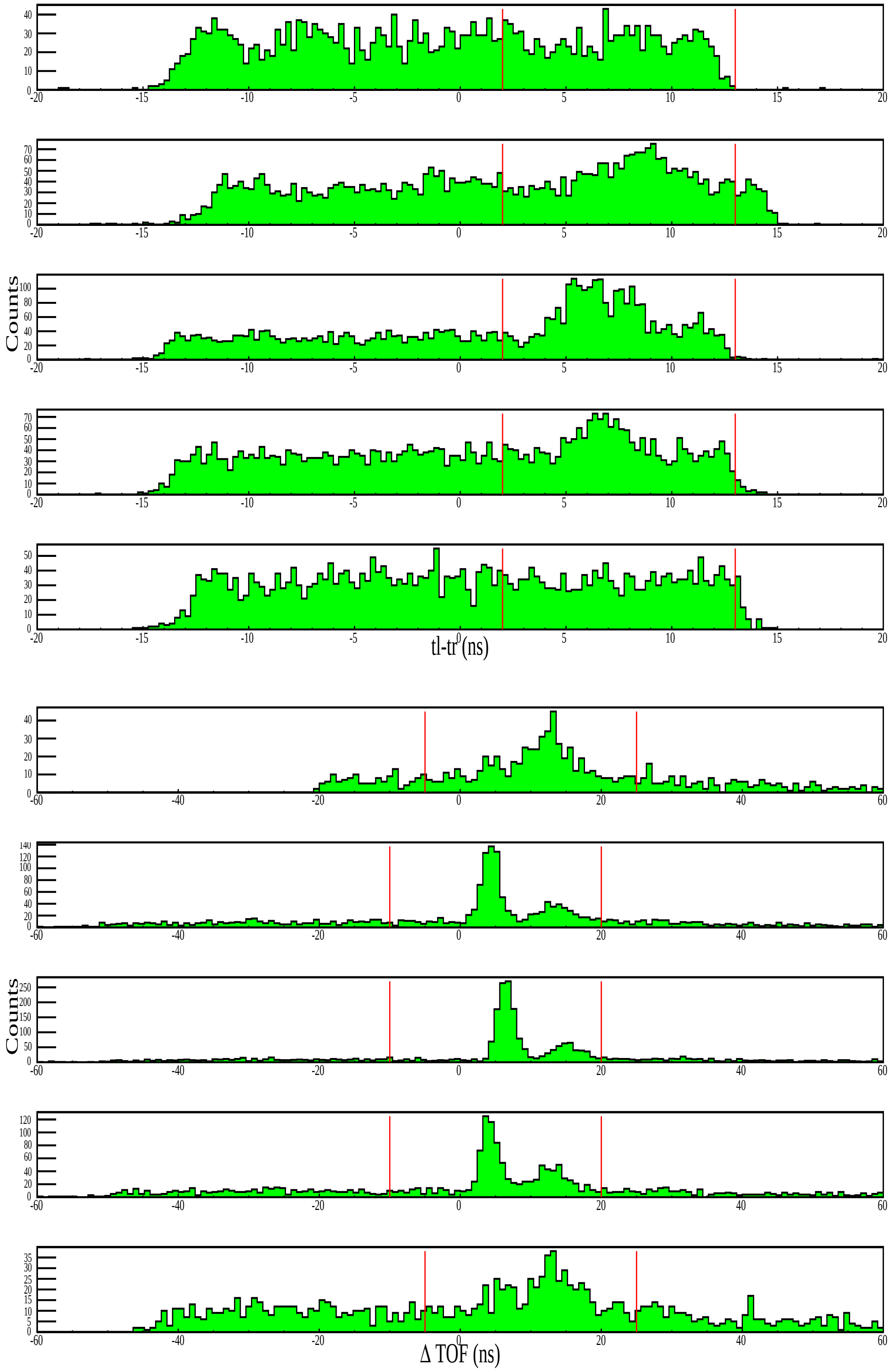

Figure A.7. Figures for 48° at 135 MeV.

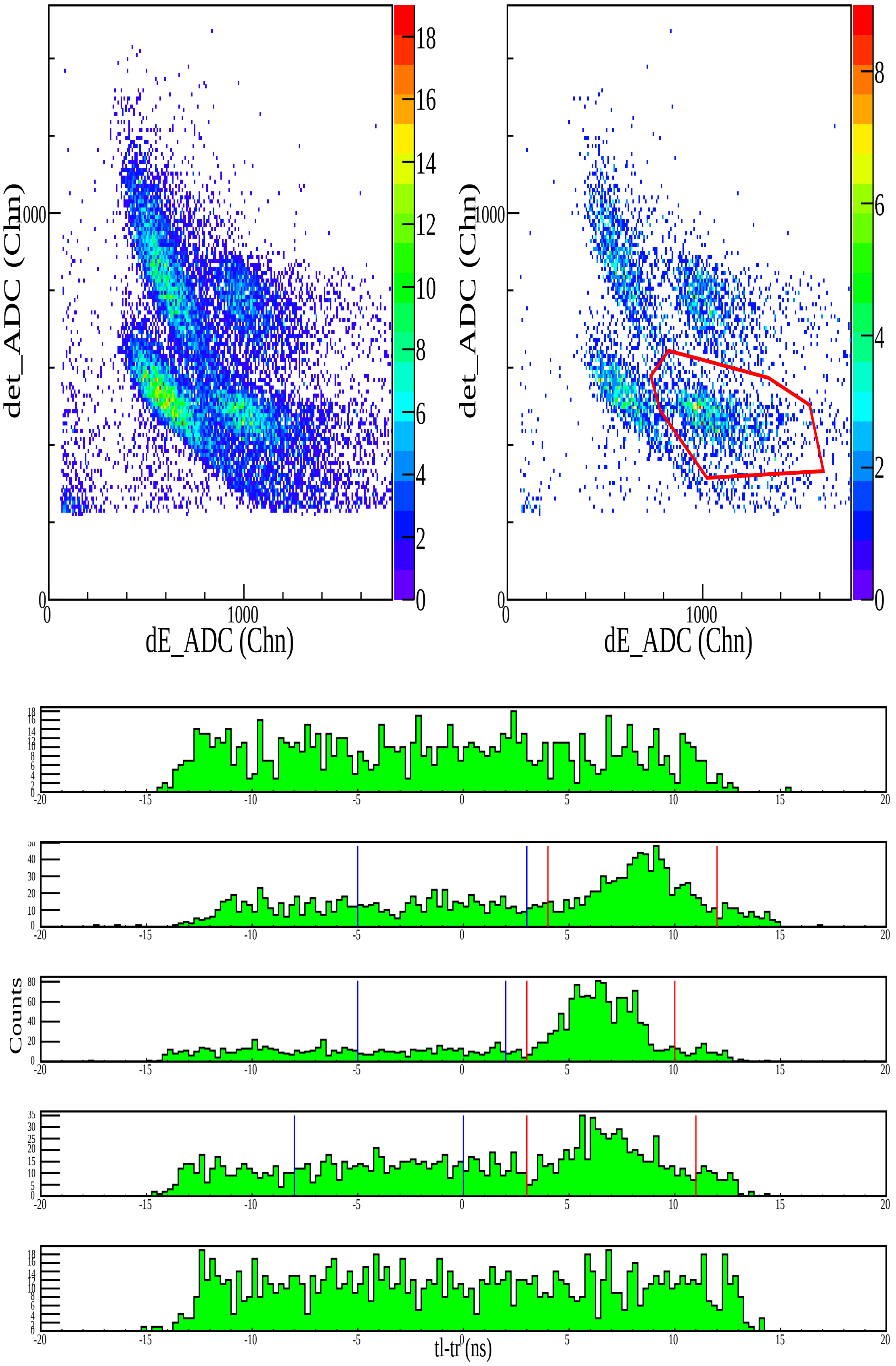

Figure A.8. Figures for 48° at 135 MeV (continued).

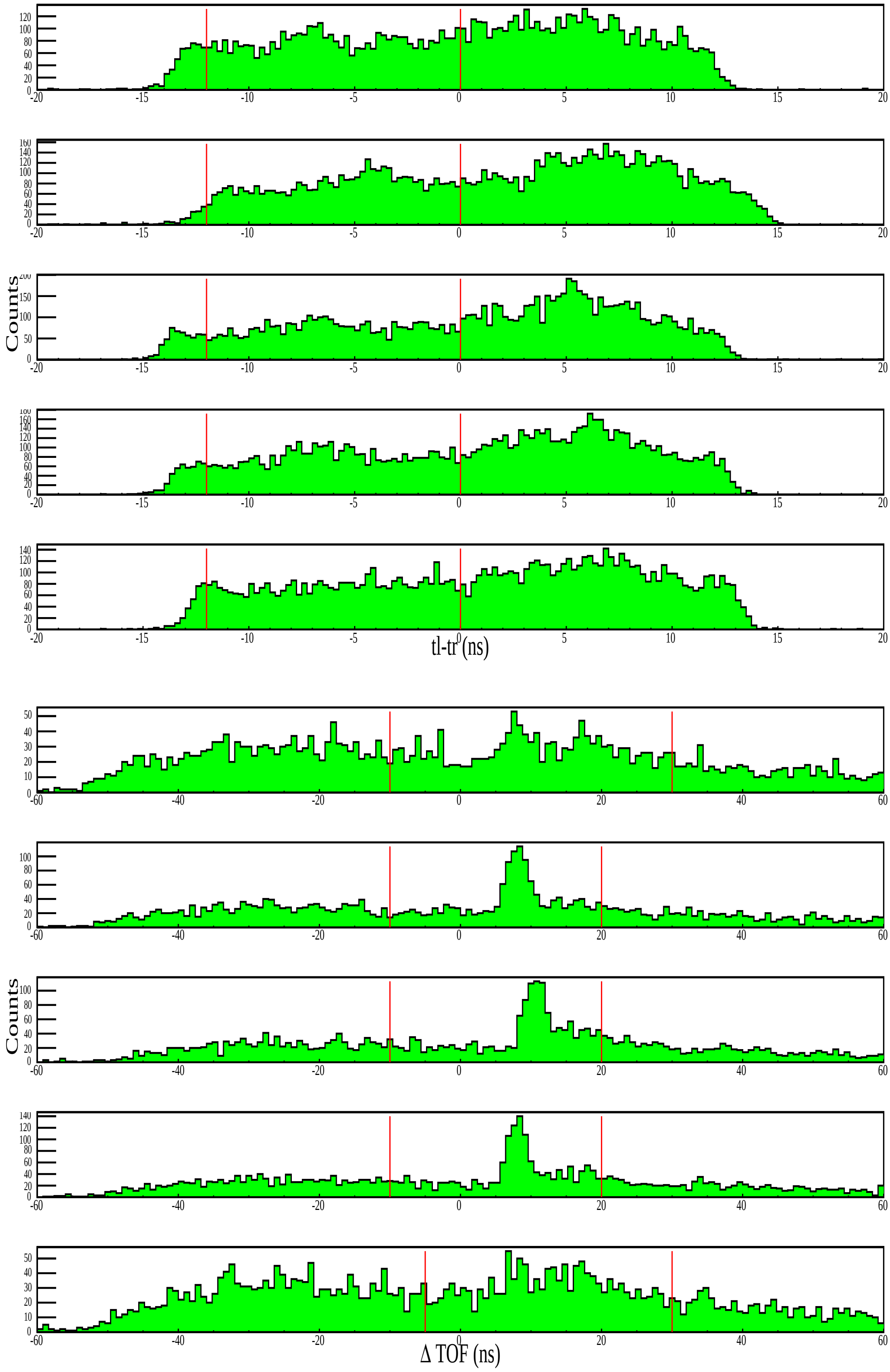

Figure A.9. Figures for 30° at 150 MeV.

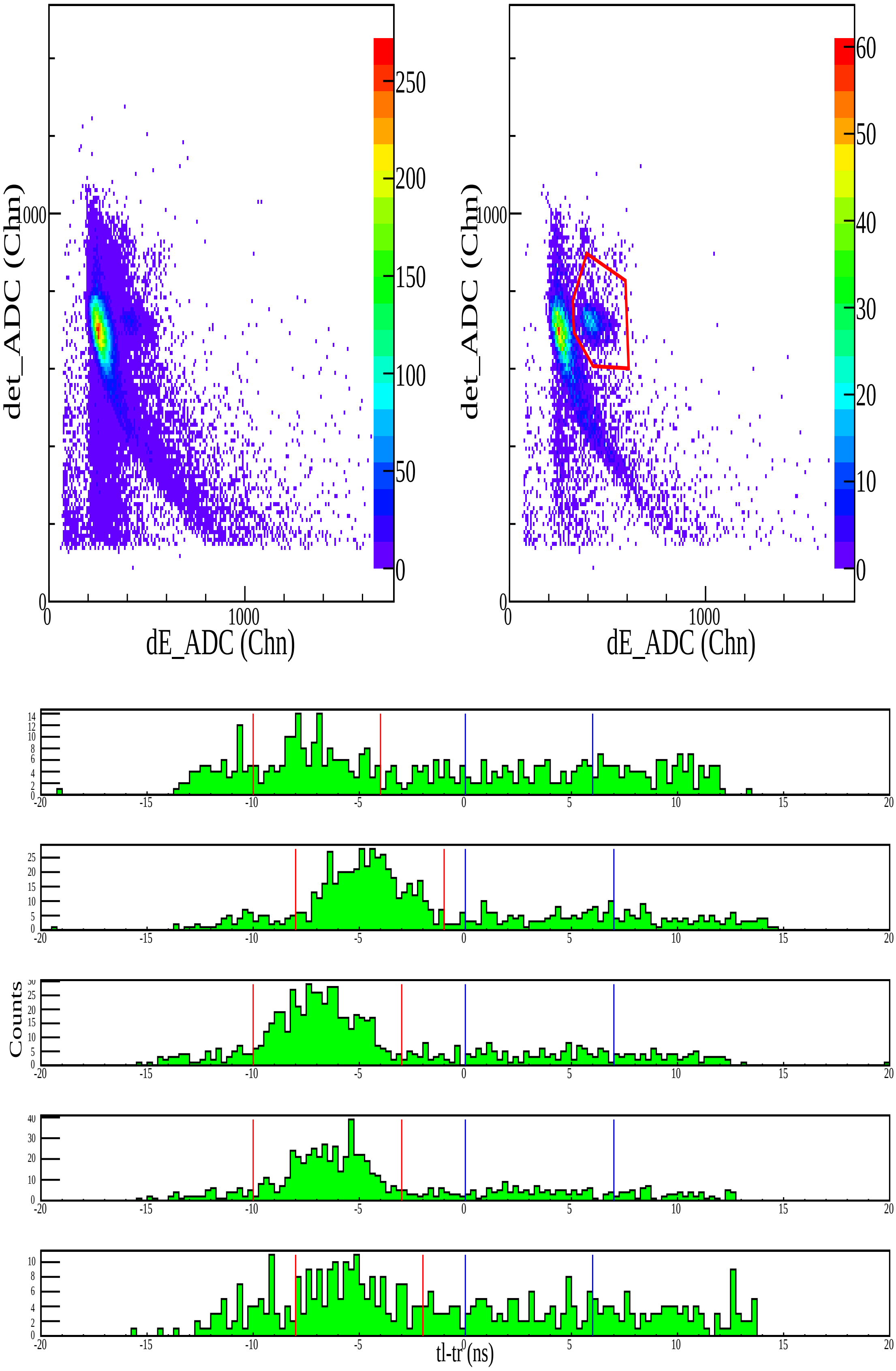

Figure A.10. Figures for 30° at 150 MeV (continued).

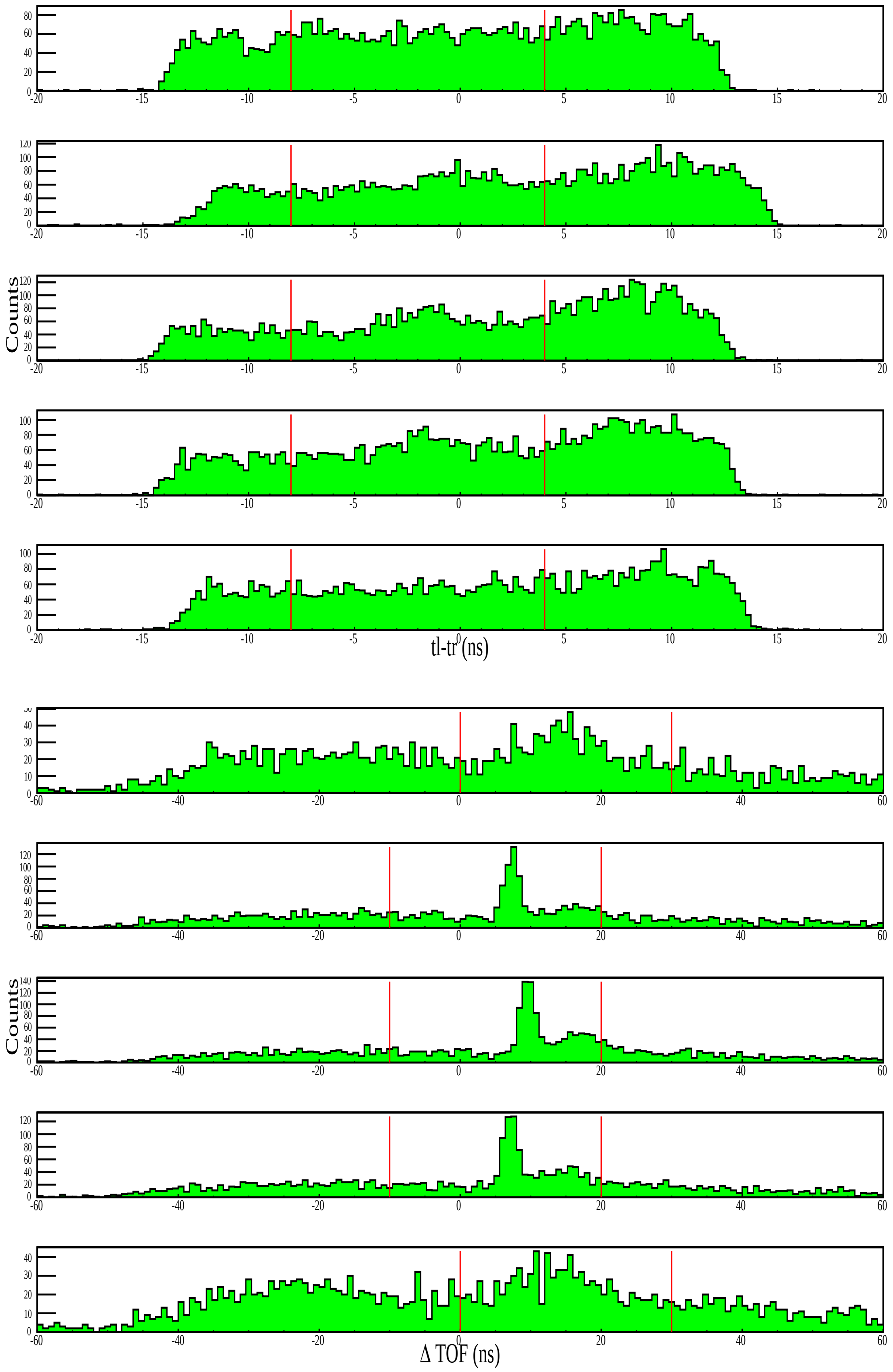

Figure A.11. Figures for 36° at 150 MeV.

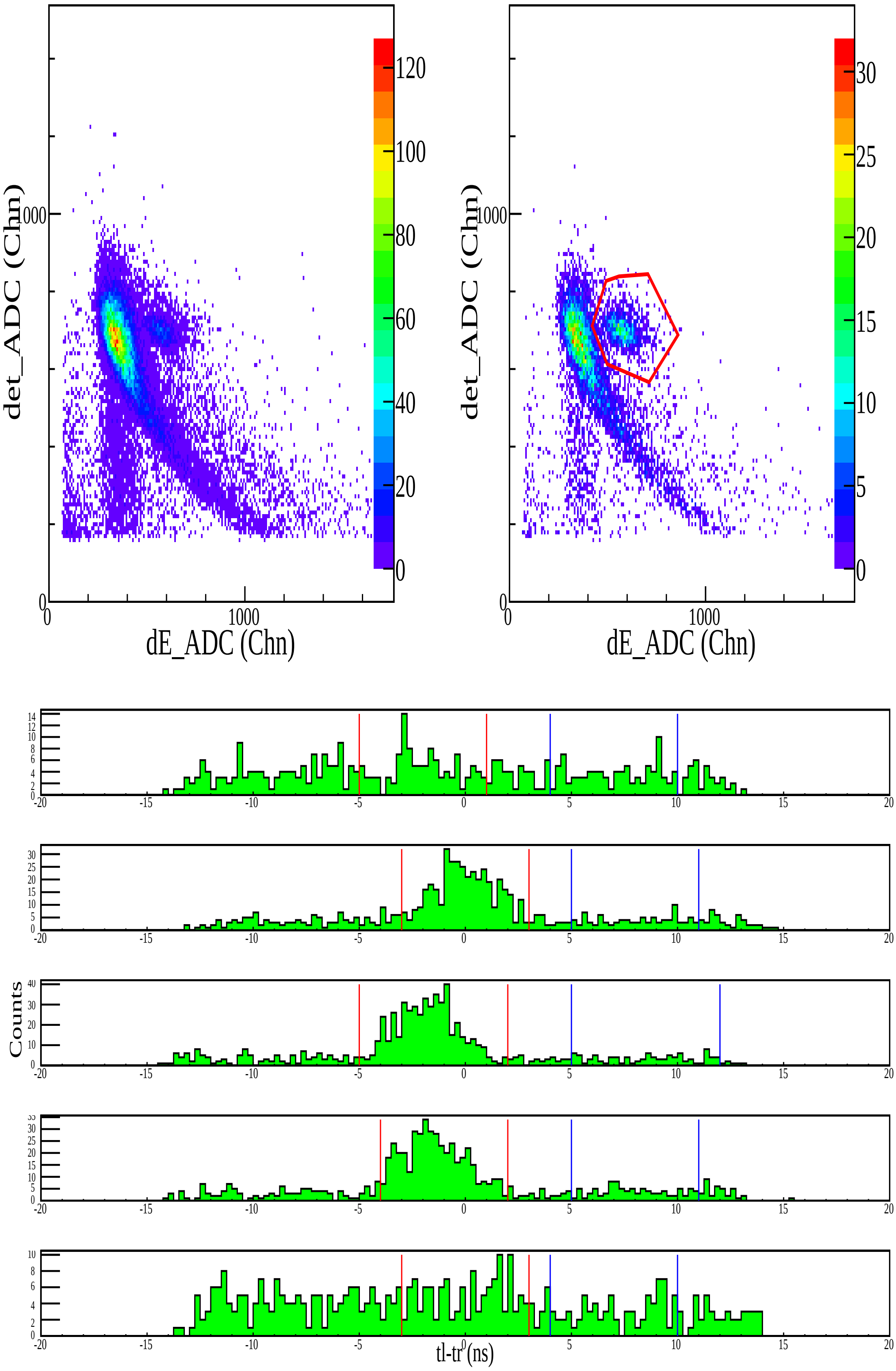

Figure A.12. Figures for 36° at 150 MeV (continued).

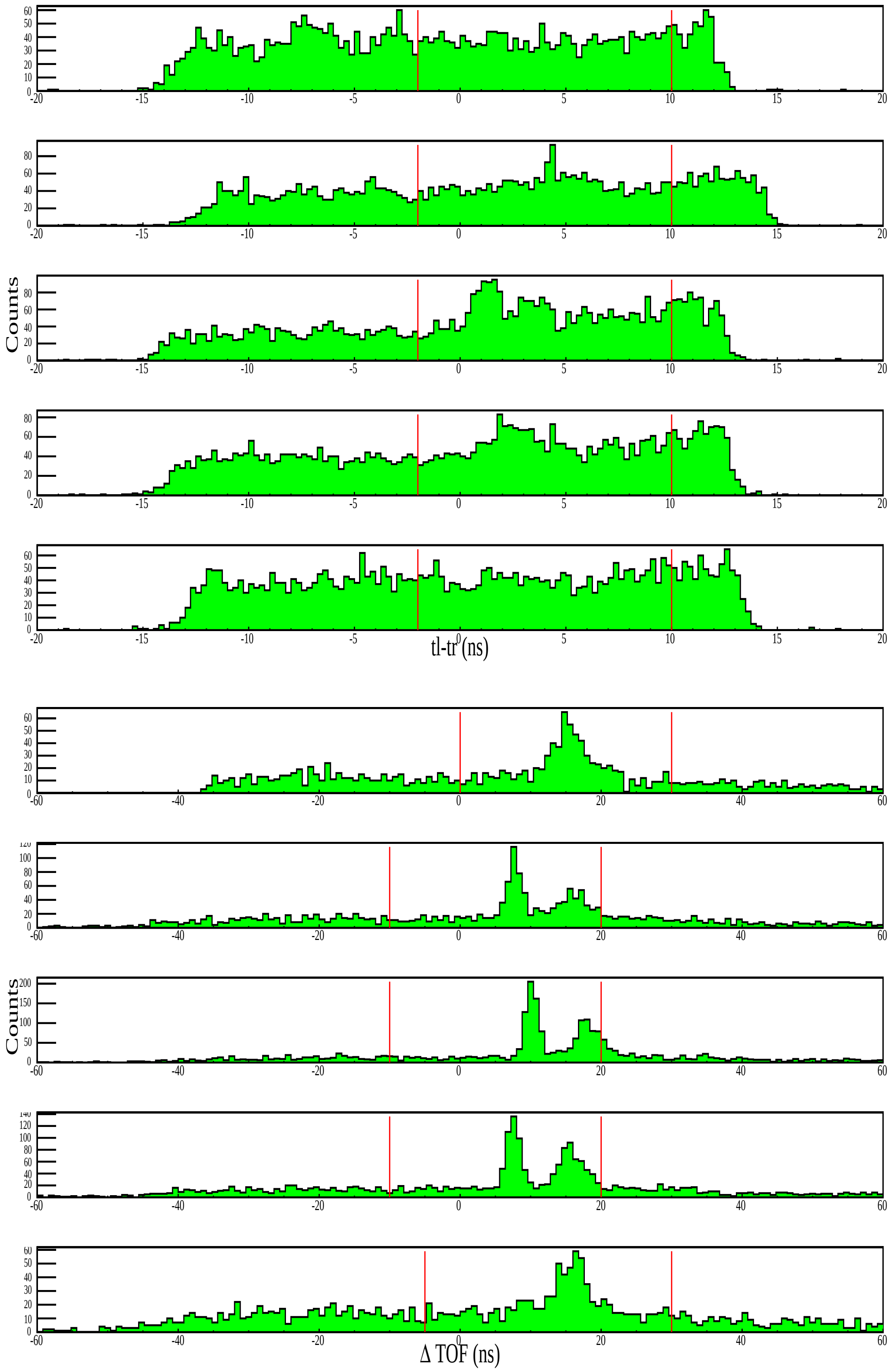

Figure A.13. Figures for 42° at 150 MeV.

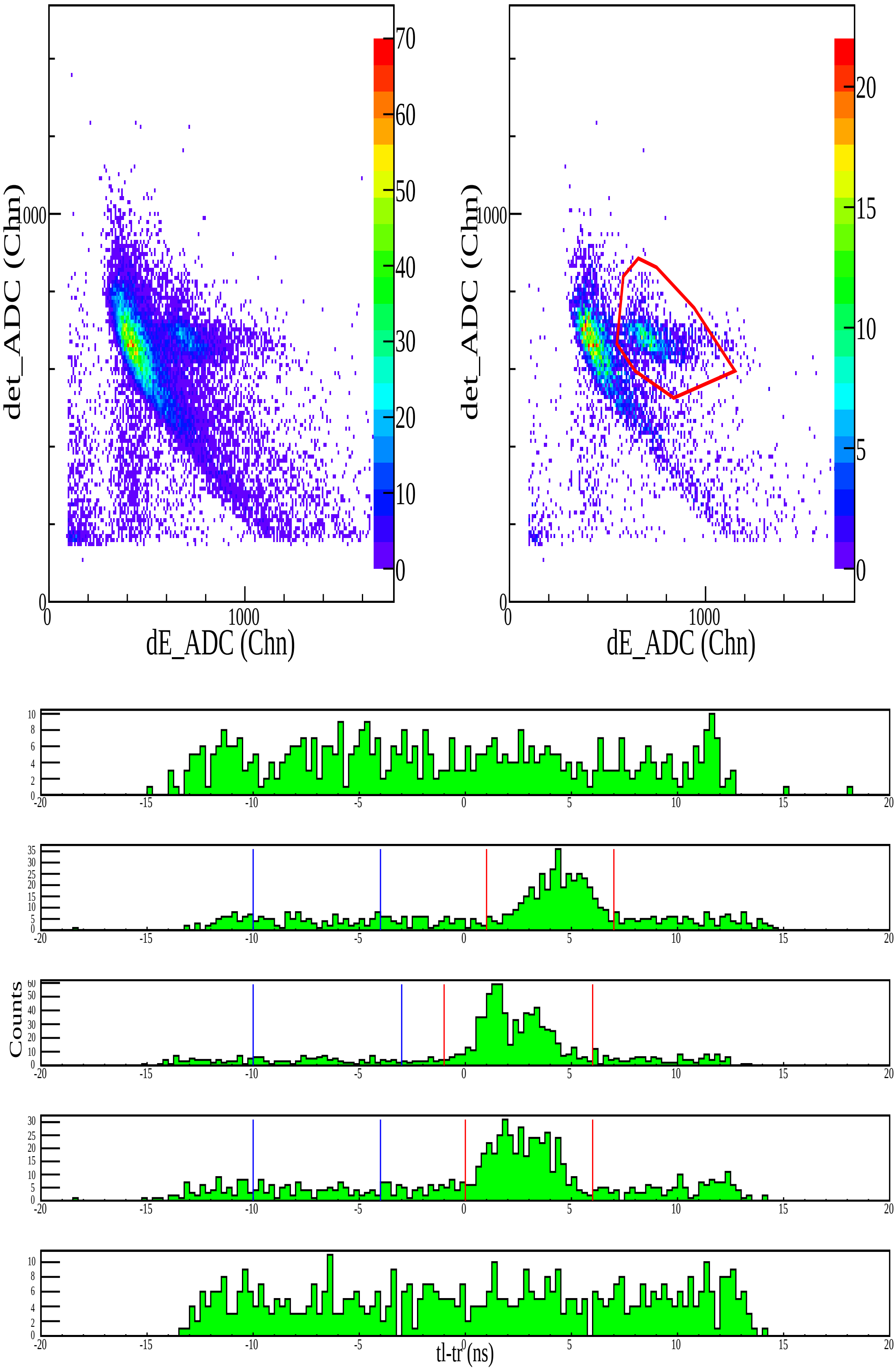

Figure A.14. Figures for 42° at 150 MeV (continued).

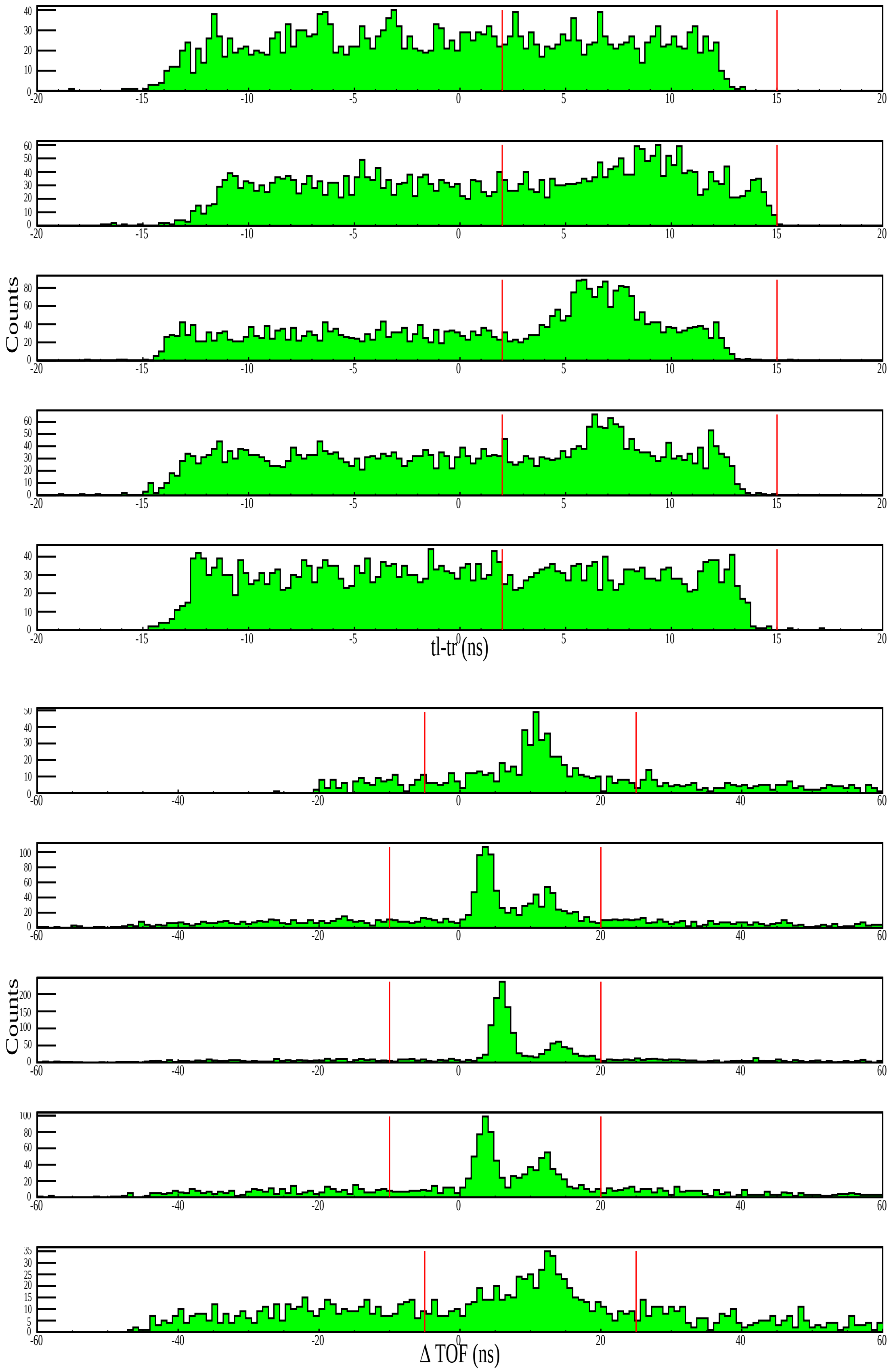

Figure A.15. Figures for 48° at 150 MeV.

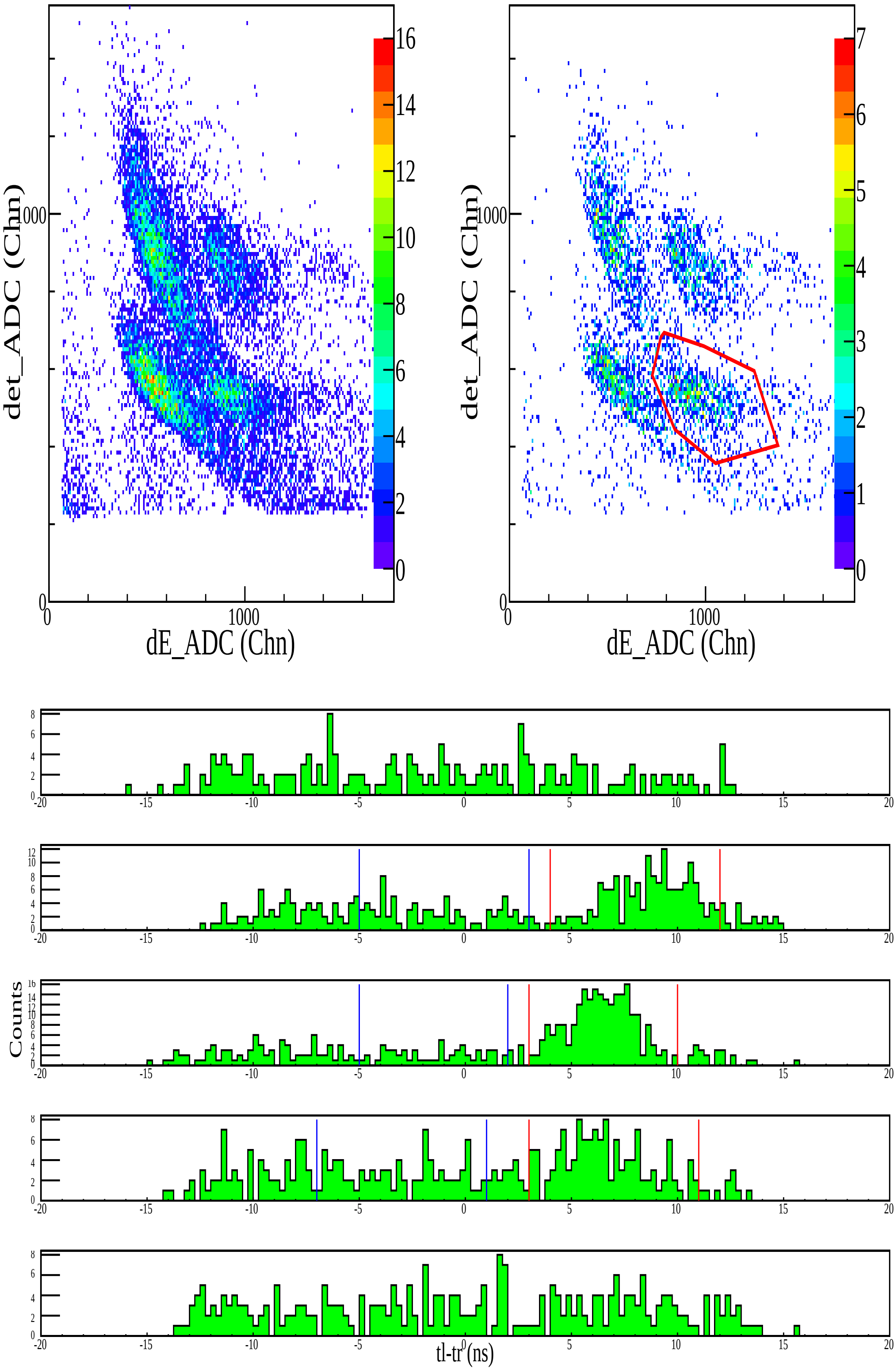

Figure A.16. Figures for 48° at 150 MeV (continued).

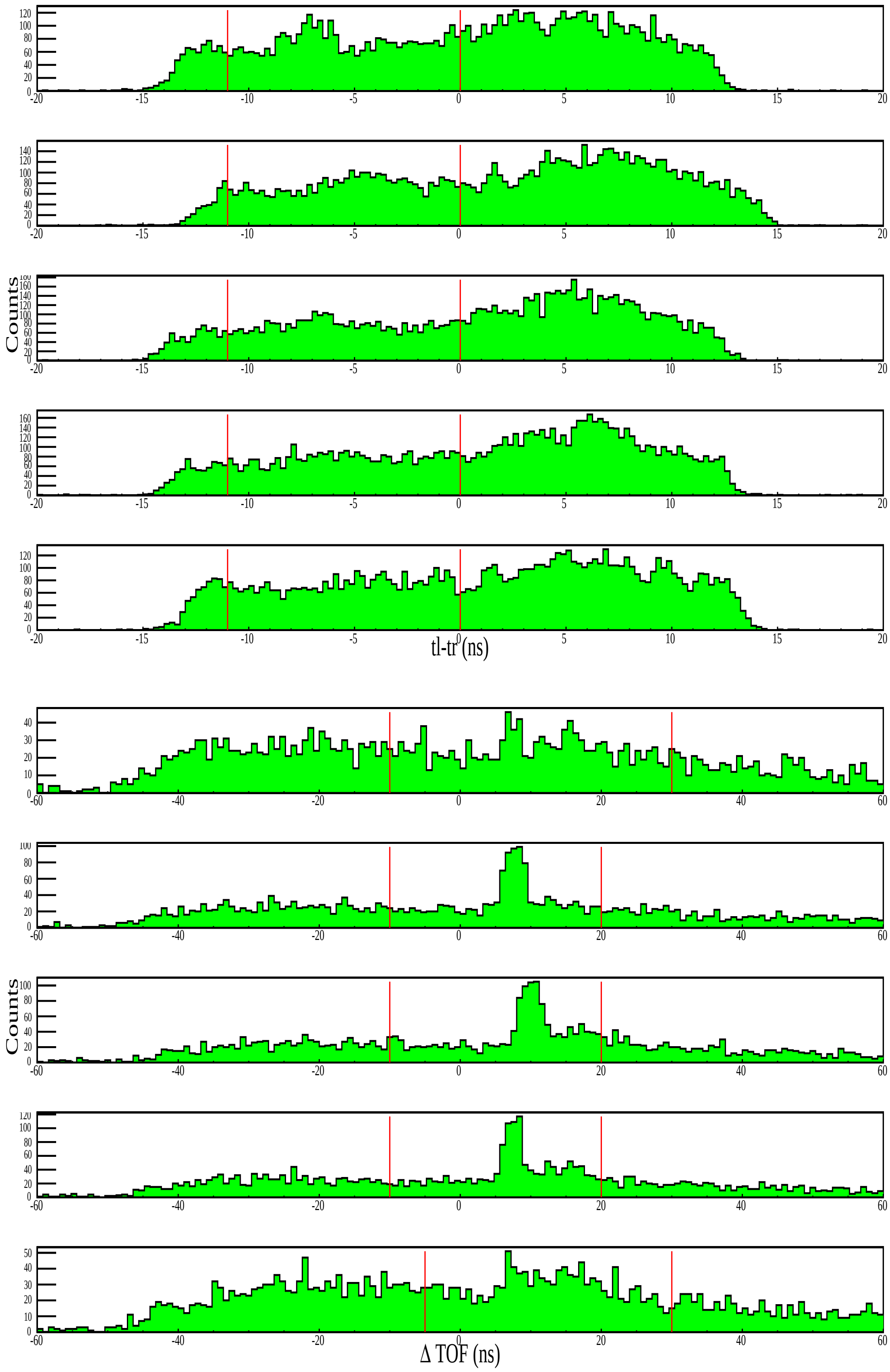

Figure A.17. Figures for 30° at 160 MeV.

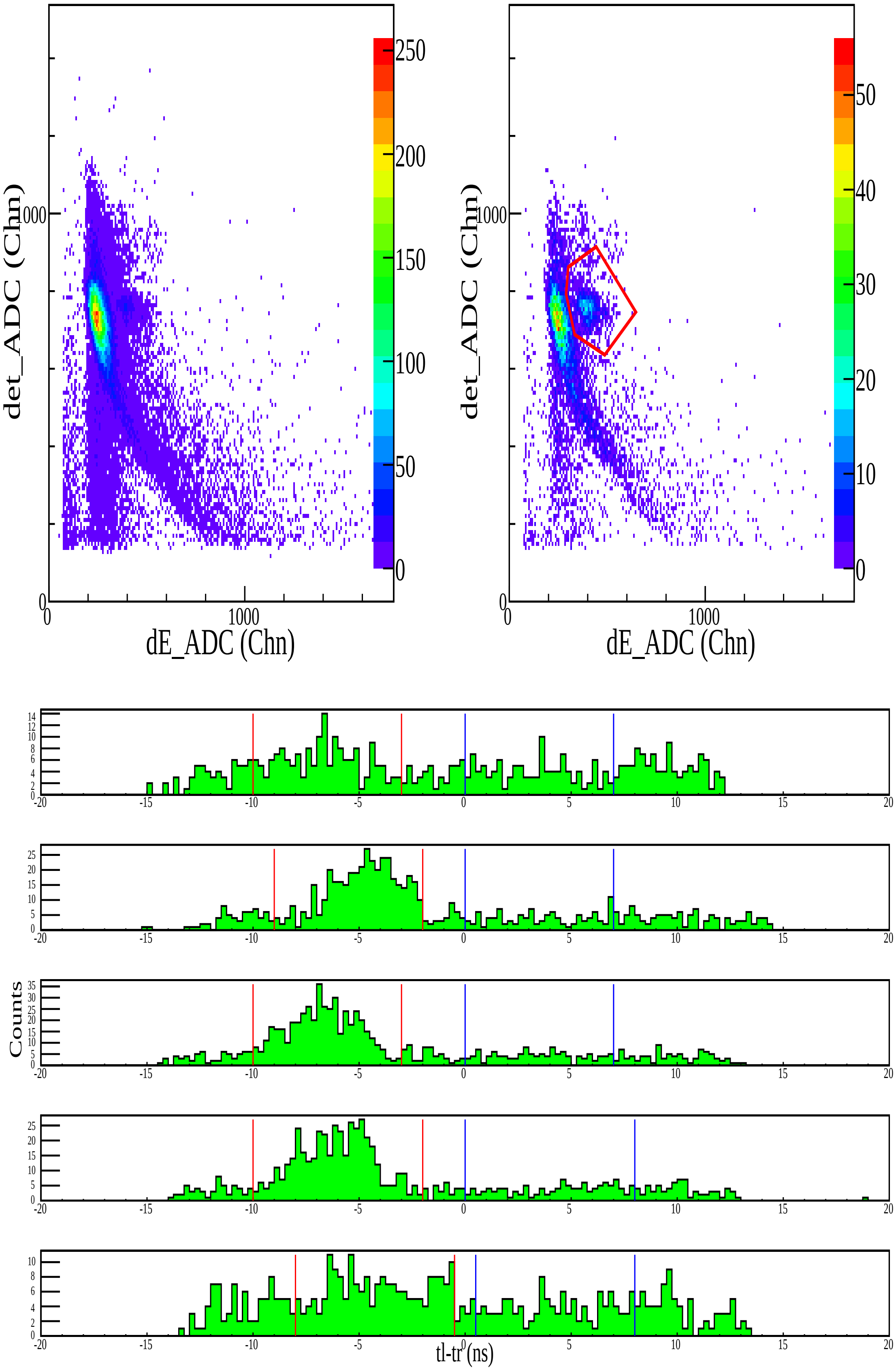

Figure A.18. Figures for 30° at 160 MeV (continued).

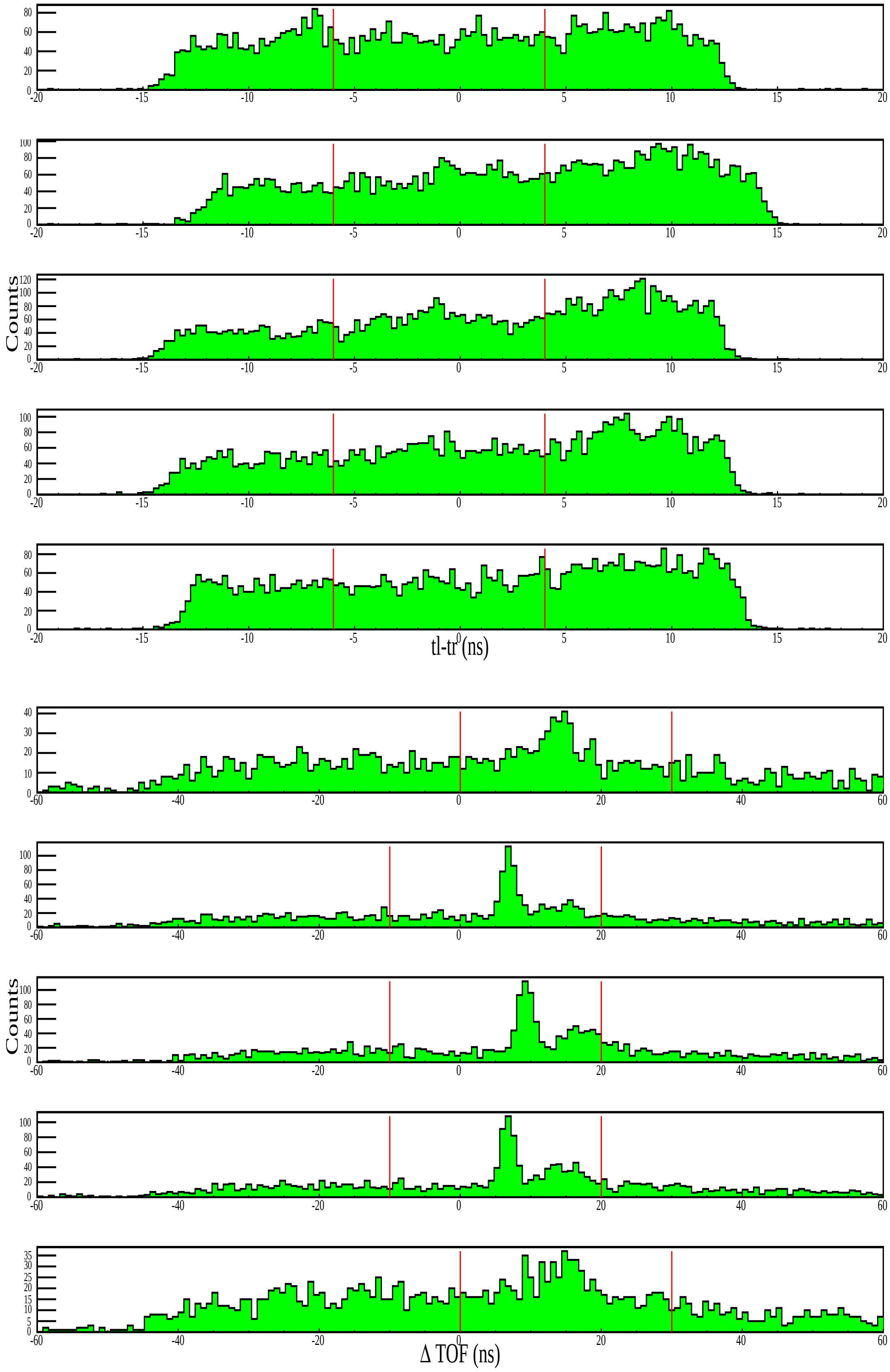

Figure A.19. Figures for 36° at 160 MeV.

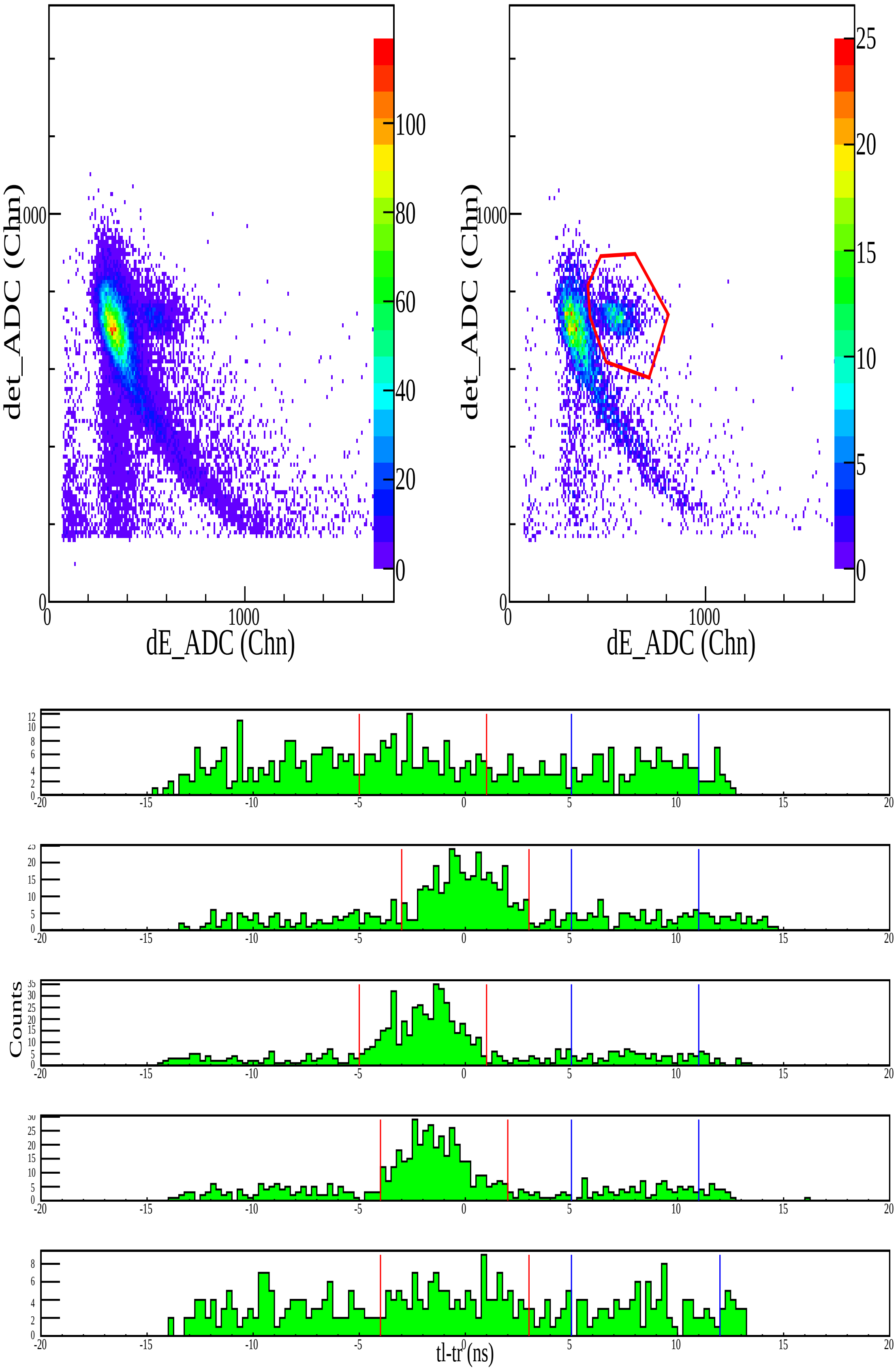

Figure A.20. Figures for 36° at 160 MeV (continued).

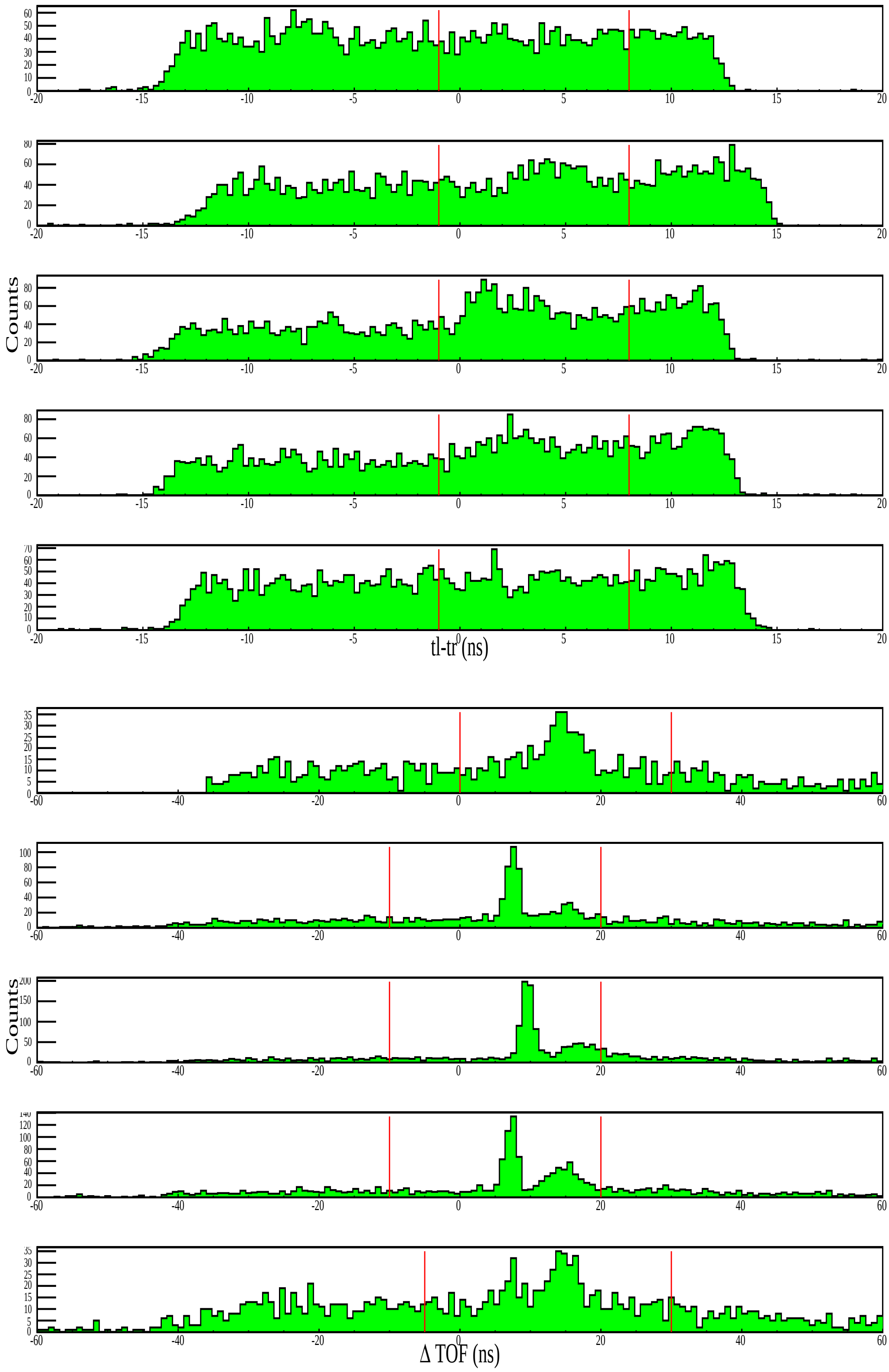

Figure A.21. Figures for 42° at 160 MeV.

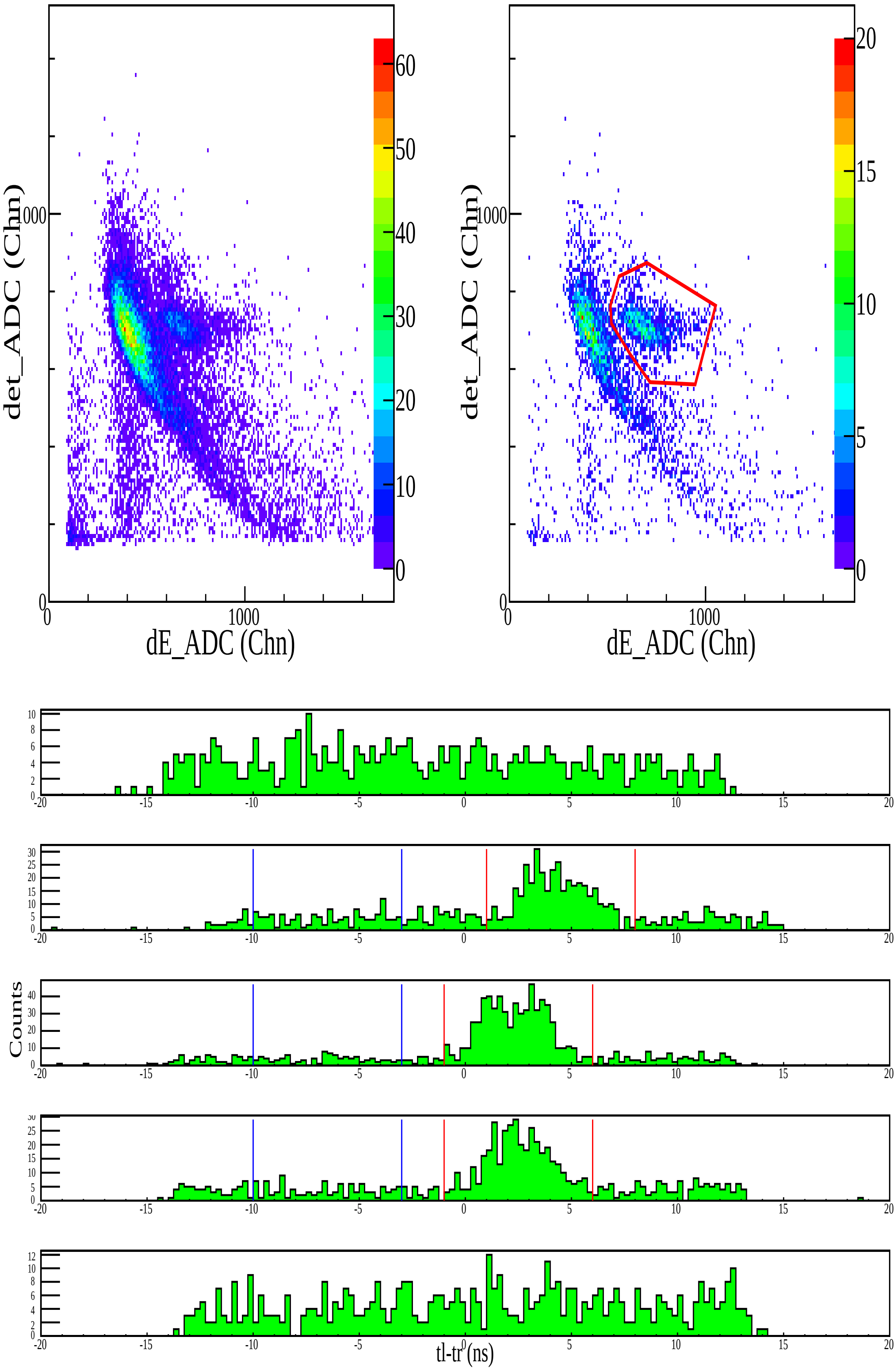

Figure A.22. Figures for 42° at 160 MeV (continued).

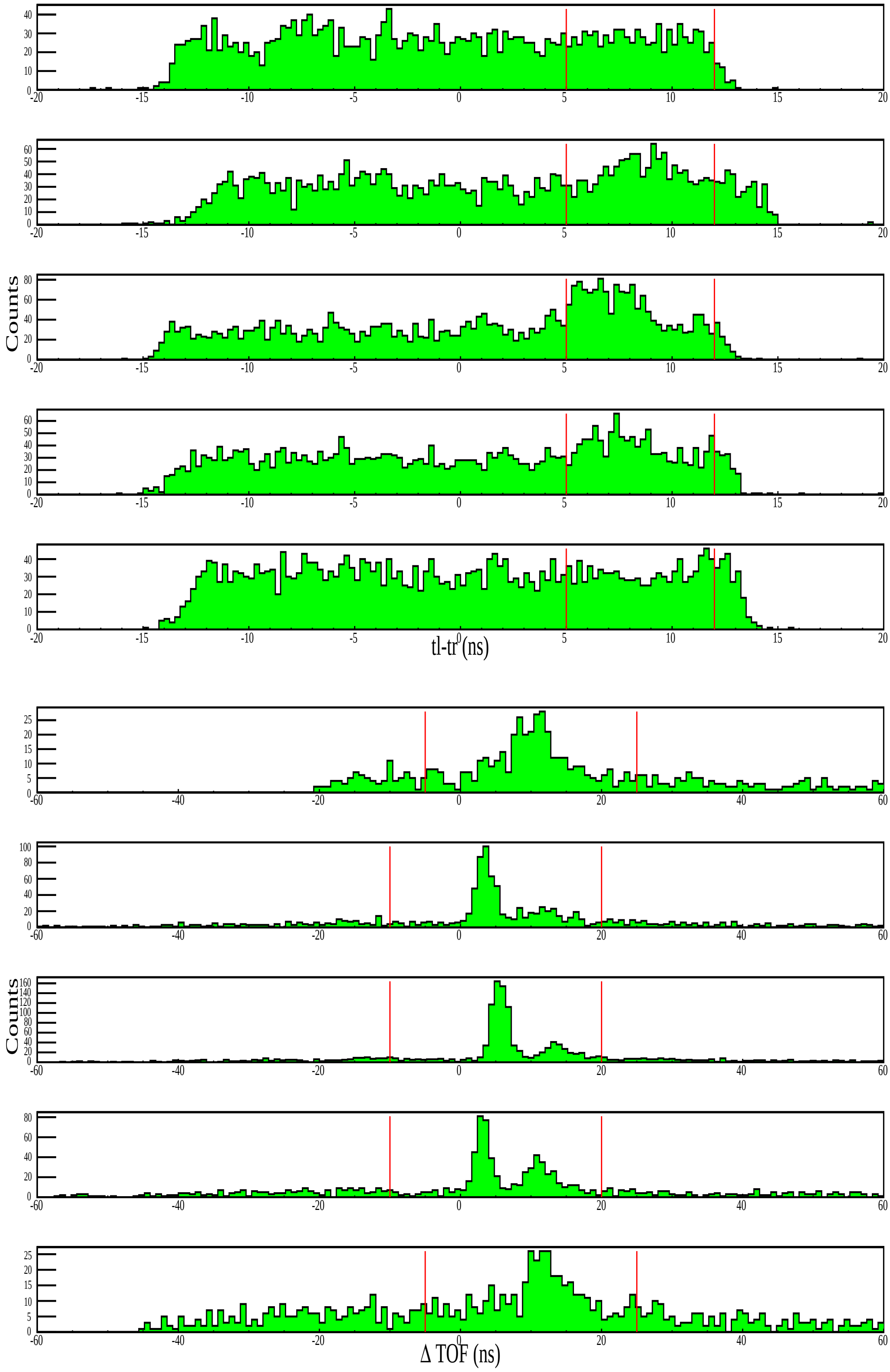

Figure A.23. Figures for 48° at 160 MeV.

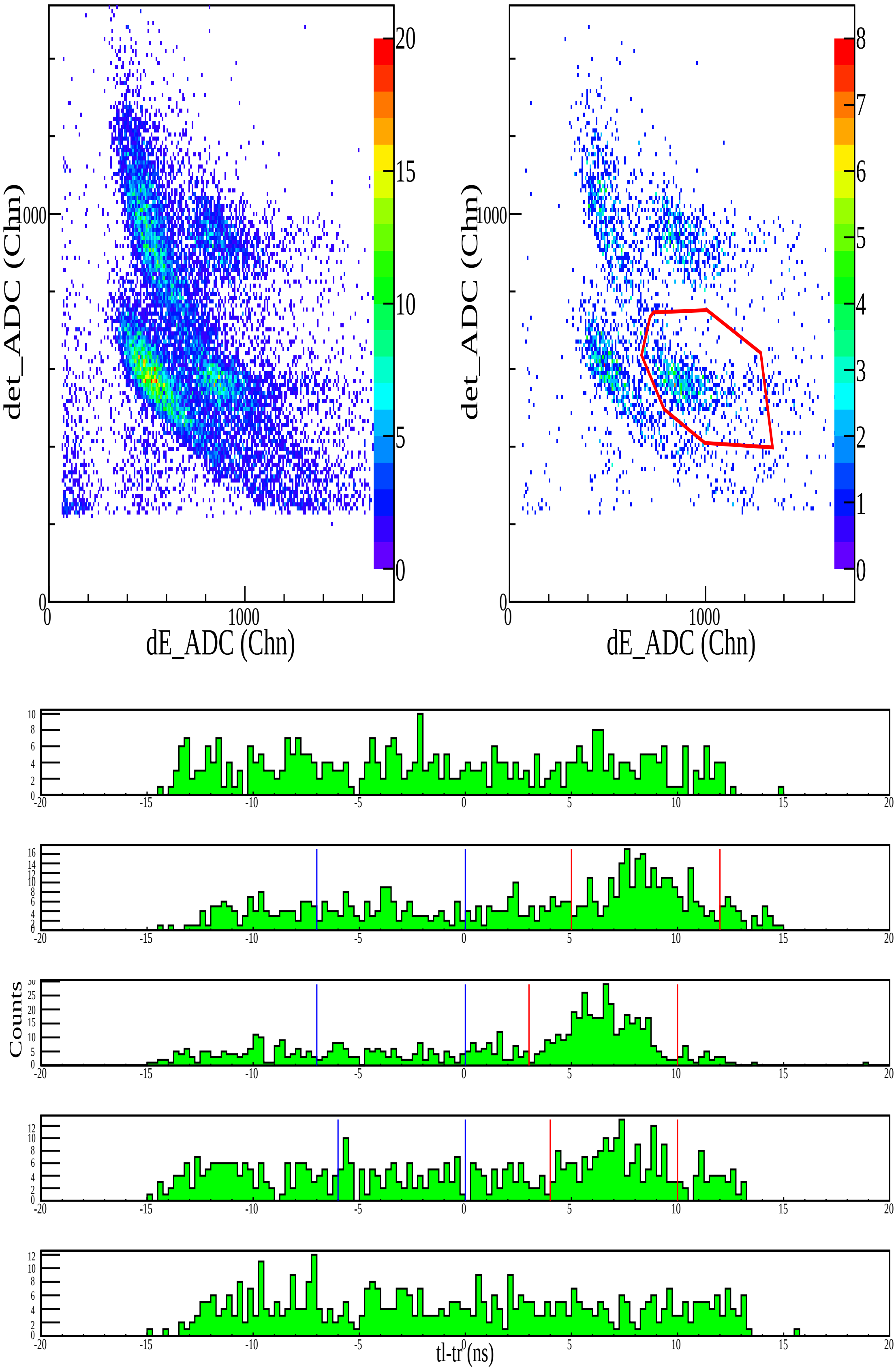

Figure A.24. Figures for 48° at 160 MeV (continued).

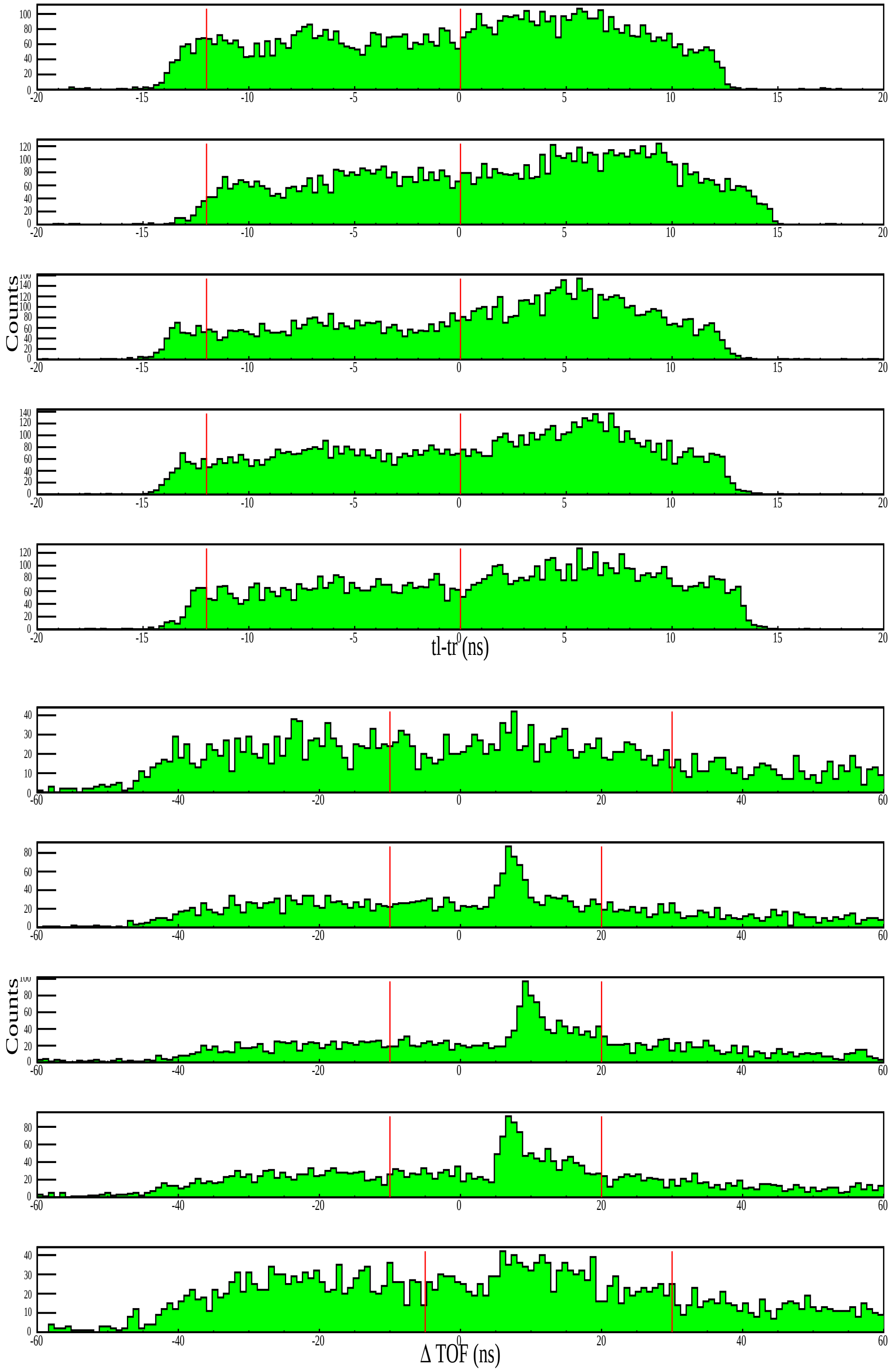

Figure A.25. Figures for 30° at 170 MeV.

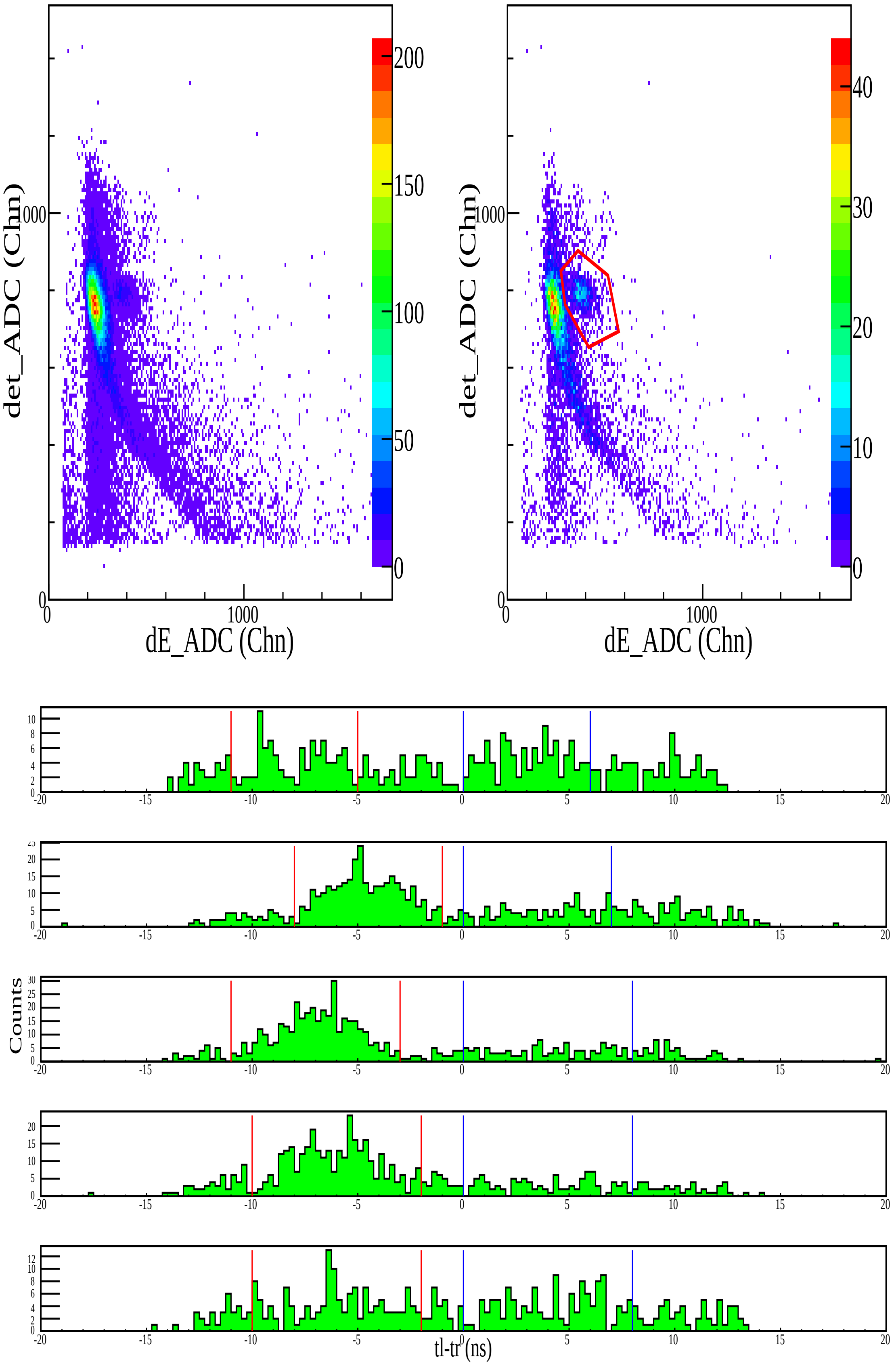

Figure A.26. Figures for 30° at 170 MeV (continued).

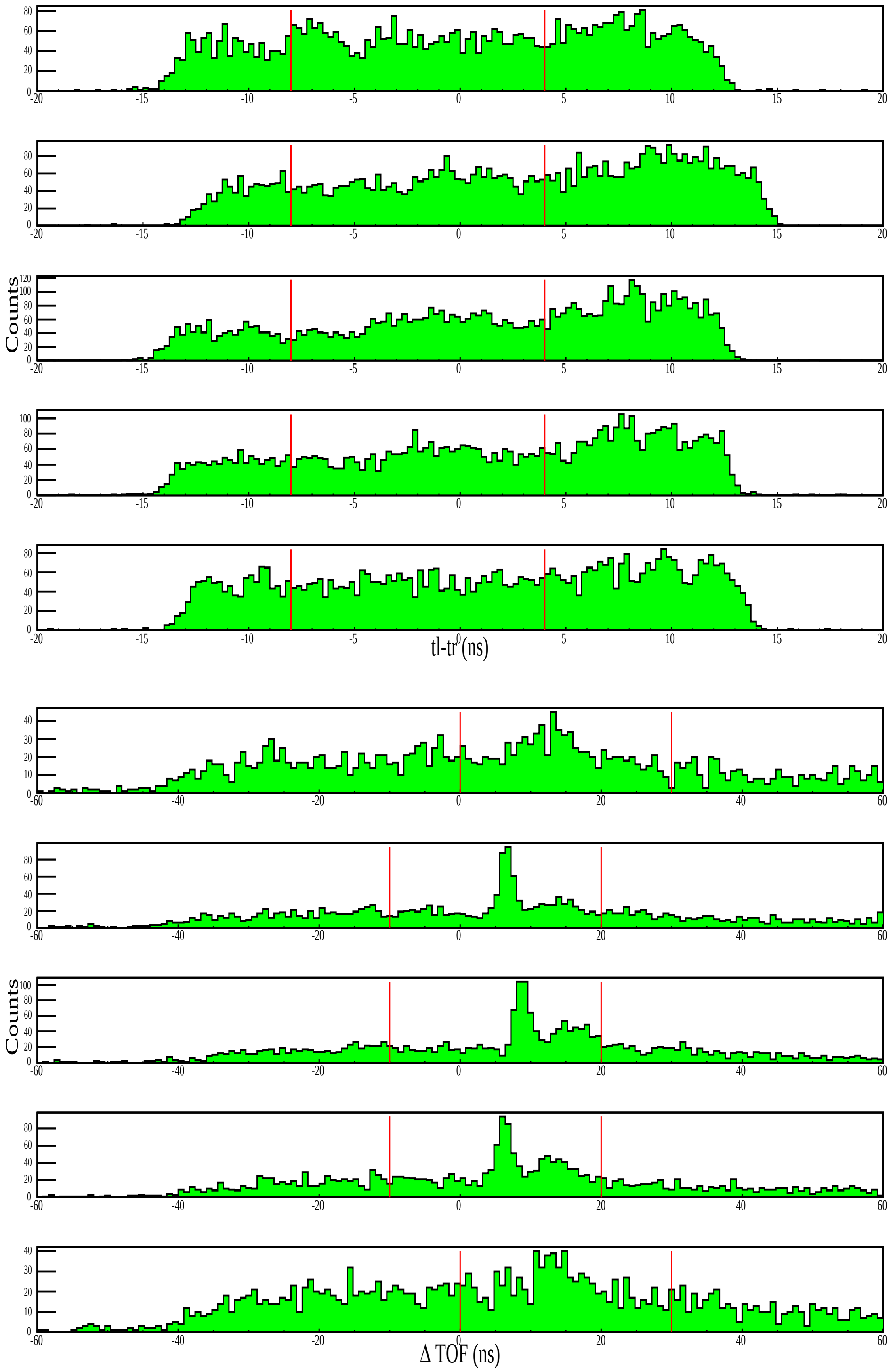

Figure A.27. Figures for 36° at 170 MeV.

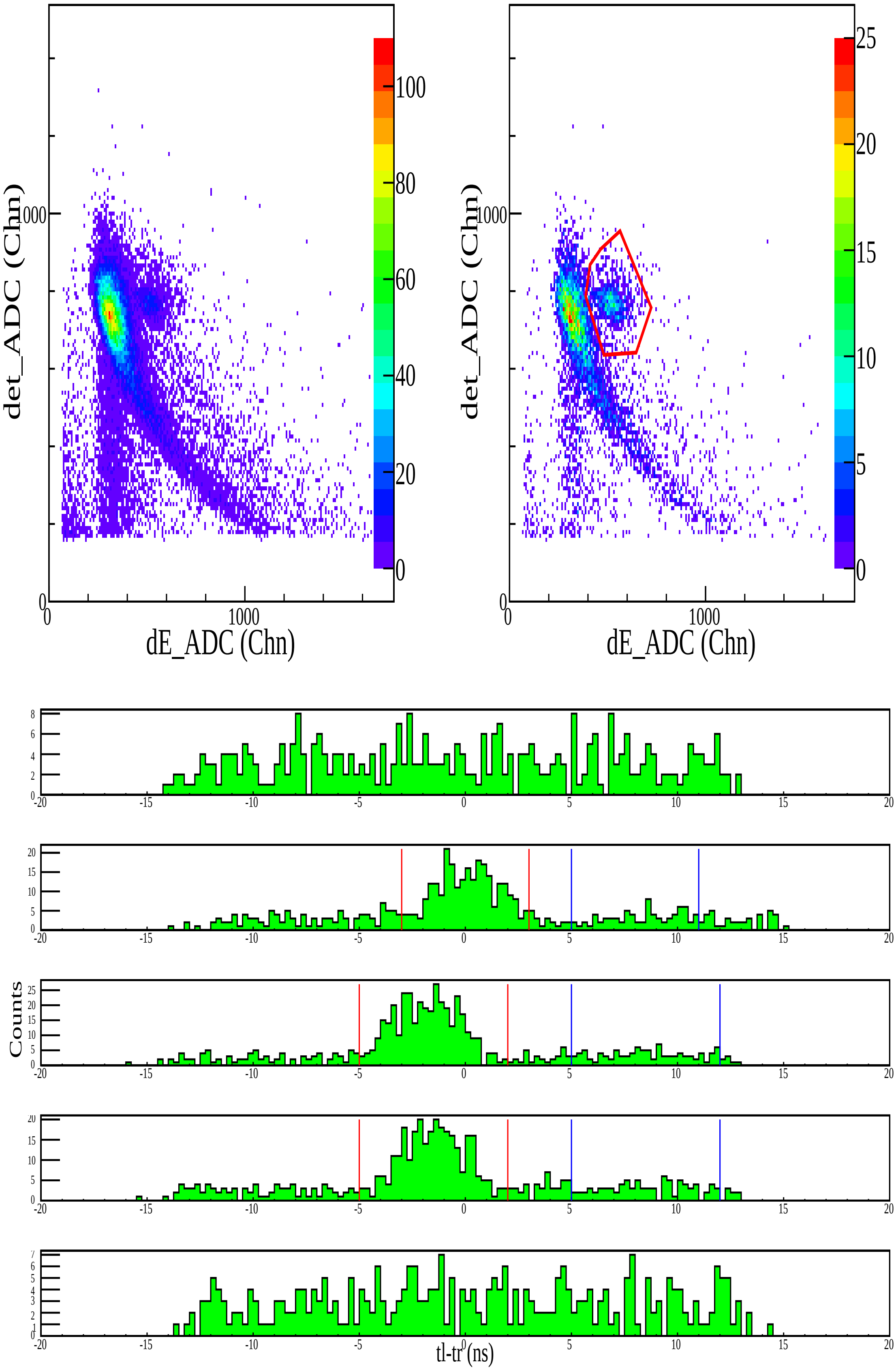

Figure A.28. Figures for 36° at 170 MeV (continued).

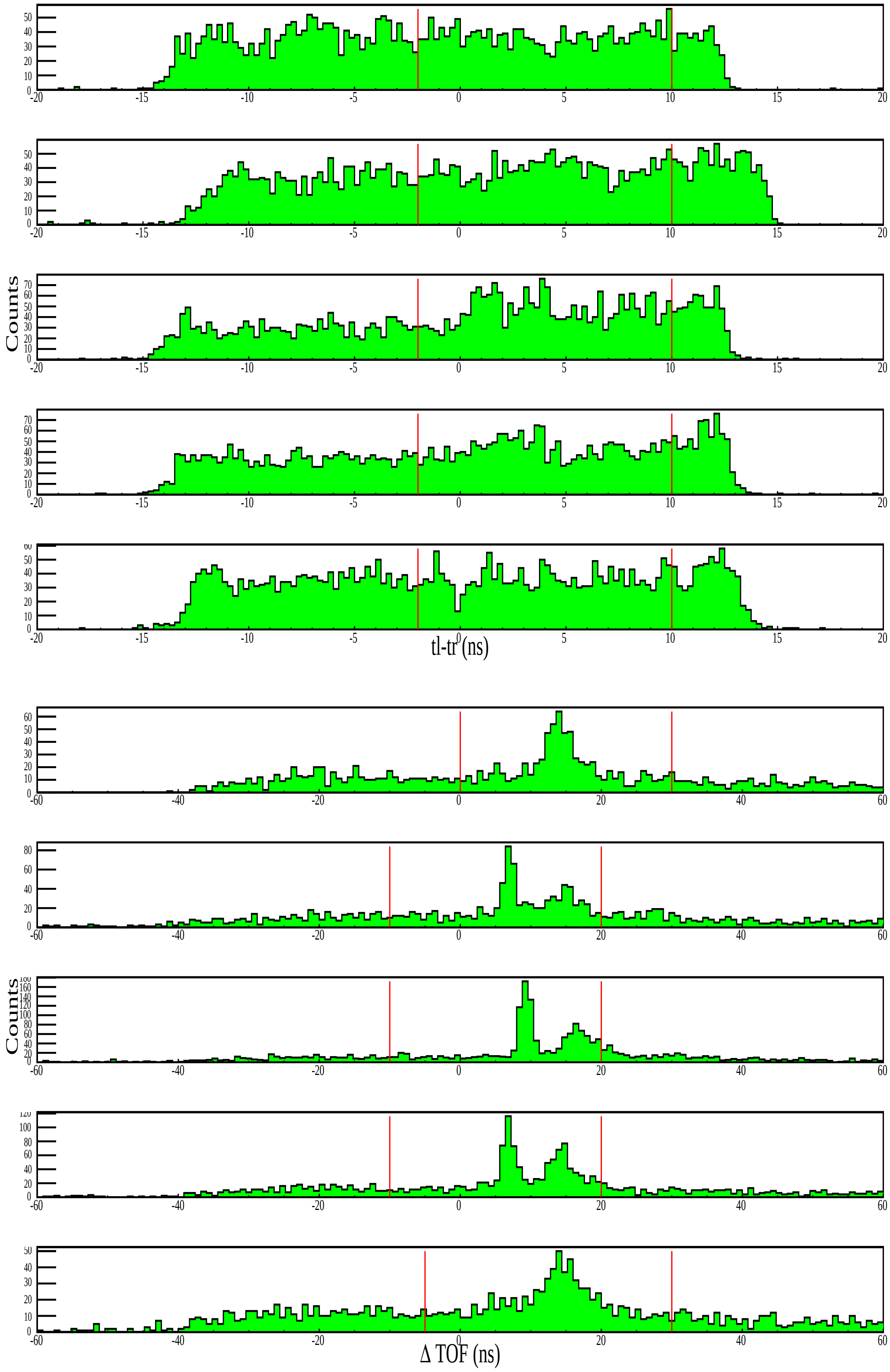

Figure A.29. Figures for 42° at 170 MeV.

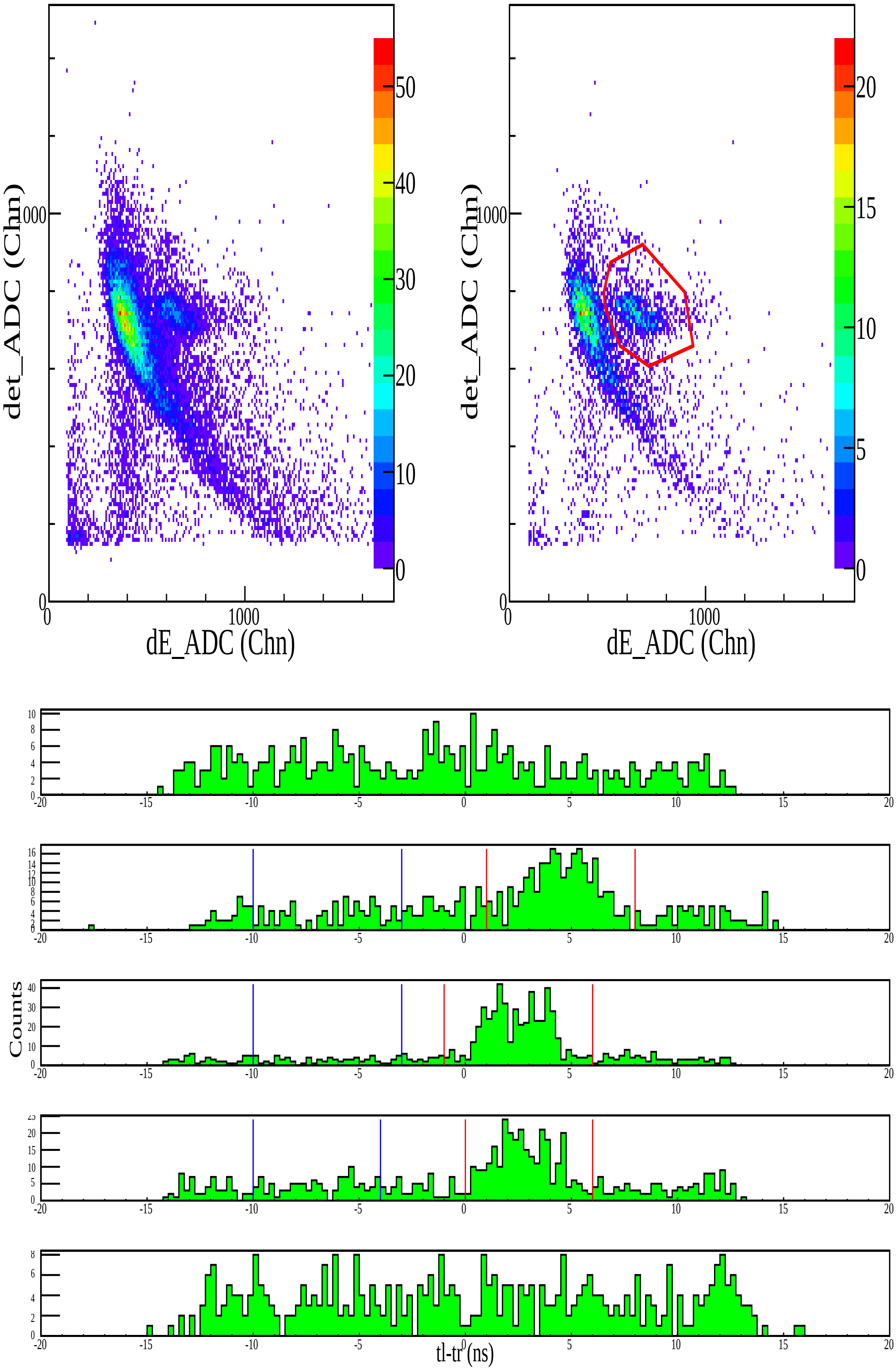

Figure A.30. Figures for 42° at 170 MeV (continued).

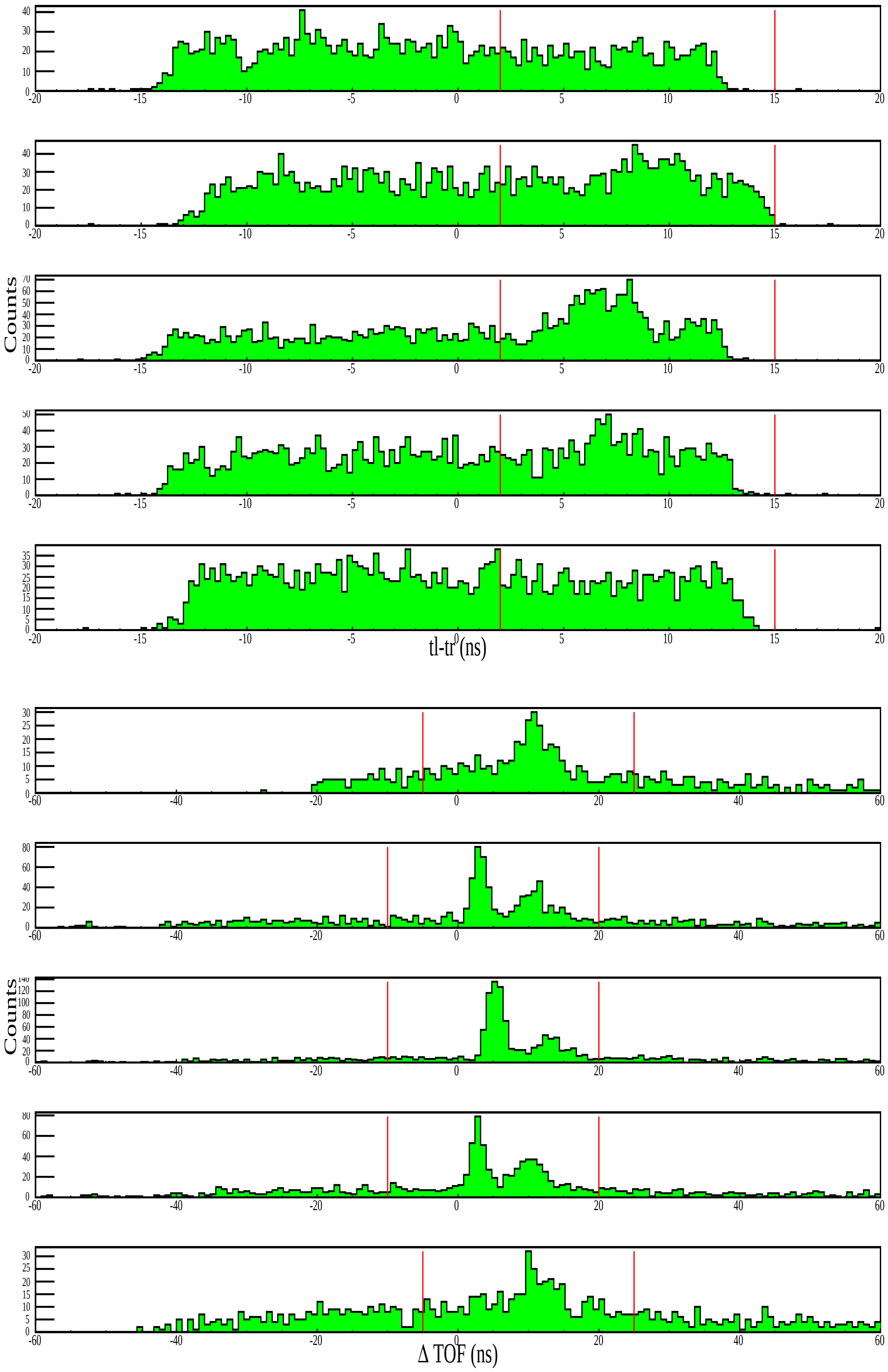

Figure A.31. Figures for 48° at 170 MeV.

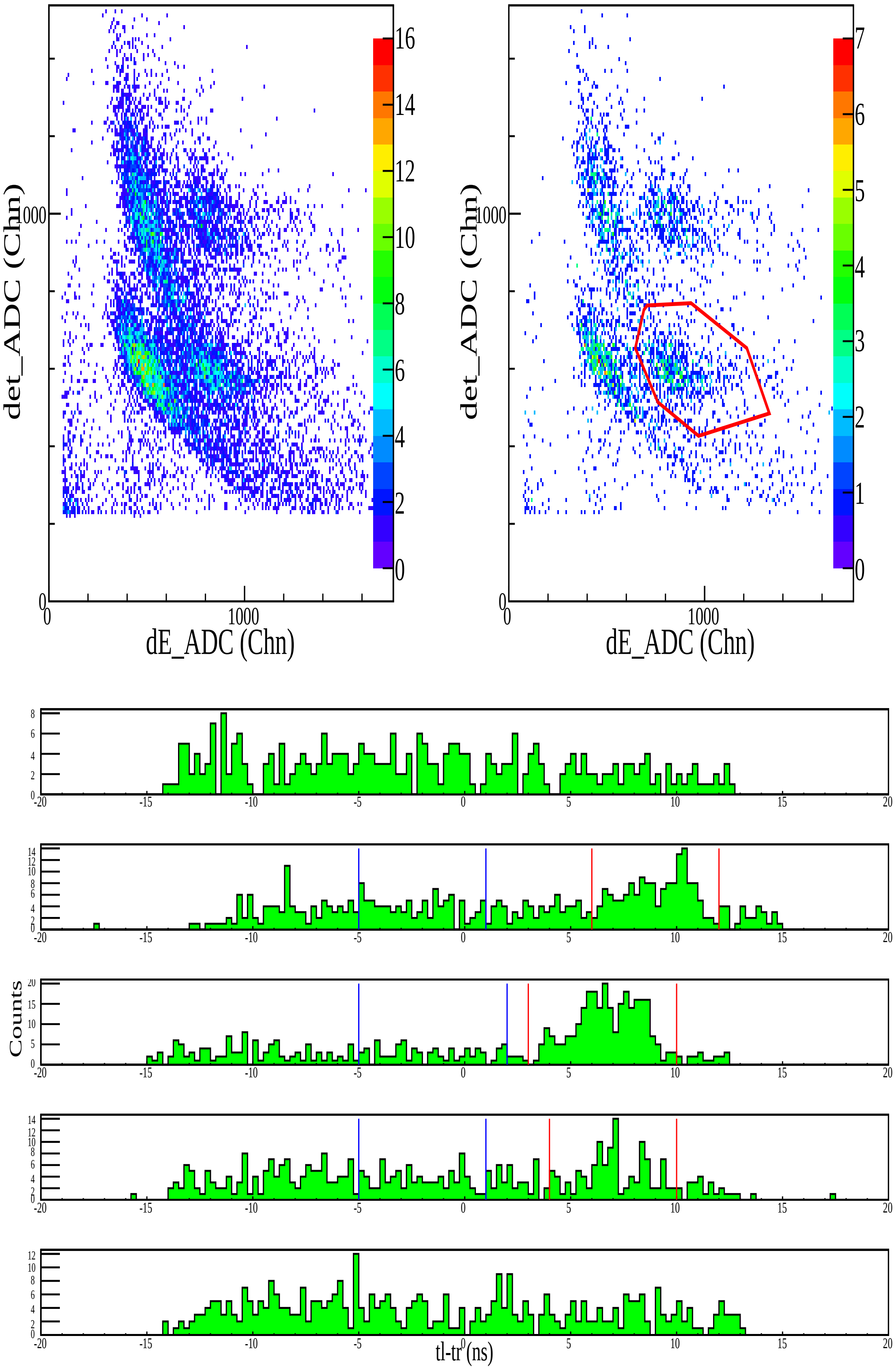

Figure A.32. Figures for 48° at 170 MeV (continued).

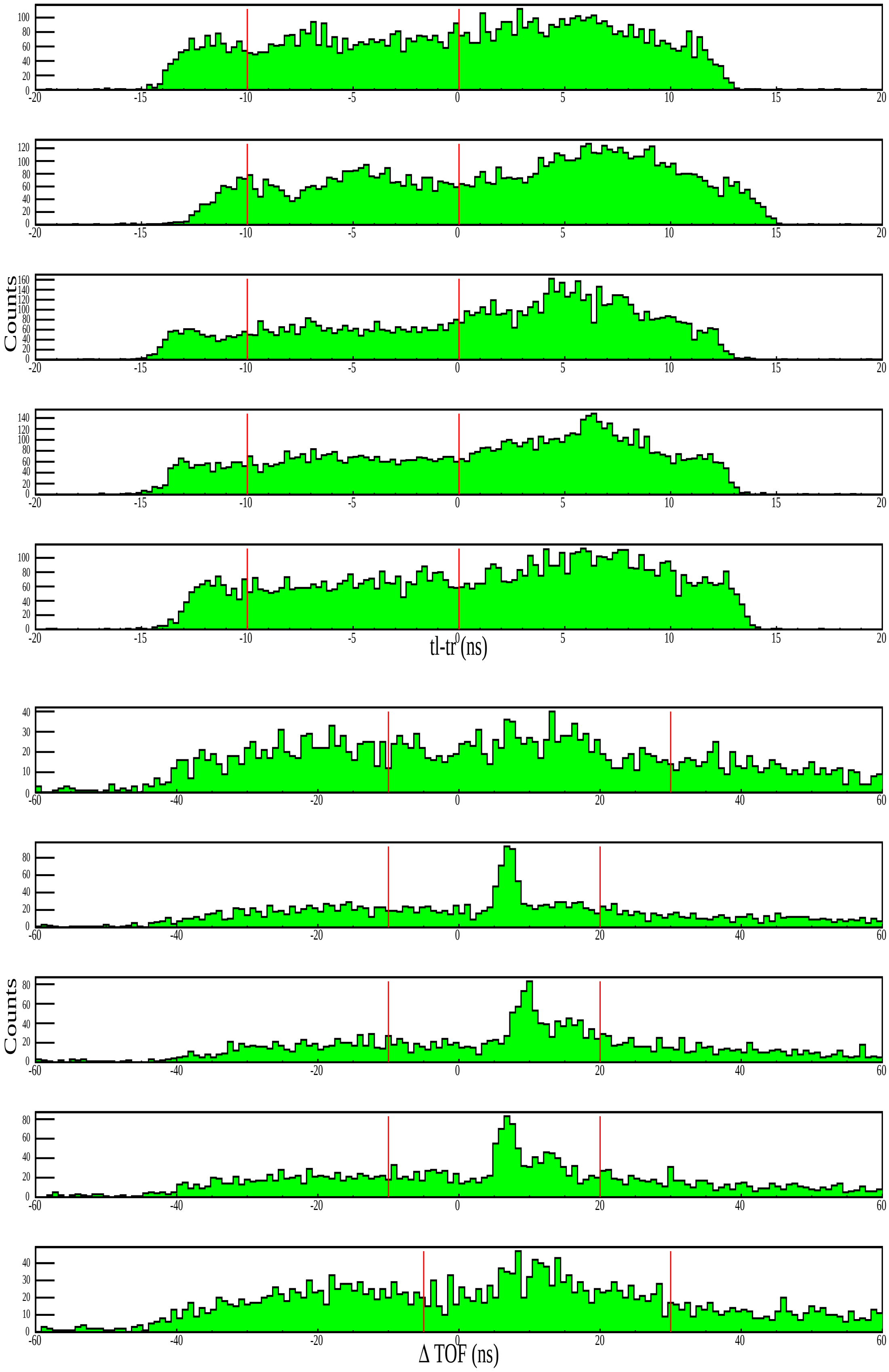

Figure A.33. Figures for 30° at 180 MeV.

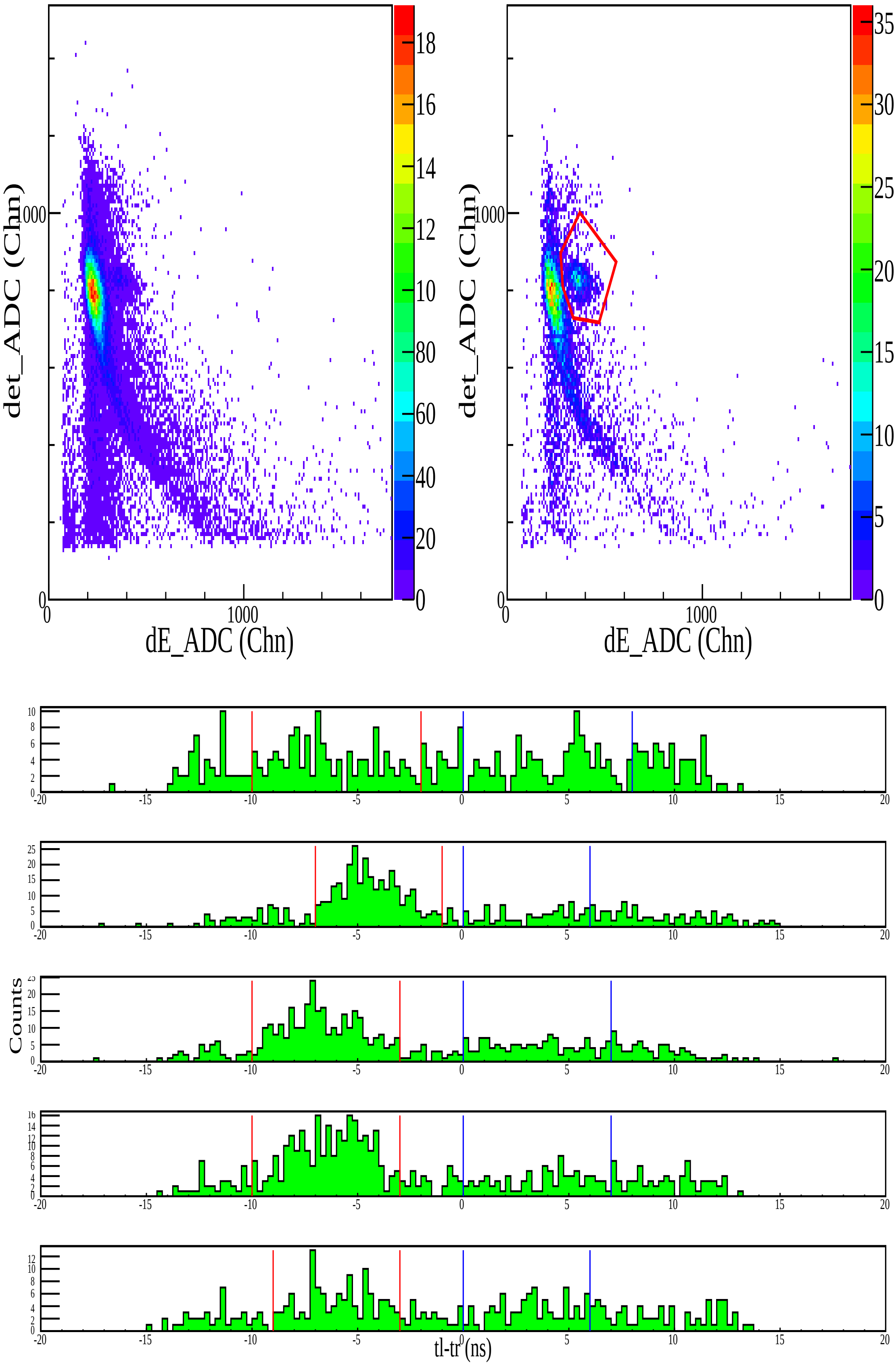

Figure A.34. Figures for 30° at 180 MeV (continued).

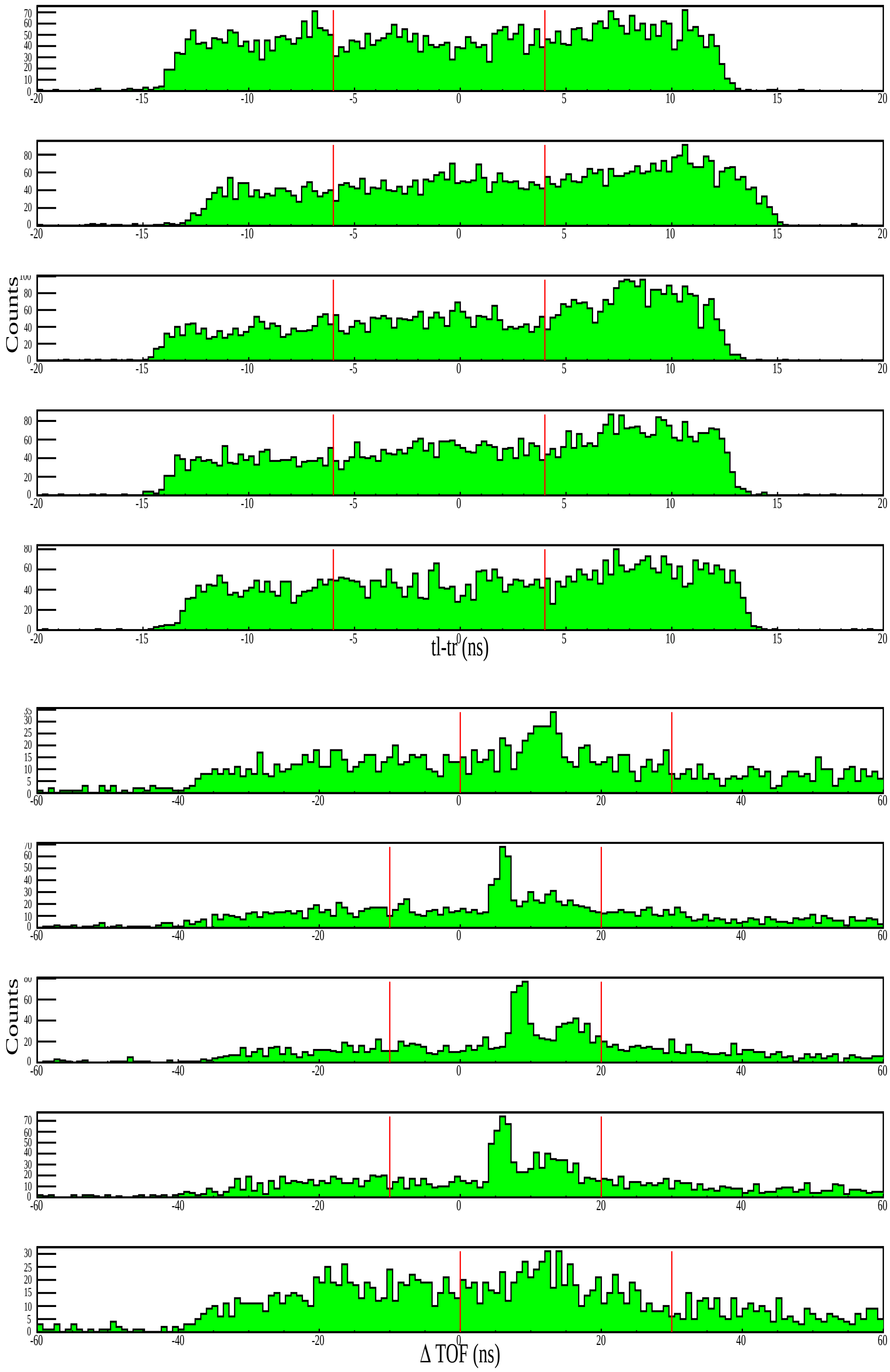

Figure A.35. Figures for 36° at 180 MeV.

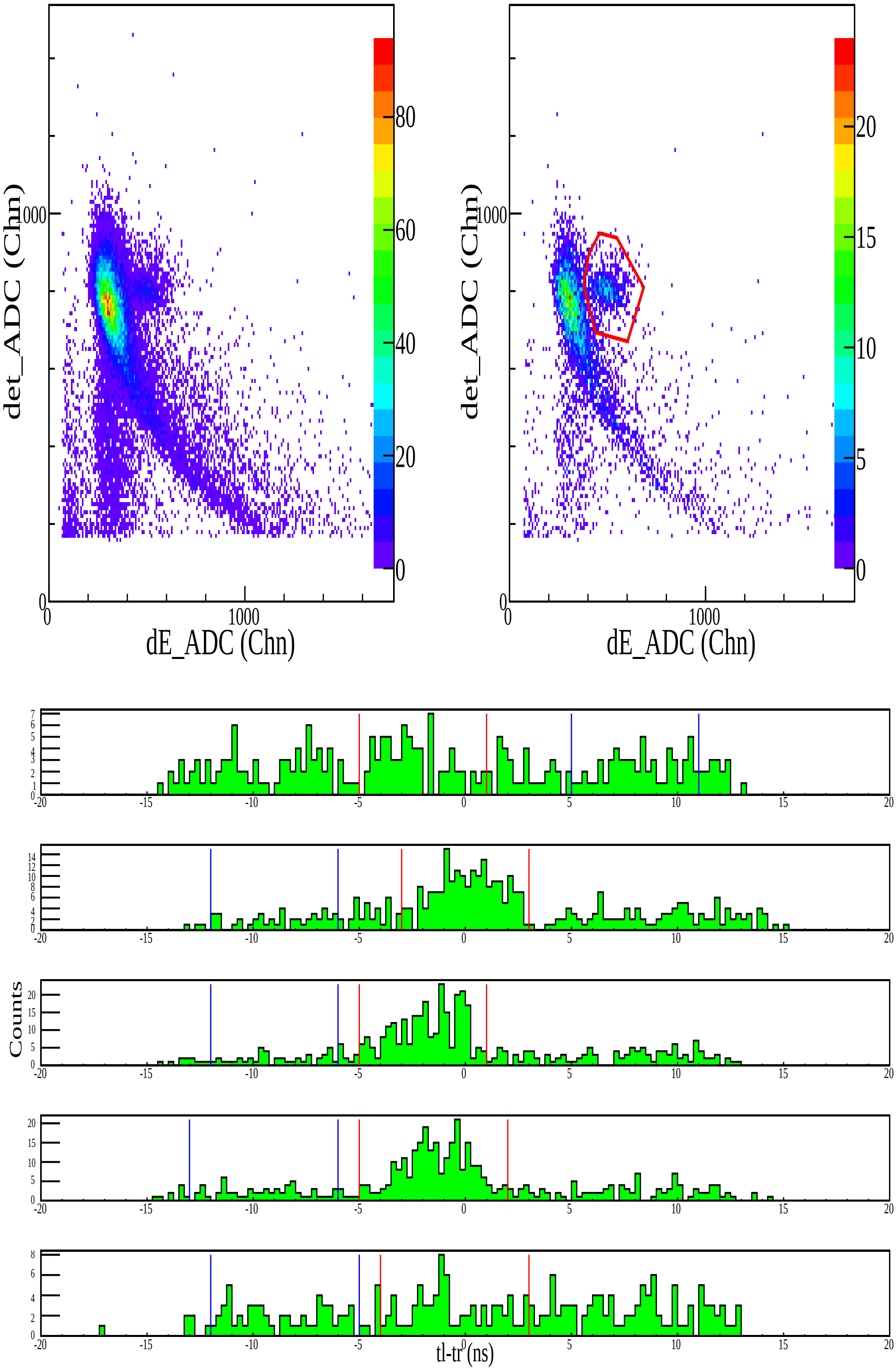

Figure A.36. Figures for 36° at 180 MeV (continued).

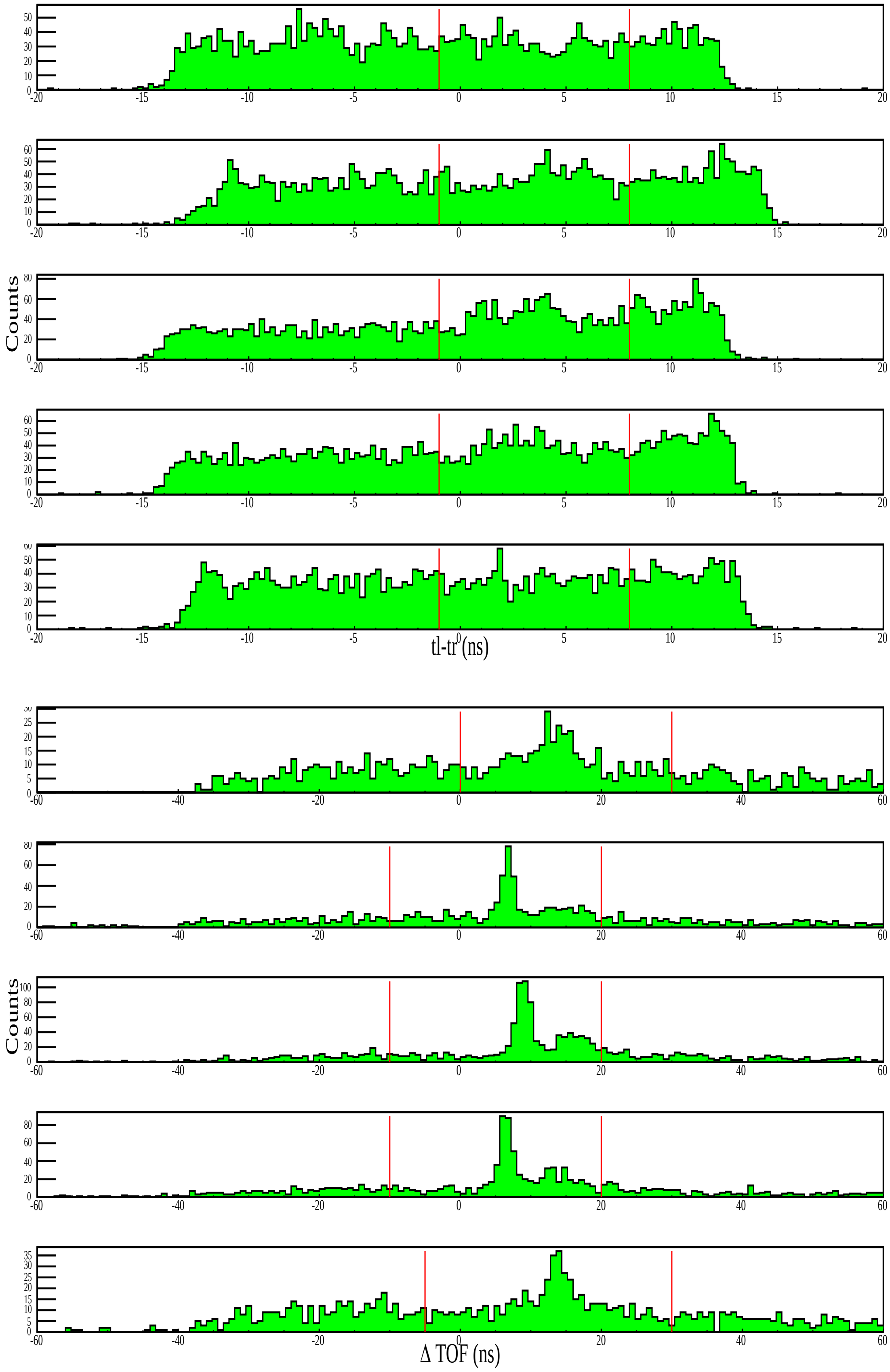

Figure A.37. Figures for 42° at 180 MeV.

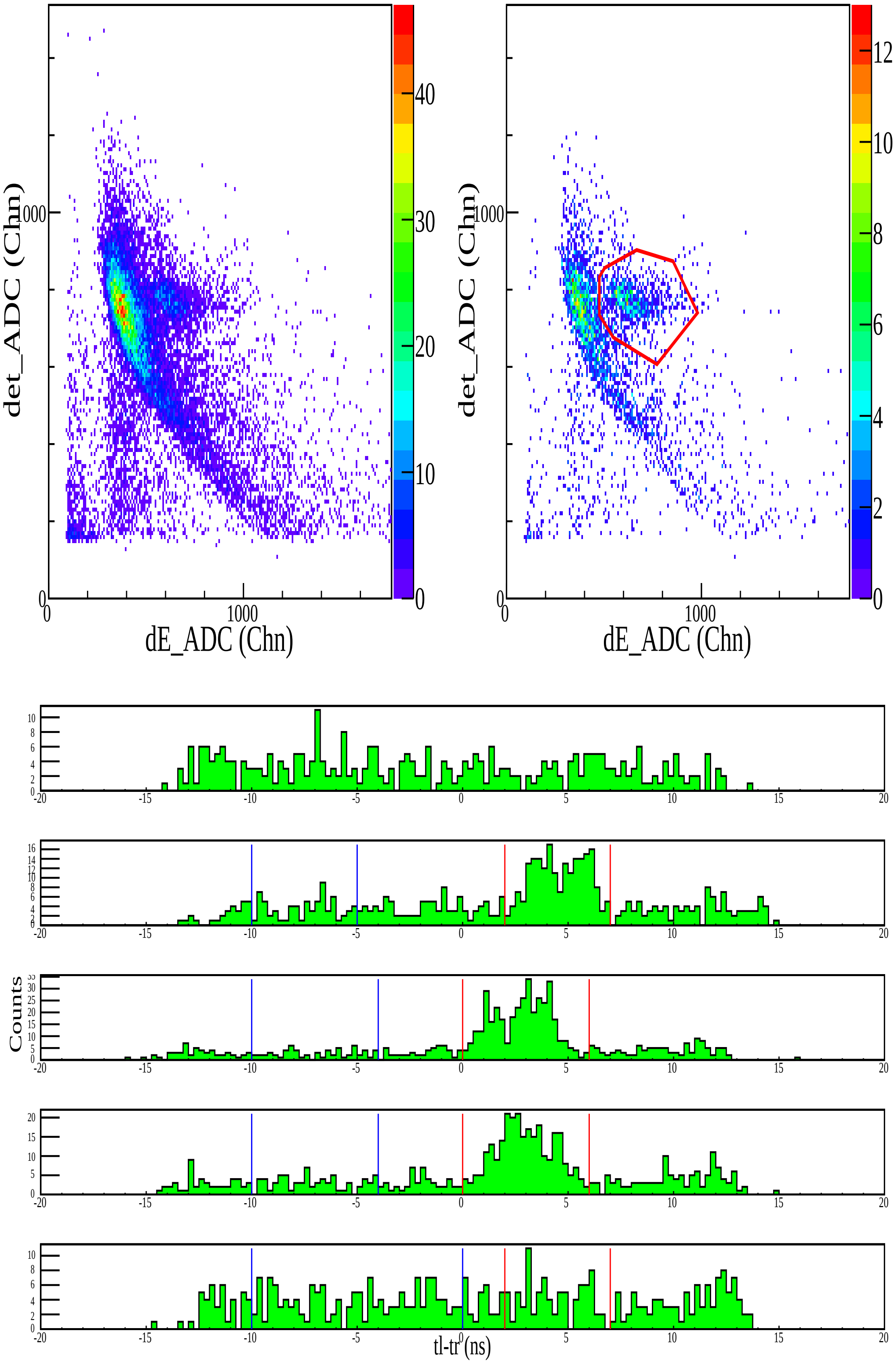

Figure A.38. Figures for 42° at 180 MeV (continued).

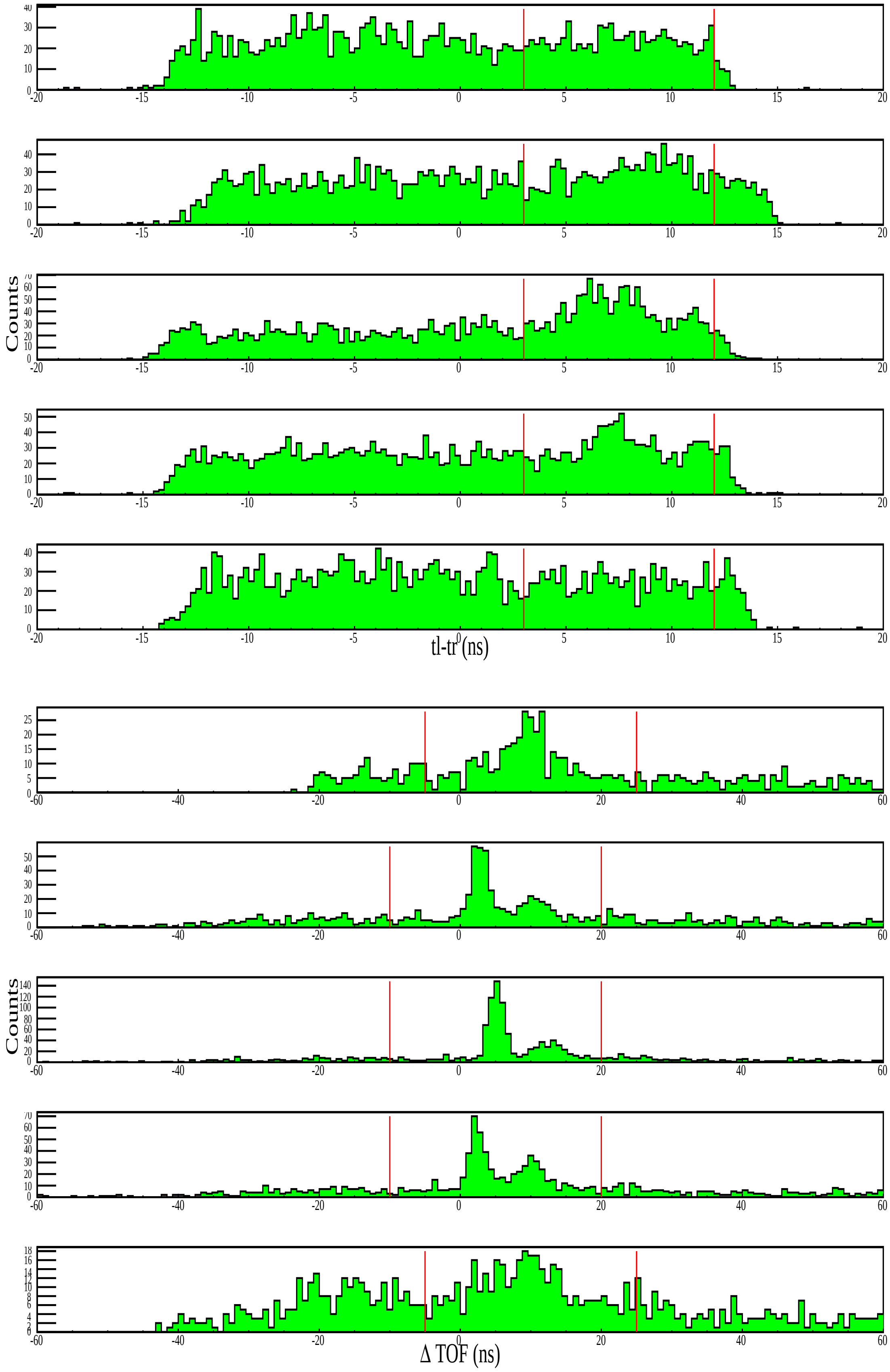

Figure A.39. Figures for 48° at 180 MeV.

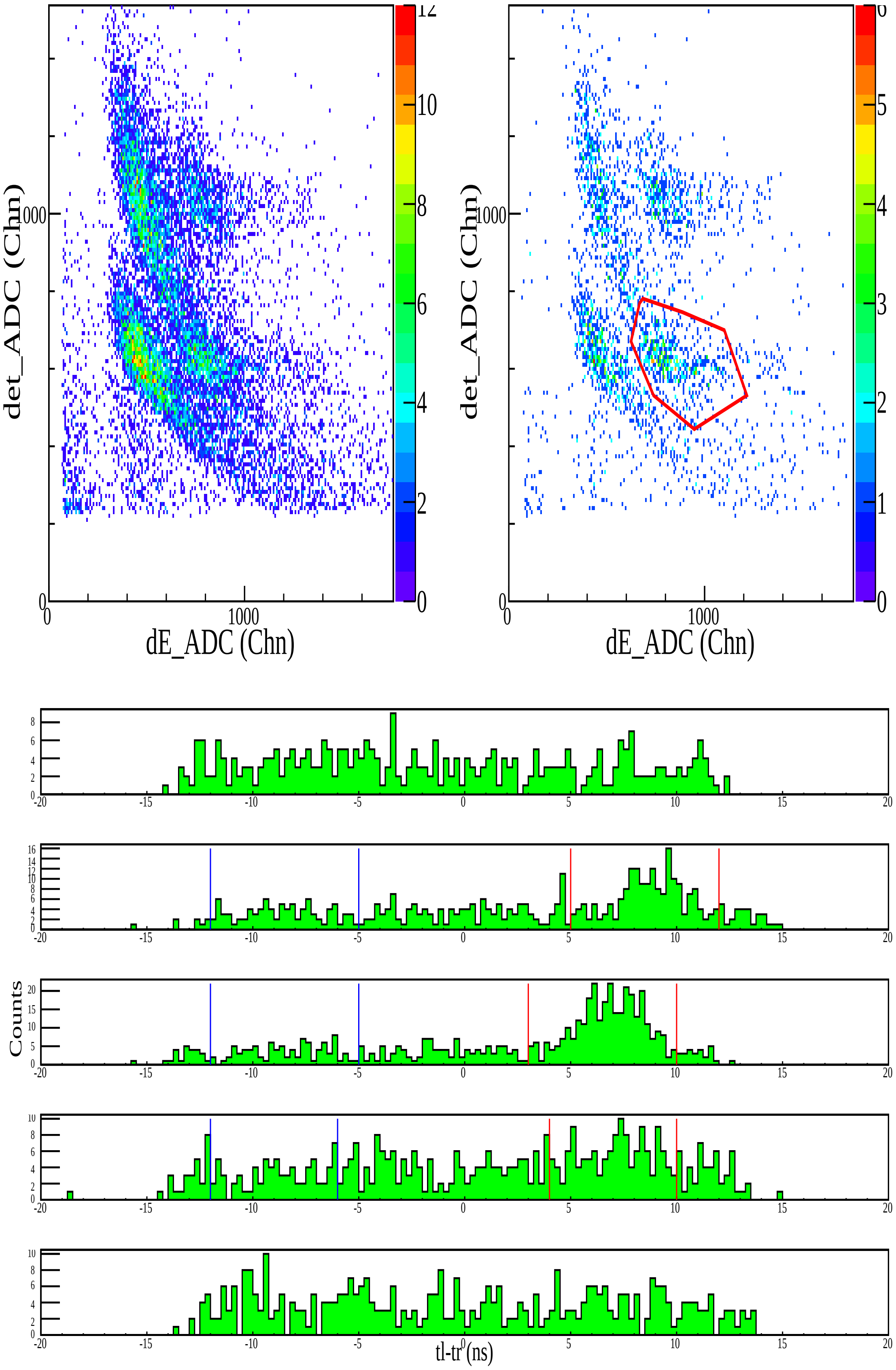

Figure A.40. Figures for 48° at 180 MeV (continued).

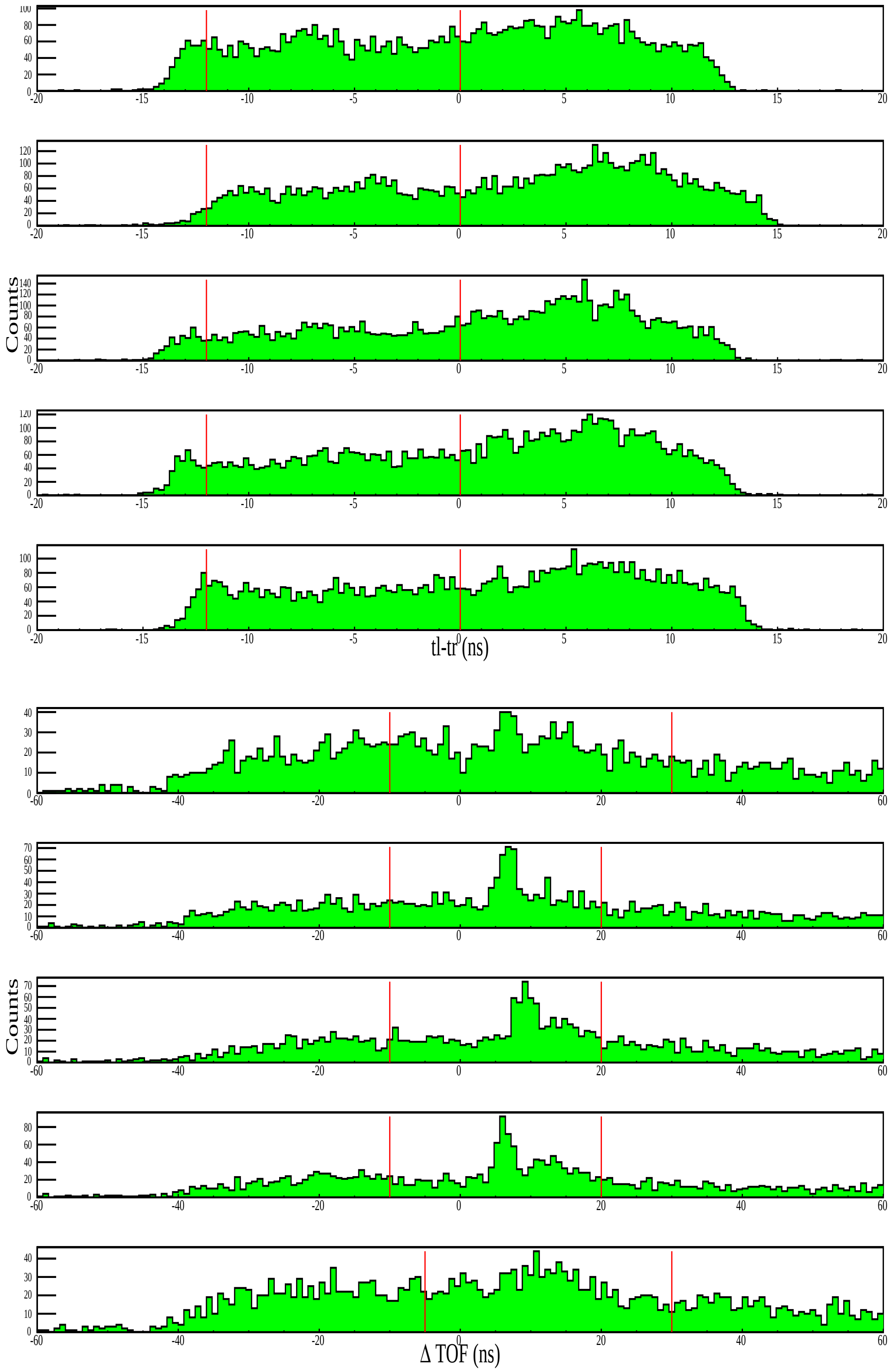

Figure A.41. Figures for 30° at 190 MeV.

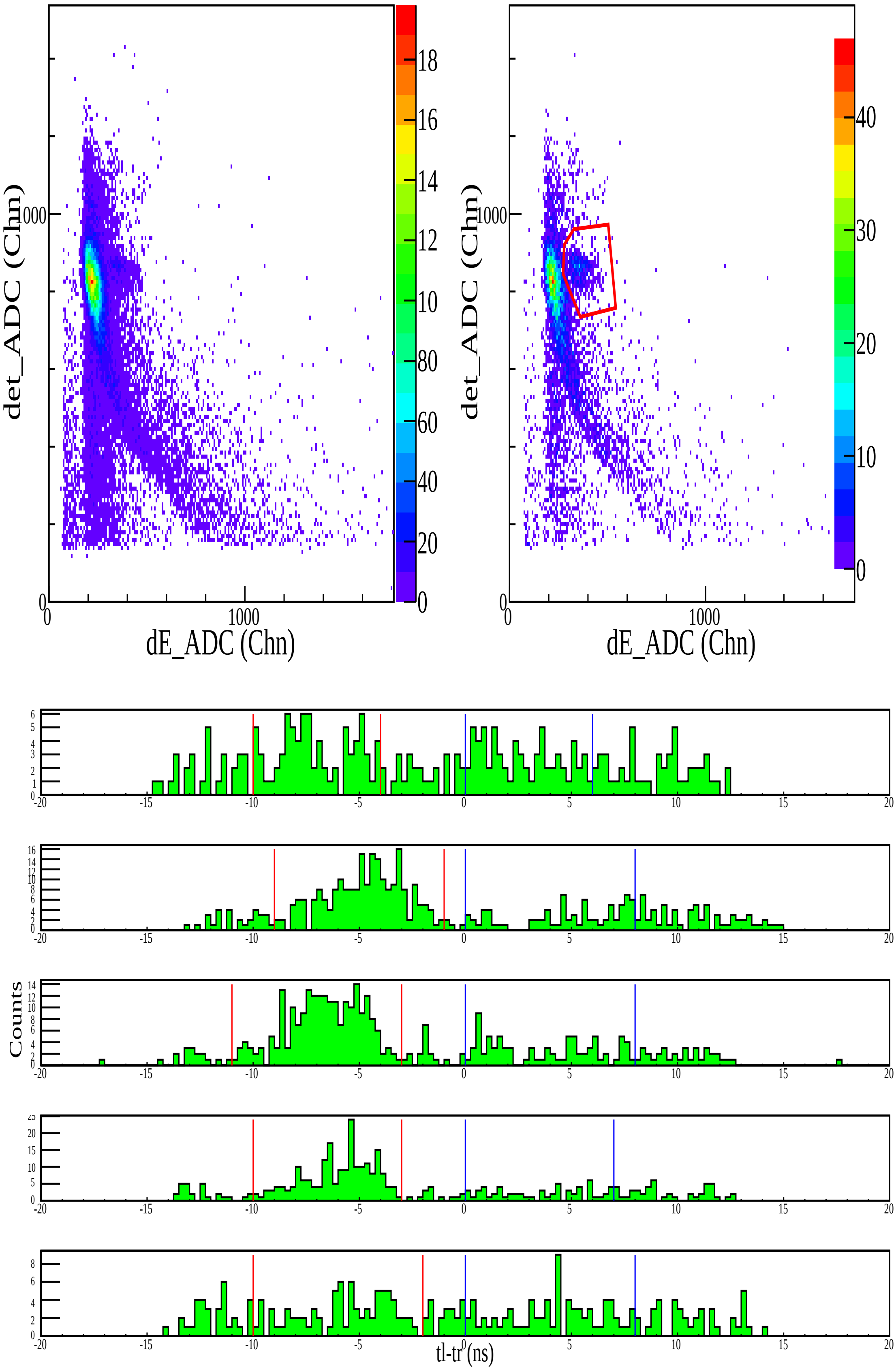

Figure A.42. Figures for 30° at 190 MeV (continued).

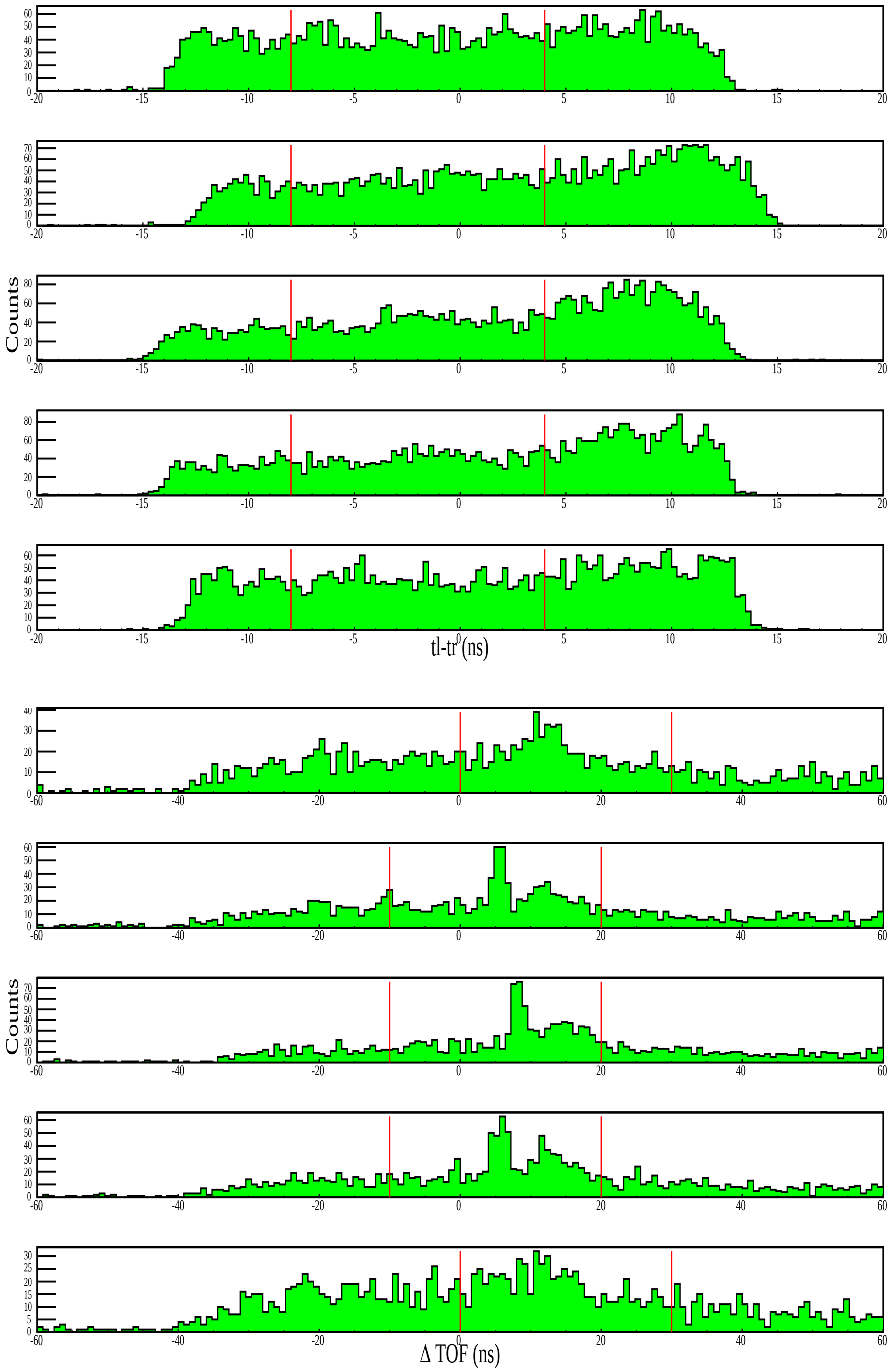

Figure A.43. Figures for 36° at 190 MeV.

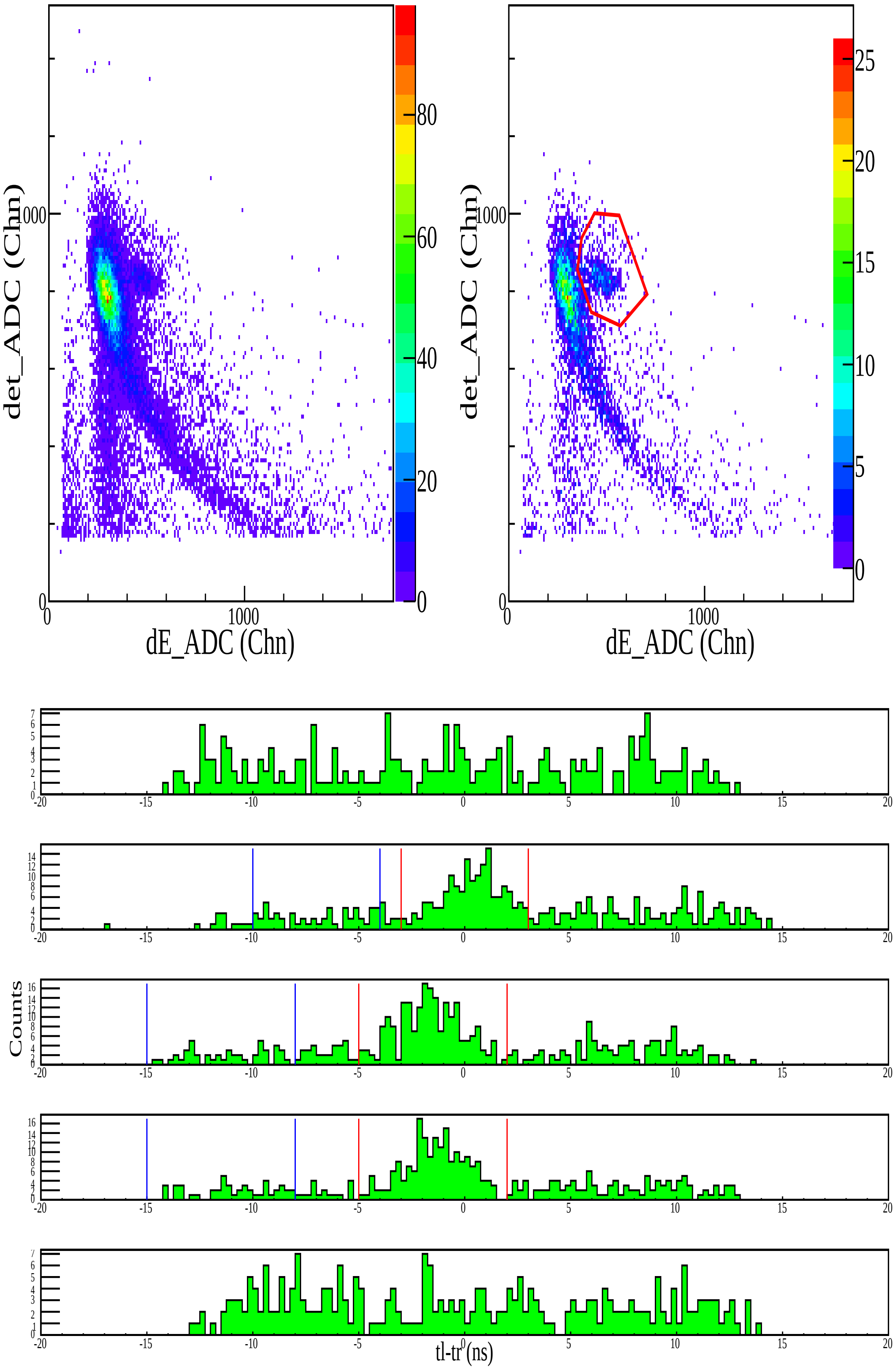

Figure A.44. Figures for 36° at 190 MeV (continued).

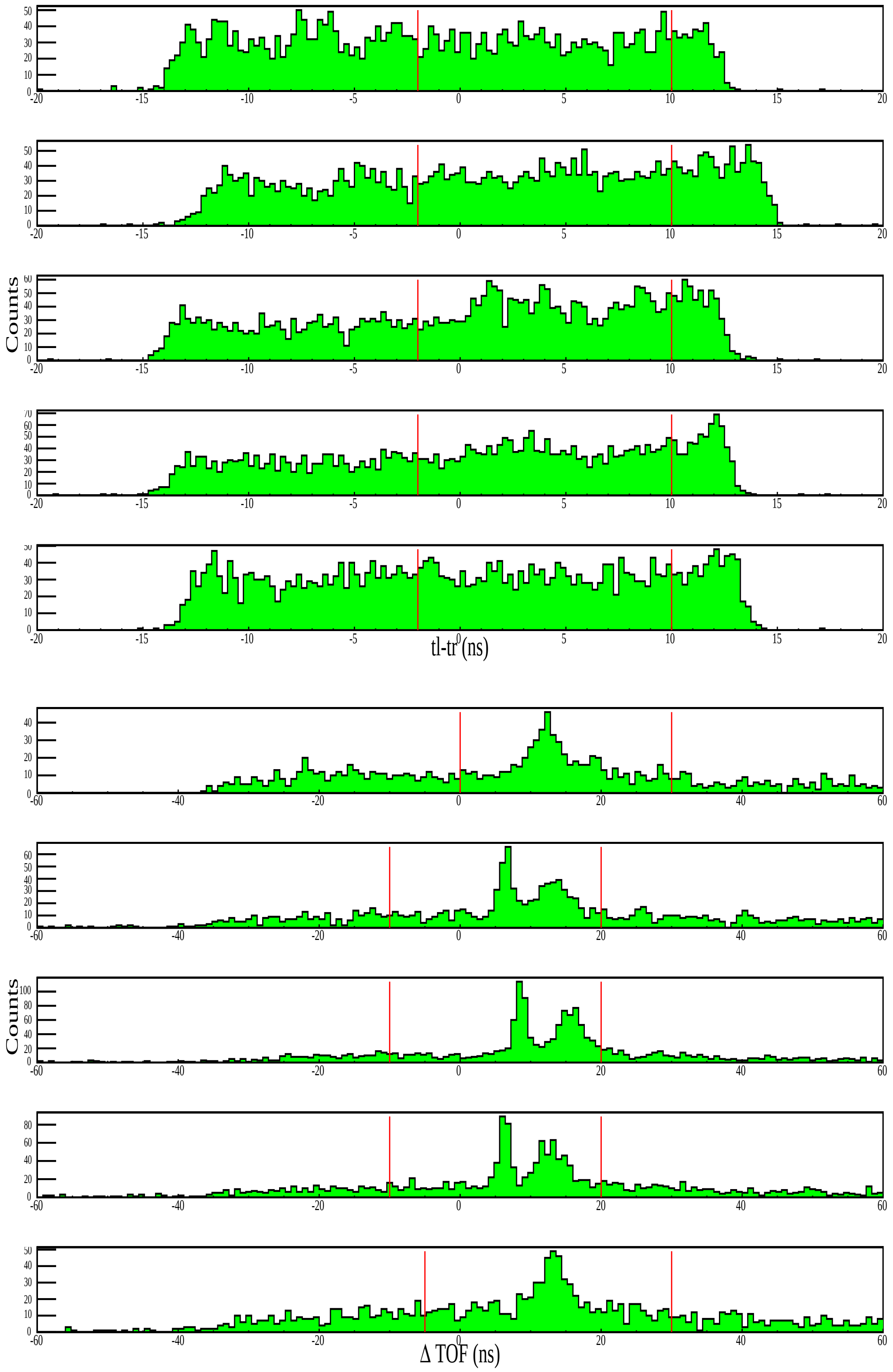

Figure A.45. Figures for 42° at 190 MeV.

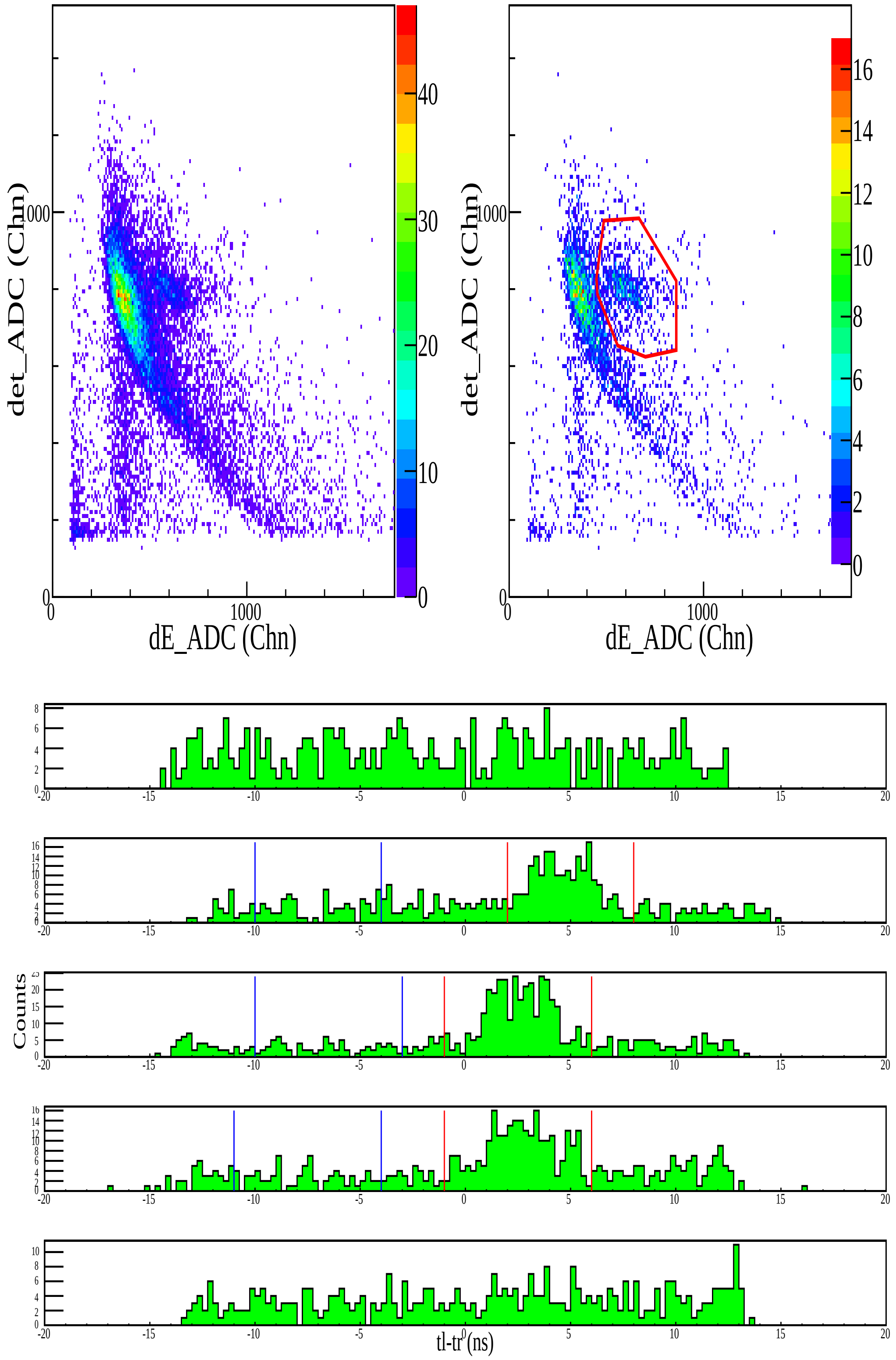

Figure A.46. Figures for 42° at 190 MeV (continued).

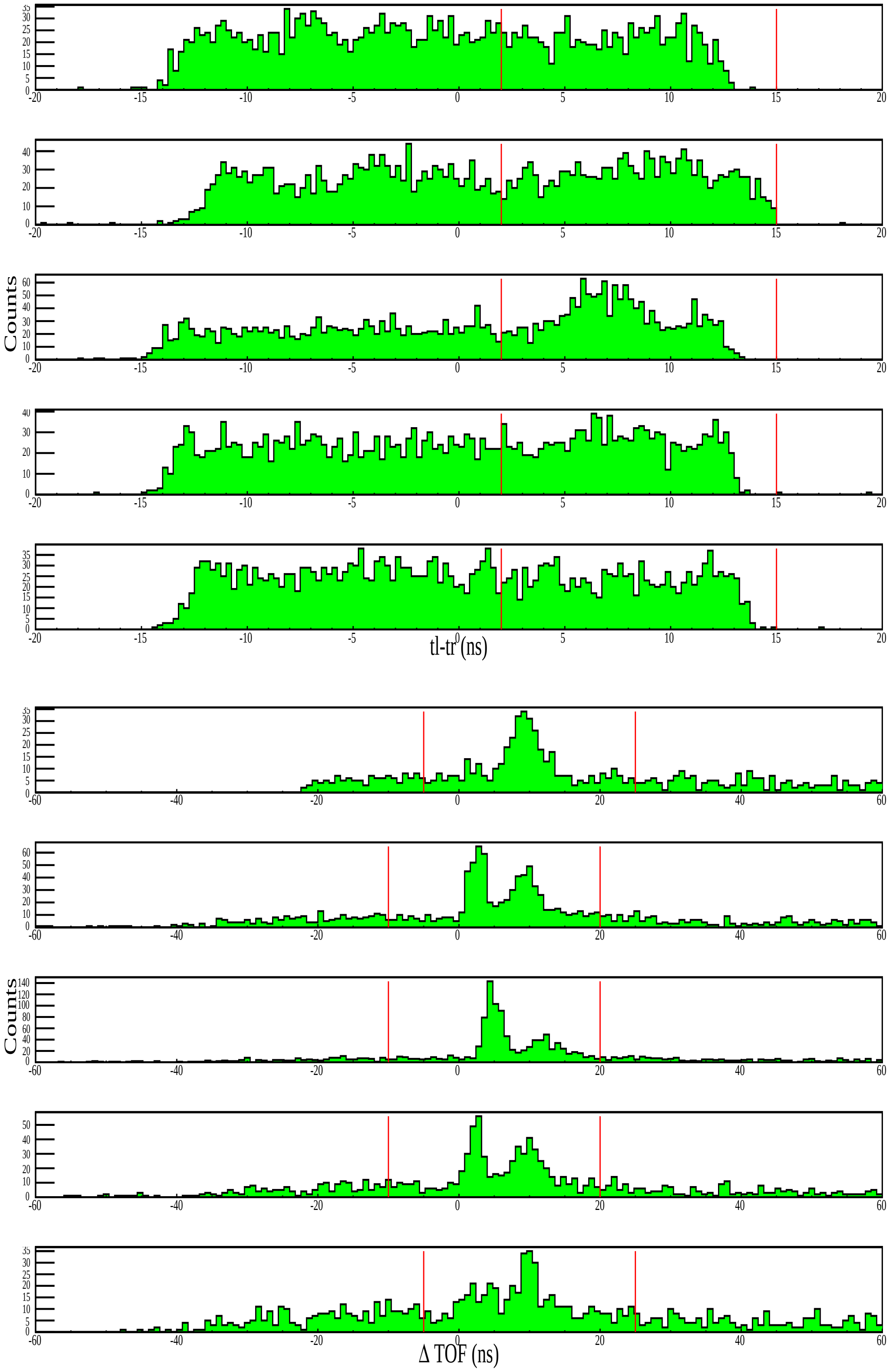

Figure A.47. Figures for 48° at 190 MeV.

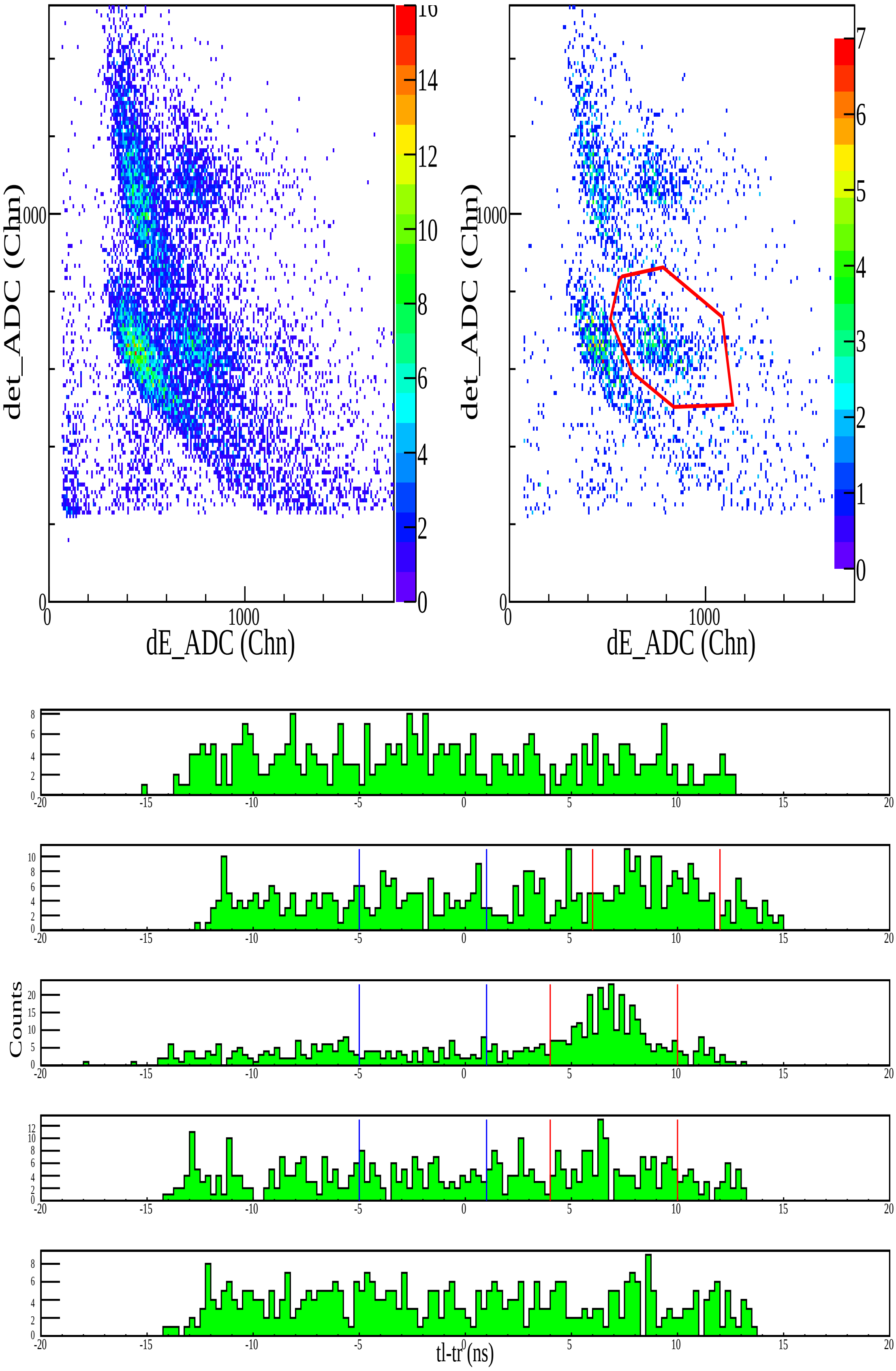

Figure A.48. Figures for 48° at 190 MeV (continued).

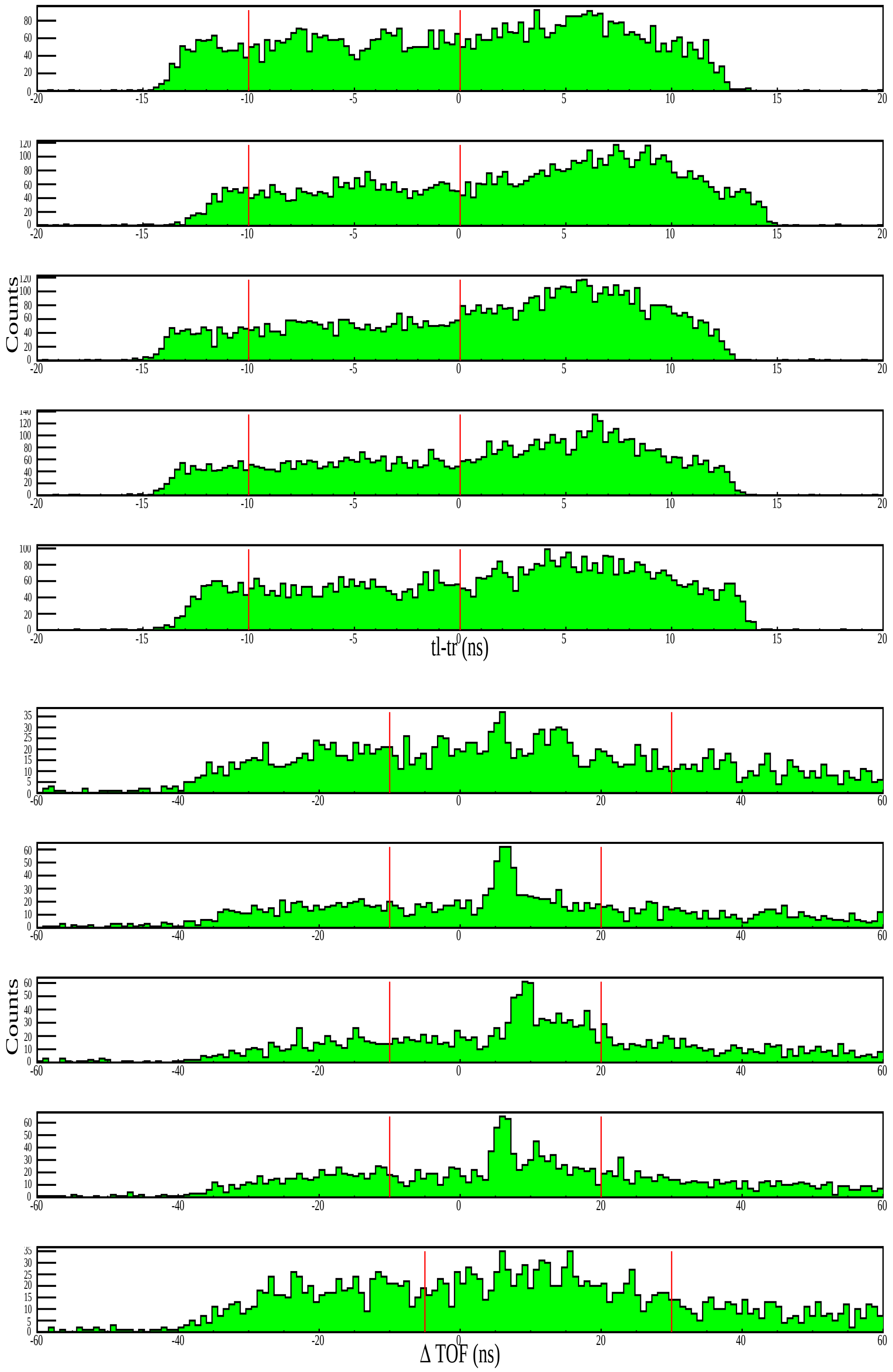

Figure A.49. Figures for 30° at 200 MeV.

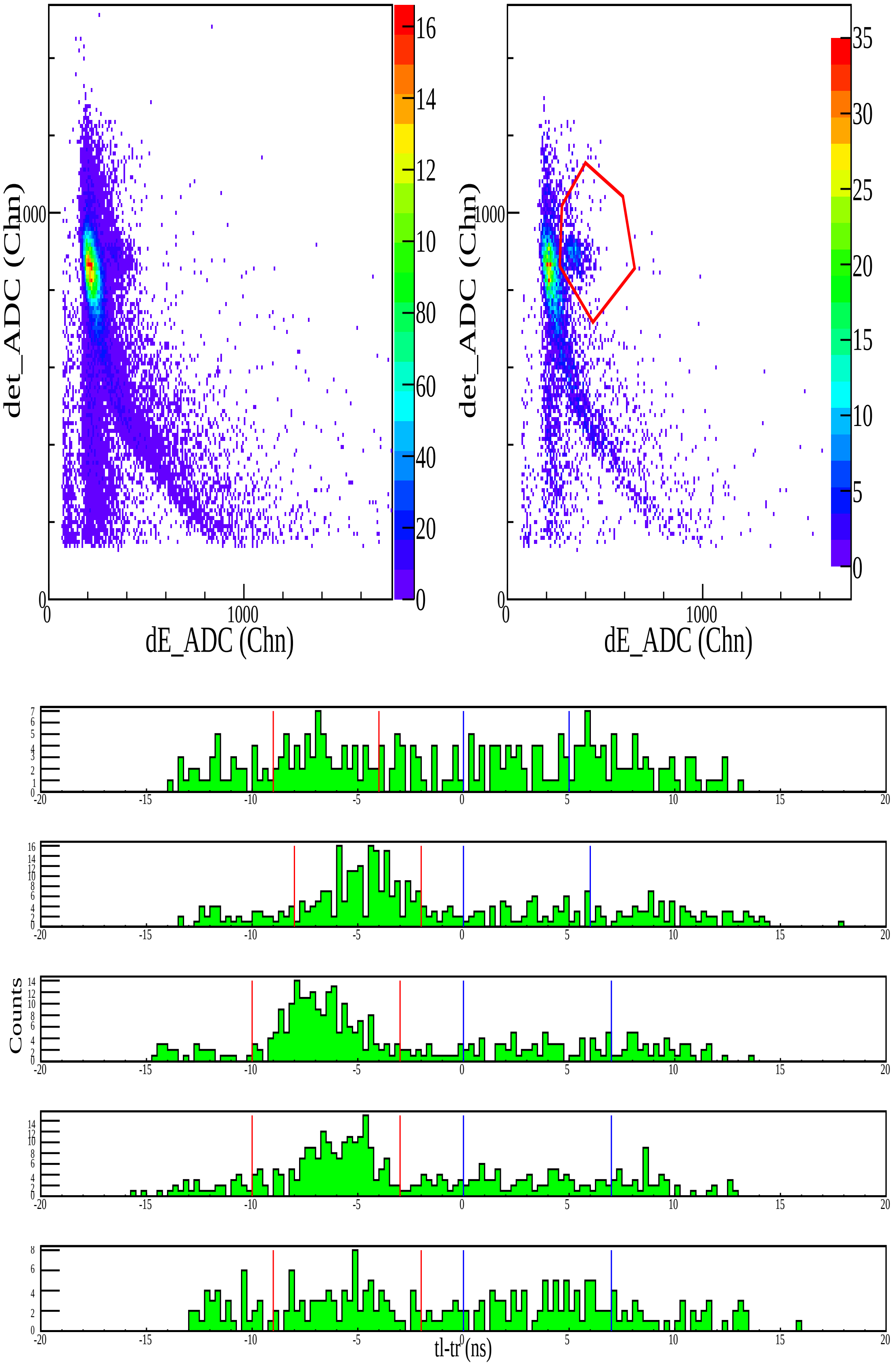

Figure A.50. Figures for 30° at 200 MeV (continued).

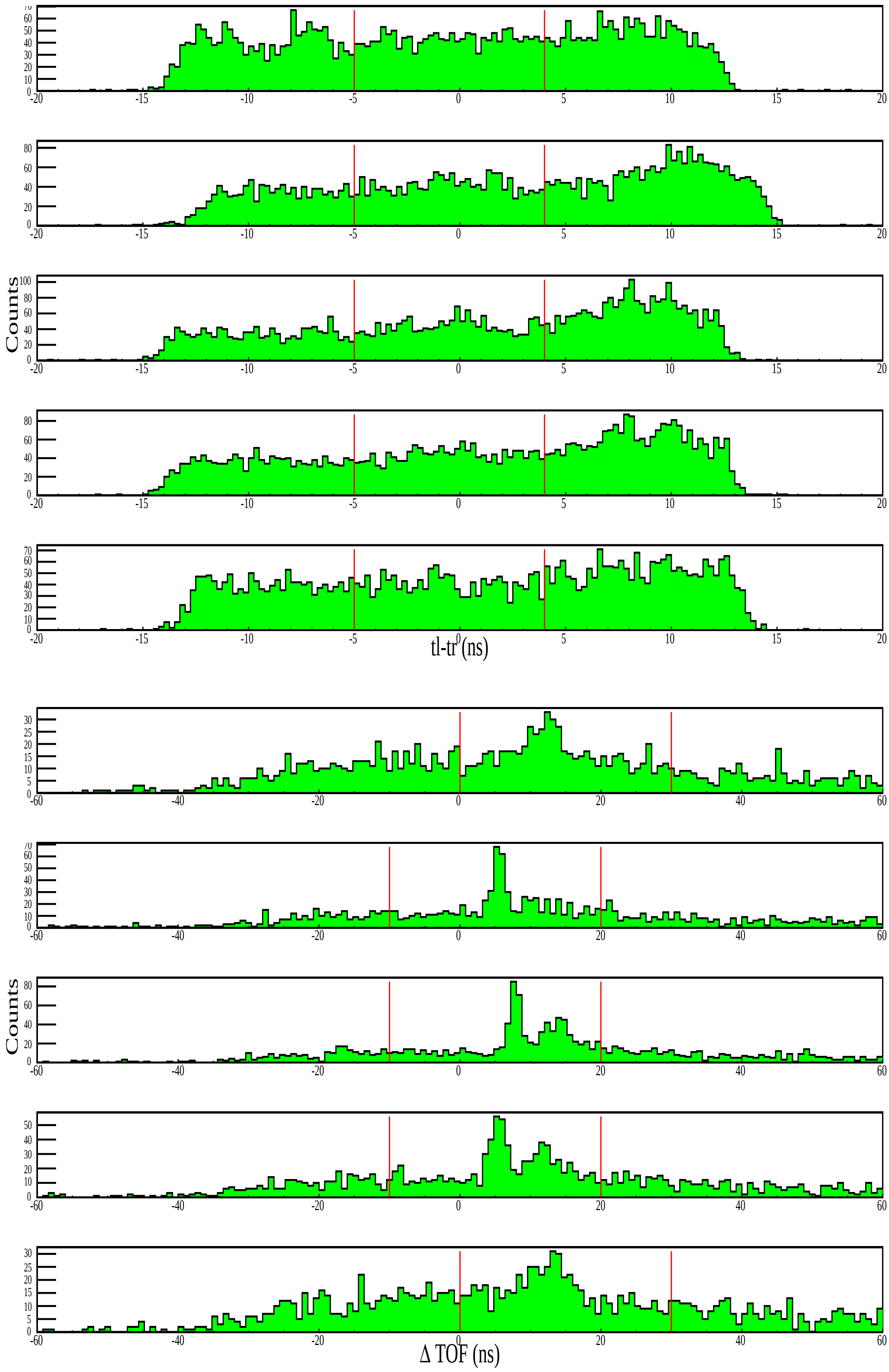

Figure A.51. Figures for 36° at 200 MeV.

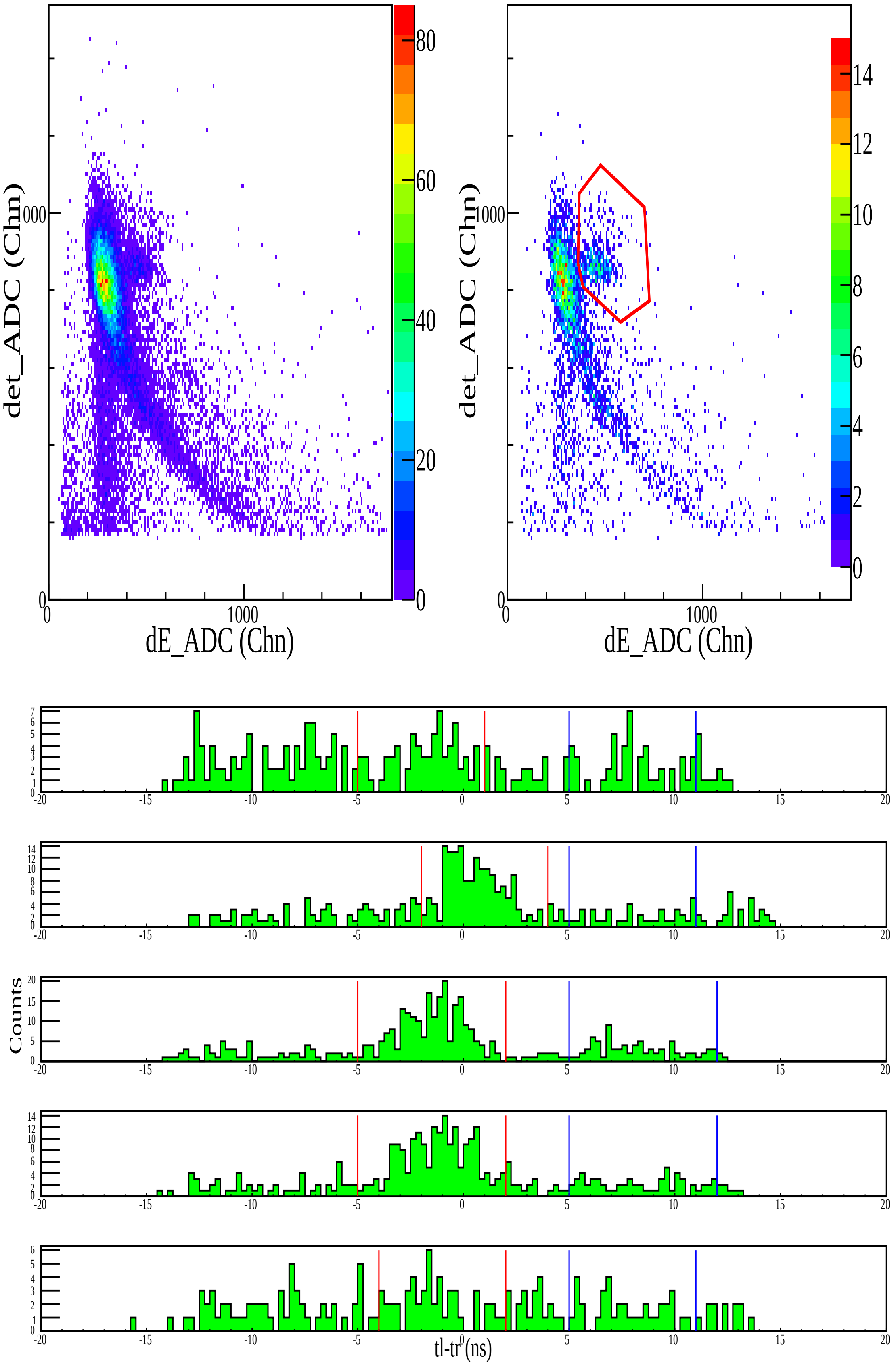

Figure A.52. Figures for 36° at 200 MeV (continued).

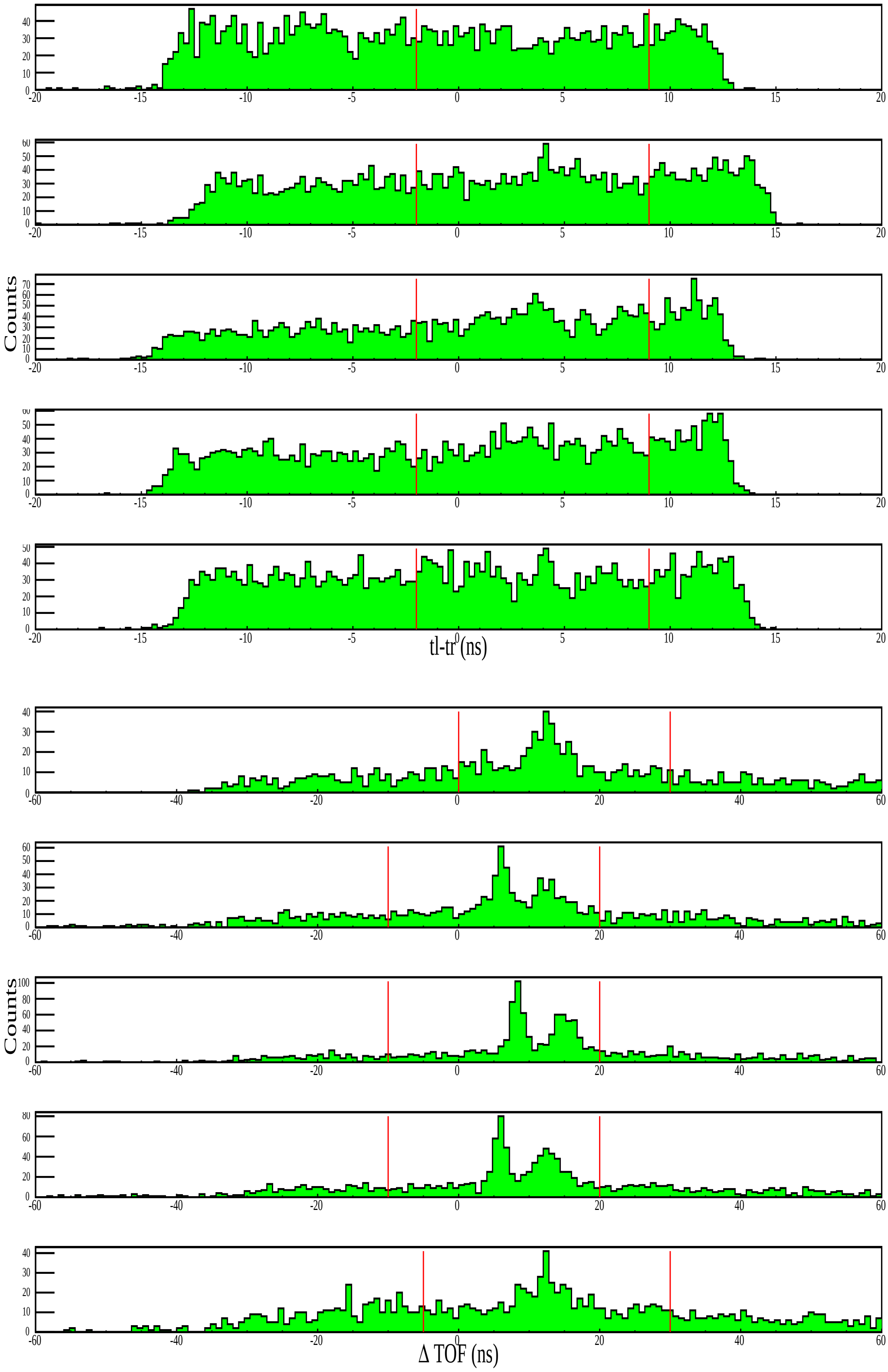

Figure A.53. Figures for 42° at 200 MeV.

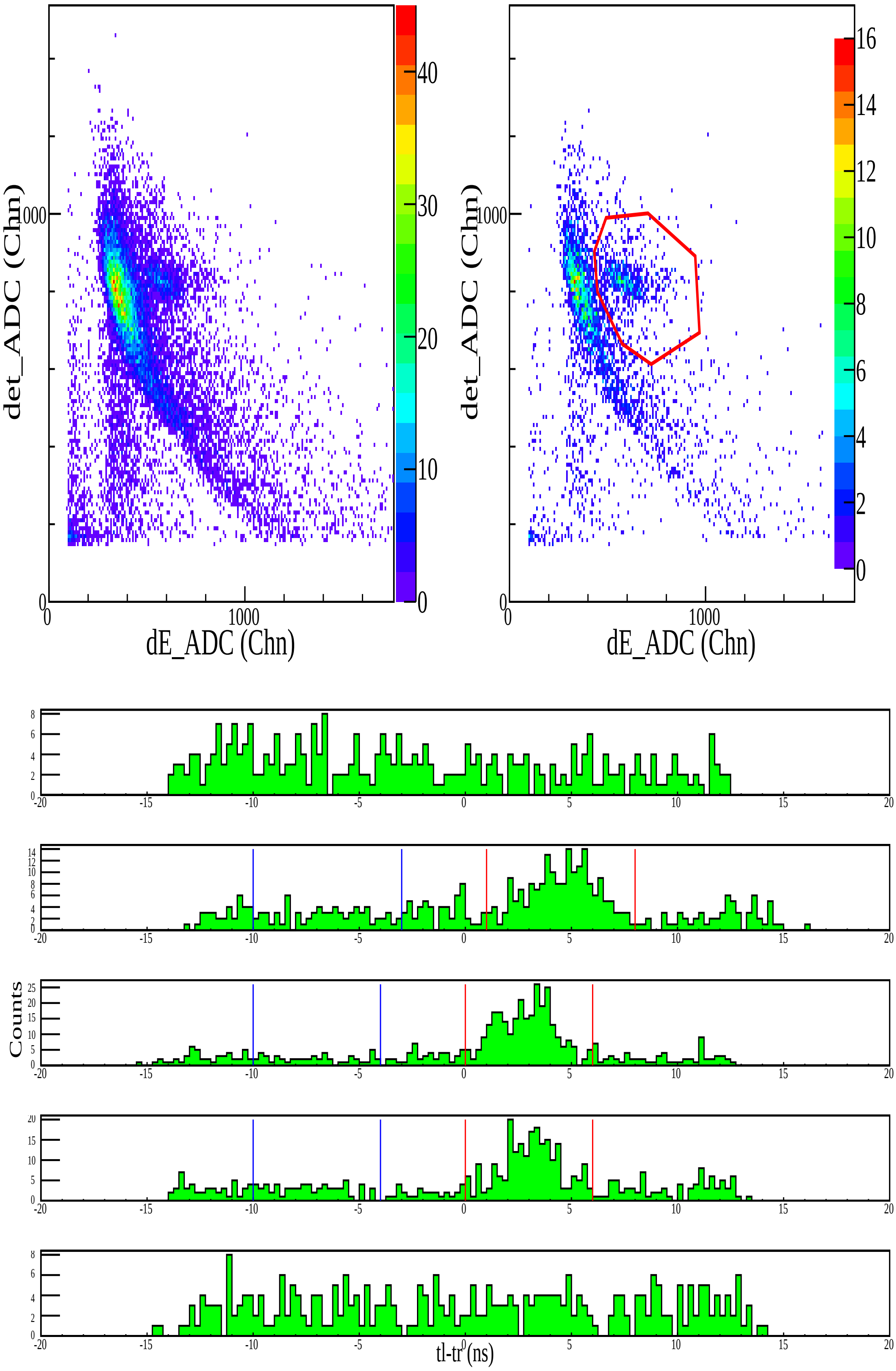

Figure A.54. Figures for 42° at 200 MeV (continued).

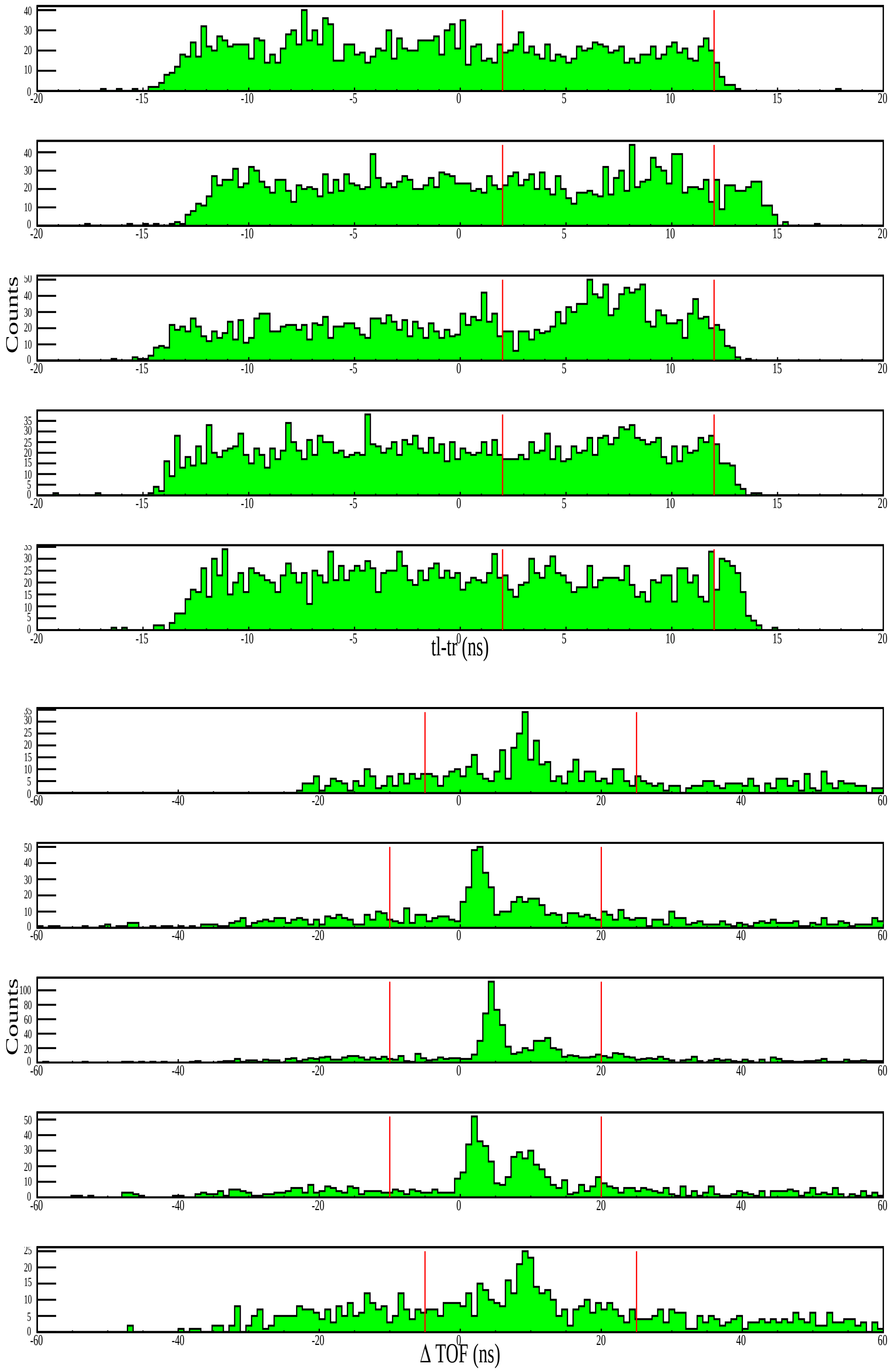

Figure A.55. Figures for 48° at 200 MeV.

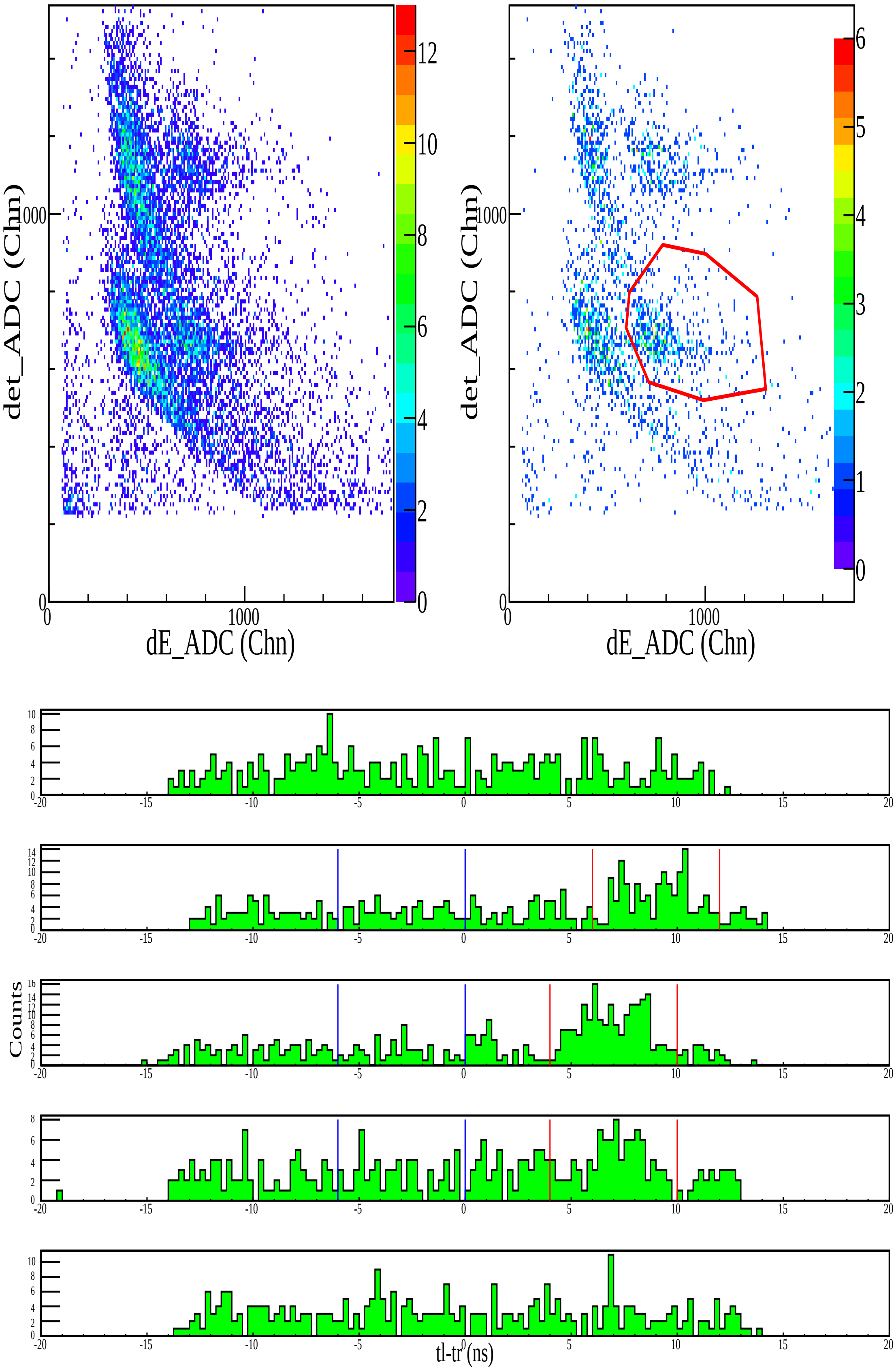

Figure A.56. Figures for 48° at 200 MeV (continued).

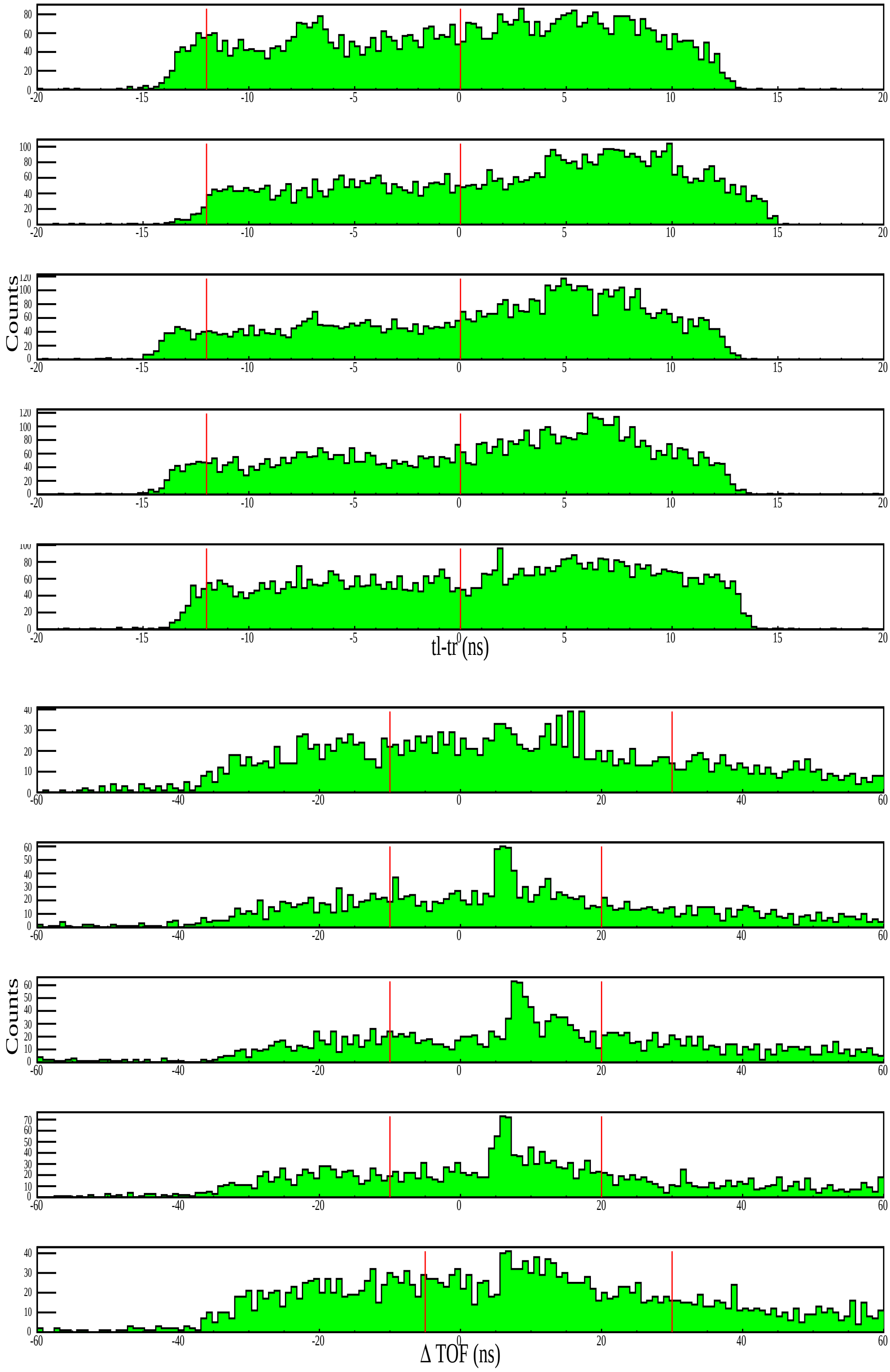

Figure A.57. Figures for 30° at 210 MeV.

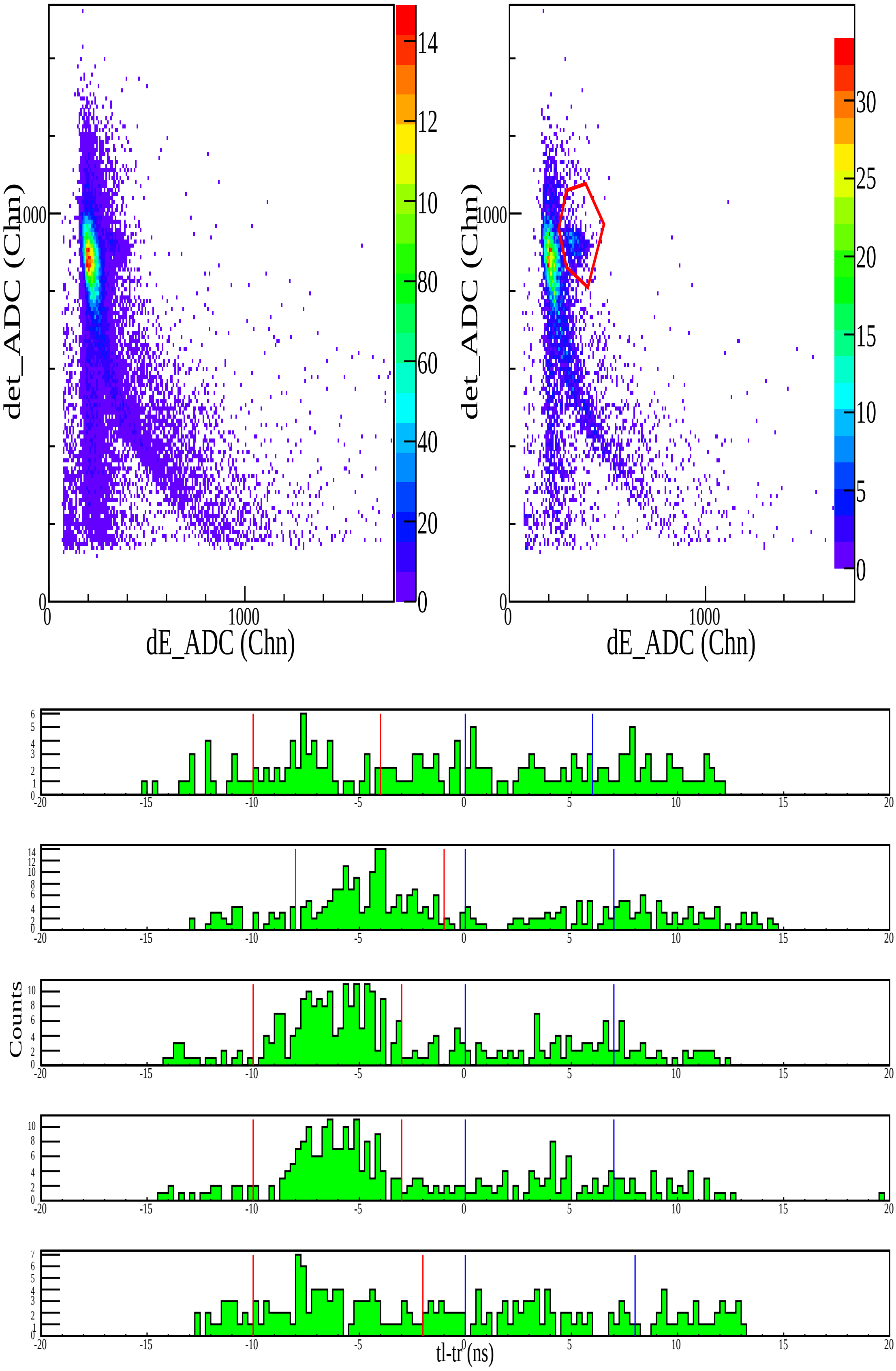

Figure A.58. Figures for 30° at 210 MeV (continued).

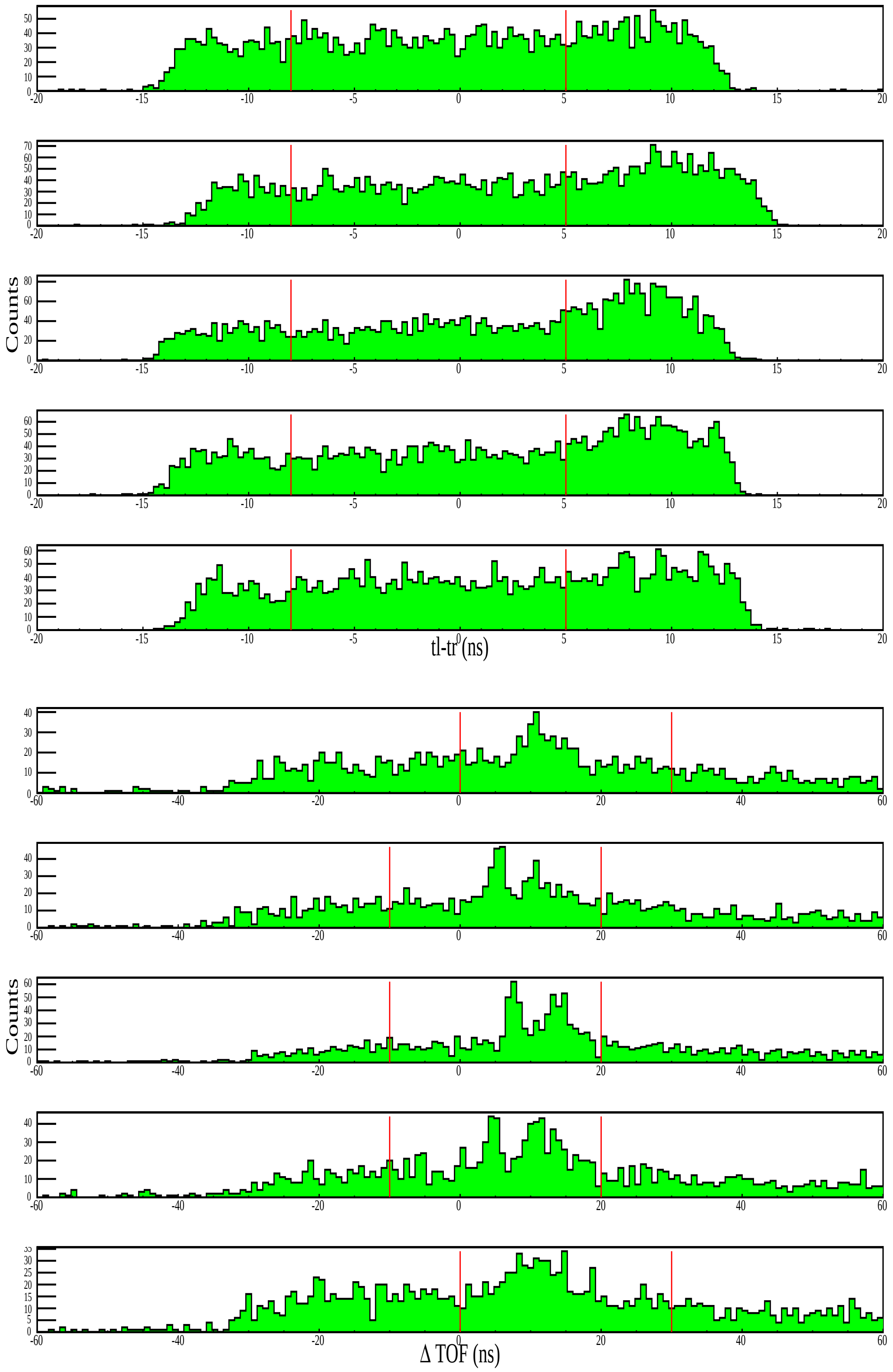

Figure A.59. Figures for 36° at 210 MeV.

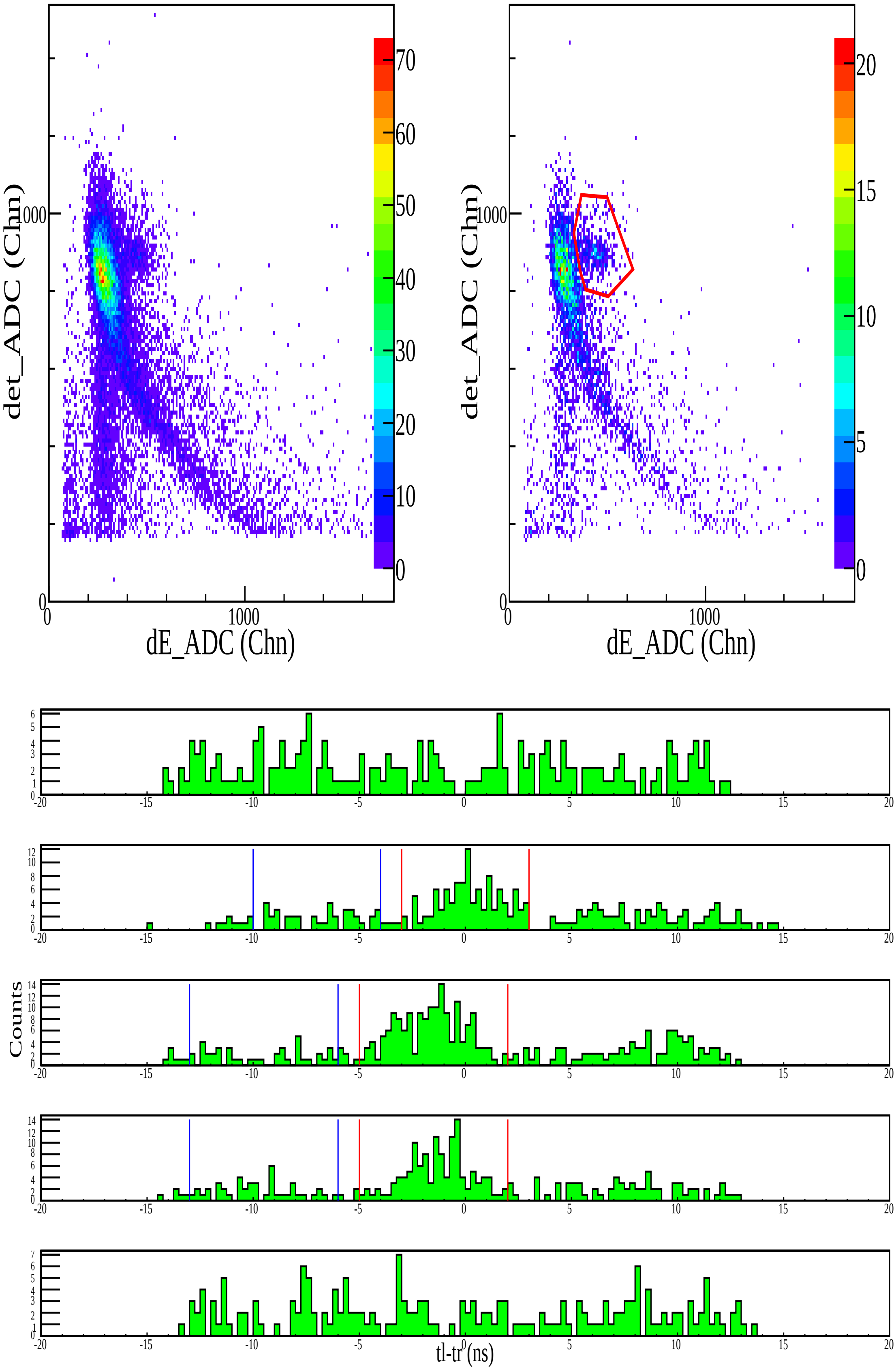

Figure A.60. Figures for 36° at 210 MeV (continued).

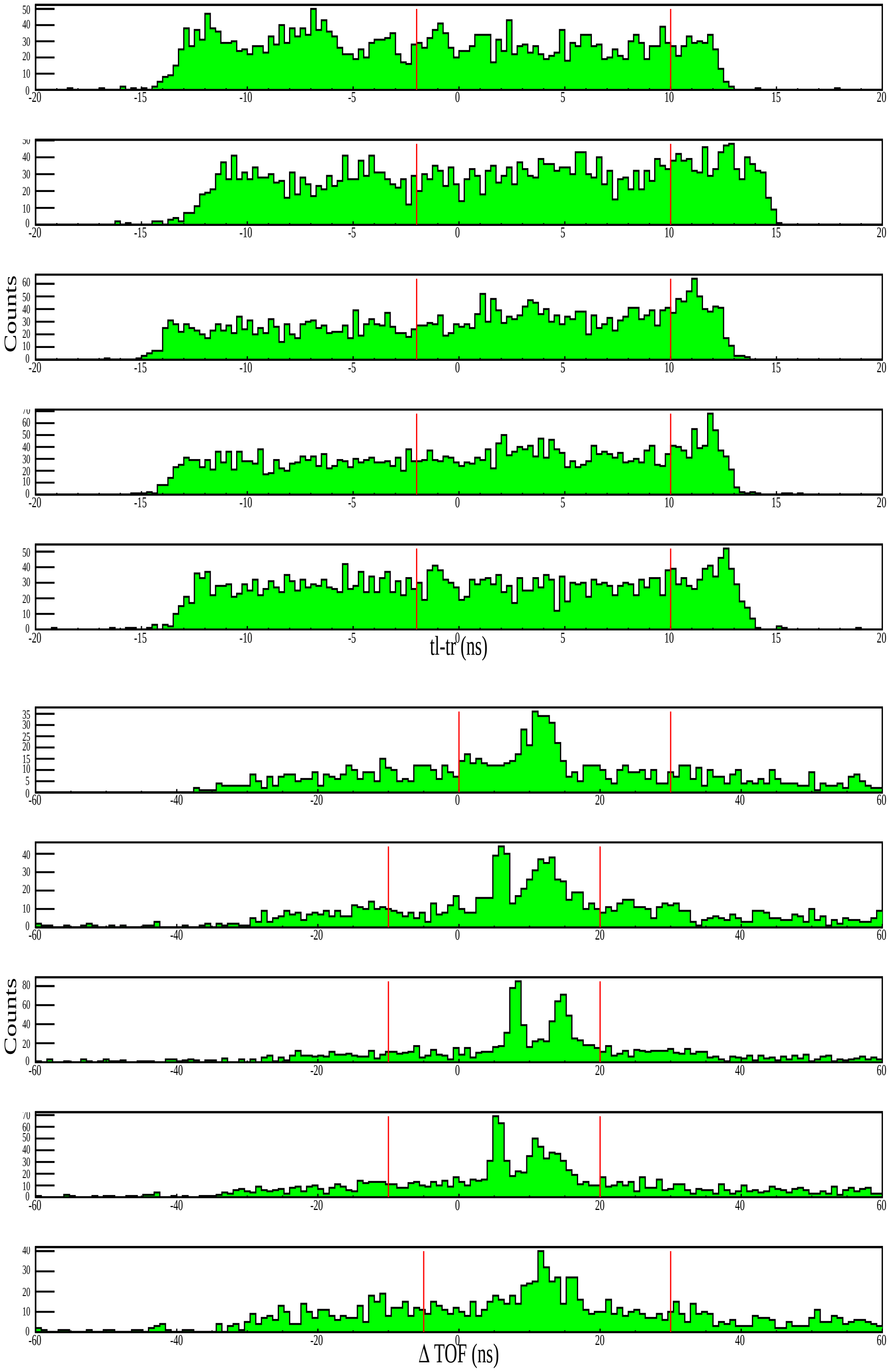

Figure A.61. Figures for 42° at 210 MeV.

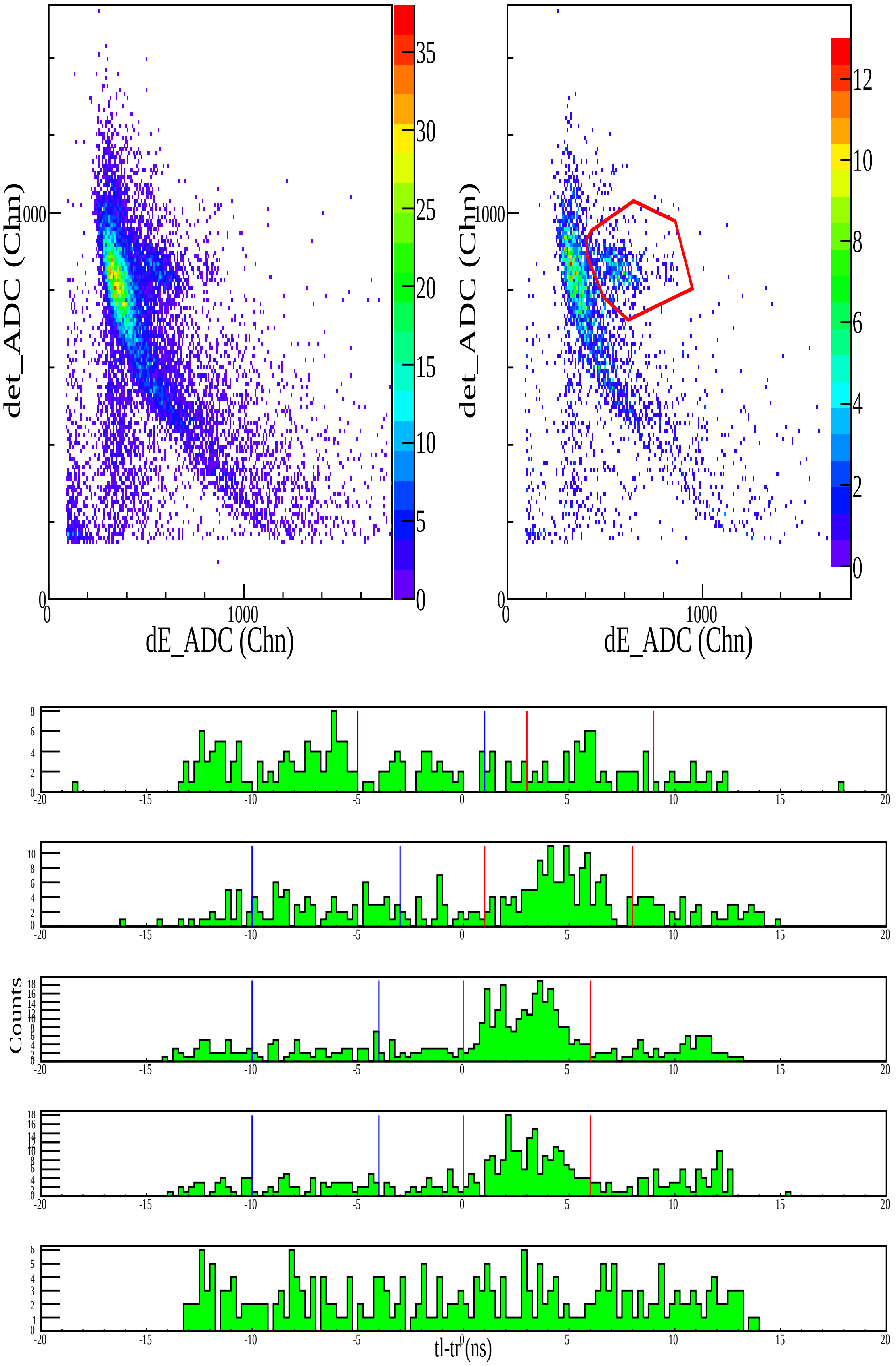

Figure A.62. Figures for 42° at 210 MeV (continued).

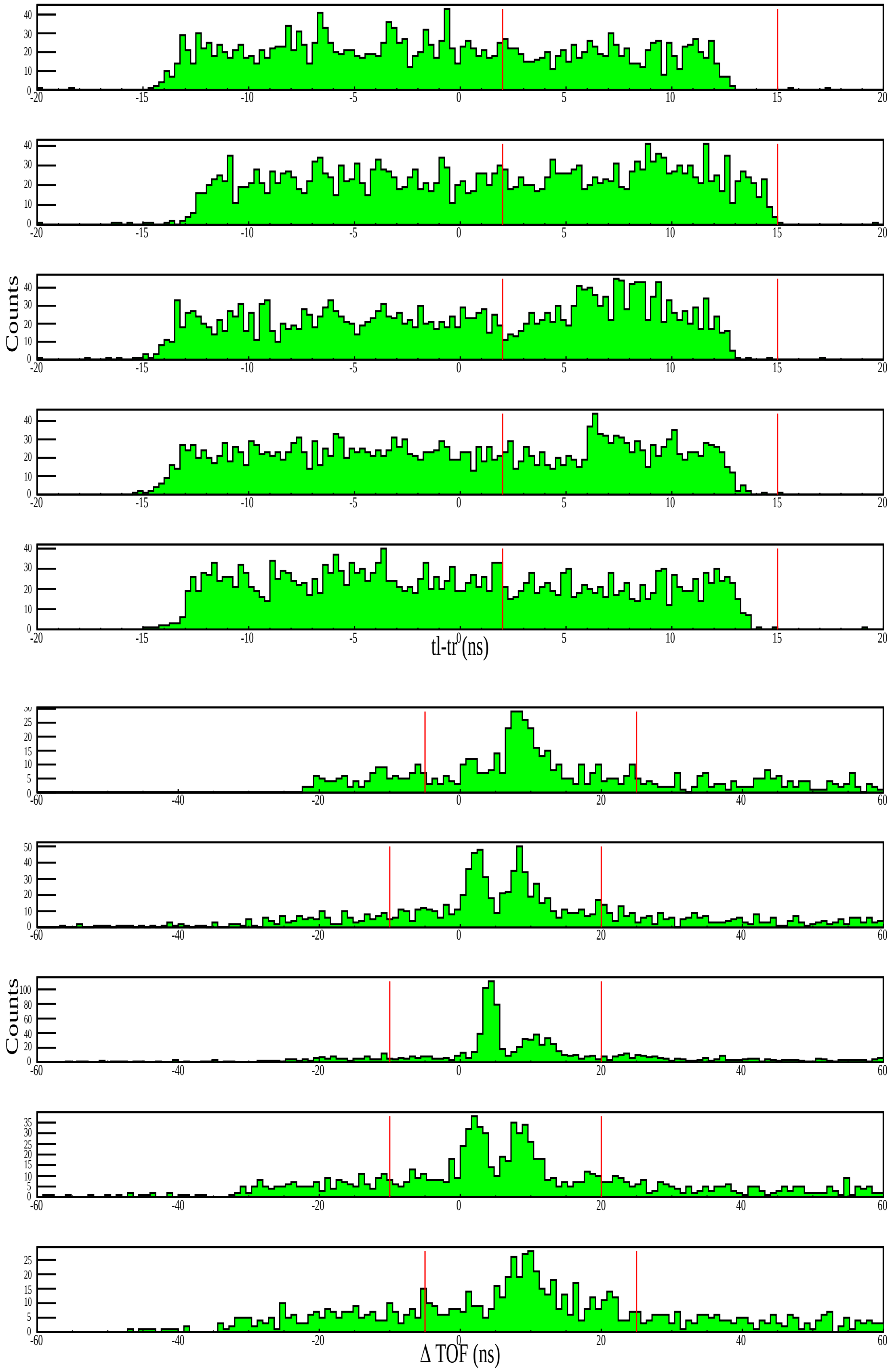

Figure A.63. Figures for 48° at 210 MeV.

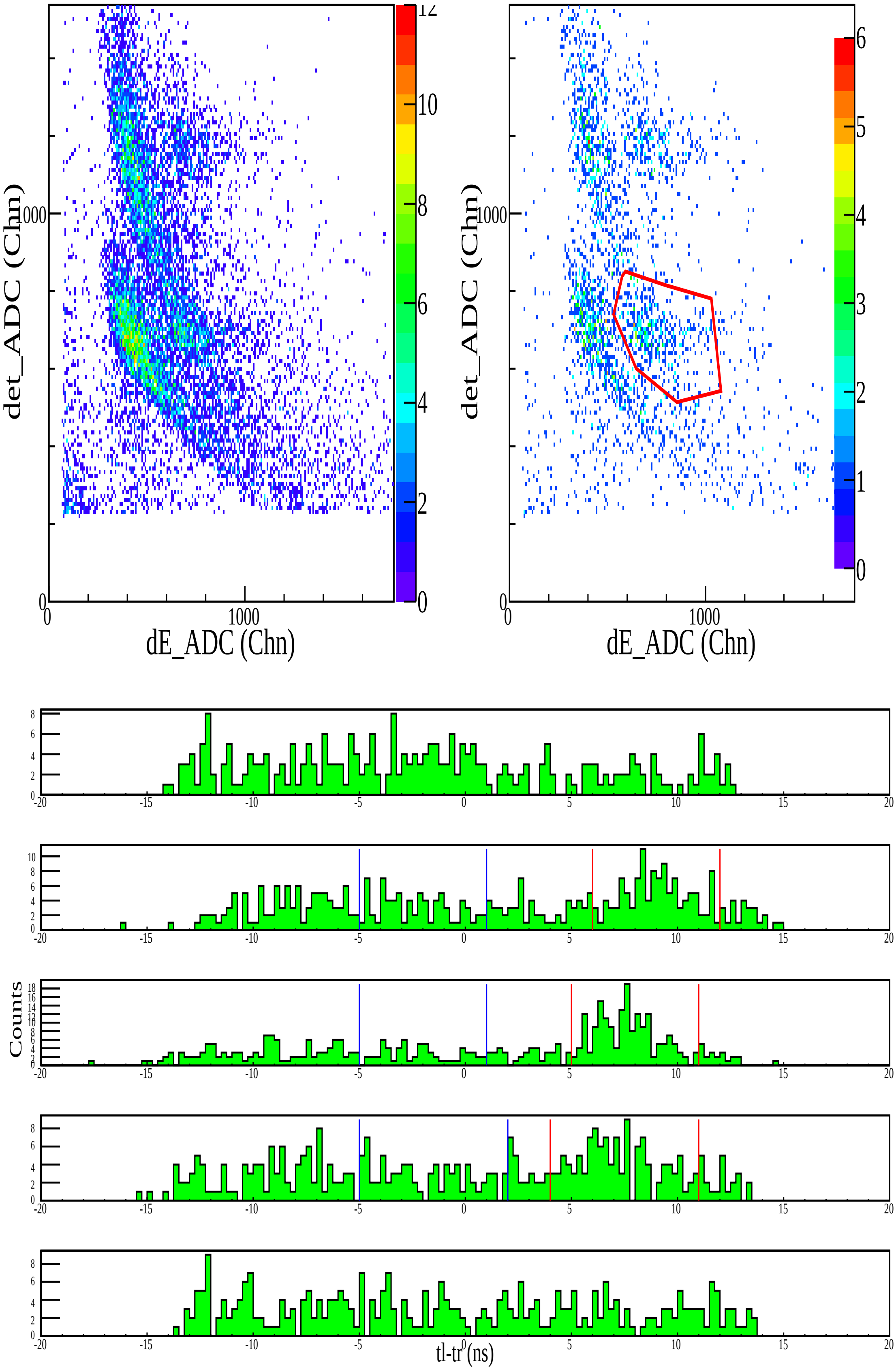

Figure A.64. Figures for 48° at 210 MeV (continued).

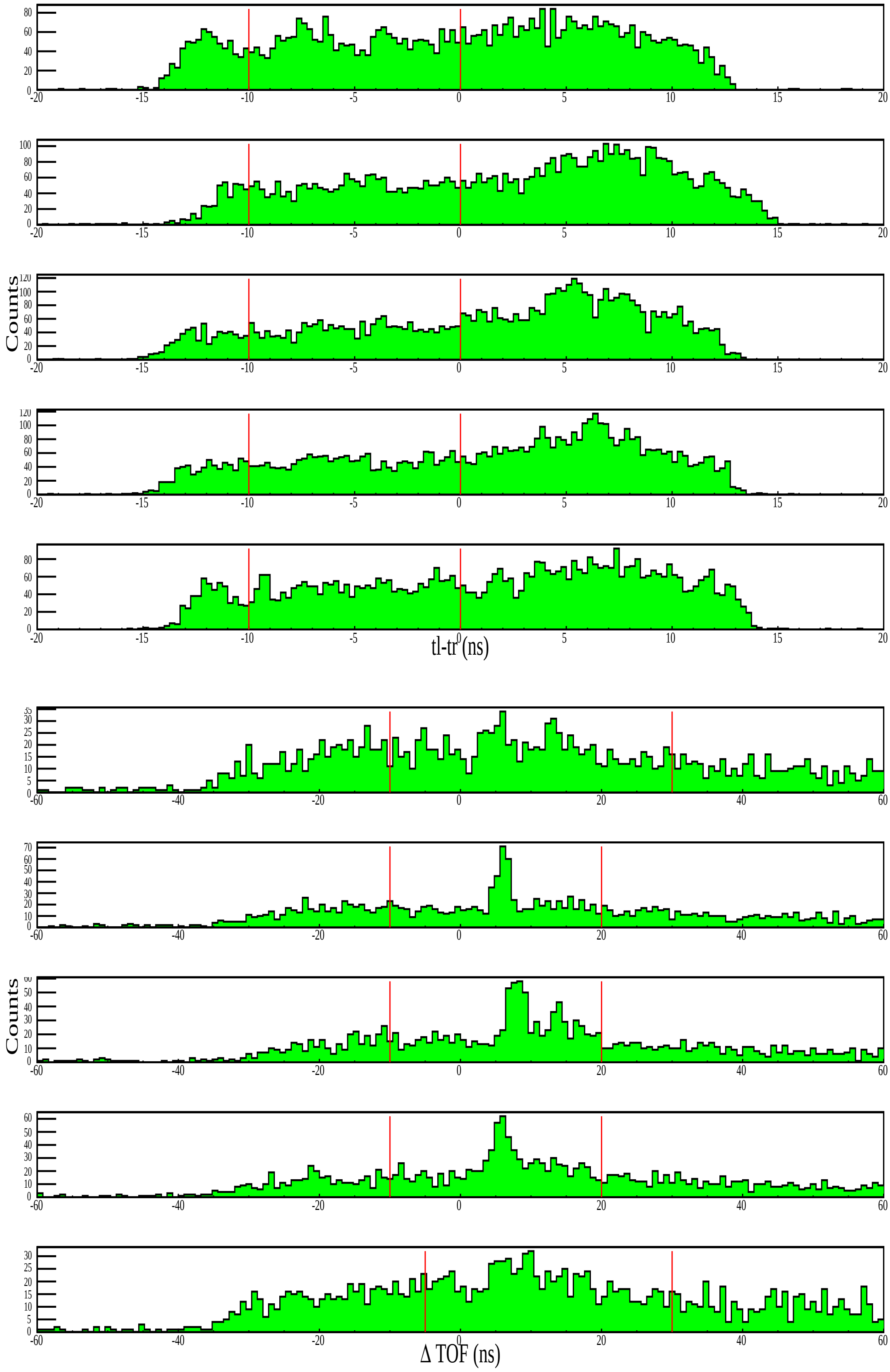

Figure A.65. Figures for 30° at 220 MeV.

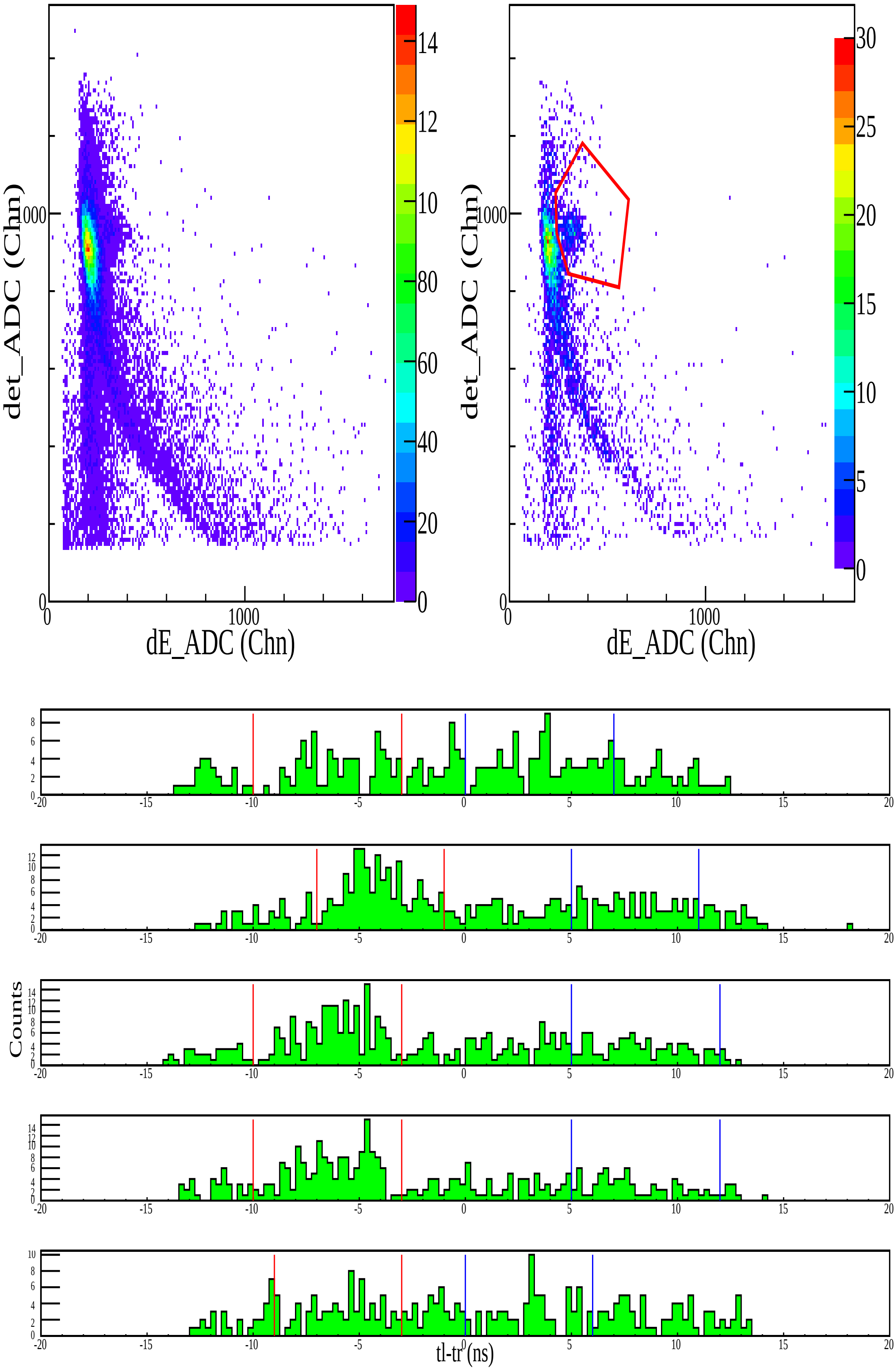

Figure A.66. Figures for 30° at 220 MeV (continued).

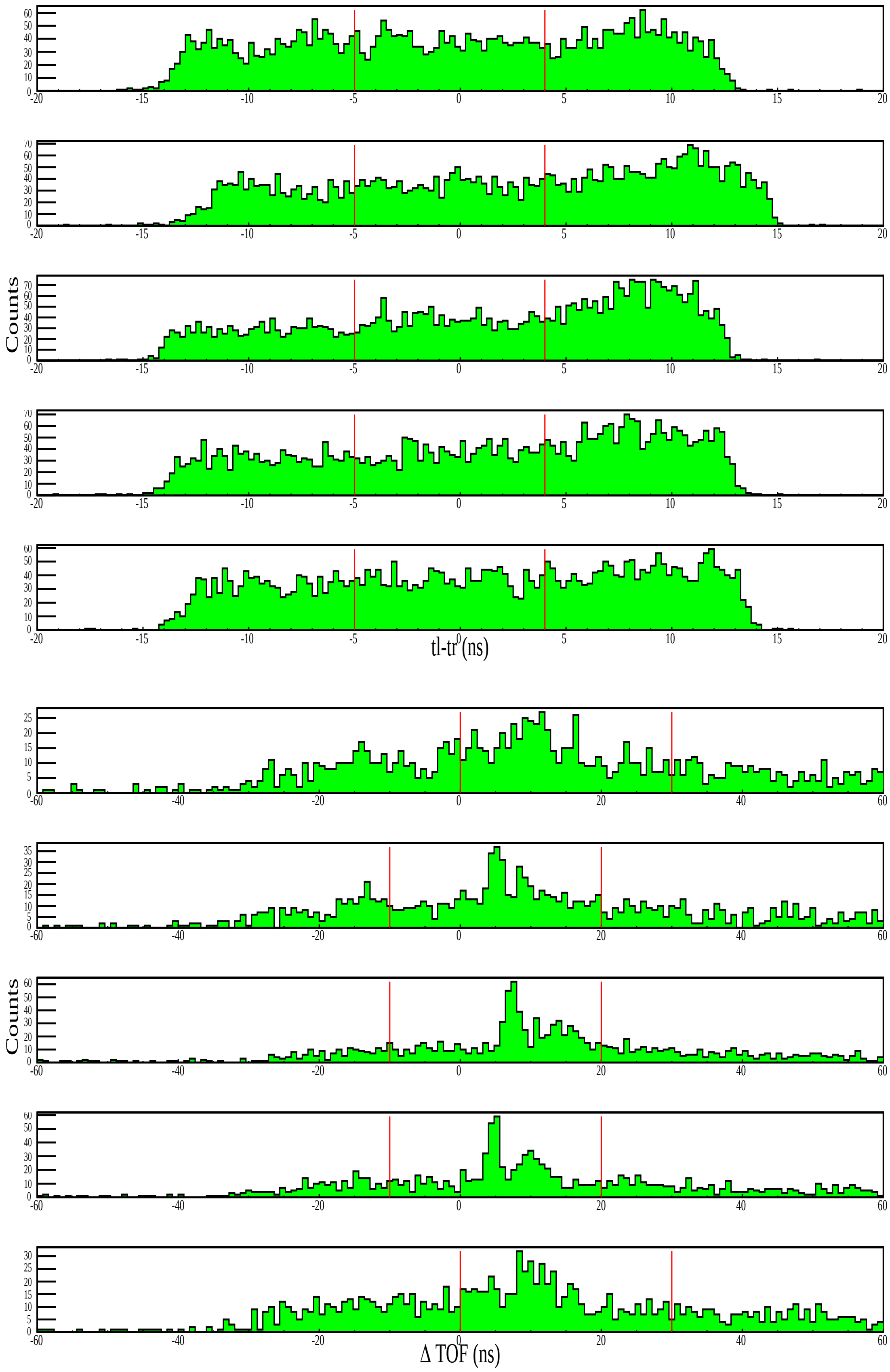

Figure A.67. Figures for 36° at 220 MeV.

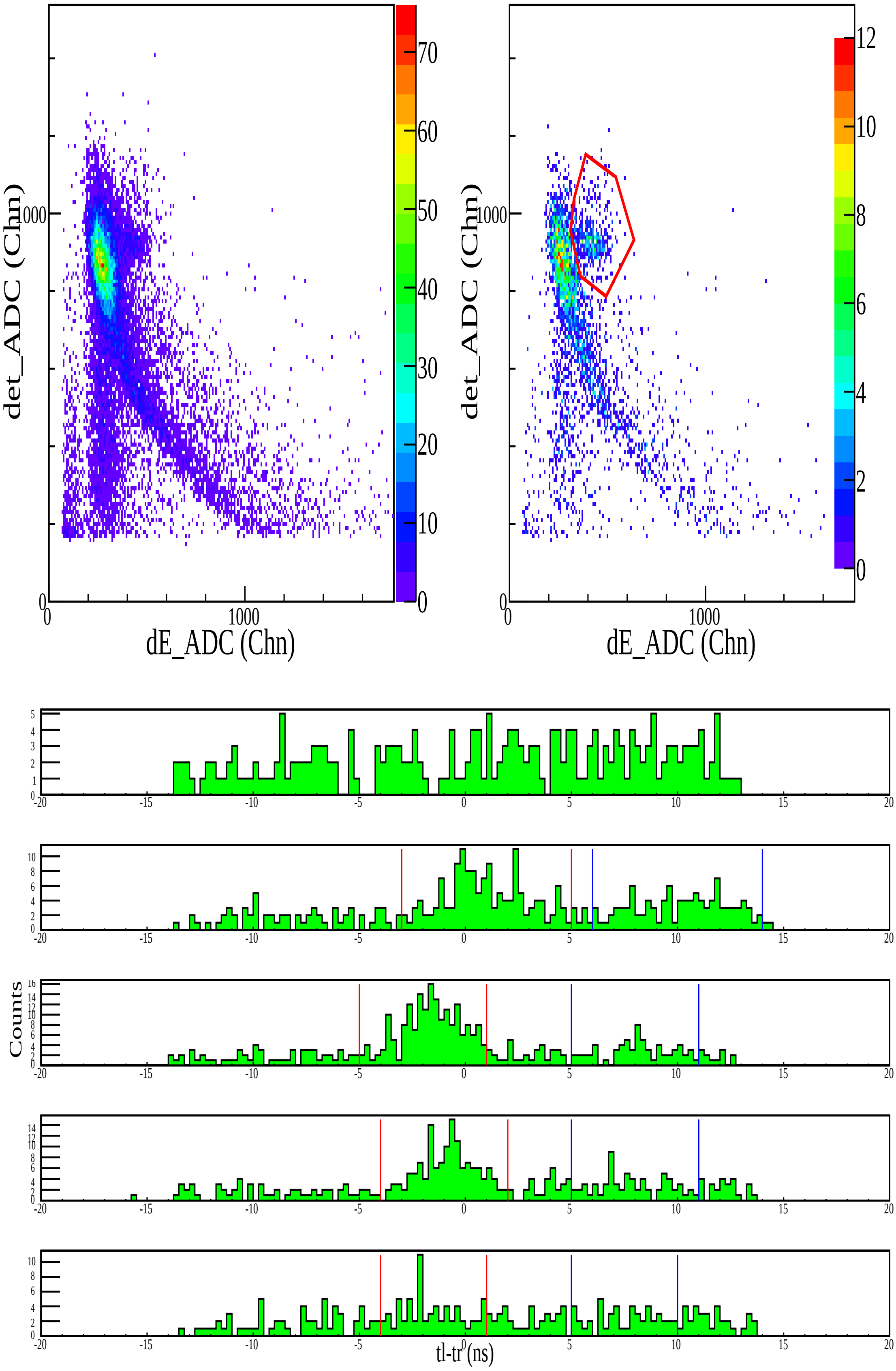

Figure A.68. Figures for 36° at 220 MeV (continued).

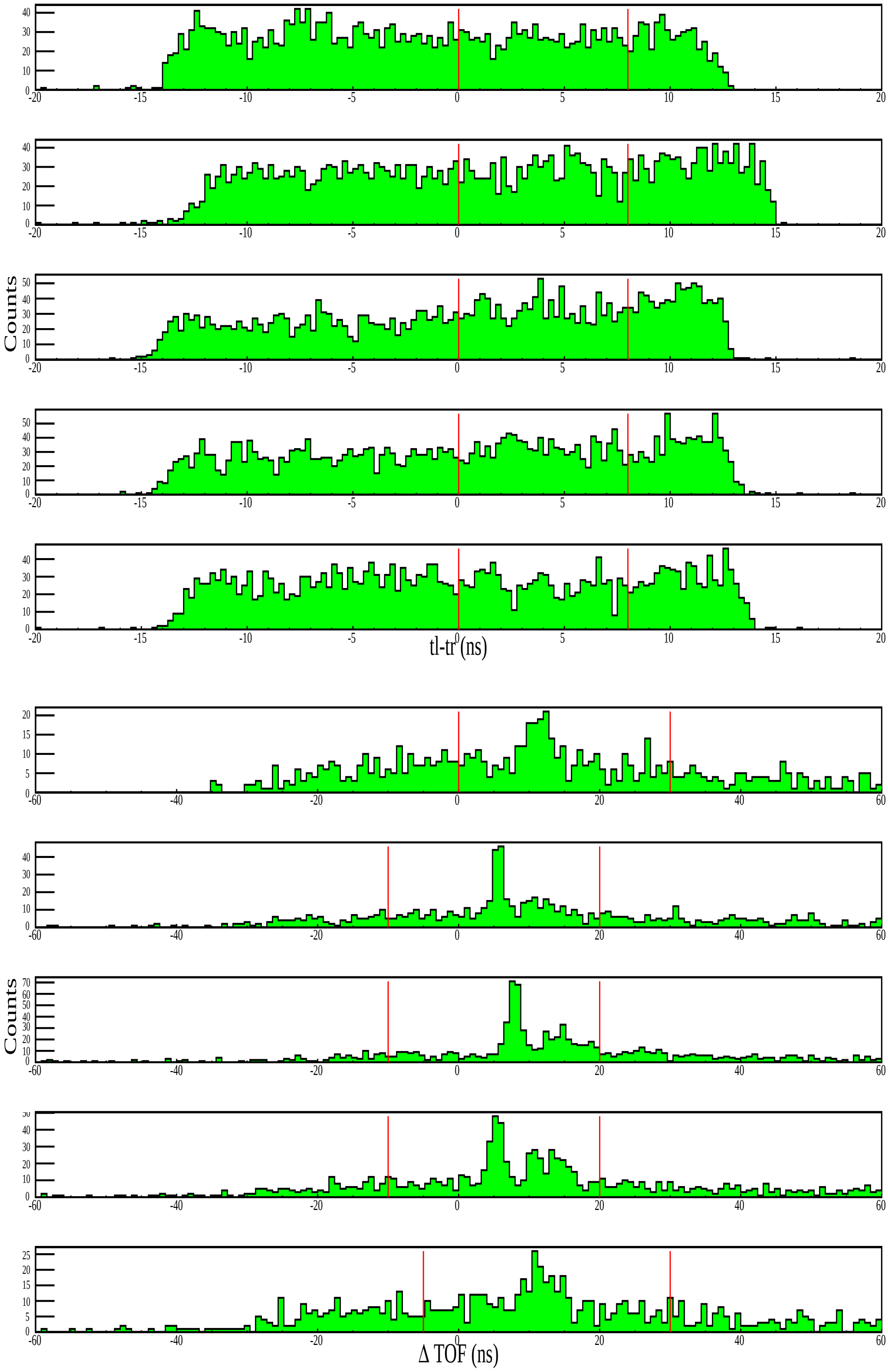

Figure A.69. Figures for 42° at 220 MeV.

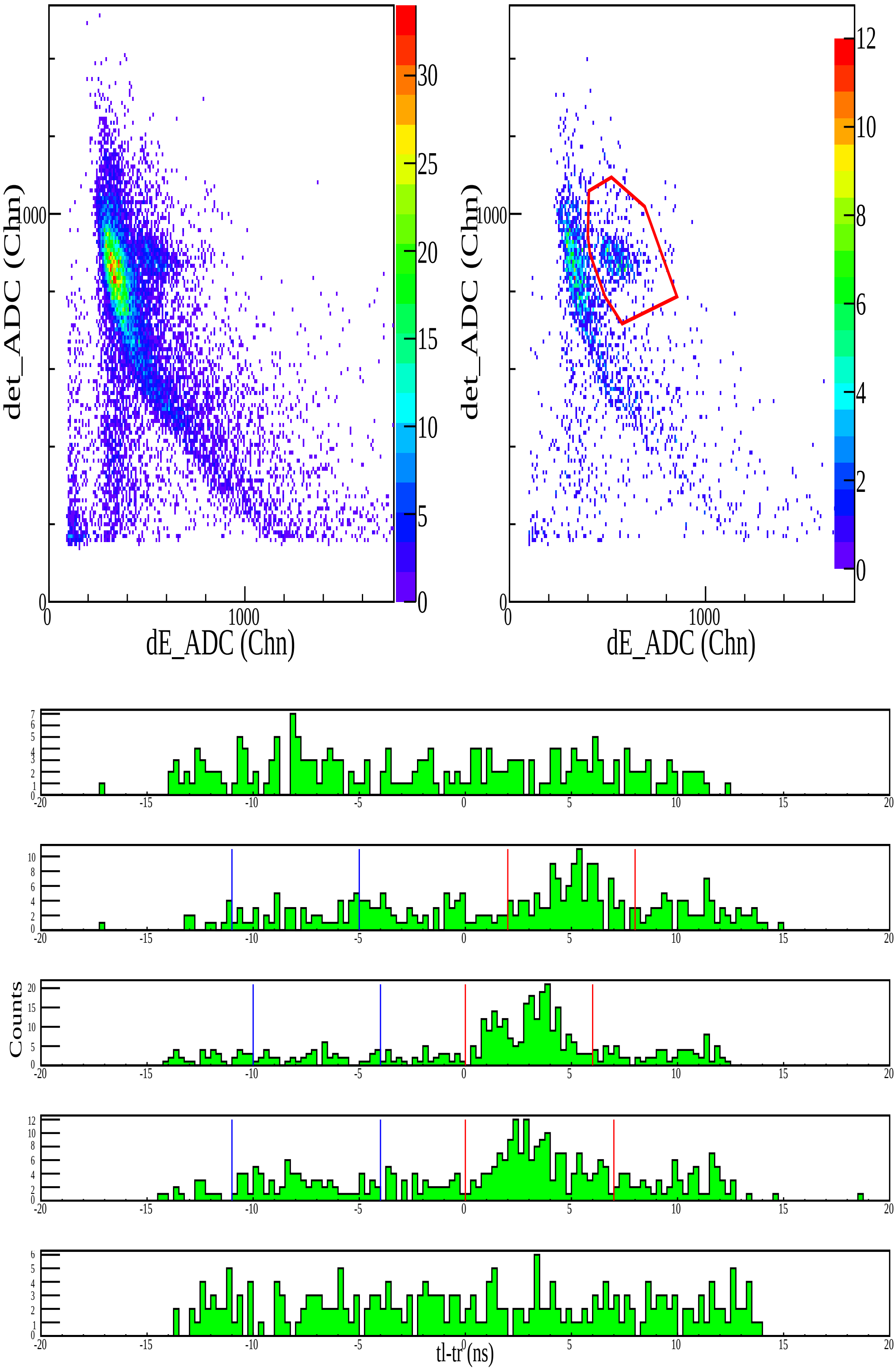

Figure A.70. Figures for 42° at 220 MeV (continued).

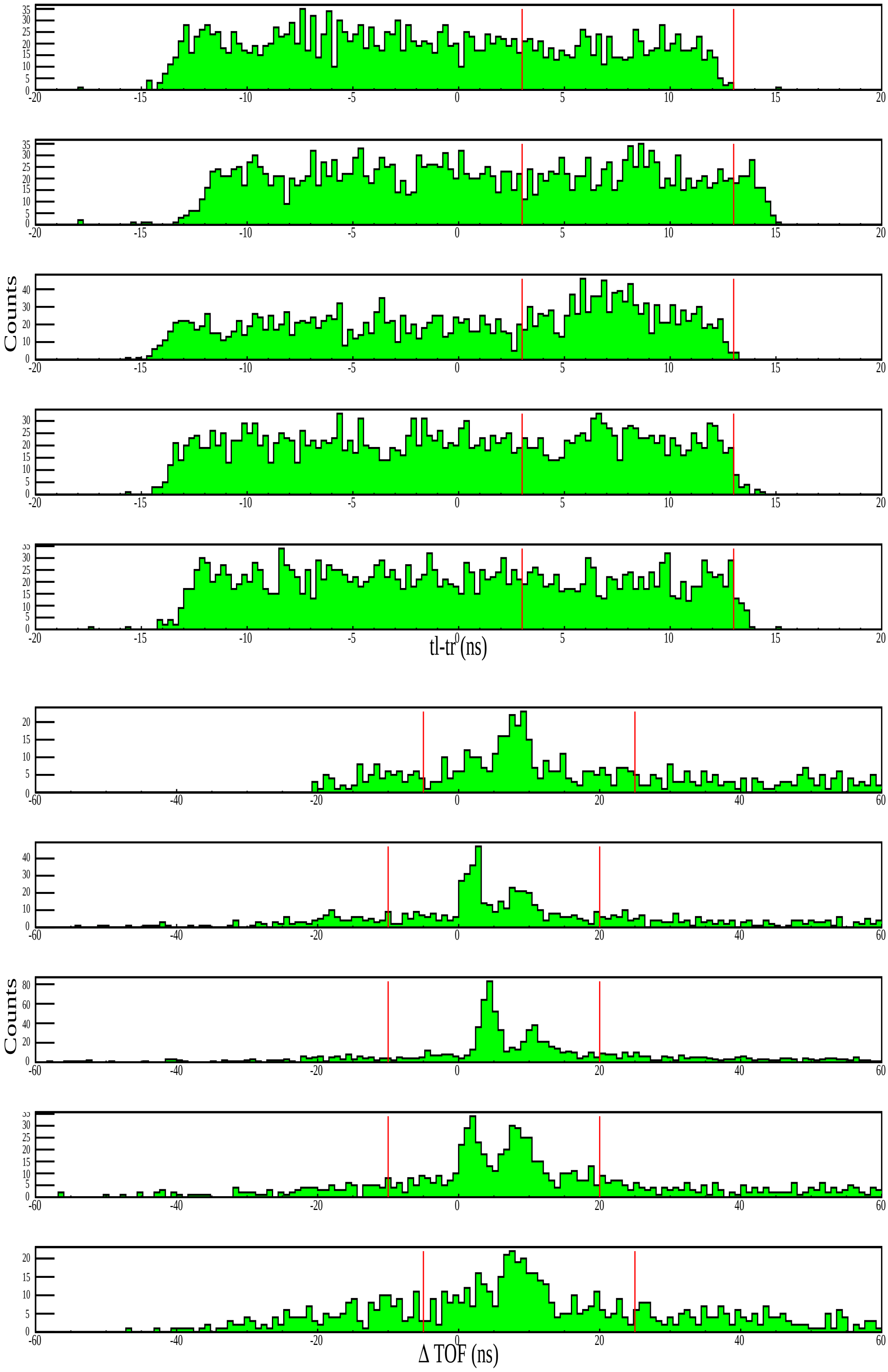

Figure A.71. Figures for 48° at 220 MeV.

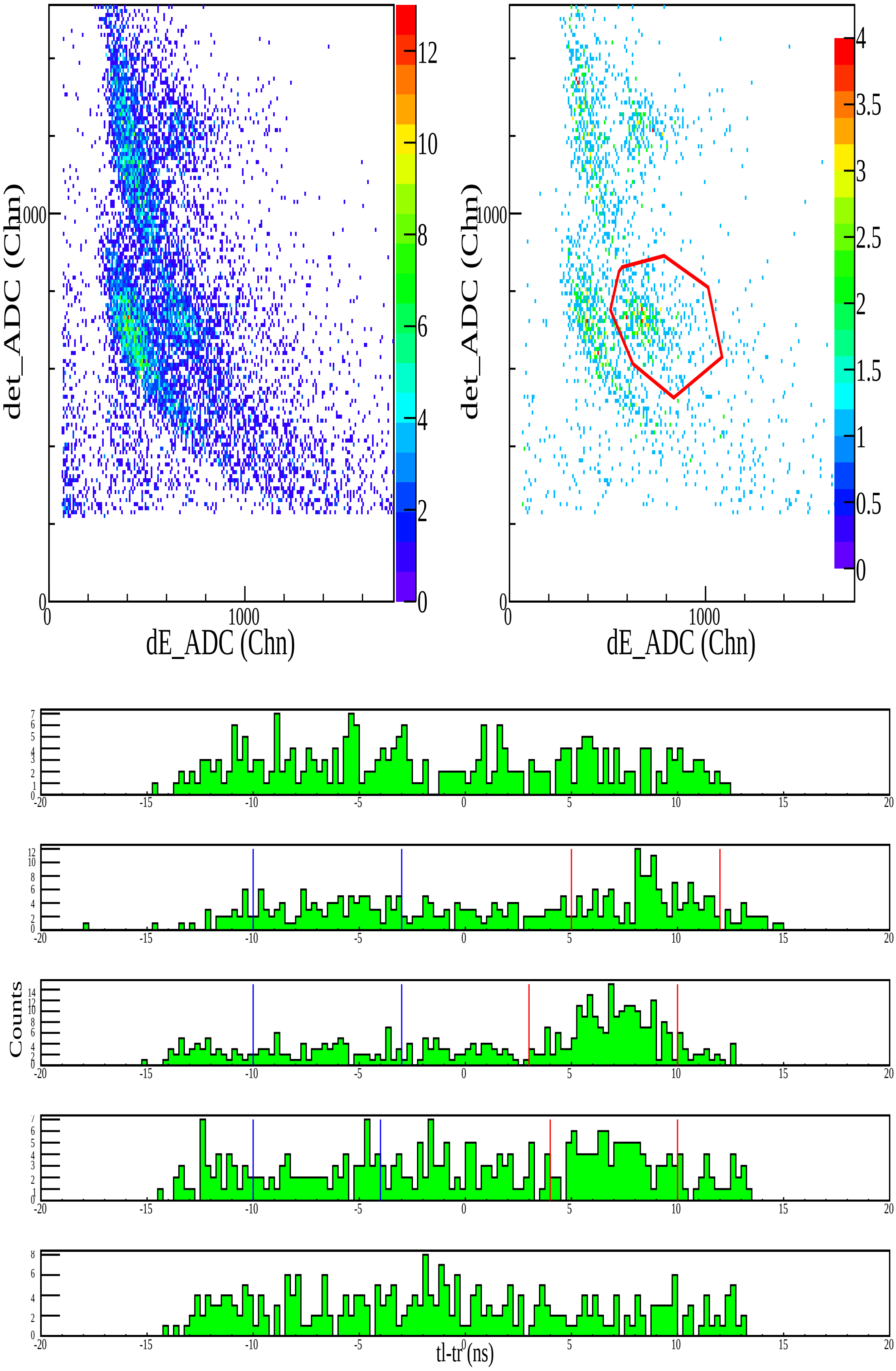

Figure A.72. Figures for 48° at 220 MeV (continued).

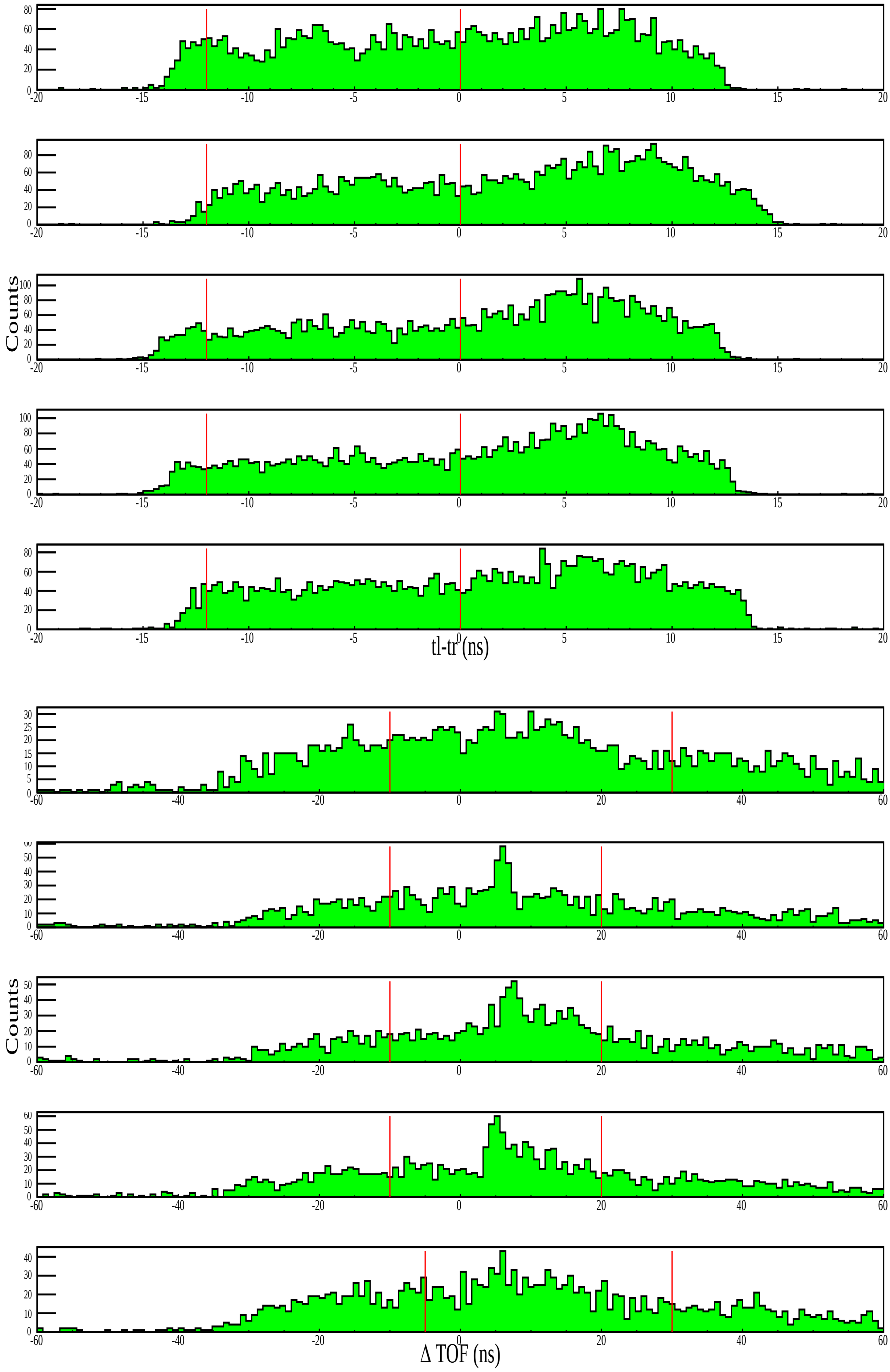

Figure A.73. Figures for 30° at 230 MeV.

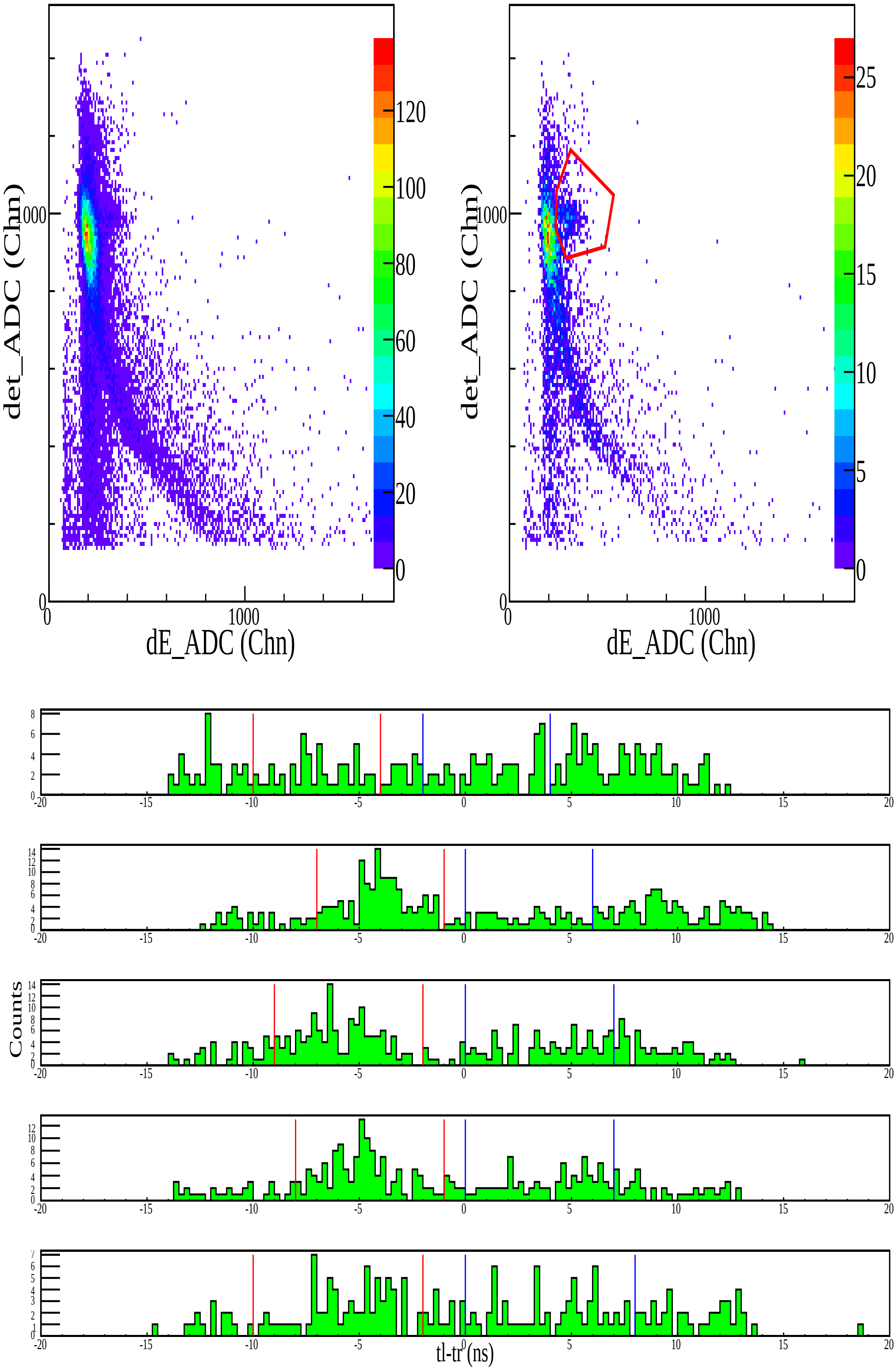

Figure A.74. Figures for 30° at 230 MeV (continued).

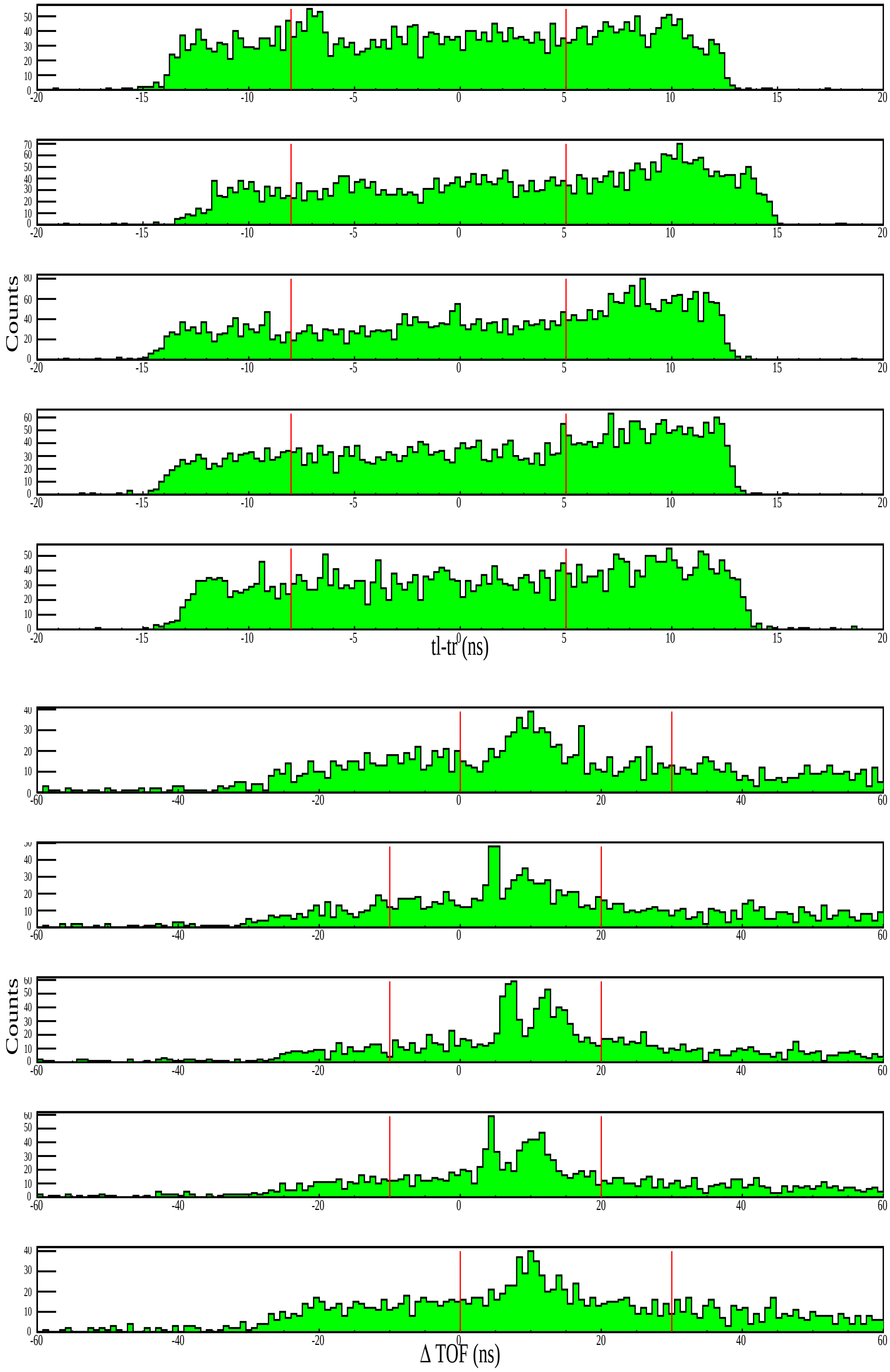

Figure A.75. Figures for 36° at 230 MeV.

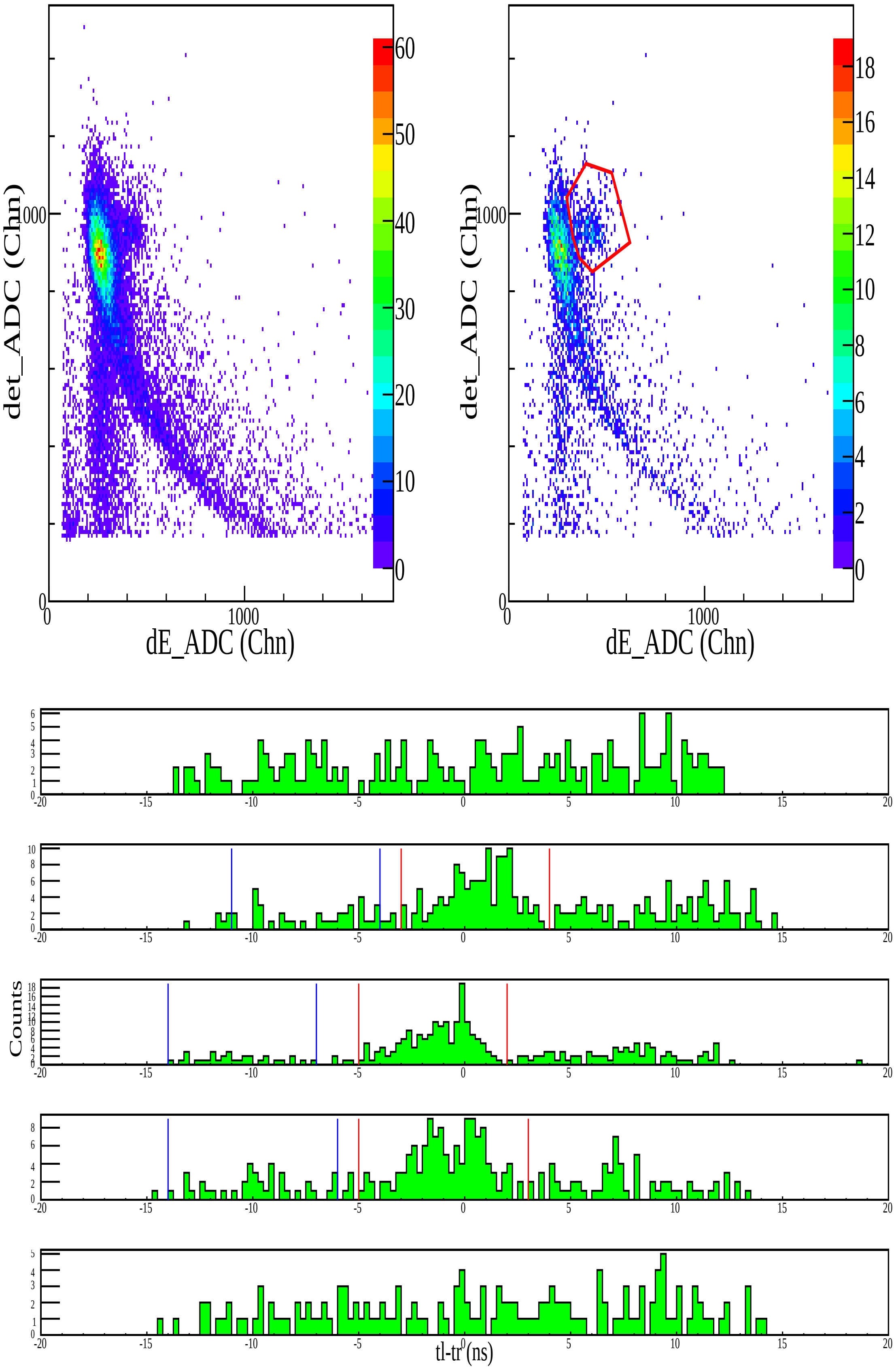

Figure A.76. Figures for 36° at 230 MeV (continued).

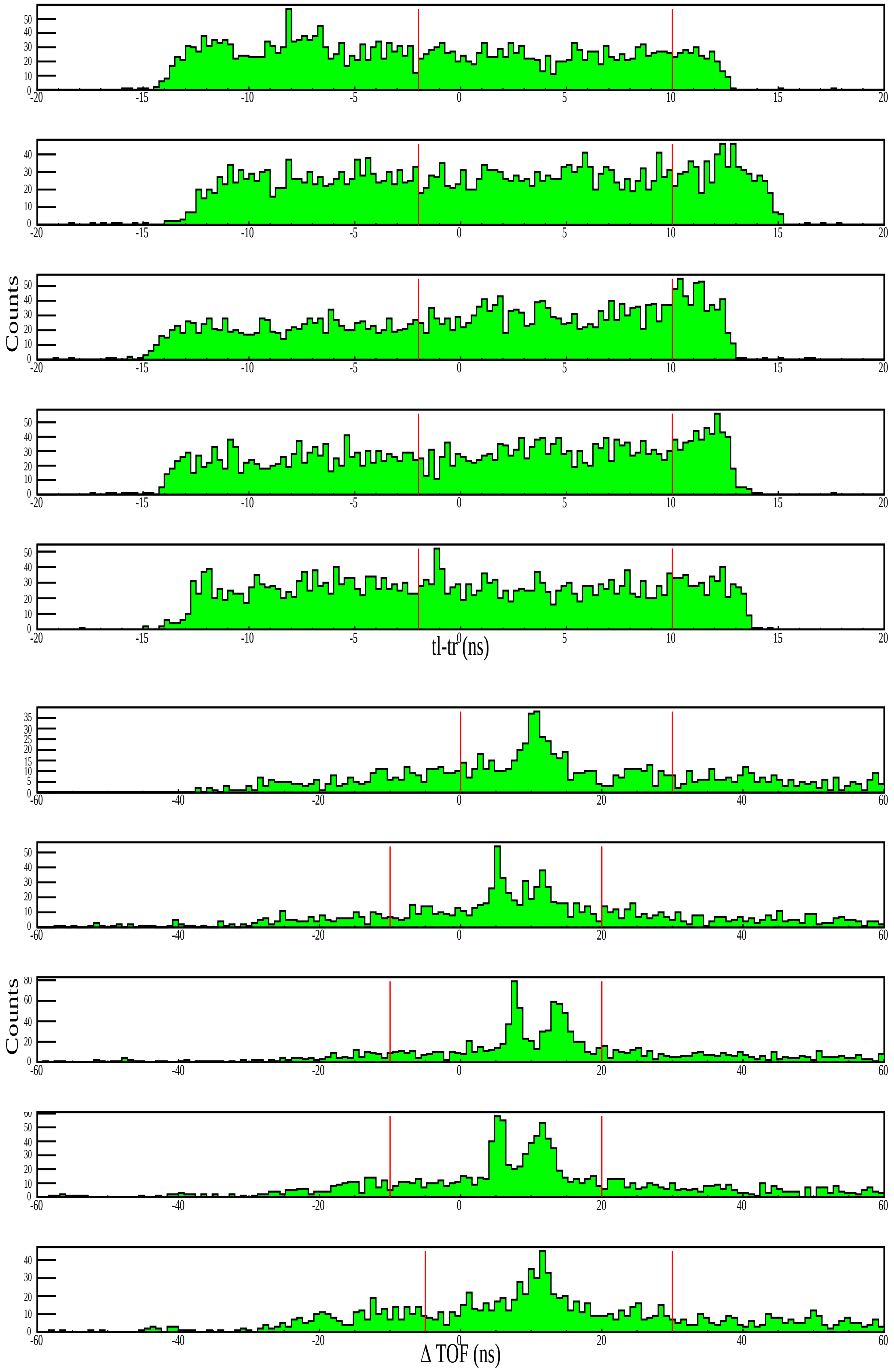

Figure A.77. Figures for 42° at 230 MeV.

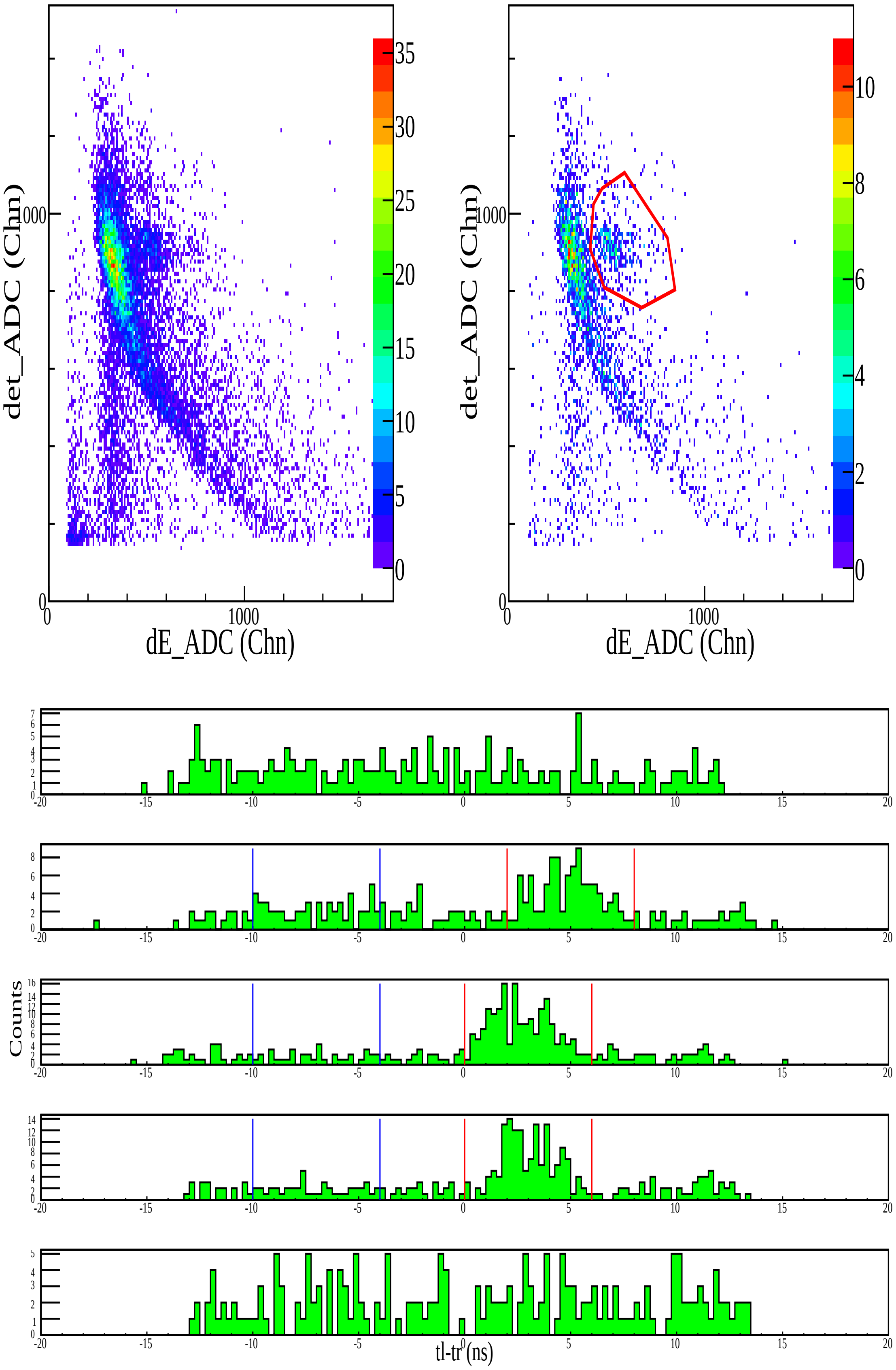

Figure A.78. Figures for 42° at 230 MeV (continued).

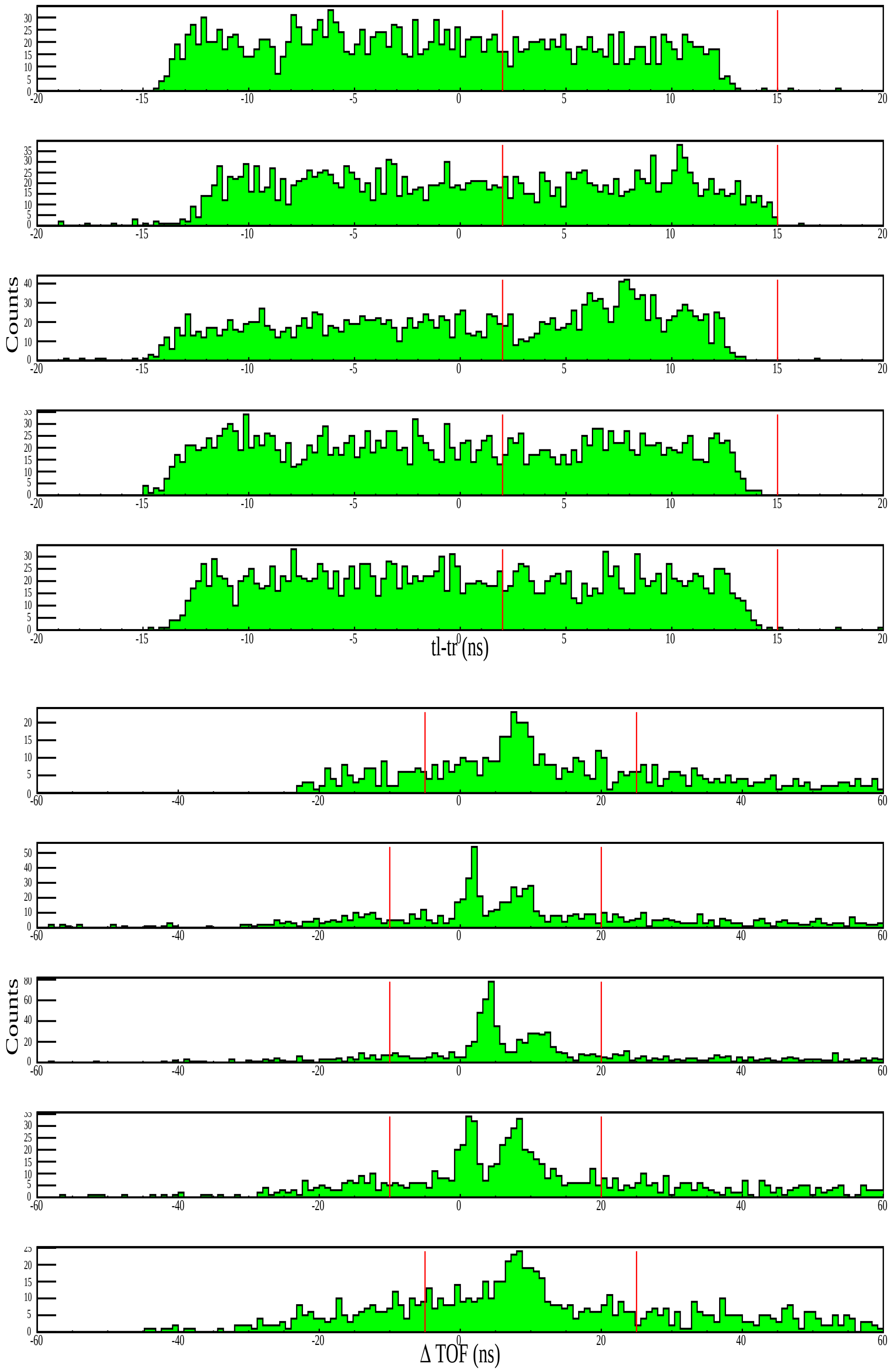

Figure A.79. Figures for 48° at 230 MeV.

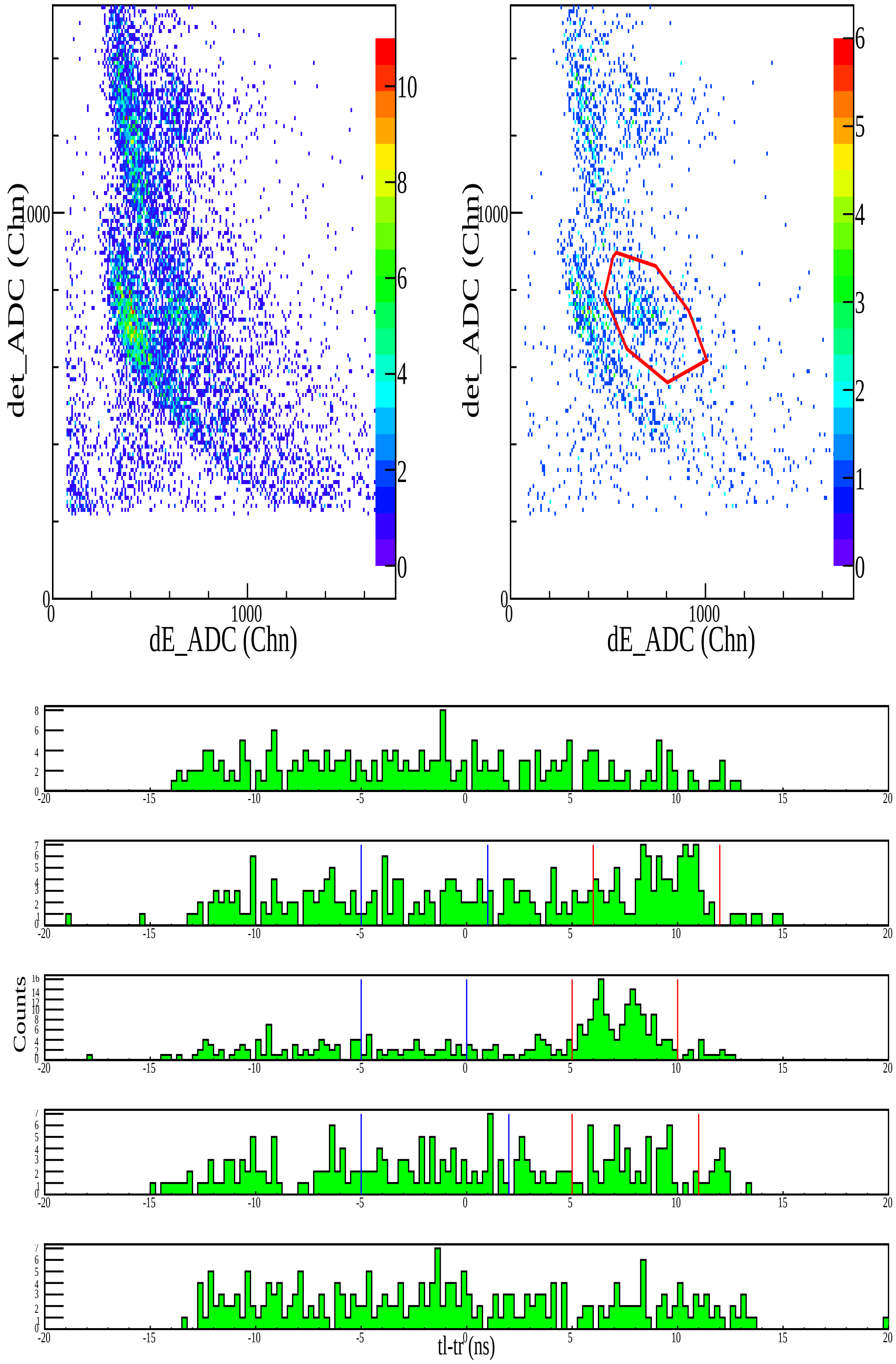

Figure A.80. Figures for 48° at 230 MeV (continued).

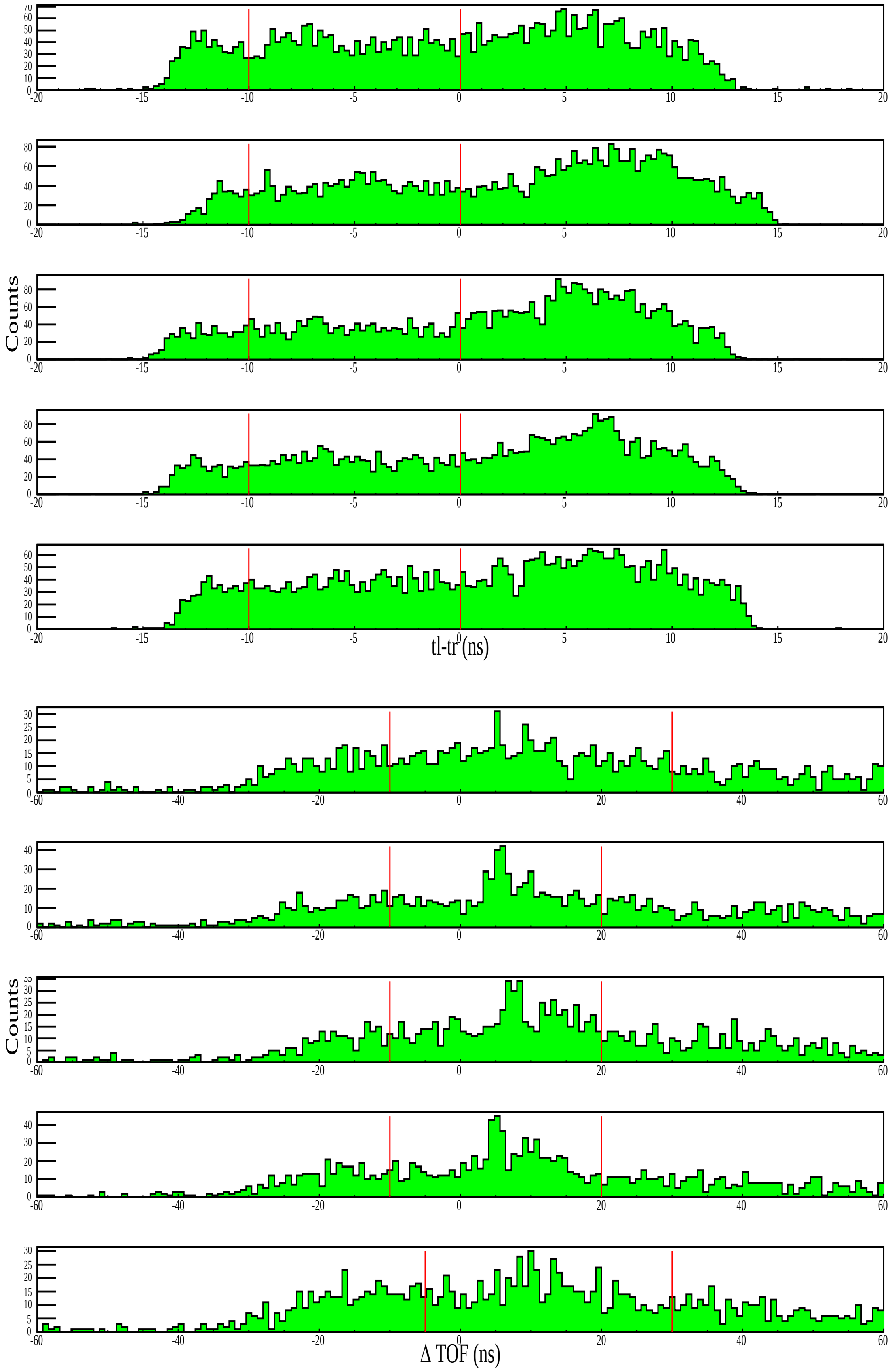

Figure A.81. Figures for 30° at 240 MeV.

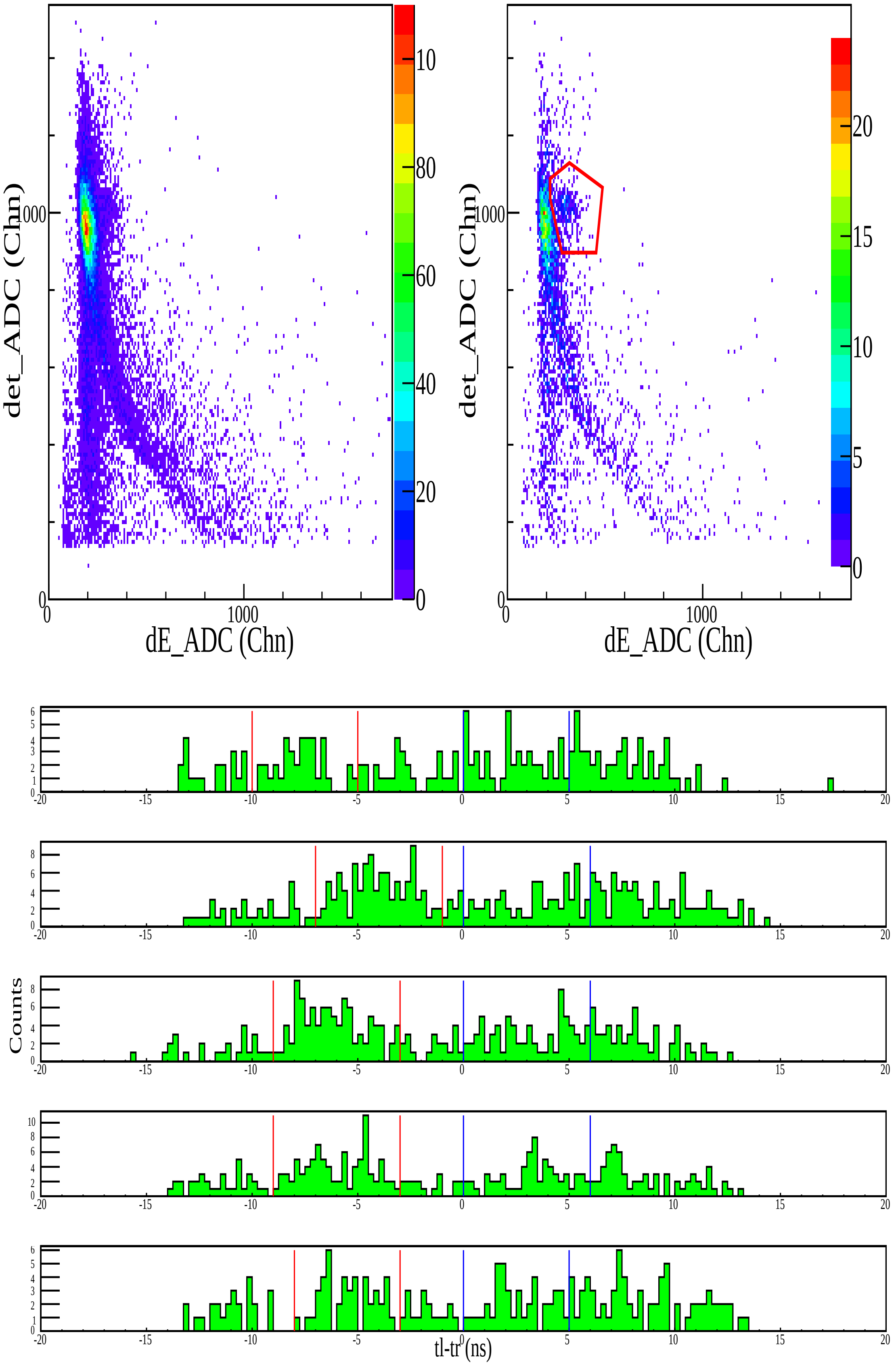

Figure A.82. Figures for 30° at 240 MeV (continued).

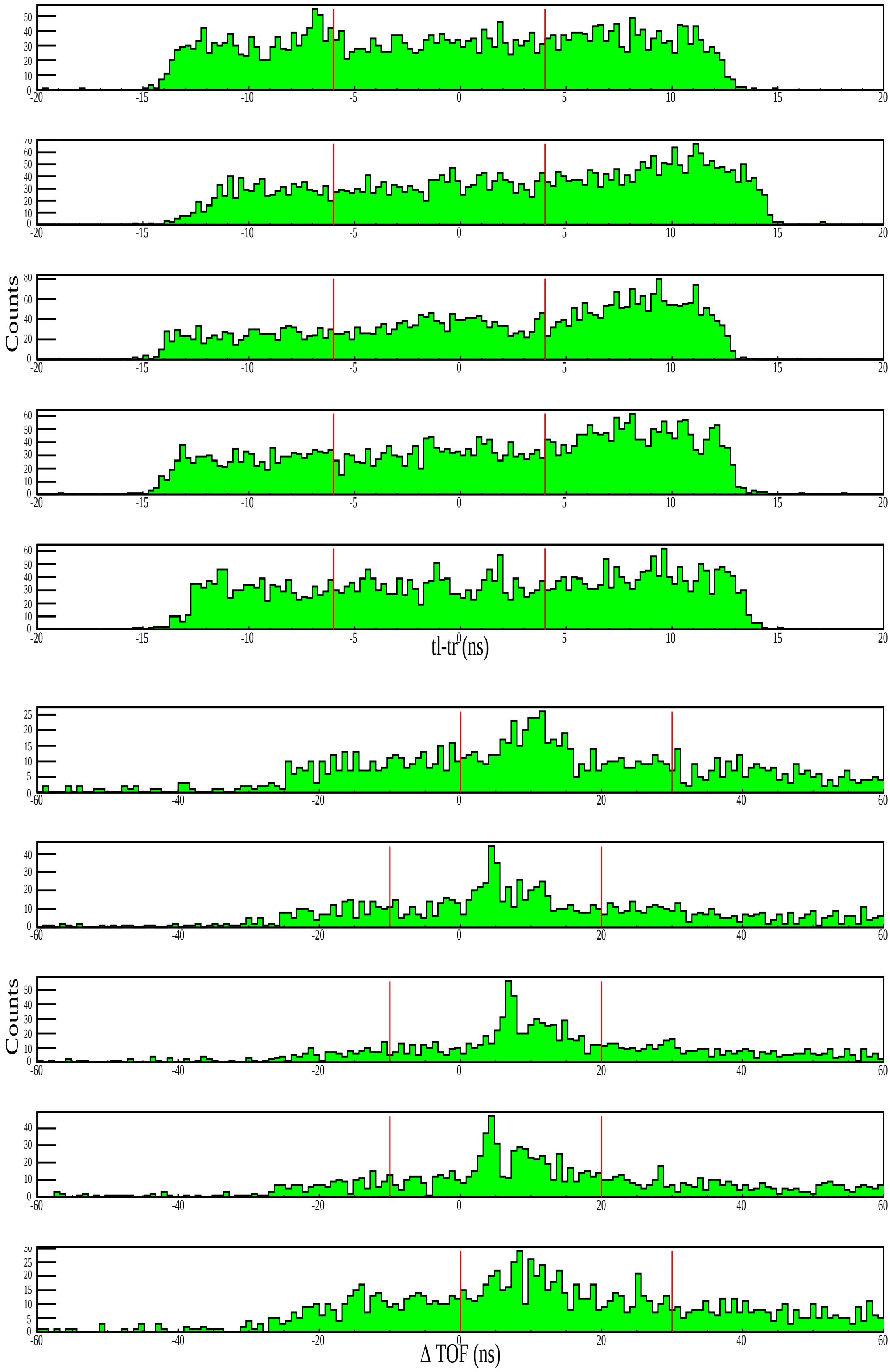

Figure A.83. Figures for 36° at 240 MeV.

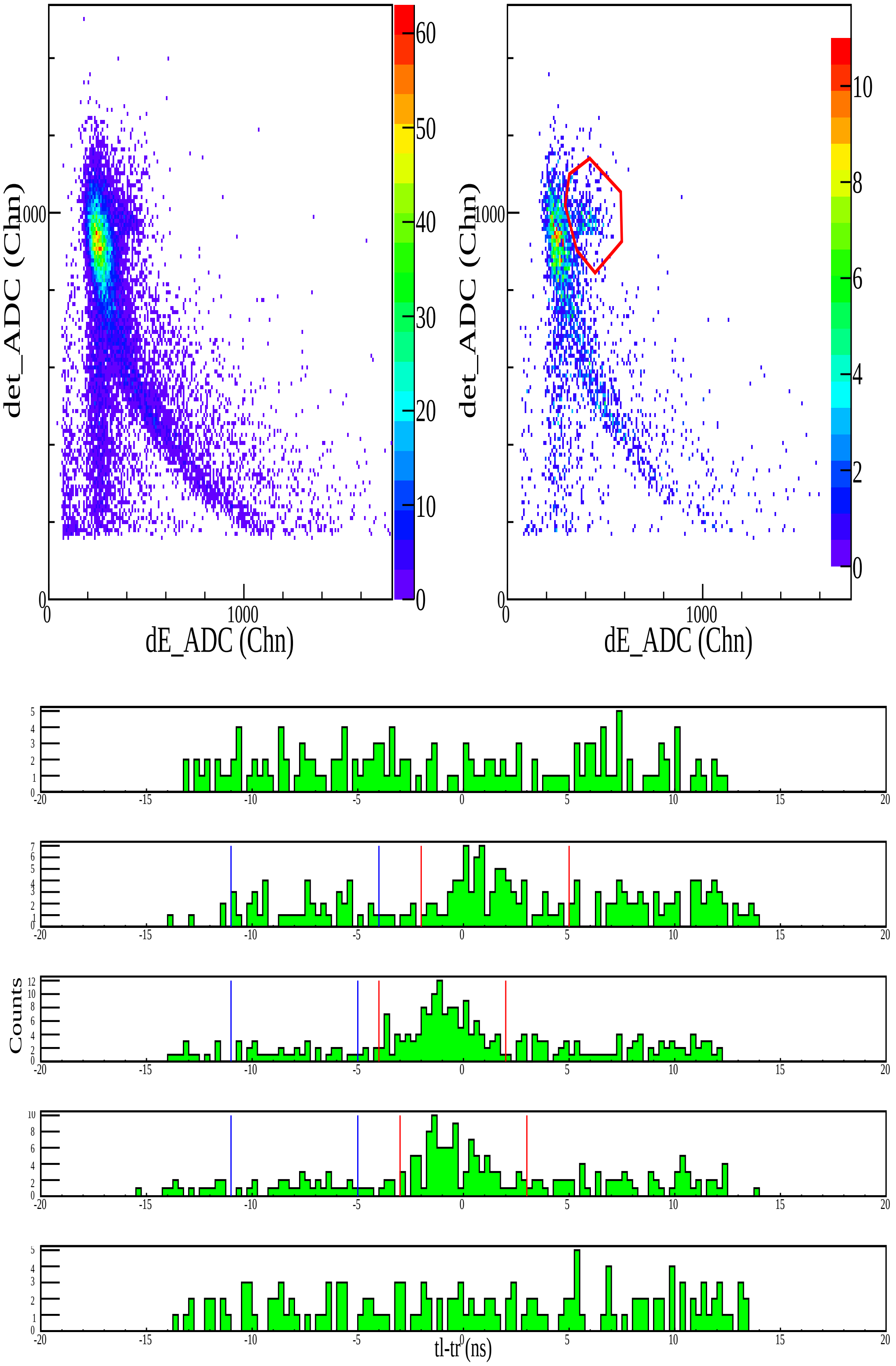

Figure A.84. Figures for 36° at 240 MeV (continued).

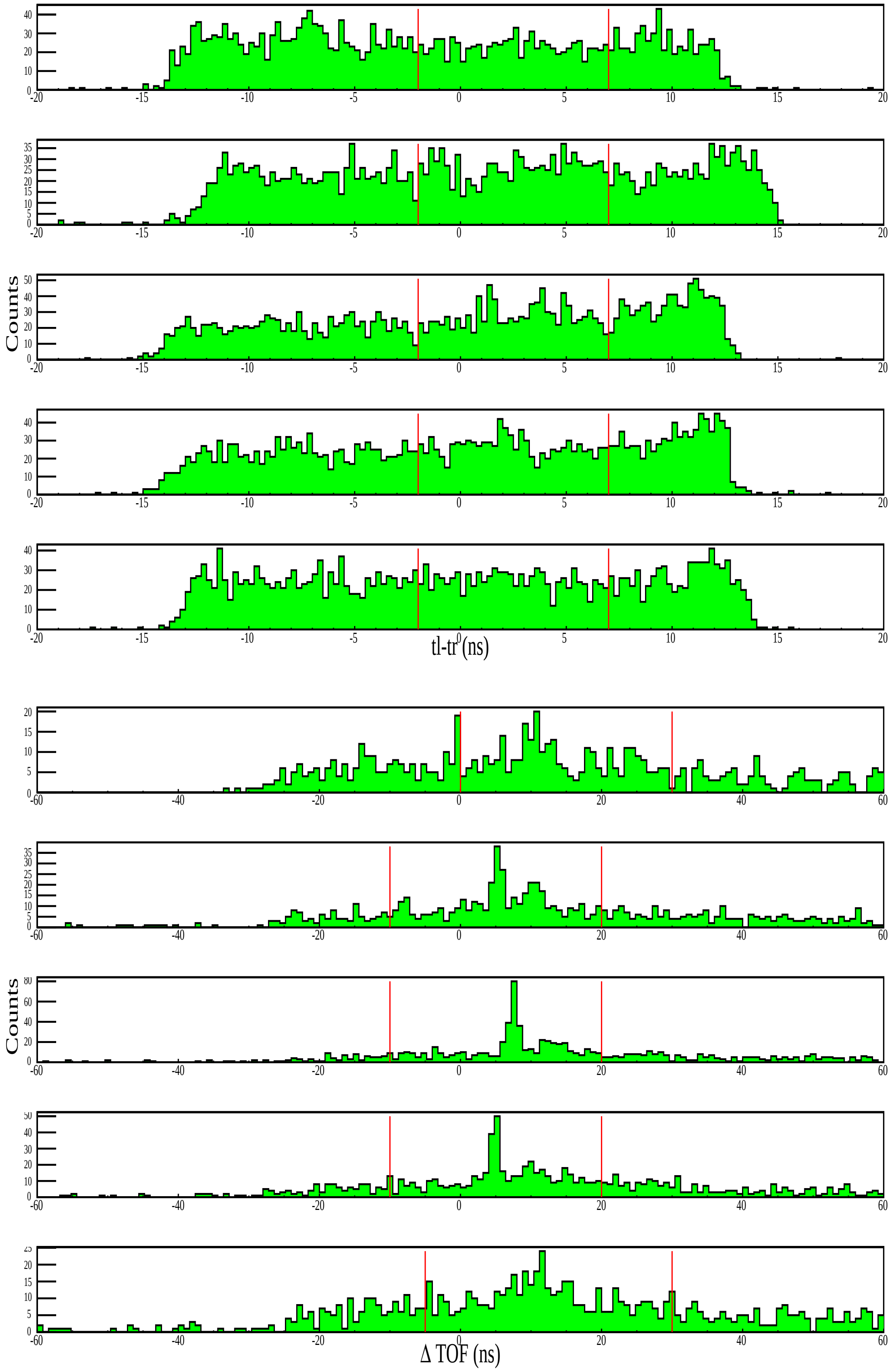

Figure A.85. Figures for 42° at 240 MeV.

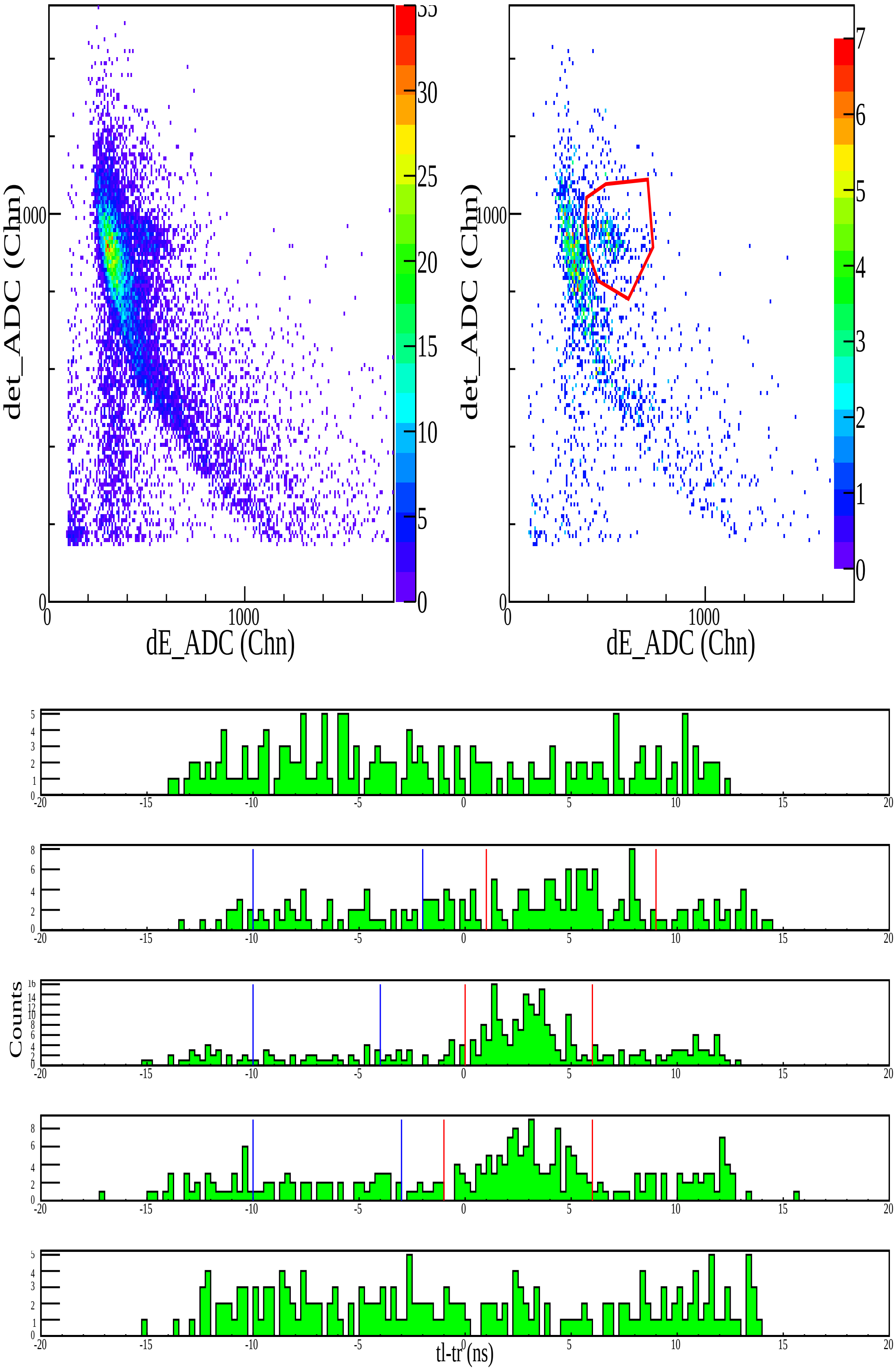

Figure A.86. Figures for 42° at 240 MeV (continued).

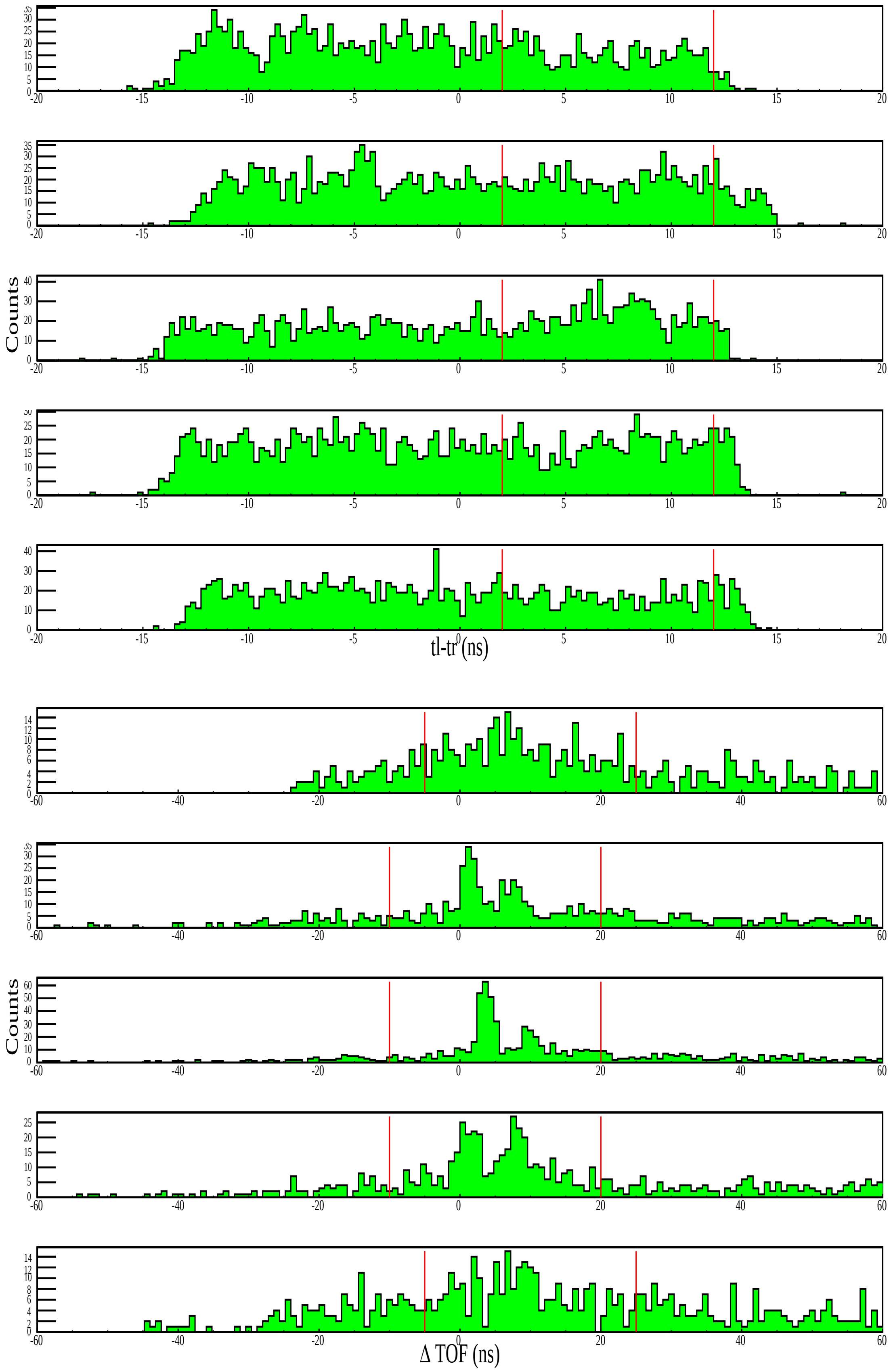

Figure A.87. Figures for 48° at 240 MeV.

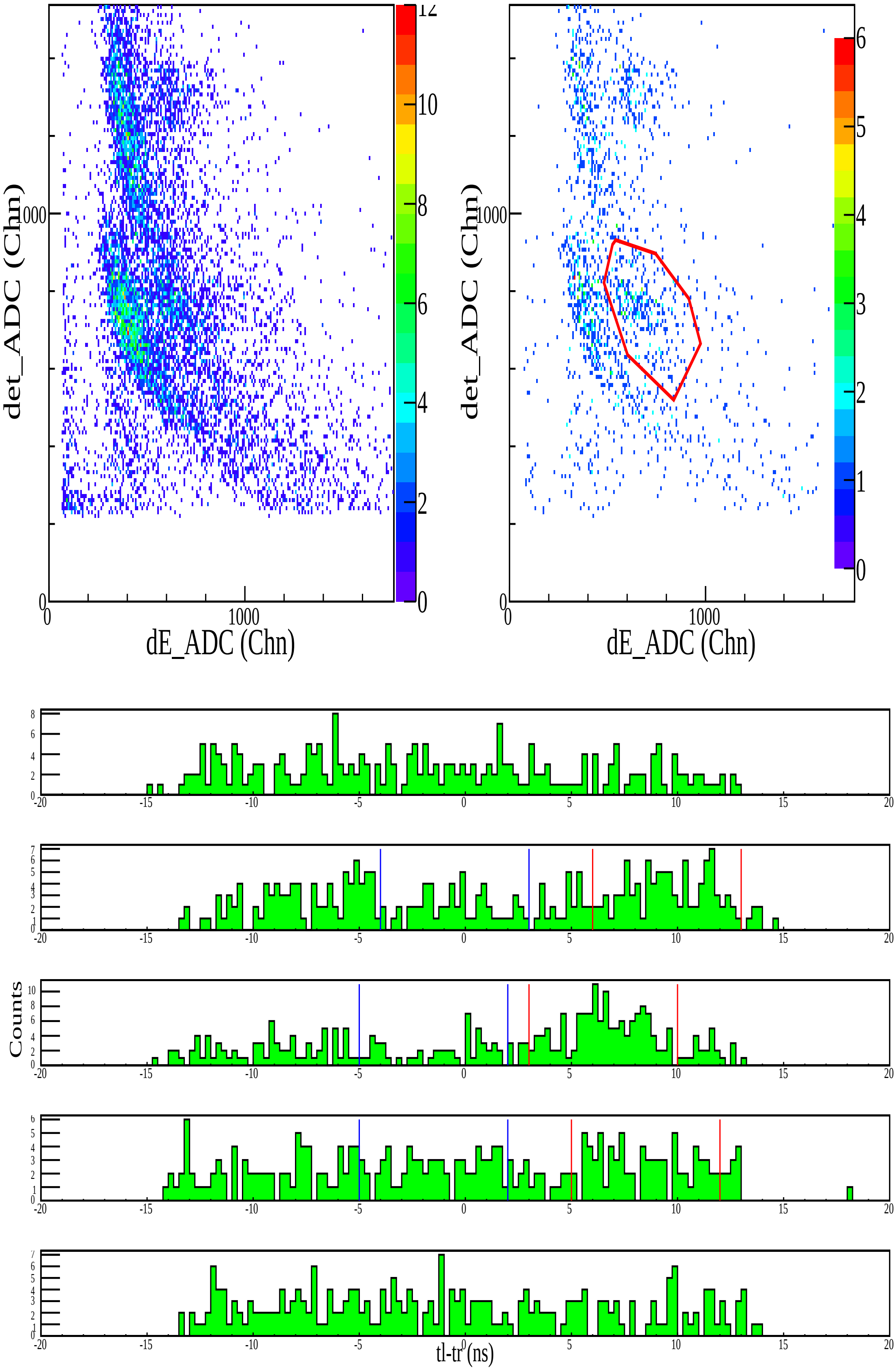

Figure A.88. Figures for 48° at 240 MeV (continued).

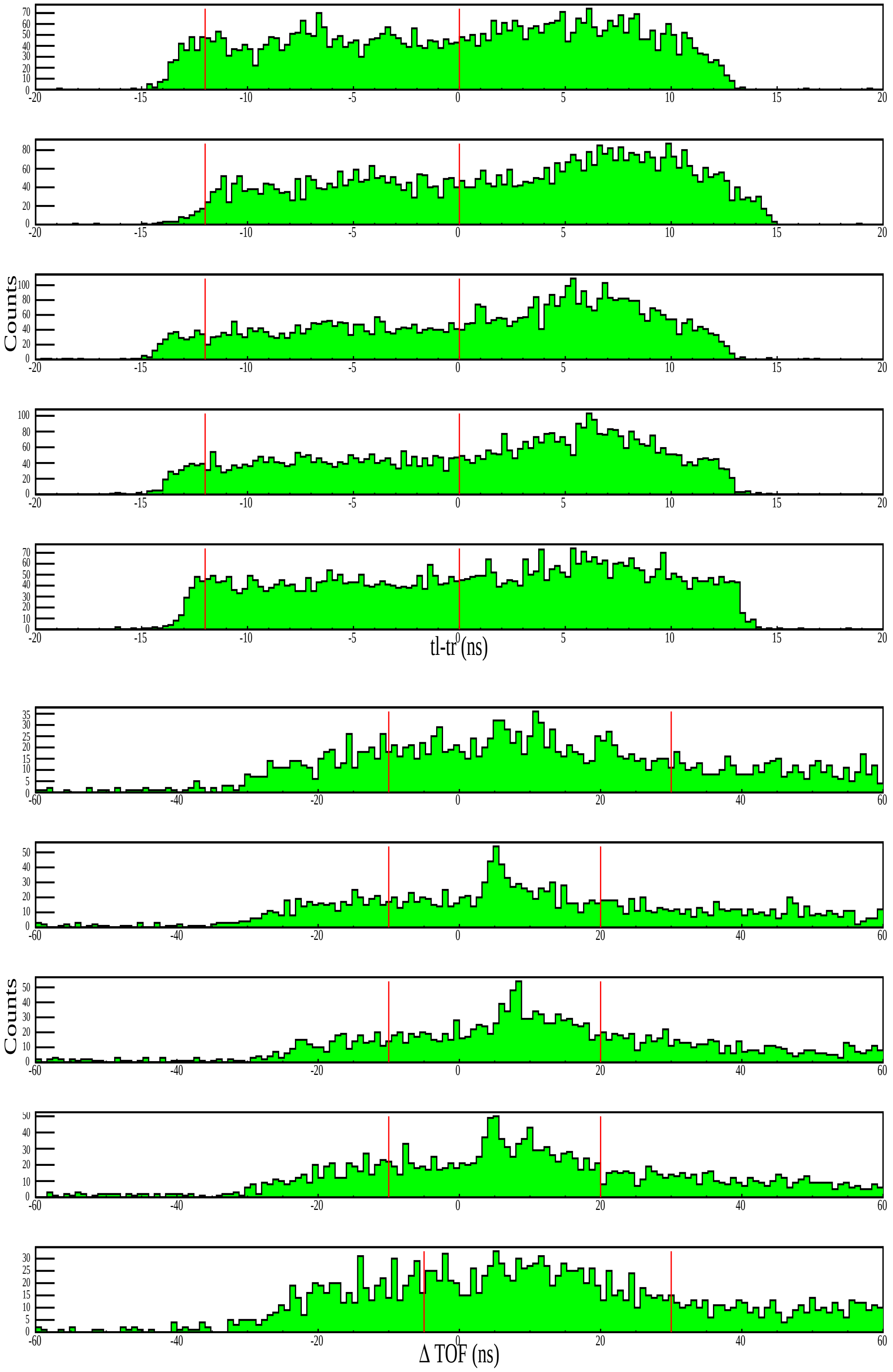

Figure A.89. Figures for 30° at 250 MeV.

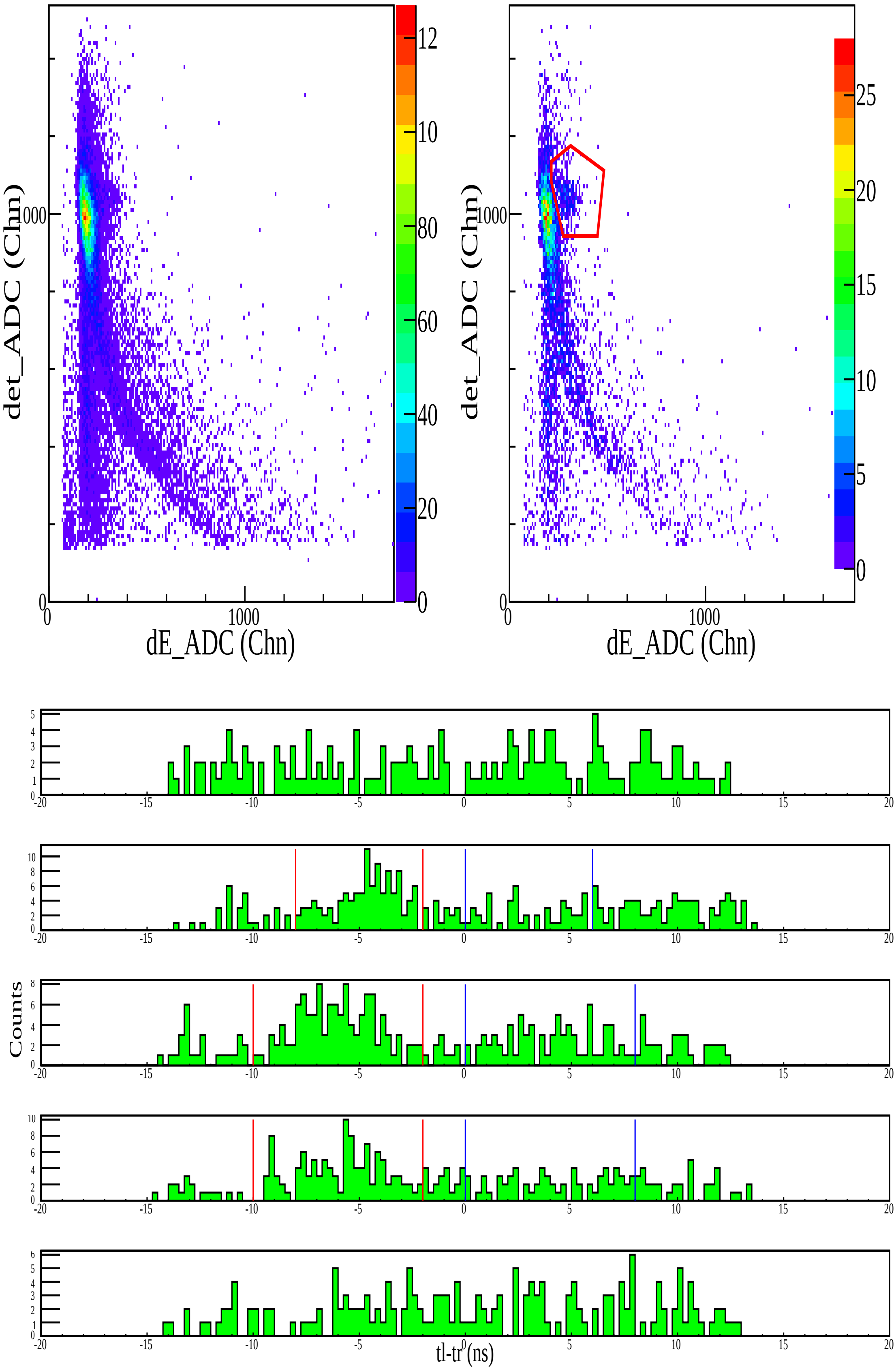

Figure A.90. Figures for 30° at 250 MeV (continued).

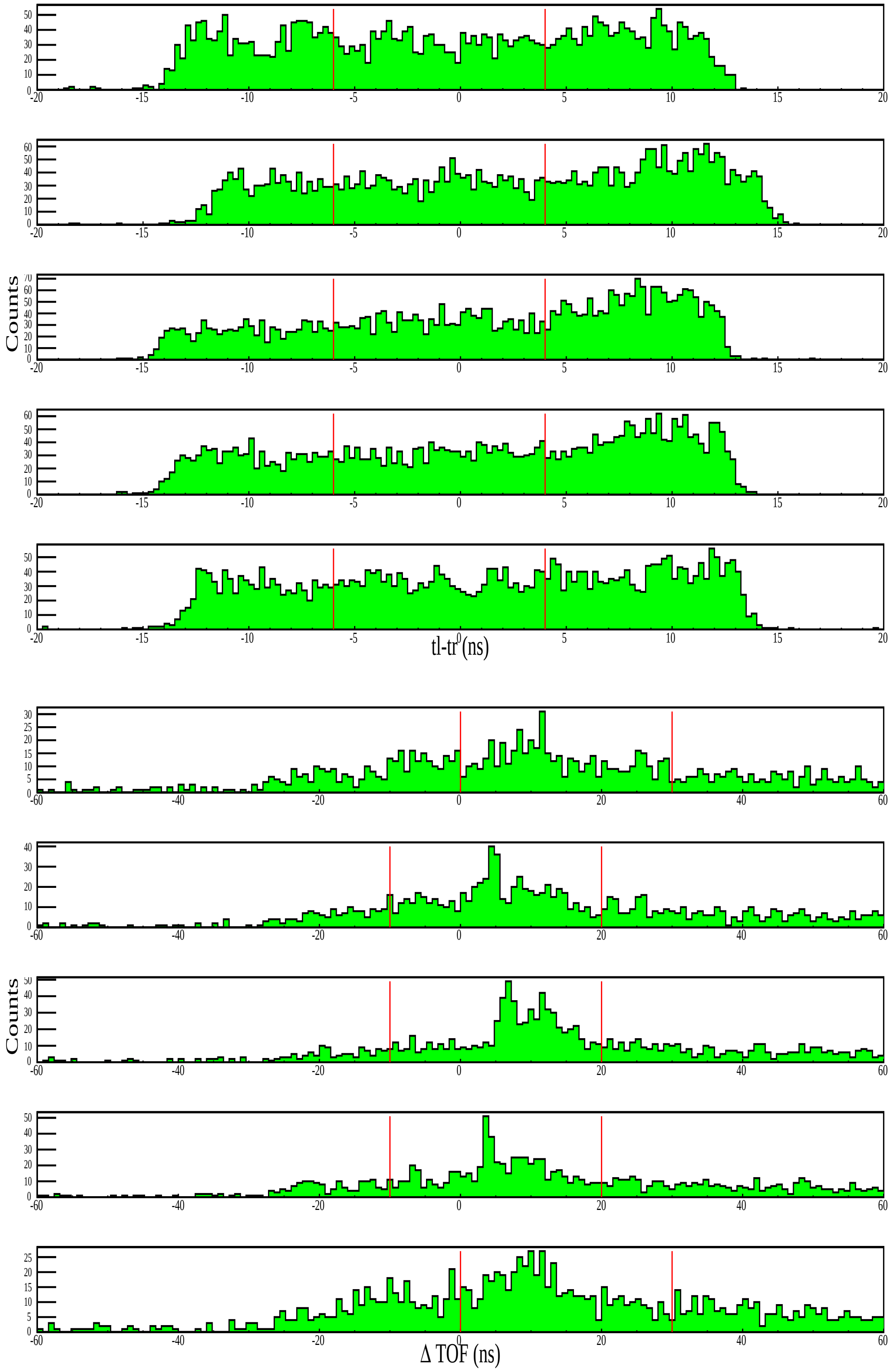

Figure A.91. Figures for 36° at 250 MeV.

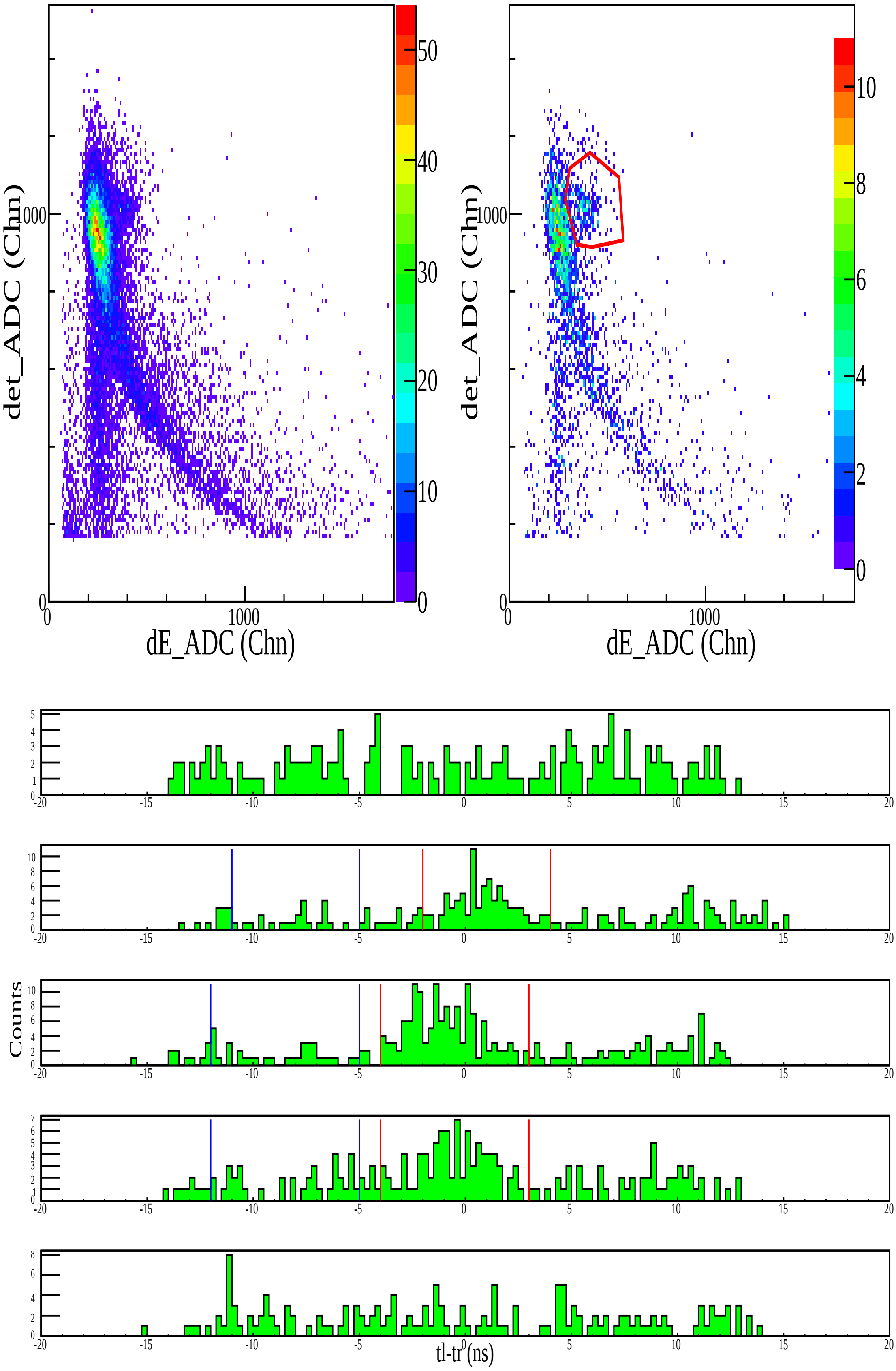

Figure A.92. Figures for 36° at 250 MeV (continued).

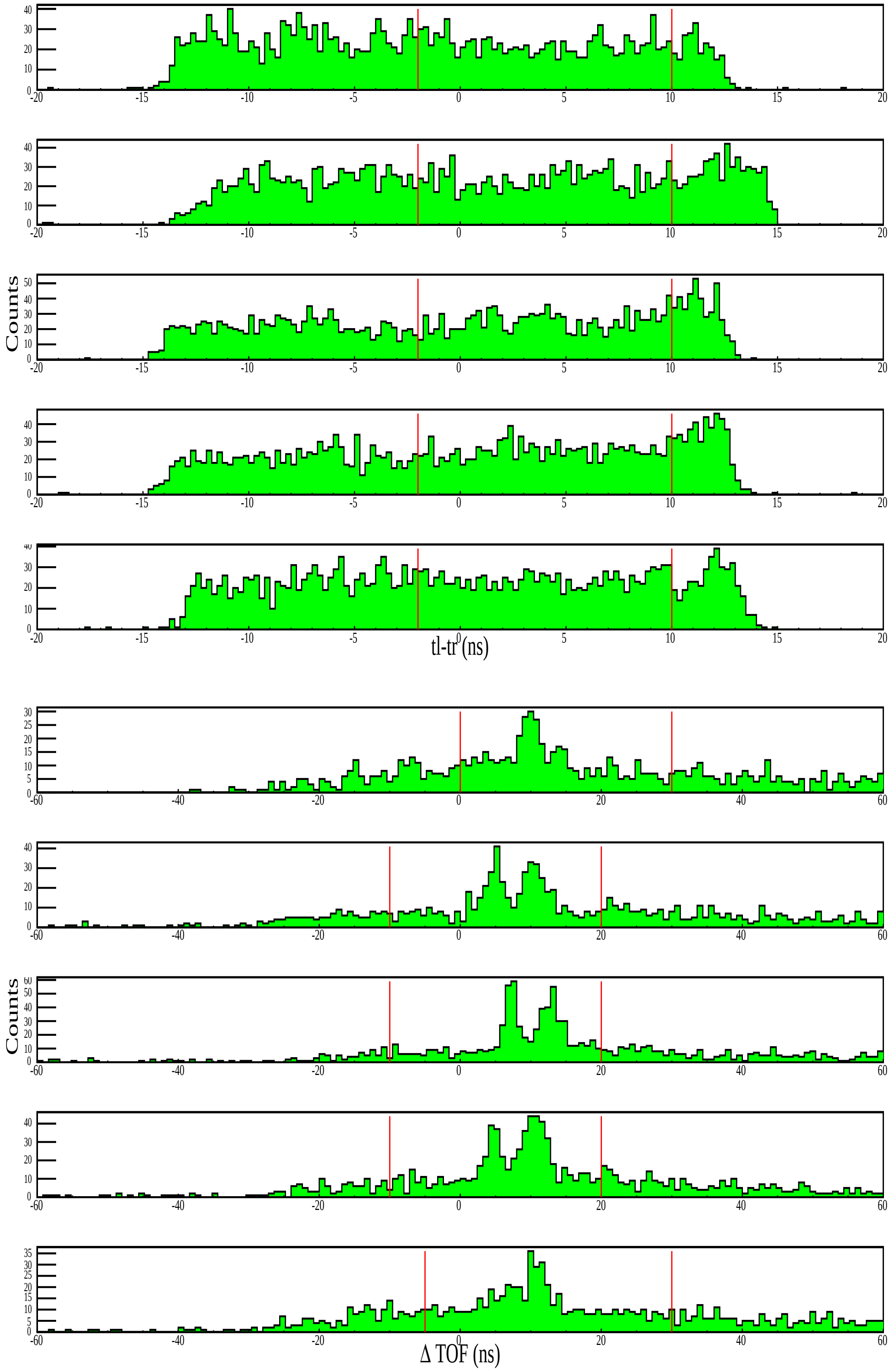

Figure A.93. Figures for 42° at 250 MeV.

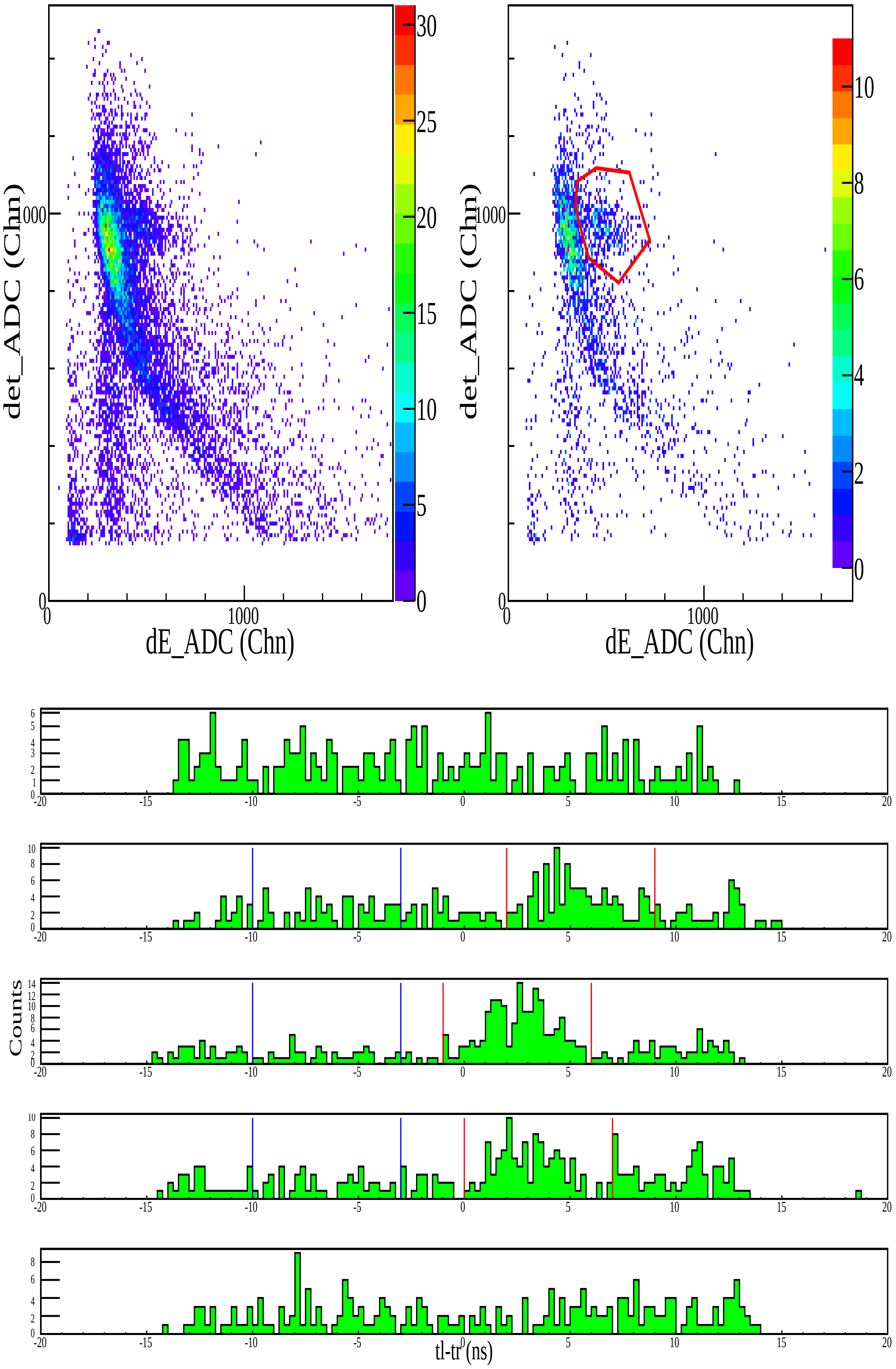

Figure A.94. Figures for 42° at 250 MeV (continued).

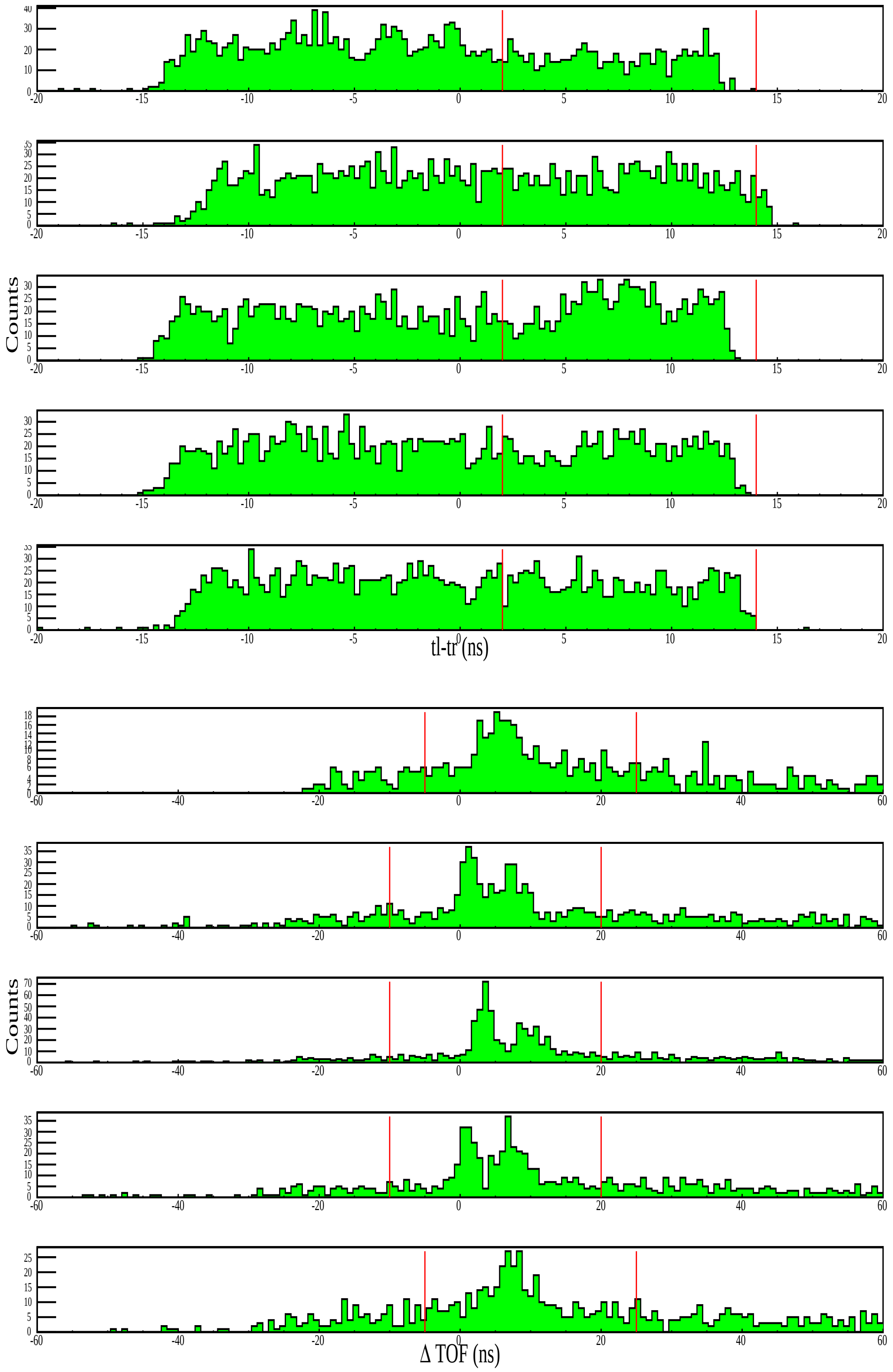

Figure A.95. Figures for 48° at 250 MeV.

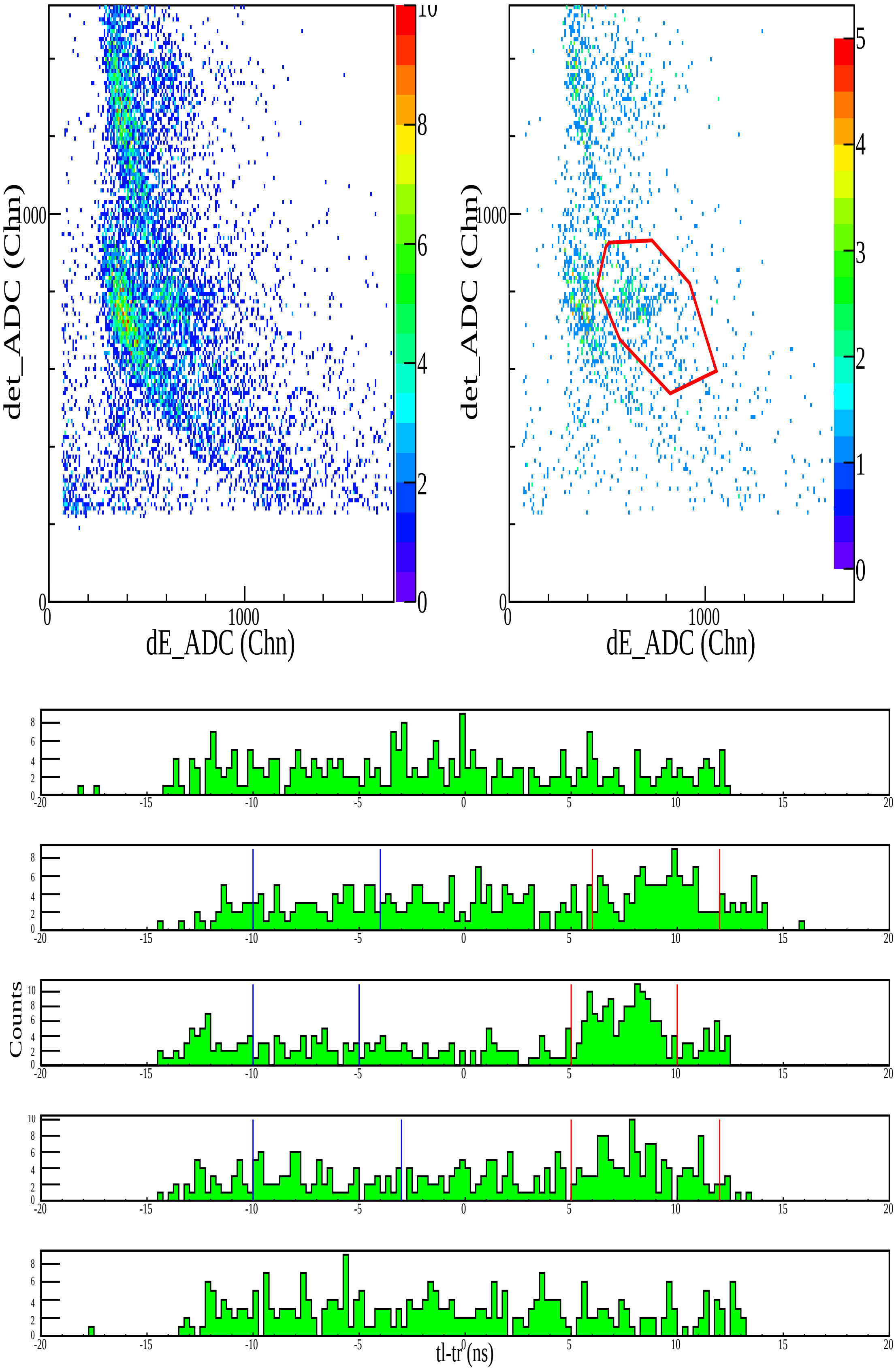

Figure A.96. Figures for 48° at 250 MeV (continued).

APPENDIX B: Target Geometry

As stated in the main text, the target bulges and it looks like two spherical caps are attache to the original cylinder. Figure B.1 shows a cross section of the geometry where the spheres that complete the caps, the inclination of the target with respect to the beam and the coordinate choice is illustrated. In accordance with the beam profile generated in the MC simulation, a point is randomly selected on the xy plane which acts as the position of the neutron inside the beam. The blue points in the figure represents the entrance of the neutron and the exit point if it does not interact, respectively. We assume that the interaction takes place randomly between these points and our aim is to determine these points using geometry given the position of the neutron, target thickness and its correction.

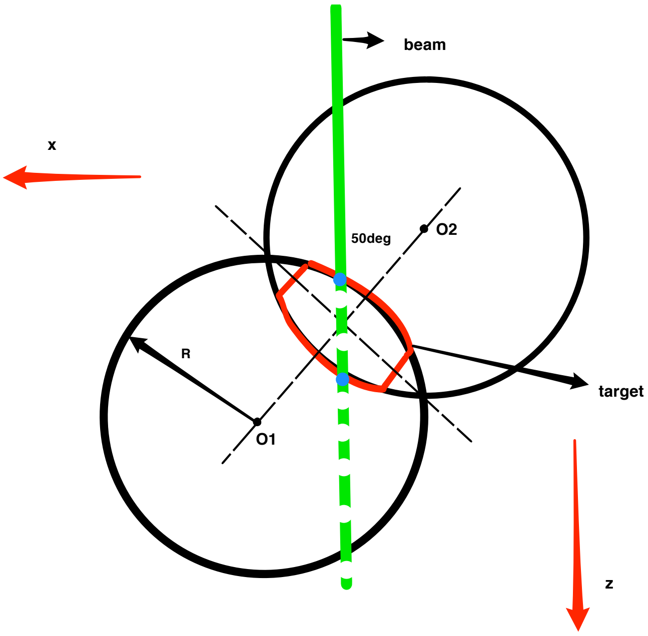

Figure B.1. The illustration of the target geometry.

The radius of the spheres (we assume the bulging is symmetrical) can be found using the difference in the thickness and trigonometry. Let

$$d = ht_{max} - ht_{min} \tag{B.1}$$

where ht_{max} and ht_{min} are the maximum (along the center of the cylinder) and minimum (along the edges or original) half thicknesses, respectively. Then we can find the radius as

$$R_s = \frac{R_c^2 + d^2}{2d} \tag{B.2}$$

where R_c is the radius of the top or bottom circles of the original cylindrical target. The coordinates of the center of the bottom sphere can be found using the inclination angle and the radius of the sphere. Let θ_{inc} be the inclination angle, then

$$\begin{aligned} O_{1x} &= (R_s - ht_{max}) \sin\theta_{inc} && \text{(B.3)} \\ O_{1y} &= 0 && \text{(B.4)} \\ O_{1z} &= (R_s - ht_{max}) \cos\theta_{inc} && \text{(B.5)} \end{aligned}$$

assuming the origin of the coordinate system being the center of mass of the target. The coordinates of the center of the top sphere, O_2, is symmetrical to O_1 with respect to the origin. The neutron inside the beam can be characterized as a 3D line whose equation can be given as

$$l = (x_0, y_0, z) \tag{B.6}$$

where x_0 and y_0 are the randomly chosen point mentioned in the first paragraph. Now, the entrance and exit points are the intersection of the this line with the bottom and top spheres, respectively. Given the size of the target and the beam radius, the entrance point, z_u, should always be negative and vice versa. Writing the intersection condition, we get

$$R_s^2 = (x_0 - O_{1x})^2 + (y_0 - O_{1y})^2 + (z_u - O_{1z})^2 \tag{B.7}$$

which leads to

$$z_u = -\sqrt{R_s^2 - (x_0 - O_{1x})^2 - y_0^2} + O_{1z}. \tag{B.8}$$

The same treatment of the upper sphere gives the exit point, z_d, as

$$z_d = \sqrt{R_s^2 - (x_0 + O_{1x})^2 - y_0^2} - O_{1z}. \tag{B.9}$$

As a result, we pick our interaction vertex randomly between these two points for each interaction in our simulation which gives rise to the vertex profile given in Figure 3.8.

APPENDIX C: Elastic Kinematics

In this section, we will illustrate the kinematical calculations and derivation of the expression for the cross section in the center-of-mass frame. The elastic collisions in our experiment can be expressed as in Equation C.1

$$P^{\mu}_{n_0} + P^{\mu}_{t} = P^{\mu}_{n} + P^{\mu}_{r} \tag{C.1}$$

in which the P^{μ}'s are the 4-momenta of the incoming neutron, target particle, scattered neutron and the recoil particle from left to right. Assigning the z-axis to the beam direction and picking the x-axis towards the recoil trajectory, the 4-momenta can be written in detail as in

$$\begin{aligned} P^{\mu}_{n_0} &= (E_{n_0}, 0, 0, p_{n_0}) && \text{(C.2)} \\ P^{\mu}_{t} &= (m_t, 0, 0, 0) && \text{(C.3)} \\ P^{\mu}_{n} &= (E_n, p_{n_x}, 0, p_{n_z}) && \text{(C.4)} \\ P^{\mu}_{r} &= (E_r, p_{r_x}, 0, p_{r_z}) && \text{(C.5)} \end{aligned}$$

using the convention $\hbar = c = 1$. Rearranging the terms and employing the scalar product of four vectors in different frames, we get,

$$m_n^2 = m_n^2 + m_r^2 + m_r^2 + 2E_r m_r - 2E_{n_0} m_r - 2E_{n_0} E_r + 2p_{n_0} p_{r_z}, \tag{C.6}$$

$$p_{n_0} p_r \cos\theta_r = (E_r - m_r)(E_{n_0} + m_r). \tag{C.7}$$

Let

$$\alpha = \frac{(E_{n_0} + m_r)}{p_{n_0} cos\theta_r}, \tag{C.8}$$

then we have

$$p_r = \sqrt{E_r^2 - m_r^2} = \alpha(E_r - m_r) \tag{C.9}$$

which leads to

$$E_r = \frac{m_r(\alpha^2 + 1)}{\alpha^2 + 1}. \tag{C.10}$$

After this point, we can also find the scattering angle again using three momentum conservation

$$\begin{aligned} p_n \sin\theta_n &= p_r \sin\theta_r & \text{(C.11)} \\ p_n \cos\theta_n &= p_{n_0} - p_r \cos\theta_r & \text{(C.12)} \end{aligned}$$

so that

$$\tan\theta_n = \frac{p_r \sin\theta_r}{p_{n_0} - p_r \cos\theta_r}. \tag{C.13}$$

Similarly, we could do the same treatment to the recoil branch to obtain

$$\tan\theta_r = \frac{p_n \sin\theta_n}{p_{n_0} - p_n \cos\theta_n}. \tag{C.14}$$

Traditionally, the cross-section results are presented in the center-of-mass frame, however, the experimental formula will give us the differential cross section in the laboratory frame. Therefore, using relativity, we need to transform our result accordingly. To put it in a more formal way, we need to get

$$\frac{d\sigma}{d\Omega^*} = \frac{d\sigma}{d\Omega_{lab}} \times \frac{d\Omega_{lab}}{d\Omega^*} \tag{C.15}$$

where the solid angle $d\Omega = \sin\theta d\theta d\phi$ in spherical coordinates and the superscript “*”

denotes the center-of-mass frame. Since the beam is chosen to lie on the z-axis, the angle ϕ remains the same in both frames, hence we can write

$$\frac{d\Omega_{lab}}{d\Omega^*} = \frac{\sin\theta}{\sin\theta^*} \times \frac{d\theta}{d\theta^*}. \tag{C.16}$$

In order to calculate this Jacobian, we need to relate the angles in both frames. Figure C.1 is a visual guide to calculate the necessary relations. In the lab frame, the recoil (sctattering) angle can be expressed through

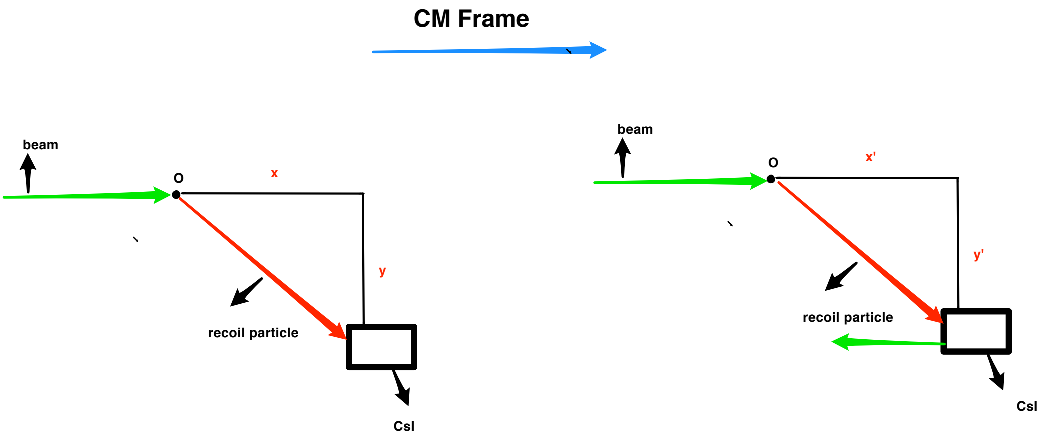

Figure C.1. The illustration of center-of-mass frame transformation.

$$\tan\theta = \frac{y}{x} \tag{C.17}$$

$$\tan\theta^* = \frac{y^*}{x^*} \tag{C.18}$$

in light of Figure C.1. Using

$$\beta_{\mathbf{cm}} = \frac{\mathbf{p_{n_0}} + \mathbf{p_t}}{E_{n_0} + E_t}, \gamma_{cm} = (1 - \beta_{cm}^2)^{-1}, \tag{C.19}$$

we can deduce

$$x^* = \frac{x}{\gamma_{cm}} - \beta_{cm} t^* \tag{C.20}$$

keeping in mind that the detector is also moving towards the interaction point. Since there is no motion in y-direction,

$$y^* = y = \beta_{cm} t^* \sin\theta^*. \tag{C.21}$$

The second equality follows from the fact that this is an elastic collision. Similarly,

$$x^* = \beta_{cm} t^* \cos\theta^*. \tag{C.22}$$

Then we have

$$\beta_{cm} t^* \cos\theta^* = \frac{x}{\gamma_{cm}} - \beta_{cm} t^*, \tag{C.23}$$

$$\frac{y}{\sin\theta^*}(\cos\theta^* + 1) = \frac{x}{\gamma_{cm}}. \tag{C.24}$$

As a result, we obtain Equation C.25 that we will use to transform our parameters.

$$\tan\theta = \frac{\sin\theta^*}{\gamma_{cm}(\cos\theta^* + 1)}. \tag{C.25}$$

Differentiating this equation, we get

$$\frac{d\theta}{d\theta^*} = \frac{1 + \gamma_{cm}^2 \tan^2\theta}{2\gamma_{cm}(1 + \tan^2\theta)}. \tag{C.26}$$

The other factor for the Jacobian can also be obtained using Equation C.25 as

$$\frac{\sin\theta}{\sin\theta^*} = \frac{(1+\gamma_{cm}^2\tan^2\theta)\cos\theta}{2\gamma_{cm}} \tag{C.27}$$

which leads to our final relation

$$\frac{d\Omega_{lab}}{d\Omega^*} = \frac{(1+\gamma_{cm}^2\tan^2\theta)^2\cos\theta}{4\gamma_{cm}^2(1+\tan^2\theta)}. \tag{C.28}$$

APPENDIX D: Monte Carlo Simulation

In this section, we will talk discuss the MC simulation that assisted us during the analysis in many areas. The majority of the program code has been written by Taylan Akdoğan for this beam line. Some additions specific to this analysis are made. This code generates a neutron beam with specified energy profile, generates an interaction vertex inside the target, generates a hit point on the detectors and as a result calculates all the kinematics. The file *A_input* includes the chracteristics of the beam and the geometry of the detectors. In particular, we can specify beam energy, the energy window of the beam and whether we wish to work with only a portion of the beam. In addititon, we can set the beam burst duration and the duration of the total simulation. The charged particle and neutron detector resolutions and thresholds in addition to the sizes and locations are also present in this file.

In fact, the simulation is composed of different parts for different uses, i.e. the elastic part can be used to test the *np* elastic cross section or energy loss part can be used to determine energy losses. To summarize the process, first a beam profile is created in parallel to the input file and a uniform beam cross section is generated in accordance with the beam size obtained from the actual experiment. Then the interaction vertex is found. Considering the geometrical constraints, the point where the particles enter the detectors are determined. After that, the calculations are made and the histograms are filled with the option of including energy loss. The usefulness of the simulations will be summarized in the following sections.

D.1. Energy Loss

The details are already explained in Section 3.3 and Appendix B.

D.2. Systematic Error Estimation

Some of the estimations of systematic errors that are related to experimental setup are calculated using MC simulations.

First, the detector distances are treated. A 5% error in the placement of the detectors is assumed and the counts obtained are compared to the original geometry which in turn gives an idea of the associated error. Second, the detectors' alignment may not be perfect. In order to account for such an error, we shifted the point of entrance at the charged particle detectors where the shifting is done in a spherically uniform manner. Again the comparison to the original counts gives an estimation of the error which turned out to be 1%.

D.3. Incident Energy Window Verification

We apply a filter of $10MeV$ on the incident energy and we tested if this choice is plausible or not using MC simulation. Due to the energy loss errors, we need to operate in an interval of energy in order not to miss the important events which correspond to that specific energy. Therefore, we needed to have an idea how large an interval we need to use or whether our window is sufficient. We use incident energy windows of 10 MeV (±5 MeV), which is a plausible choice as seen in Figure D.1. This is a histogram of the difference between the measured beam energy with the energy loss and the generated beam, which are obtained by our Monte Carlo simulation, versus the beam energy with loss. One can clearly see that our energy window is more than enough as the worst case spread is ±3 MeV and also this choice gives us enough data for good statistics.

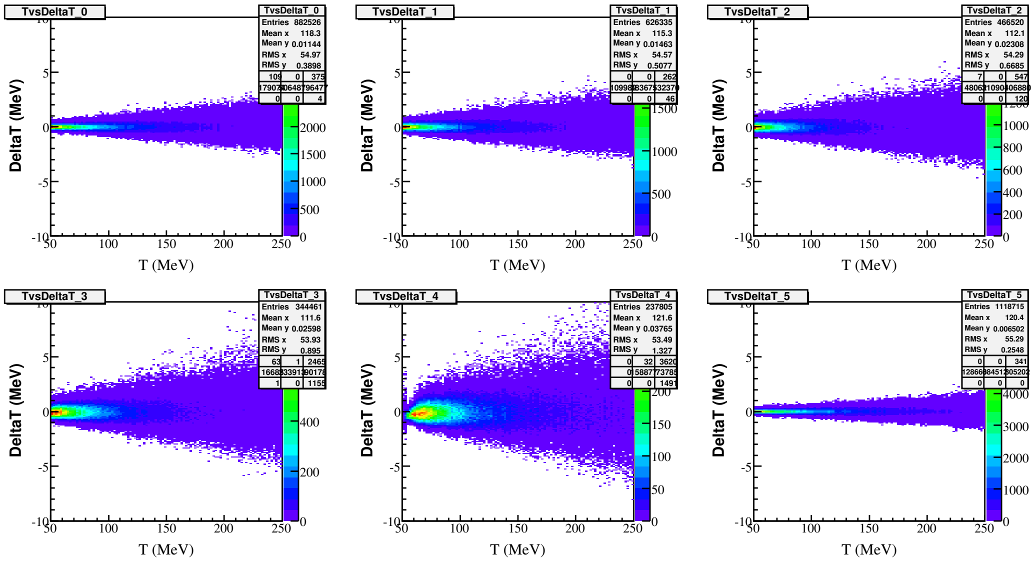

Figure D.1. The difference of beam energy with energy loss and generated beam energy vs beam energy with loss corresponding to all six deuteron angles.

D.4. Energy Threshold of CsI Detectors

At some point during the analysis, we suspected that the thresholds of the CsI detectors may be higher than we expected. This is indeed important since the energies of the recoil particles hitting the backward angle detectors are the lowest and some of the particles may not overcome the threshold. Thus our cross-section result may come out lower than it should be. Hence we used the simulation again to obtain Figure D.2. Inspecting the figure, we see that the threshold is around 30 MeV and the deuterons hitting the backward angle detector are exclusively above that energy, so there is no issue with regard to the CsI threshold.

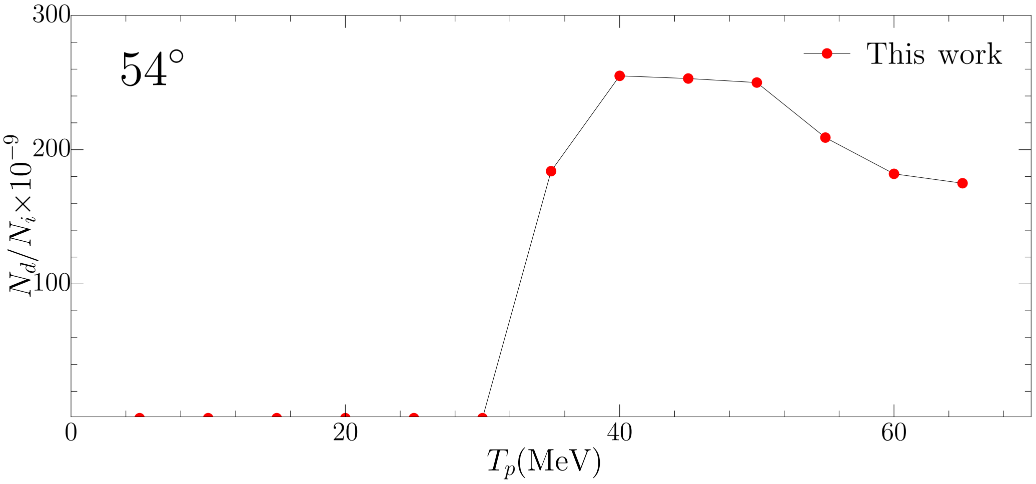

Figure D.2. The ratio of the detected deuterons to the incident neutrons w.r.t. deuteron energy.

APPENDIX E: Figures for Alternative Method Analysis at 200 ± 5 MeV

Here, we present all the figures resulting from our fitting method and one can identify the graphs by their captions. The letters d and f in the caption represent in-the-cut and outside-the-cut events, respectively. The first number is the index for CsI detectors which ranges from 0 to 5 (backward to forward neutron angle), the second is the neutron bar index going from top to bottom. For instance, *nbar200_d_0_2* represents the middle bar histogram corresponding 24° CsI with the graphical cut and *nbar200_f_1_1* is the second from top bar corresponding 30° CsI accepting events outside the cut.

E.1. The fits for the analysis

E.1.1. The fits for 200 MeV with normal cut

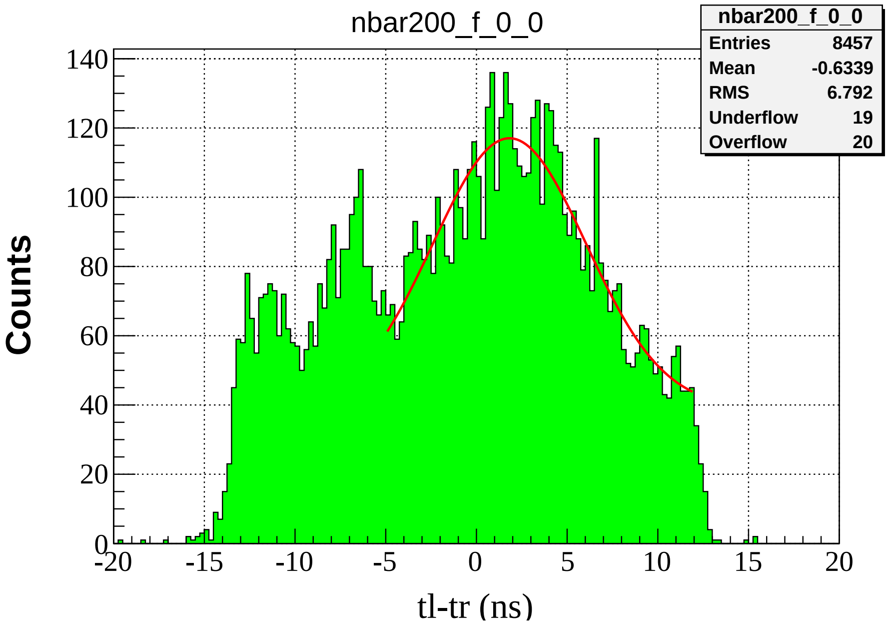

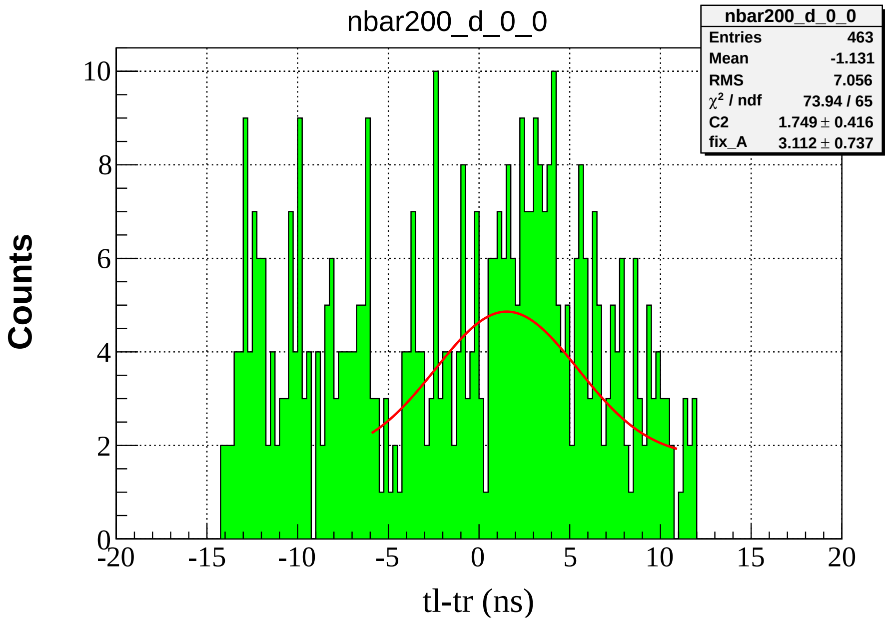

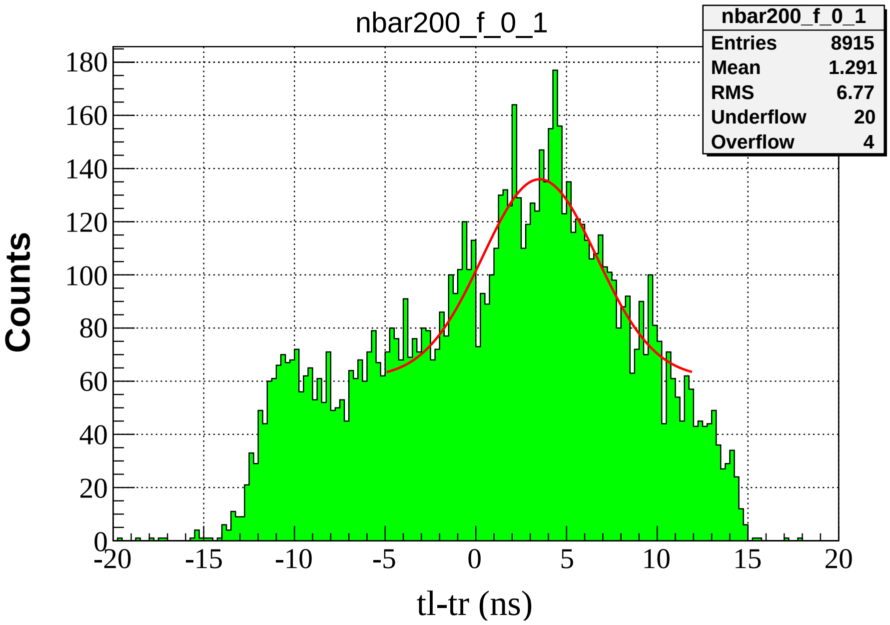
nbar200_f_0_1
nbar200_f_0_1
Entries 8915
Mean 1.291
RMS 6.77
Underflow 20
Overflow 4
Counts
0
20
40
60
80
100
120
140
160
180
-20
-15
-10
-5
0
5
10
15
20
tl-tr (ns)

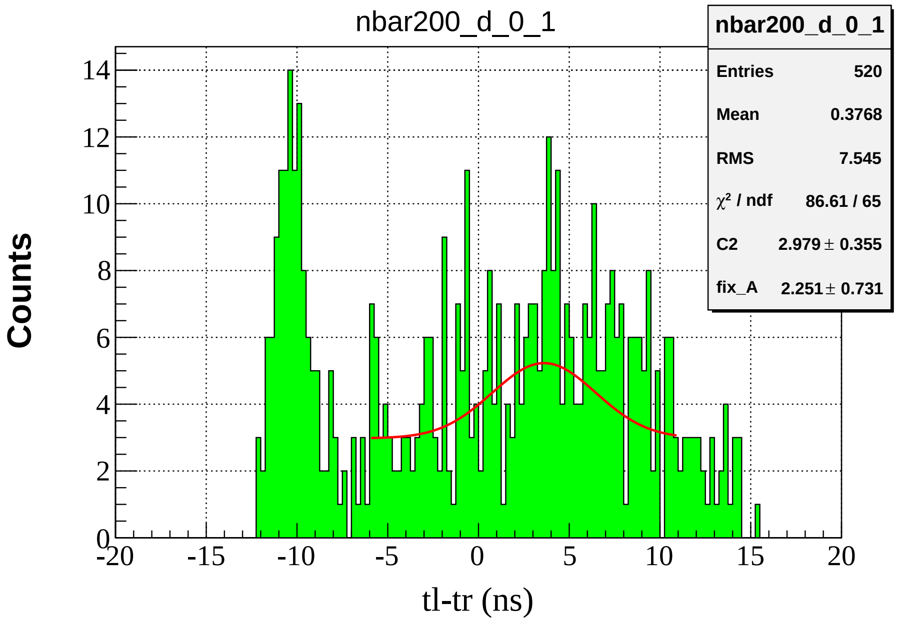
nbar200_d_0_1
nbar200_d_0_1
Entries 520
Mean 0.3768
RMS 7.545
χ^2 / ndf 86.61 / 65
C2 2.979 ± 0.355
fix_A 2.251 ± 0.731
Counts
0
2
4
6
8
10
12
14
-20
-15
-10
-5
0
5
10
15
20
tl-tr (ns)

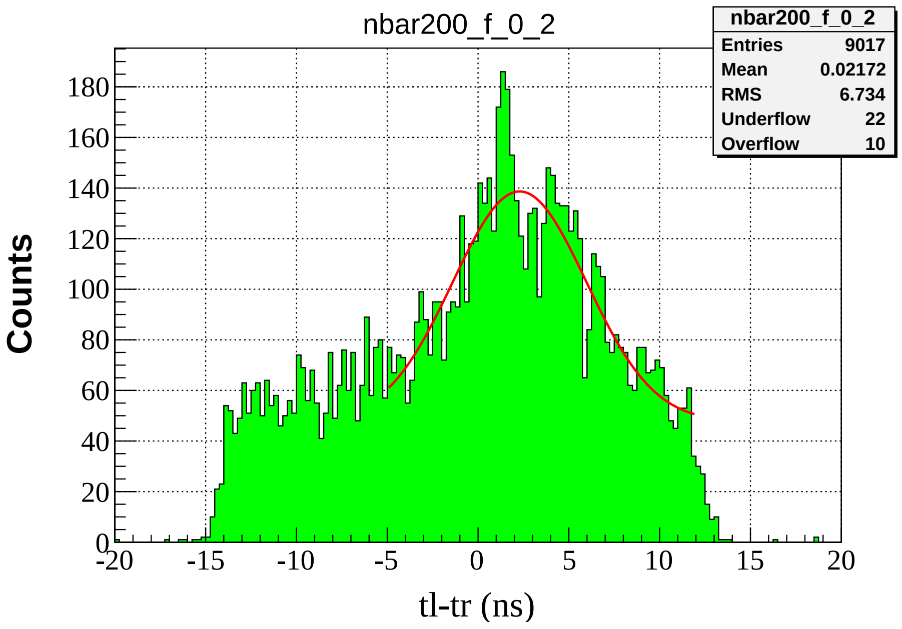
nbar200_f_0_2
nbar200_f_0_2
Entries 9017
Mean 0.02172
RMS 6.734
Underflow 22
Overflow 10
Counts
0
20
40
60
80
100
120
140
160
180
-20
-15
-10
-5
0
5
10
15
20
tl-tr (ns)

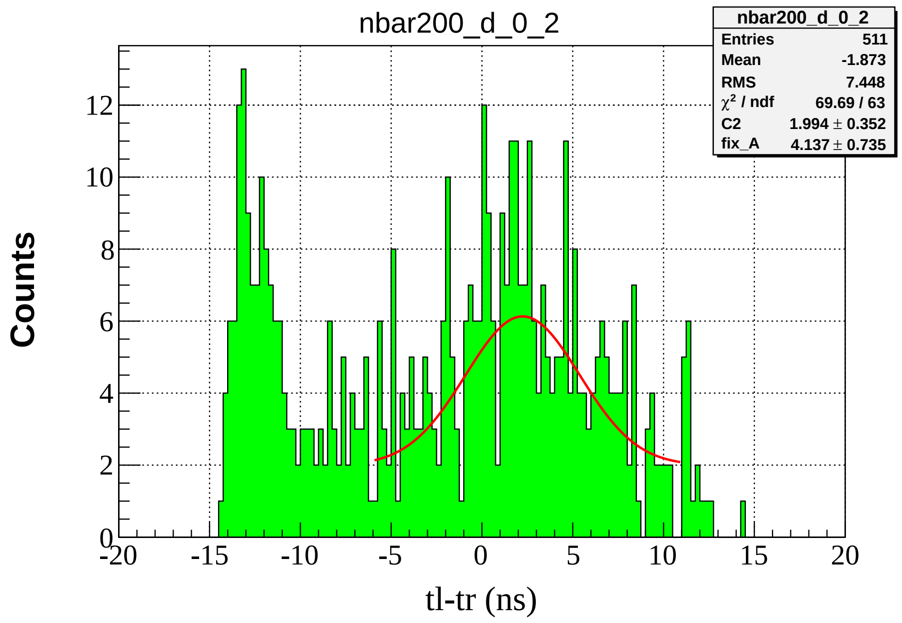
nbar200_d_0_2
nbar200_d_0_2
Entries 511
Mean -1.873
RMS 7.448
χ^2 / ndf 69.69 / 63
C2 1.994 ± 0.352
fix_A 4.137 ± 0.735
Counts
0
2
4
6
8
10
12
-20
-15
-10
-5
0
5
10
15
20
tl-tr (ns)

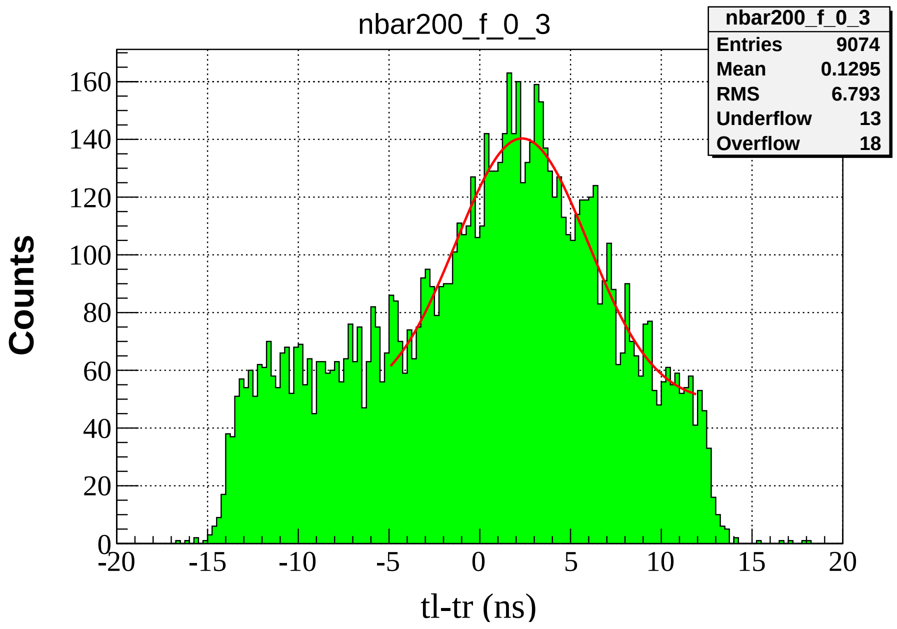
nbar200_f_0_3
nbar200_f_0_3
Entries 9074
Mean 0.1295
RMS 6.793
Underflow 13
Overflow 18
Counts
0
20
40
60
80
100
120
140
160
-20
-15
-10
-5
0
5
10
15
20
tl-tr (ns)

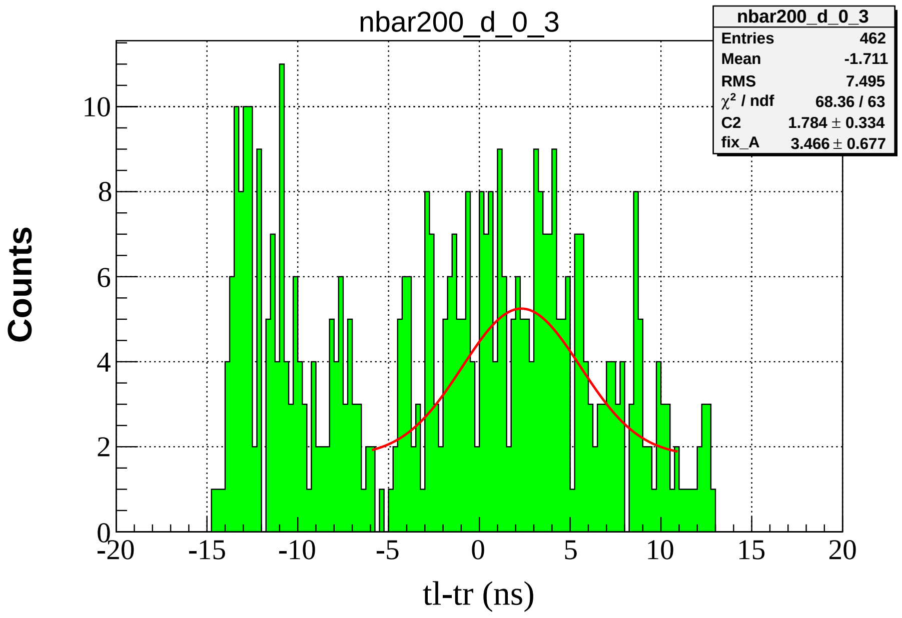
nbar200_d_0_3
nbar200_d_0_3
Entries 462
Mean -1.711
RMS 7.495
χ^2 / ndf 68.36 / 63
C2 1.784 ± 0.334
fix_A 3.466 ± 0.677
Counts
0
2
4
6
8
10
-20
-15
-10
-5
0
5
10
15
20
tl-tr (ns)

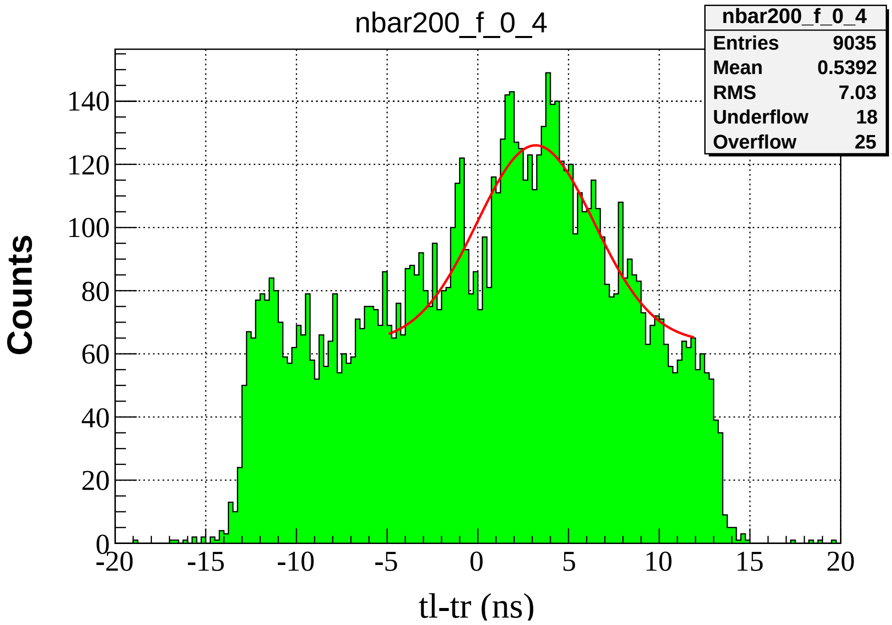
nbar200_f_0_4
nbar200_f_0_4
Entries 9035
Mean 0.5392
RMS 7.03
Underflow 18
Overflow 25
Counts
0
20
40
60
80
100
120
140
-20
-15
-10
-5
0
5
10
15
20
tl-tr (ns)

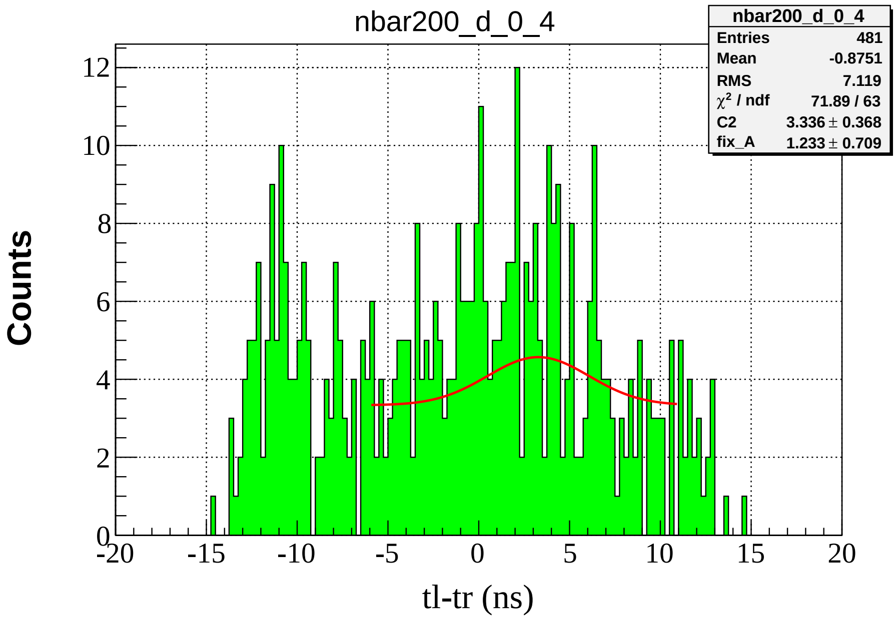
nbar200_d_0_4
nbar200_d_0_4
Entries 481
Mean -0.8751
RMS 7.119
χ^2 / ndf 71.89 / 63
C2 3.336 ± 0.368
fix_A 1.233 ± 0.709
Counts
0
2
4
6
8
10
12
-20
-15
-10
-5
0
5
10
15
20
tl-tr (ns)

E.1.2. The fits for 200 MeV with tight cut

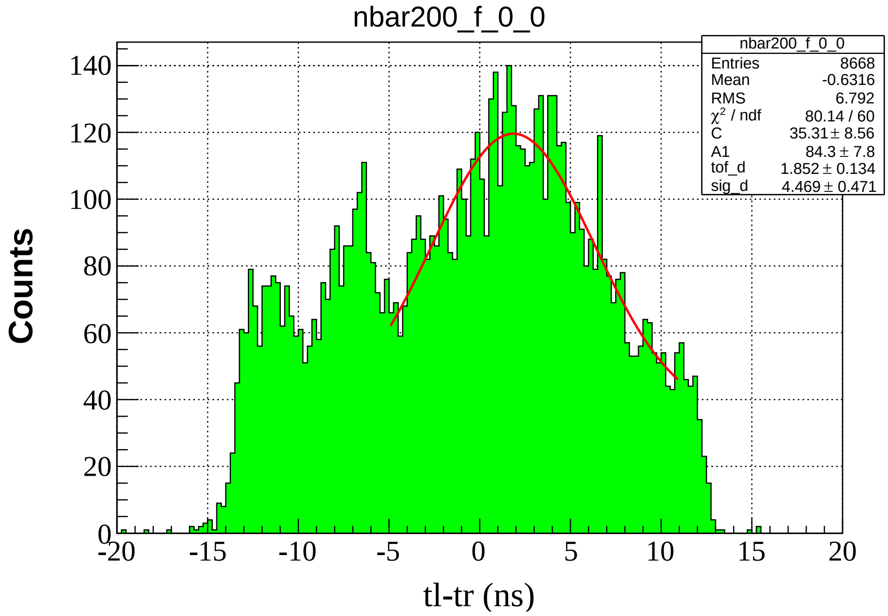

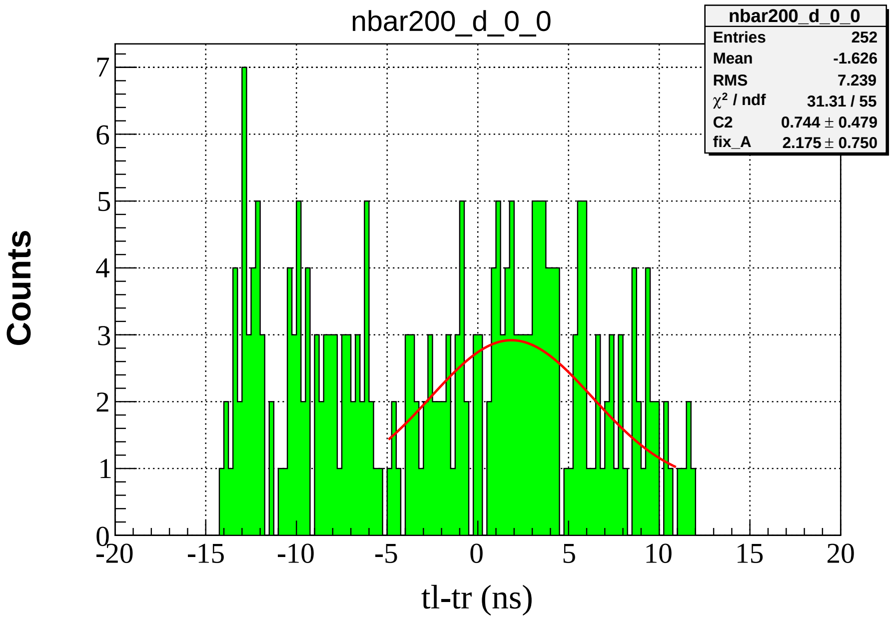

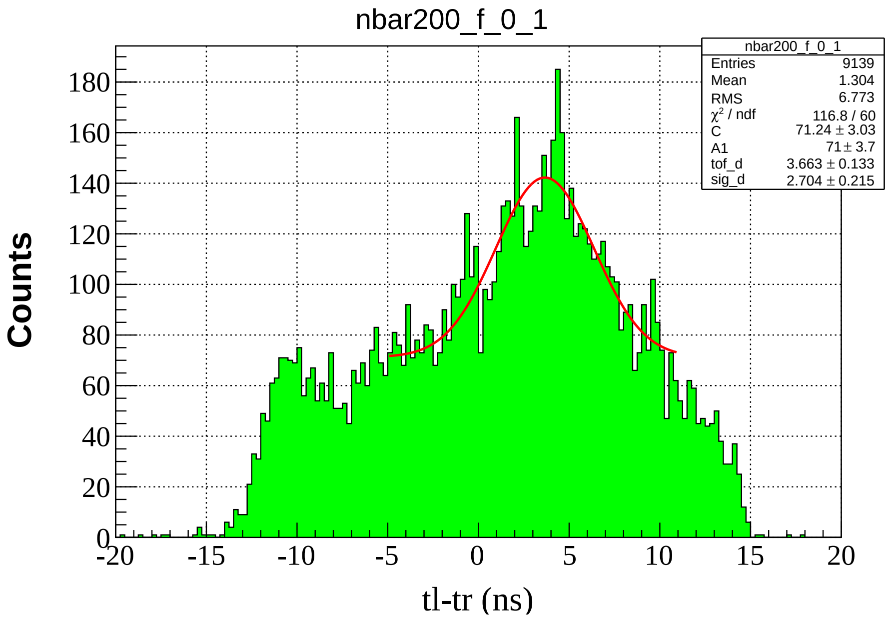
nbar200_f_0_1
nbar200_f_0_1
Entries 9139
Mean 1.304
RMS 6.773
χ^2 / ndf 116.8 / 60
C 71.24 ± 3.03
A1 71 ± 3.7
tof_d 3.663 ± 0.133
sig_d 2.704 ± 0.215
Counts
0
20
40
60
80
100
120
140
160
180
-20
-15
-10
-5
0
5
10
15
20
tl-tr (ns)

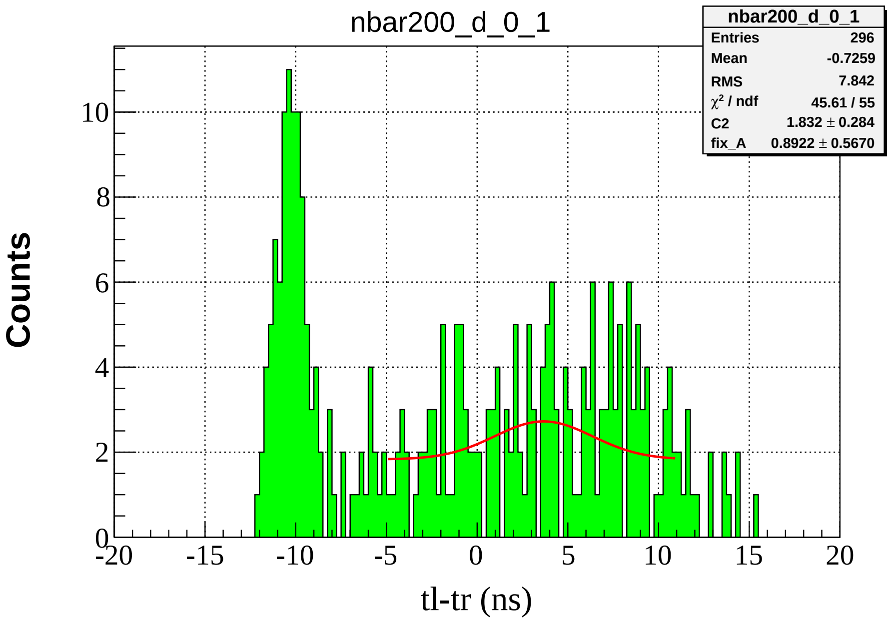
nbar200_d_0_1
nbar200_d_0_1
Entries 296
Mean -0.7259
RMS 7.842
χ^2 / ndf 45.61 / 55
C2 1.832 ± 0.284
fix_A 0.8922 ± 0.5670
Counts
0
2
4
6
8
10
-20
-15
-10
-5
0
5
10
15
20
tl-tr (ns)

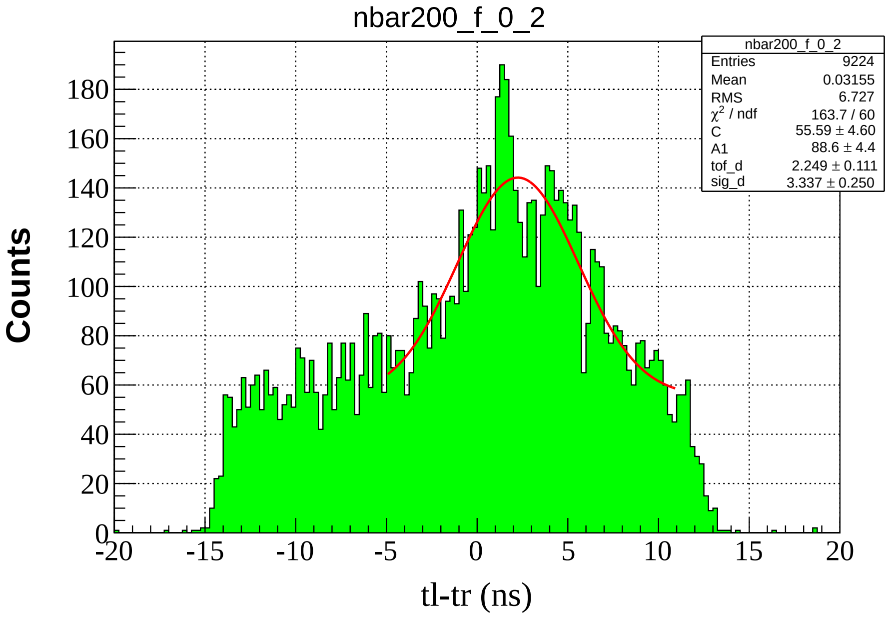
nbar200_f_0_2
nbar200_f_0_2
Entries 9224
Mean 0.03155
RMS 6.727
χ^2 / ndf 163.7 / 60
C 55.59 ± 4.60
A1 88.6 ± 4.4
tof_d 2.249 ± 0.111
sig_d 3.337 ± 0.250
Counts
tl-tr (ns)
0
20
40
60
80
100
120
140
160
180
-20
-15
-10
-5
0
5
10
15
20

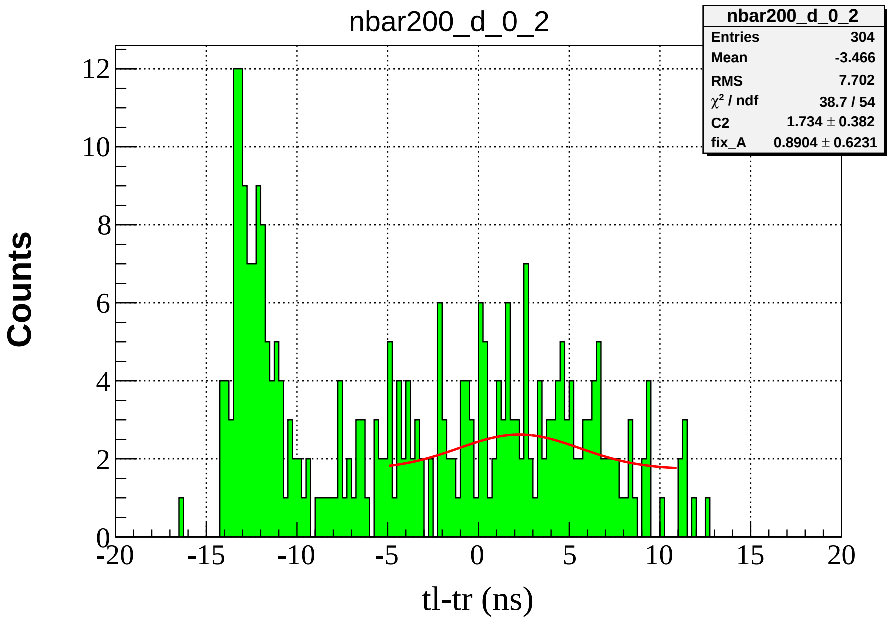
nbar200_d_0_2
nbar200_d_0_2
Entries 304
Mean -3.466
RMS 7.702
χ^2 / ndf 38.7 / 54
C2 1.734 ± 0.382
fix_A 0.8904 ± 0.6231
Counts
tl-tr (ns)
0
2
4
6
8
10
12
-20
-15
-10
-5
0
5
10
15
20

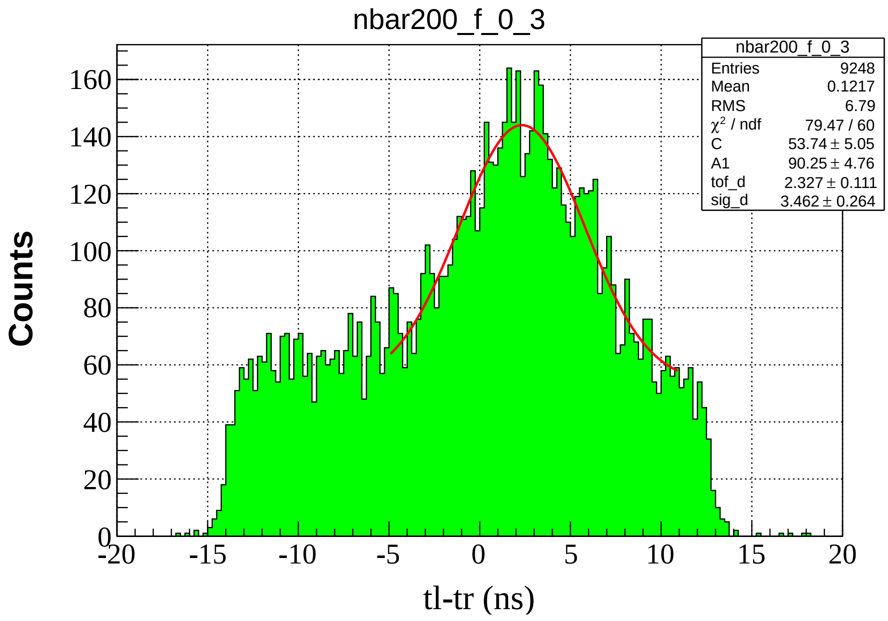
nbar200_f_0_3
nbar200_f_0_3
Entries 9248
Mean 0.1217
RMS 6.79
χ^2 / ndf 79.47 / 60
C 53.74 ± 5.05
A1 90.25 ± 4.76
tof_d 2.327 ± 0.111
sig_d 3.462 ± 0.264
Counts
0
20
40
60
80
100
120
140
160
-20
-15
-10
-5
0
5
10
15
20
tl-tr (ns)

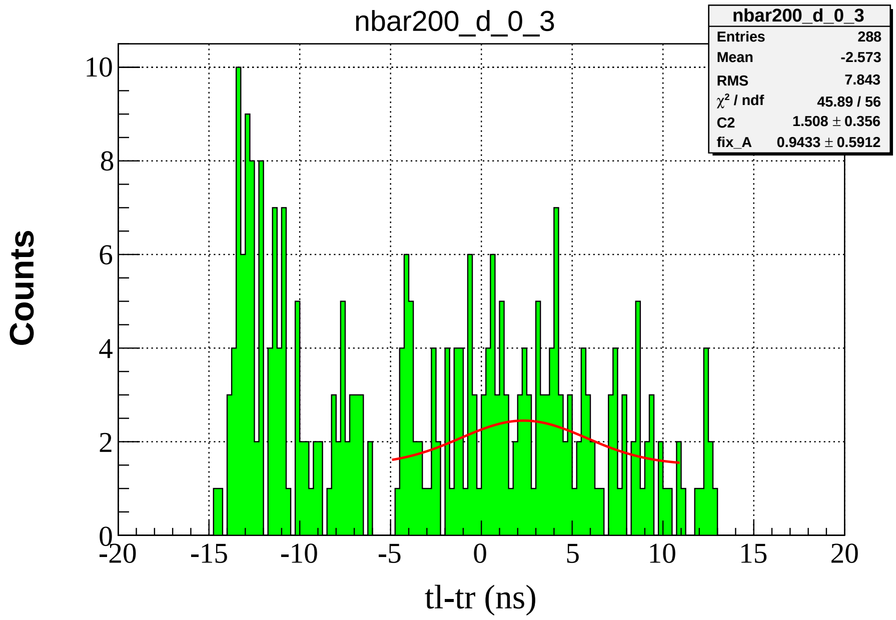
nbar200_d_0_3
nbar200_d_0_3
Entries 288
Mean -2.573
RMS 7.843
χ^2 / ndf 45.89 / 56
C2 1.508 ± 0.356
fix_A 0.9433 ± 0.5912
Counts
0
2
4
6
8
10
-20
-15
-10
-5
0
5
10
15
20
tl-tr (ns)

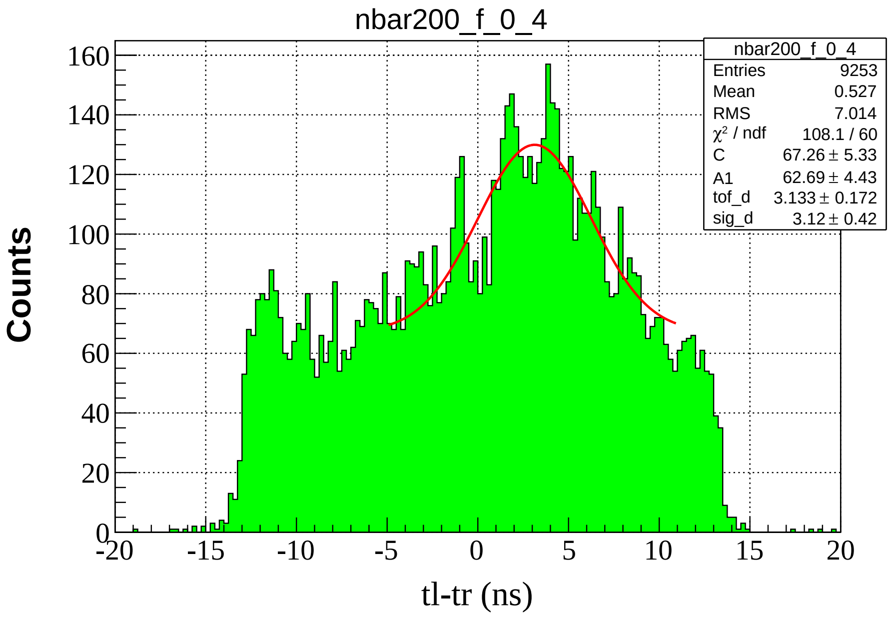
nbar200_f_0_4
nbar200_f_0_4
Entries 9253
Mean 0.527
RMS 7.014
χ^2 / ndf 108.1 / 60
C 67.26 ± 5.33
A1 62.69 ± 4.43
tof_d 3.133 ± 0.172
sig_d 3.12 ± 0.42
Counts
0
20
40
60
80
100
120
140
160
-20
-15
-10
-5
0
5
10
15
20
tl-tr (ns)

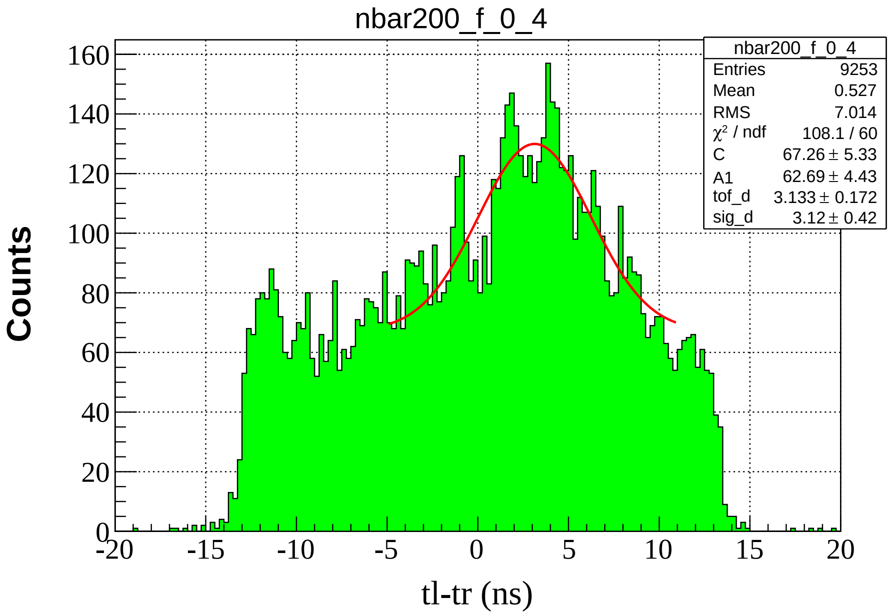
nbar200_f_0_4
nbar200_f_0_4
Entries 9253
Mean 0.527
RMS 7.014
χ^2 / ndf 108.1 / 60
C 67.26 ± 5.33
A1 62.69 ± 4.43
tof_d 3.133 ± 0.172
sig_d 3.12 ± 0.42
Counts
0
20
40
60
80
100
120
140
160
-20
-15
-10
-5
0
5
10
15
20
tl-tr (ns)

E.1.3. The fits for 200 MeV with wide cut

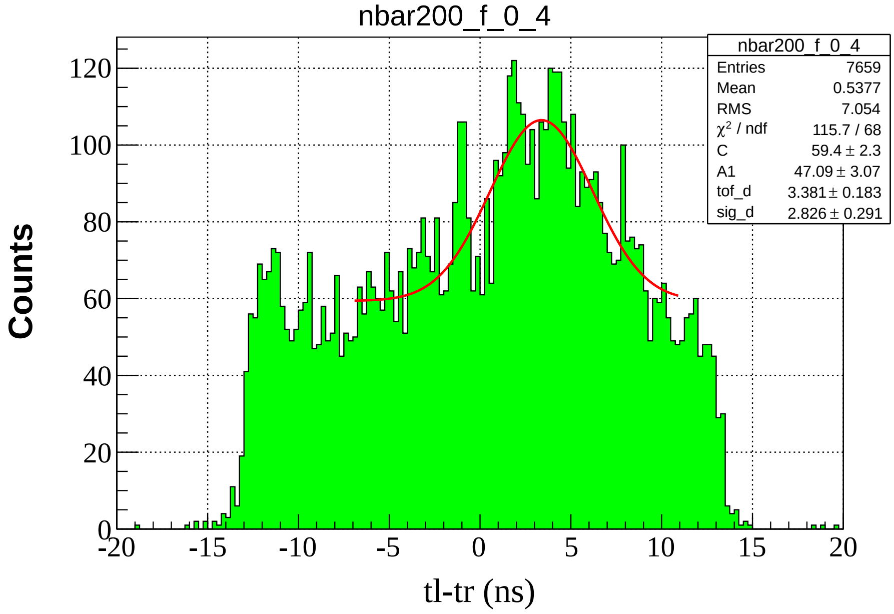

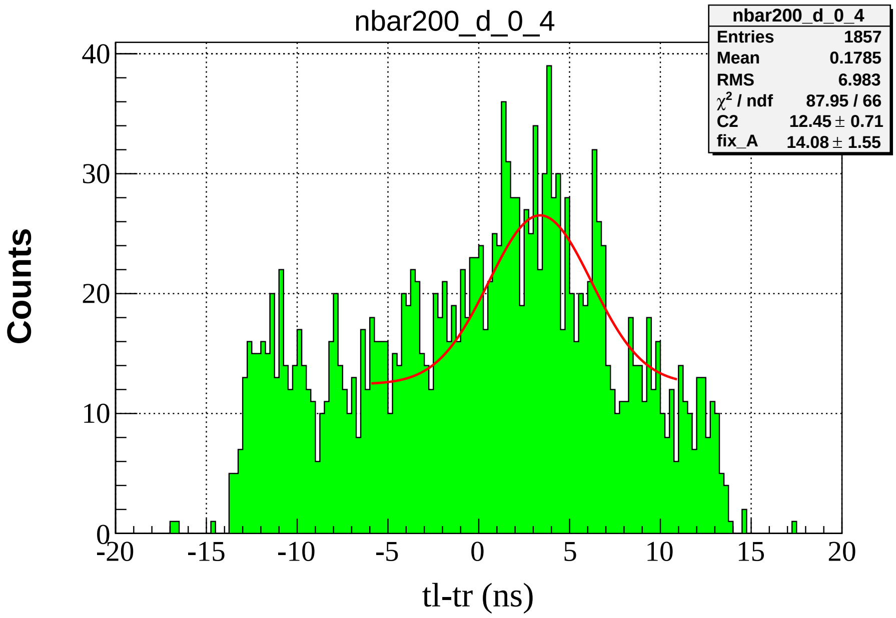

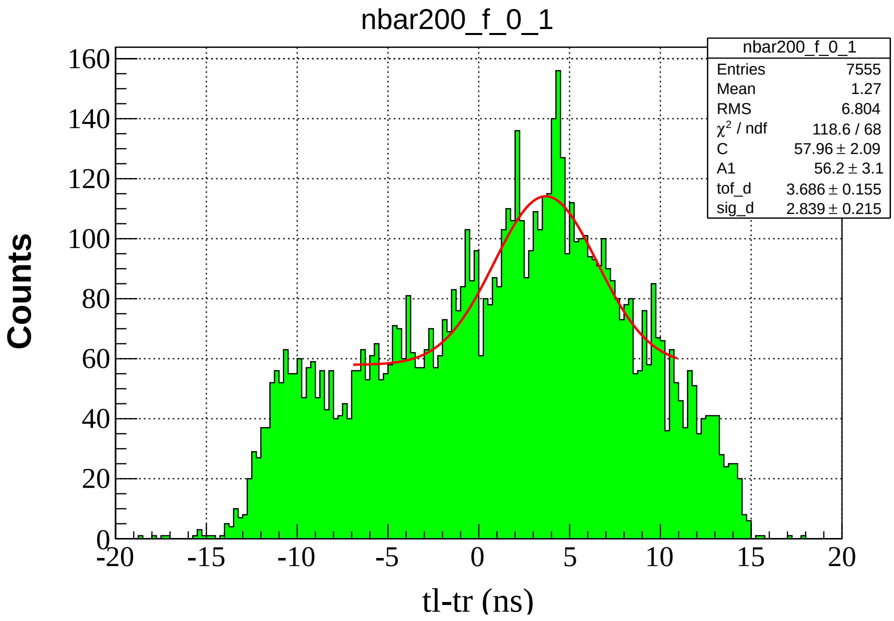
nbar200_f_0_1
nbar200_f_0_1
Entries 7555
Mean 1.27
RMS 6.804
χ^2 / ndf 118.6 / 68
C 57.96 ± 2.09
A1 56.2 ± 3.1
tof_d 3.686 ± 0.155
sig_d 2.839 ± 0.215
Counts
160
140
120
100
80
60
40
20
0
-20
-15
-10
-5
0
5
10
15
20
tl-tr (ns)

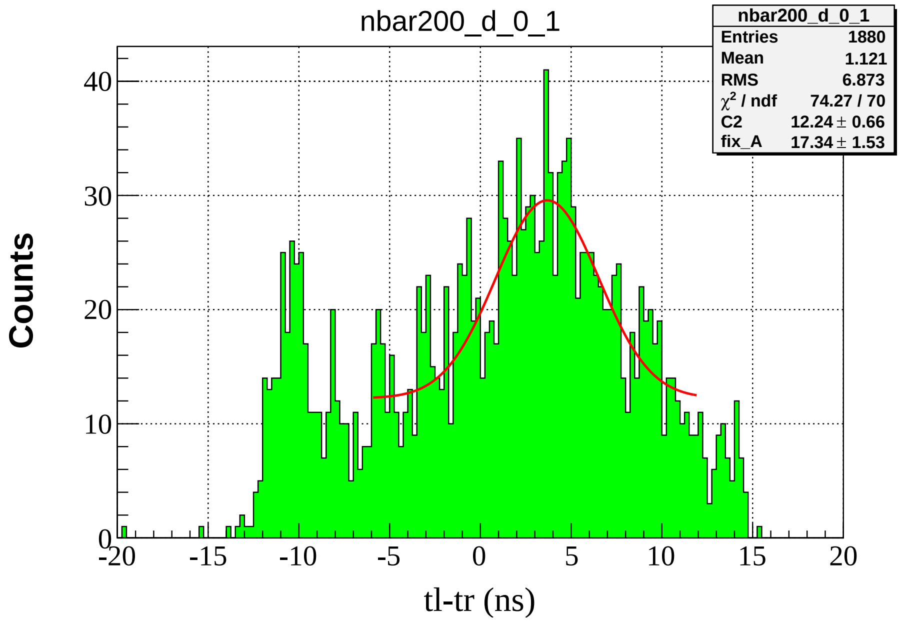
nbar200_d_0_1
nbar200_d_0_1
Entries 1880
Mean 1.121
RMS 6.873
χ^2 / ndf 74.27 / 70
C2 12.24 ± 0.66
fix_A 17.34 ± 1.53
Counts
40
30
20
10
0
-20
-15
-10
-5
0
5
10
15
20
tl-tr (ns)

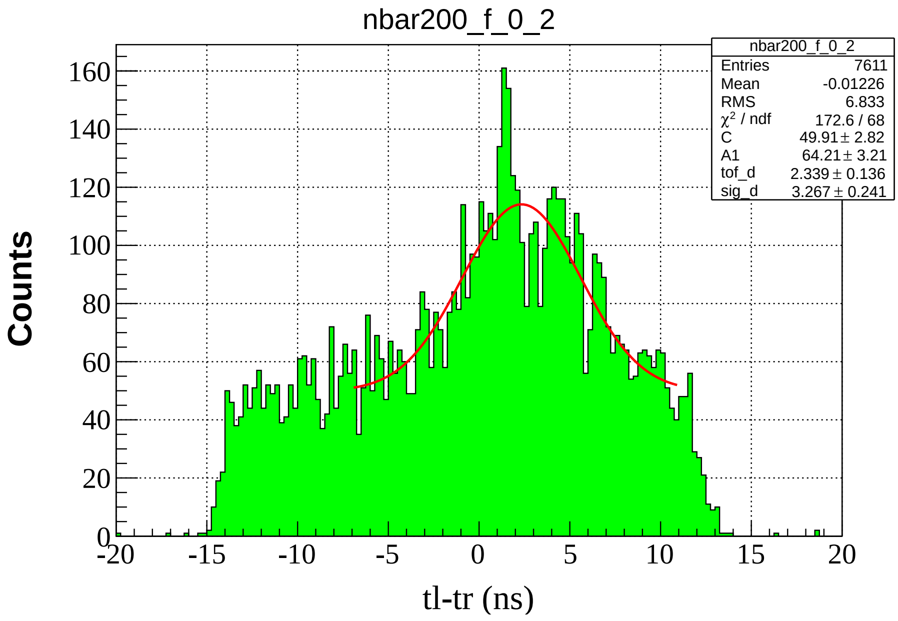
nbar200_f_0_2
nbar200_f_0_2
Entries 7611
Mean -0.01226
RMS 6.833
χ^2 / ndf 172.6 / 68
C 49.91 ± 2.82
A1 64.21 ± 3.21
tof_d 2.339 ± 0.136
sig_d 3.267 ± 0.241
Counts
0
20
40
60
80
100
120
140
160
-20
-15
-10
-5
0
5
10
15
20
tl-tr (ns)

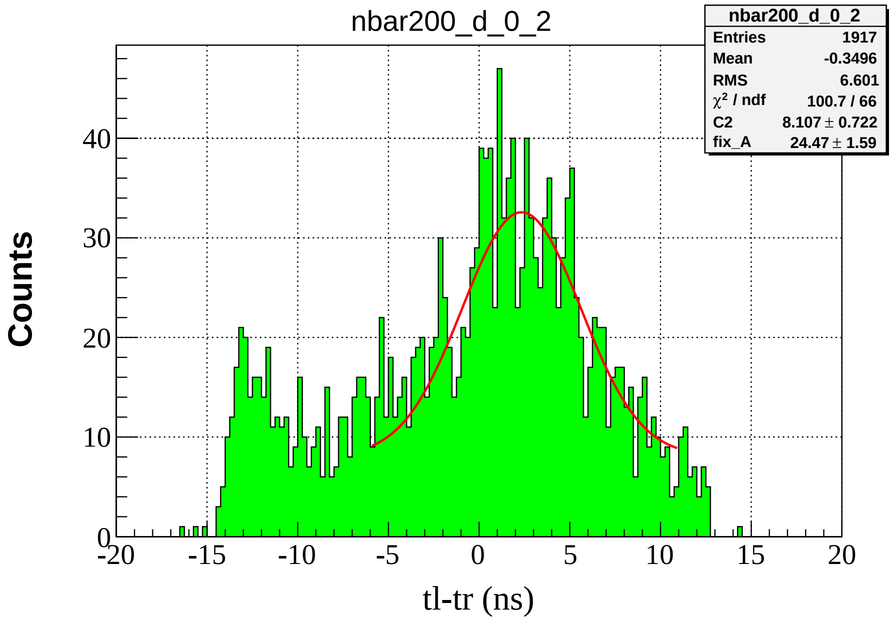
nbar200_d_0_2
nbar200_d_0_2
Entries 1917
Mean -0.3496
RMS 6.601
χ^2 / ndf 100.7 / 66
C2 8.107 ± 0.722
fix_A 24.47 ± 1.59
Counts
0
10
20
30
40
-20
-15
-10
-5
0
5
10
15
20
tl-tr (ns)

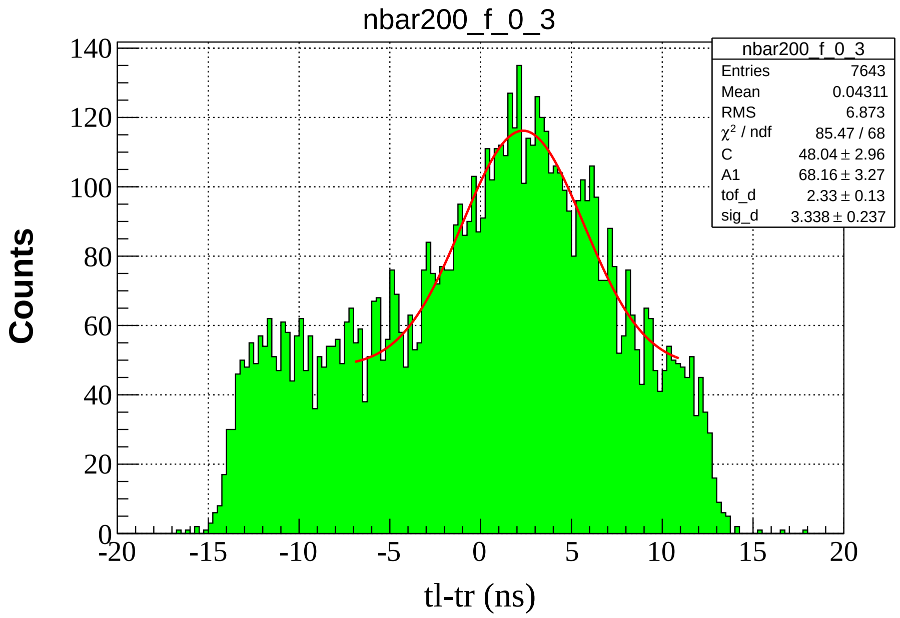
nbar200_f_0_3
nbar200_f_0_3
Entries 7643
Mean 0.04311
RMS 6.873
χ^2 / ndf 85.47 / 68
C 48.04 ± 2.96
A1 68.16 ± 3.27
tof_d 2.33 ± 0.13
sig_d 3.338 ± 0.237
Counts
0
20
40
60
80
100
120
140
-20
-15
-10
-5
0
5
10
15
20
tl-tr (ns)

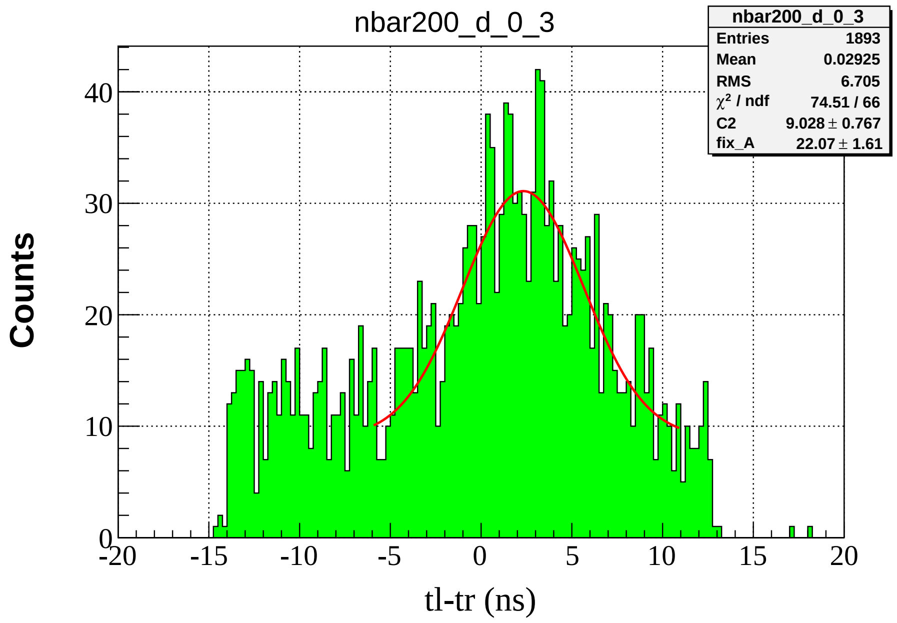
nbar200_d_0_3
nbar200_d_0_3
Entries 1893
Mean 0.02925
RMS 6.705
χ^2 / ndf 74.51 / 66
C2 9.028 ± 0.767
fix_A 22.07 ± 1.61
Counts
0
10
20
30
40
-20
-15
-10
-5
0
5
10
15
20
tl-tr (ns)

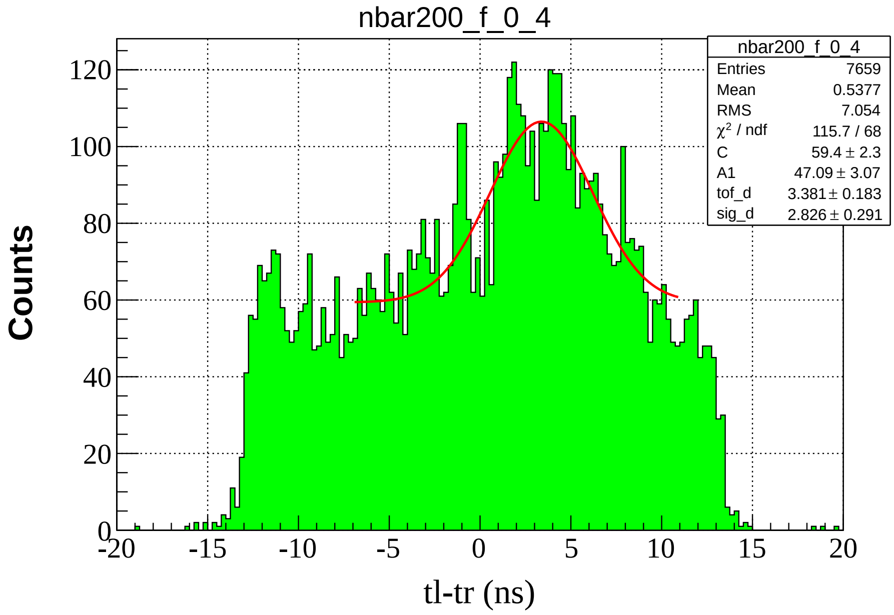
nbar200_f_0_4
nbar200_f_0_4
Entries 7659
Mean 0.5377
RMS 7.054
χ^2 / ndf 115.7 / 68
C 59.4 ± 2.3
A1 47.09 ± 3.07
tof_d 3.381 ± 0.183
sig_d 2.826 ± 0.291
Counts
0
20
40
60
80
100
120
-20
-15
-10
-5
0
5
10
15
20
tl-tr (ns)

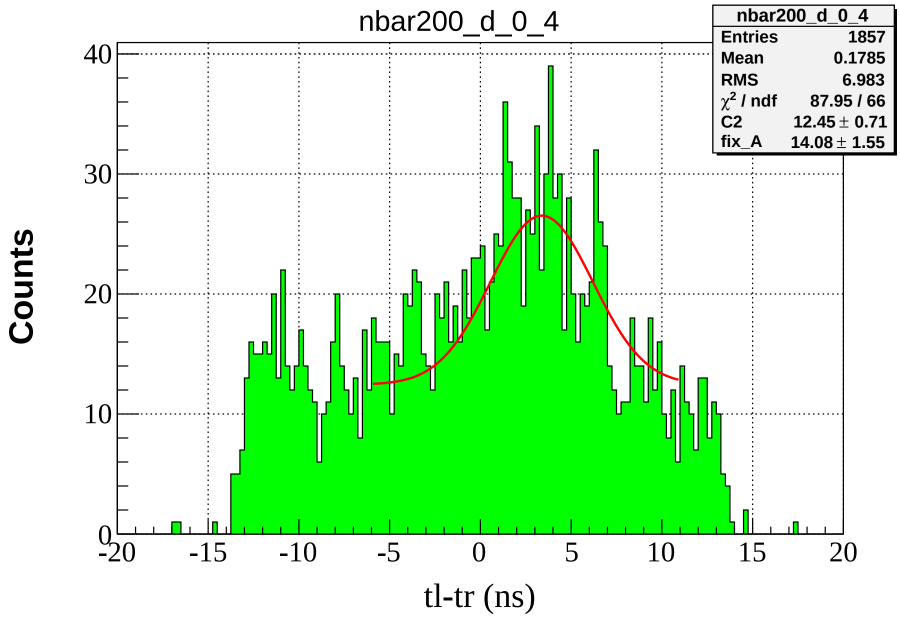
nbar200_d_0_4
nbar200_d_0_4
Entries 1857
Mean 0.1785
RMS 6.983
χ^2 / ndf 87.95 / 66
C2 12.45 ± 0.71
fix_A 14.08 ± 1.55
Counts
0
10
20
30
40
-20
-15
-10
-5
0
5
10
15
20
tl-tr (ns)

REFERENCES

1. Ertan, E., T. Akdogan, M. B. Chtangeev, W. A. Franklin, P. A. M. Gram, M. A. Kovash, J. L. Matthews and M. Yuly, “Cross Sections for Neutron-Deuteron Elastic Scattering in the Energy Range 135-250 MeV”, *Physical Review C*, Vol. 87, p. 034003, 2013.

2. Chtangeev, M. B., *Neutron-Deuteron Elastic Scattering and Three-Nucleon Force*, M.S. Thesis, Massachusetts Institute of Technology, 2005.

3. Machleidt, R., “High-Precision, Charge-Dependent Bonn Nucleon-Nucleon Potential”, *Physical Review C*, Vol. 63, p. 024001, 2001.

4. Stoks, V. G. J., R. A. M. Klomp, C. P. F. Terheggen and J. J. de Swart, “Construction of High-Quality NN Potential Models”, *Physical Review C*, Vol. 49, pp. 2950–2962, 1994.

5. Wiringa, R. B., V. G. J. Stoks and R. Schiavilla, “Accurate Nucleon-Nucleon Potential With Charge-Independence Breaking”, *Physical Review C*, Vol. 51, No. 1, 1995.

6. Kuros-Zolnierchuk, J. , *Three-Body Effects in Neutron-Deuteron Scattering*, Ph.D. Thesis, 2002.

7. Ishii, N., S. Aoki and T. Hatsuda, “Nuclear Force from Lattice QCD”, *Physical Review Letters*, Vol. 99, p. 022001, 2007.

8. Cecil, R. A., B. D. Anderson and R. Madey, “Improved Predictions of Neutron Detection Efficiency for Hydrocarbon Scintillators from 1 MeV to about 300 MeV”, *Nuclear Instruments and Methods*, Vol. 161, pp. 439–447, 1979.

9. Hough, J., *Polarization of High Energy Neutrons in Proton-Nucleus Scattering*, B.S. Thesis, Massachusetts Institute of Technology, 2001.

10. Ermisch, K. *et al.*, "Systematic Investigation of Three-Nucleon Force Effects in Elastic Scattering of Polarized Protons from Deuterons at Intermediate Energies", *Physical Review C*, Vol. 71, p. 064004, 2005.

11. Ramazani-Moghaddam-Arani, A. *et al.*, "Elastic Proton-Deuteron Elastic Scattering at Intermediate Energies", *Physical Review C*, Vol. 78, p. 014006, 2008.

12. Palmieri, J. N., "Neutron-Deuteron Scattering at 152 MeV", *Nuclear Physics A*, Vol. 188, 1972.

13. Postma, H. and R. Wilson, "Elastic Scattering of 146-Mev Polarized Protons by Deuterons", *Physical Review*, Vol. 121, pp. 1229–1244, 1961.

14. Igo, G., J. Fong, S. Verbeck, M. Goitein, D. Hendrie, J. Carroll, B. McDonald, A. Stetz and M. Makino, "Large-Angle Elastic Scattering of Deuterons from Hydrogen: Tk = 433, 362 and 291 MeV", *Nuclear Physics A*, Vol. 195, No. 1, pp. 33 – 56, 1972.

15. Adelberger, R. E. and C. N. Brown, "$p-d$ Elastic Cross Section and Polarization at $198MeV$", *Physical Review D*, Vol. 9, p. 2139, 1972.

16. Hatanaka, A. *et al.*, "Cross Section and Complete Set of Proton Spin Observables in pd Elastic Scattering at 250 MeV", *Physical Review C*, Vol. 66, p. 044002, 2002.

17. Maeda, Y. *et al.*, "Differential Cross Section and Analyzing Power Measurements for nd Elastic Scattering at 248 MeV", *Physical Review C*, Vol. 76, p. 014004, 2007.

18. Sakai, H. *et al.*, "Precise Measurement of dp Elastic Scattering at 270 MeV and Three-Nucleon Force Effects", *Physical Review Letters*, Vol. 84, No. 23, p. 5288, 2000.

19. Witała, H., W. Glöckle, D. Hüber, J. Golak and H. Kamada, "Cross Section Minima in Elastic *Nd* Scattering: Possible Evidence for Three-Nucleon Force Effects", *Physical Review Letters*, Vol. 81, pp. 1183–1186, 1998.

20. Deltuva, A., R. Machleidt and P. U. Sauer, “Realistic Two-Baryon Potential Coupling Two-Nucleon and Nucleon-Delta-Isobar States: Fit and Applications to Three-Nucleon System”, *Physical Review C*, Vol. 68, p. 024005, 2003.

21. Witała, H., J. Golak, R. Skibiński, W. Glöckle, H. Kamada and W. N. Polyzou, “Three-Nucleon Force in Relativistic Three-Nucleon Faddeev Calculations”, *Physical Review C*, Vol. 83, p. 044001, 2011.

22. Chodos, A., R. L. Jaffe, K. Johnson and C. B. Thorn, “Baryon Structure in the Bag Theory”, *Physical Review D*, Vol. 10, pp. 2599–2604, 1974.

23. Primakoff, H. and T. Holstein, “Many-Body Interactions in Atomic and Nuclear Systems”, *Physical Review*, Vol. 55, pp. 1218–1234, 1939.

24. Sekiguchi, K. *et al.*, “Resolving the Discrepancy of 135 MeV pd Elastic Sacattering Cross Sections and Relativistic Effects”, *Physical Review Letters*, Vol. 95, 2005.

25. Nogga, A., H. Kamada, W. Glöckle and B. R. Barrett, “The α Particle Based on Modern Nuclear Forces”, *Physical Review C*, Vol. 65, p. 054003, 2002.

26. Nogga, A., H. Kamada and W. Glöckle, “Modern Nuclear Force Predictions for the Alpha Particle”, *Physical Review Letters*, Vol. 85, pp. 944–947, 2000.

27. Fujita, J. and H. Miyazawa, “Pion Theory of Three-body Forces”, *Progress of Theoretical Physics*, Vol. 17, No. 3, 1957.

28. Coon, S. A. and W. Glöckle, “Two-Pion-Exchange Three-Nucleon Potential: Partial Wave Analysis in Momentum Space”, *Physical Review C*, Vol. 23, pp. 1790–1802, 1981.

29. Coon, S. A. and M. T. Pena, “Momentum and Coordinate Space Three-nucleon Potentials”, *Physical Review C*, Vol. 48, No. 6, 1993.

30. Carlson, J., V. R. Pandharipande and R. B. Wiringa, “Large-Angle Elastic Scat-

tering of Deuterons from Hydrogen: $T_k = 433, 362, 291 MeV$", *Nuclear Physics A*, Vol. 401, pp. 59–85, 1982.

31. Pudliner, B. S., V. R. Pandharipande, J. Carlson, S. C. Pieper and R. B. Wiringa, "Quantum Monte Carlo Calculations of Nuclei with A $<\sim$ 7", *Physical Review C*, Vol. 56, pp. 1720–1750, 1997.

32. Faddeev, L. D., "Three-Nucleon Force in Relativistic Three-Nucleon Faddeev Calculations", *Soviet Physics JETP*, Vol. 83, 1961.

33. Taylor, J., *Scattering Theory: The Quantum Theory of Nonrelativistic Collisions*, Dover Publications Incorporated, 1972.

34. Glöckle, W., *The Quantum Mechanical Few-Body Problem*, Theoretical and Mathematical Physics Series, Springer London, Limited, 2011.

35. Nagels, M. M., T. A. Rijken and J. J. de Swart, "Low-Energy Nucleon-Nucleon Potential from Regge-Pole Theory", *Physical Review D*, Vol. 17, pp. 768–776, 1978.

36. Coon, S. A., M. T. Peña and D. O. Riska, "Repulsive Short-Range Three-Nucleon Interaction", *Physical Review C*, Vol. 52, pp. 2925–2935, 1995.

37. Witała, H., D. Hüber, W. Glöckle, J. Golak, A. Stadler and J. Adam, "Effects of the Three-Nucleon Forces due to π and ρ Meson Exchanges in the Three-Nucleon Continuum", *Physical Review C*, Vol. 52, pp. 1254–1259, 1995.

38. Keister, B. and R. Wiringa, "Implications of Dirac Nucleon Dynamics for the Binding of Light Nuclei", *Physics Letters B*, Vol. 173, No. 1, pp. 5 – 9, 1986.

39. Friar, J. L., D. Hüber and U. van Kolck, "Chiral Symmetry and Three-Nucleon Forces", *Physical Review C*, Vol. 59, pp. 53–58, 1999.

40. Hüber, D., J. L. Friar, A. Nogga, H. Witała and U. van Kolck, "Novel Three-Nucleon-Force Terms in the Three-Nucleon System", *Few-Body Systems*, Vol. 30,

pp. 95–120, 2001.

41. Liu, H., *Studies of the Nuclear Three-Body System with Three Dimensional Faddeev Calculations*, Ph.D. Thesis, Ohio University, 2005.
42. Greiner, W., S. Schramm, E. Stein and D. A. Bromley, *Quantum Chromodynamics*, Springer, 2007.
43. Metropolis, N., A. W. Rosenbluth, M. N. Rosenbluth, A. H. Teller and E. Teller, “Equation of State Calculations by Fast Computing Machines”, *The Journal of Chemical Physics*, Vol. 21, No. 6, pp. 1087–1092, 1953.
44. Ermisch, K. *et al.*, “Systematic Investigation of the Elastic Proton-Deuteron Differential Cross Section at Intermediate Energies”, *Physical Review C*, Vol. 68, p. 051001, 2003.
45. Arndt, R., I. Strakovsky and R. Workman, “Nucleon-nucleon elastic scattering to 3 GeV”, *Physical Review D*, Vol. 62, p. 034005, 2000.
46. Akdogan, T., *Pion production in the neutron-proton interaction*, Ph.D. Thesis, Massachusetts Institute of Technology, 2003.
47. Wender, S. A. *et al.*, “A Fission Ionization Detector for Neutron Flux Measurements at a Spallation Source”, *Nuclear Instruments and Methods in Physics Research A*, Vol. 336, pp. 226–231, 1993.
48. Berger, M. J., *ESTAR, PSTAR, and ASTAR: Computer programs for calculating stopping-power and range tables for electrons, protons, and helium ions*, Tech. rep., 1992.